

Rock-slope failures in Norway - temporal development and climatic conditioning

Paula Hilger



Dissertation submitted for the degree of Philosophiae Doctor (PhD)

Department of Geosciences
Faculty of Mathematics and Natural Sciences
University of Oslo

Oslo, Norway
March 2019

© **Paula Hilger, 2019**

*Series of dissertations submitted to the
Faculty of Mathematics and Natural Sciences, University of Oslo
No. 2102*

ISSN 1501-7710

All rights reserved. No part of this publication may be
reproduced or transmitted, in any form or by any means, without permission.

Cover: Hanne Baadsgaard Utigard.
Print production: Representralen, University of Oslo.

Abstract

In previously glaciated mountain regions rock-slope failure processes contribute significantly to landscape development and may pose a direct or indirect threat to the population and infrastructure in inhabited areas. In Norway, most of the population lives along fjords and valleys which are highly exposed to rock-slope failures and potential secondary effects, such as displacement waves and catastrophic flooding due to the breaching of landslide dams. To minimise potential consequences, it is important to understand the preparatory factors destabilising rock slopes before they fail catastrophically. Rock-slope destabilisation in paraglacial landscapes is driven by several internal and external factors, adding to the structural pre-conditions, which are a significant component in crystalline rocks. In this thesis, it is demonstrated that the temporal distribution of catastrophic rock-slope failures (CRSF) in Norway is strongly linked to climatic factors, such as ground temperatures and permafrost, as well as to debuitressing effects after deglaciation.

For the age determination of rock-slope failure events, terrestrial cosmogenic nuclide (TCN) dating techniques were applied, which was complemented with Quaternary geological mapping. As a first step, uncertainty of inheritance was evaluated on a recent rock avalanche in Patagonia (Chile), determining the amount of inherited ^{10}Be concentrations in each sample. The analysis showed that CRSF boulders are likely to be affected by inheritance, leading to a general age overestimation. The effect, however, is dependent on the real exposure age and the exposure and burial history of the pre-failure surface.

In northern and western Norway, the failure timing of several pre-historic CRSFs at Rombakstøtta in Nordland, at Mannen in Møre og Romsdal and at Ramnanosi in Sogn og Fjordane was determined. During the last decades, ^{10}Be dating has become increasingly popular for dating such rock-slope failure deposits. In this thesis, the approach was taken one step further, targeting near vertical sliding surfaces of actively deforming rock-slope instabilities for surface exposure dating. This allows for an estimation of the timing of initial failure and the subsequent rates of progressive deformation. The deformation history of six rock-slope instabilities was analysed, including Skjeringahaugane, Oppstadhornet and Mannen in western Norway, and Revdalsfjellet 1, Revdalsfjellet 2 and

Gamanjunni 3 in northern Norway. To set this into the context of climatic variations, the results of three temperature and precipitation reconstructions are analysed using one of them as forcing for a long-term reconstruction of the permafrost distribution in rock-walls.

The temporal distribution of CRSF events in Norway generally peaks shortly after deglaciation. At five sites, rock-slope failure activity was observed to follow the deglaciation closely, including the initial failure timing of at least two rock-slope instabilities. This early destabilisation is most likely related to debuitressing effects, when the glacial ice as counterweight was removed from the oversteepened rock slopes. At the Mannen site, a ‘stability crisis’ was identified, where the same slope failed 3-6 times within a few hundred years. Climatic conditions related to permafrost degradation and increased precipitation may have added to the sudden slope destabilisation 4.9 ± 0.6 ka ago. The initial failure timing of four rock-slope instabilities fall into the period of the Holocene thermal maximum (HTM). At Mannen (62°N , 1295 m asl.) and Revdalsfjellet 2 (69°N , 650 m asl.), the modelled ground temperatures were close to or above 0°C , when deformation started early in the HTM. Late permafrost degradation at Gamanjunni 3 (69°N , 1200 m asl.), which is located close to Revdalsfjellet, explains a time lag of over two millennia before initial failure.

The results of this thesis strengthen the hypothesis that climatic variability and related permafrost fluctuations have an effect on rock-slope stability in Norway. The temporal distribution generally reflects the results of other independent studies, with a peak shortly after deglaciation, high rock-slope failure activity during the HTM and a third period of activity between 5 and 2 ka ago.

Acknowledgements

This thesis is the result of a PhD project which could not have been more interesting and exciting in any way. I had the fortune to start my PhD with one month of fieldwork in the mountains and fjords of Norway where I have seen more than any tourist could ever hope for. Many field trips were to follow, in addition to research visits to Canada and conference attendances all over the world; permafrost courses in Japan and Svalbard were just two of many highlights. I feel very privileged that I have been given the opportunity to join and contribute to the CryoWALL project, which wouldn't have been possible without funding from the Norwegian Research Council and significant contributions from several people:

First of all, I want to thank my supervisor Reginald, without whom this part of the project would not have existed. I appreciate our many, many discussions in the field and in the office. I enjoyed working independently, but I could always come to you when I needed support and you often worked out of office hours to give me feedback. Thank you for a great time!

Bernd, thank you for organising and leading such a great project. You are the PhD supervisor that every PhD student can wish for. You were there for me 24/7, no matter if it was for a scientific or 'typical-PhD-student-psychological' issue and your feedback was always efficient and appropriate. You contributed significantly to an overall positive experience with many interesting meetings, courses and field trips.

Further I want to thank my third supervisor John for his support related to the exposure dating. I had two great and productive stays at your laboratory at Dalhousie University where I felt very welcome and always learned a lot. Thanks also to Guang, who introduced me to the lab procedures and provided great support during these stays.

My PhD project would not have been the same without my CryoWALL friends and colleagues. I want to thank Michael and Sebastian for valuable discussions and feedback during field work and meetings. Thank you Florence and Ben for fun field seasons and for your input and work during office hours. And Kristin, I especially want to thank you for your unwearrying motivation and personal support.

I also thank my colleagues and friends at the Geological Survey of Norway, and especially Ivanna, Martina and Gro, for their great impact on an always positive scientific and social environment at work. Thank you for all the valuable discussions during many, many coffee breaks.

Finally, I want to thank all my friends and family for the trips, breaks, games, training, coffees, and other distractions recharging my batteries. Thank you for your patience in stressful times and for all the fun in fun times. This applies especially for Ben, who supported all my travels and could not run away when I was at home but being a pain in the ... Not only have you actively contributed to this thesis by correcting my English, but also you have been there for me at any moment. You are my rock in the surf!

There have been many more people positively affecting and contributing to my life during the past years and I ask for indulgence from those I forgot to mention here. If so, give me a hint and you will get a personal acknowledgment.

Contents

Abstract	i
Acknowledgements	iii
I Overview	1
1 Introduction	3
1.1 Aim and Objectives	6
1.2 Outline	7
2 Rock-slope instabilities and failures	9
2.1 General failure mechanisms	9
2.2 Governing factors on rock-slope stability	11
2.2.1 Internal factors	12
2.2.2 External factors	14
2.2.3 Triggering events	17
2.3 Mapping and research activities on rock-slope instabilities in Norway	18
3 Principles of terrestrial cosmogenic nuclide (TCN) dating	21
3.1 Theory	21
3.2 Shielding	24
3.3 Inheritance	26
3.4 Dating landslides	26
4 Geographic setting	31
4.1 Norway	31
4.1.1 Geology and glacial history	31
4.1.2 Holocene and recent climate	33
4.1.3 Present and past permafrost distribution	36

Contents

4.1.4	Study sites	38
4.2	Aysén Fjord, Patagonia (Chile)	51
4.2.1	The Punta Cola rock avalanche	52
5	Methods and data acquisition	55
5.1	Quaternary geological mapping	55
5.1.1	Field mapping and digital relief analyses	55
5.1.2	Geophysical methods	57
5.2	Terrestrial cosmogenic nuclide (TCN) dating	58
5.2.1	Sampling and sample processing	59
5.2.2	Shielding considerations	60
5.2.3	Data reduction and age calculation	64
5.3	Climate data acquisition	67
5.4	Long-term thermal modelling with CryoGRID 2D	68
6	Results	71
6.1	The role of inheritance when dating rock-slope failures with ^{10}Be (Paper I)	71
6.2	Mapping and exposure dating reveal multiple rock-slope failures at Man- nen, Romsdal valley (Paper II)	73
6.3	Temporal distribution of rock-slope failures at two sites in northern and western Norway	75
6.3.1	Rombakstøtta, Nordland	77
6.3.2	Ramnanosi, Sogn og Fjordane	77
6.4	Reconstructing the sliding and permafrost history of rockslides (Paper III)	81
7	Discussion	85
7.1	Uncertainties when dating catastrophic rock-slope failures (CRSFs) and rock-slope instabilities with cosmogenic nuclides	85
7.1.1	Inherited cosmogenic nuclides	85
7.1.2	Topographic shielding along steep rock slopes	86
7.2	Post-glacial processes at Rombakstøtta and Ramnanosi	89
7.2.1	CRSF activity following deglaciation at Rombakstøtta	89
7.2.2	Mass-movement processes at Ramnanosi	92
7.3	Temporal distribution and evolution of CRSFs and unstable rock-slopes in Norway	94
7.4	Implications for paraglacial landscape development	98

7.5 Recommendations for future research	101
8 Conclusions	103
References	107
II Journal publications	137
Paper I: How significant is inheritance when dating rockslide boulders with terrestrial cosmogenic nuclide dating? — a case study of an historic event . .	139
Paper II: Multiple rock-slope failures from Mannen in Romsdal Valley, western Norway, revealed from Quaternary geological mapping and ¹⁰ Be exposure dating	151
Paper III: Is climate a first order control on rock-slope deformation in Norway? - Reconstructing the sliding and permafrost history of selected rockslides .	167
III Appendices	191
A Tables	192
B Publications	197
B.1 Peer-reviewed journal publications	197
B.2 Conference paper	197
B.3 Conference proceedings	198
B.4 Blog	199

Acronyms and Abbreviations

AMS	accelerator mass spectrometry
AOI	area of interest
CRISDaI	Cosmic Ray Isotope Sciences at Dalhousie University
CRSF	catastrophic rock-slope failure
DC	direct current
DEM	digital elevation model
DoD	DEM of difference
DSGSD	deep seated gravitational slope deformation
ERT	electrical resistivity tomography
GIS	geographical information system
GPR	ground penetrating radar
GPS	global positioning system
HTM	Holocene thermal maximum
InSAR	interferometric synthetic-aperture radar
LGM	last glacial maximum
LIA	Little Ice Age
LiDAR	Light detection and ranging
LOFZ	Liquiñe Ofqui Fault Zone
MAAT	mean annual air temperature
MAGT	mean annual ground temperature
MAP	mean annual precipitation
NFR	Research council of Norway
NGU	Geological survey of Norway
TCN	terrestrial cosmogenic nuclide
TIN	triangular irregular network
YD	Younger Dryas

Part I

Overview

1 Introduction

Natural landscape development in alpine regions all over the world conditions, amongst other processes, large-scale mass wasting events, which are often connected to glacially oversteepened rock slopes and tectonic activity. In these areas, infrastructure, private property and human lives are often highly exposed to rock-slope failures with potentially catastrophic consequences, either by direct impact or secondary effects. The latter can include the damming of a river by landslide debris, causing upriver flooding and potential catastrophic downriver floods or landslide generated displacement waves in fjords and lakes (e.g. Evans and DeGraff, 2002; Eidsvig et al., 2011; Hermanns et al., 2014). The historical frequency of rock avalanches with a volume of $\geq 20 \text{ Mm}^3$ in the European Alps is estimated to be one in 100 years, while the global recurrence interval, based on data from the 20th century, seems to be as high as 2.7 years (Evans, 2006).

In Norway, rock-slope failures of large volume, causing outburst floods or subsequent displacement waves, represent the natural hazard with the third highest death toll in historical times, after snow avalanches and clay slides (Figure 1.1; Furseth, 1985; Grimstad and Nesdal, 1990; Hermanns et al., 2012a). Because of ongoing mass wasting activity along steep rock slopes, active rock-slope instabilities and small-scale rock-fall and landslide events damaging national infrastructure on a high frequency, the Norwegian government has identified the threat as a major issue. In this thesis, however, the objects of research are unstable rock slopes and catastrophic rock-slope failure (CRSF) events of large volumes. The latter comprises sudden mass wasting events from steep rock walls with high displacement velocities. In many cases of this study, the investigated objects can be defined as rock avalanches, but the term CRSF also includes mass-wasting events with smaller volumes (cf. Ch. 2; Evans et al., 2006; Hermanns and Longva, 2012).

While the first order control on rock-slope stability is internal structural conditions, it is affected by many more factors, whereof several are closely related to climatic conditions and changes. For example, it is generally accepted that changes in permafrost conditions and its distribution alter rock-slope stability (e.g. Haeberli, 1992; Krautblatter et al., 2013). However, the identification of major driving factors and potential triggering

1 Introduction

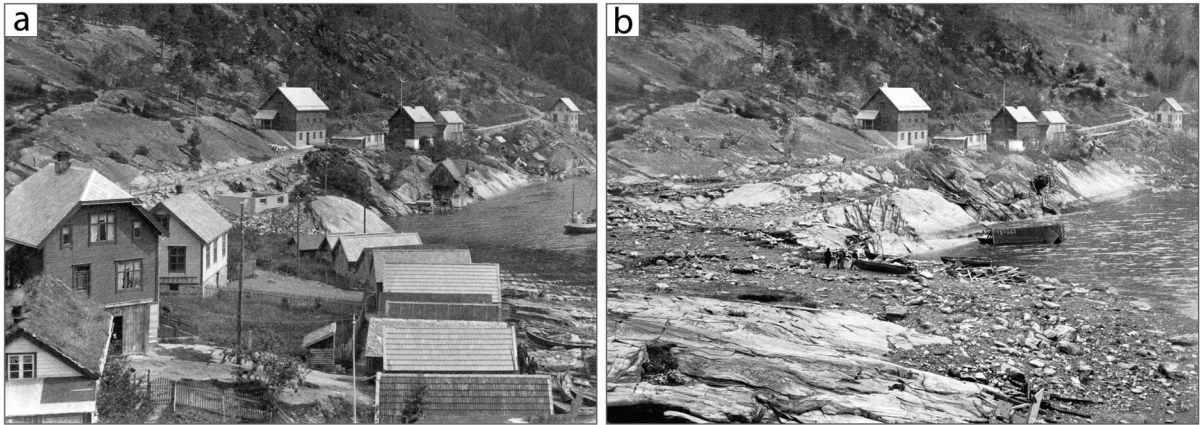


Figure 1.1: April 7th, 1934, a 3 Mm³ large rock avalanche caused a displacement wave of 64 m height in Tafjorden, Norway. The wave hit two small towns, Tafjord and Fjørå, and killed 40 people. The photographs show Fjørå before (a) and after (b) the disaster. Photo archive A. Furseth.

mechanisms on a local scale remains challenging. A globally ongoing increase in air temperature affects both ground temperatures and weather phenomena (e.g. Easterling et al., 2000; Huang et al., 2000; Guhathakurta et al., 2017). The latter may impact previously destabilised rock slopes directly, triggering failures of various sizes. Increased ground temperatures in turn result in permafrost degradation along the boundary of arctic cold regions and in alpine areas (e.g. Jorgenson et al., 2006; Gruber and Haeberli, 2007; Farbroth et al., 2013). Thawing mountain permafrost, and a subsequent rise of lower permafrost boundaries, are observed worldwide (e.g. Fukui et al., 2007; Harris et al., 2009), including Norway (Christiansen et al., 2010; Lilleøren et al., 2012).

Several studies outside of Scandinavia document a relationship between climatic variability and large-scale rock-slope failures in mountain regions, such as the European Alps, the Southern Alps of New Zealand, the Caucasus and the Himalaya (e.g. Gruber and Haeberli, 2007; Allen et al., 2009; Huggel et al., 2010). However, though large parts of the Norwegian Scandes are influenced by altitudinal permafrost only individual studies discuss a direct coupling of rock-slope failures and permafrost processes connected to climatic variability (Blikra and Christiansen, 2014; Böhme et al., 2015a; Frauenfelder et al., 2016). Being aware of the changing climate and increasing temperatures, further investigations of the spatial and temporal distribution of CRSF and slope instabilities in Norway are necessary to establish a potential link to degrading permafrost, weather phenomena and other climatic impacts.

With this background in mind, the Research council of Norway (NFR) finances, together with the Geological survey of Norway (NGU) and University of Oslo, a research project, focussing on the relation between rock-slope stability and permafrost distribution in Norway. Within the CryoWALL project, national and regional maps will be compiled, featuring the probability for steep rock slopes affected by permafrost. Furthermore, the evolution of the thermal regime of steep rock slopes and related stability changes in space and time is assessed. The project is divided into four research topics, which are closely linked. One of four project partners has the main responsibility for each research topic, though close collaboration is necessary in order to fulfill and combine the objectives of each topic (Fig. 1.2).

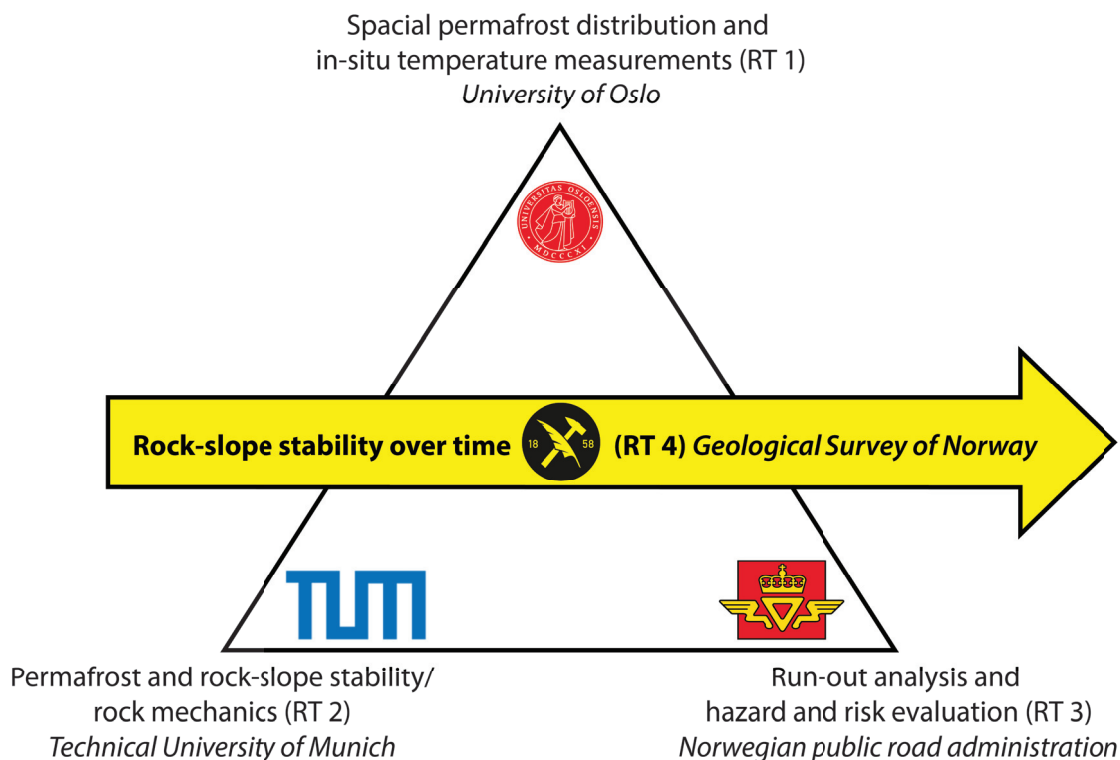


Figure 1.2: Schematic illustration of the work plan for the CryoWALL-project (modified from Etzelmüller et al., 2014, Fig. 3)

This doctoral study is embedded in the CryoWALL project and represents most of the research connected to the temporal evolution of CRSFs and unstable rock-slopes in Norway (RT 4). Close collaboration and data exchange with project partners allowed for integrative and interdisciplinary approaches and discussions.

1 Introduction

Despite the strong focus of CryoWALL on permafrost influenced rock walls, this study focusses on the spatial and temporal distribution and evolution of CRSFs in Norway, including areas below the regional lower permafrost boundary. Eliminating the focus on, but recognizing permafrost, a wide range of parameters affecting rock-slope stability is considered and discussed.

1.1 Aim and Objectives

The aim of the thesis is to:

Investigate the temporal distribution of rock-slope failures with terrestrial cosmogenic nuclide exposure dating and assess the role of climatic factors affecting rock-slope stability in Norway.

In order to address this issue, the following main topics have been investigated.

- How accurate is the terrestrial cosmogenic nuclide (TCN) dating technique, when dating rockslide deposits using the cosmogenic nuclide ^{10}Be ?

This investigation focuses on the methodology of ^{10}Be dating. In order to correctly interpret the results of analysed CRSF deposits, it is crucial to understand potential limitations and uncertainties, as well as possibilities and chances. The applicability of ^{10}Be dating is tested on a recent rock-avalanche event of known age.

- How are pre-historical CRSFs temporally distributed in Norway?

The objective is to identify temporal clusters of CRSFs and discover potential destabilising events, adding to the inherited controlling factor of structural geological conditions. Stratigraphical age bracketing using geophysical applications and Quaternary geological mapping complement a number of numeric age determinations at several sites, applying the ^{10}Be dating technique.

- Is there an impact of climatic variations on the evolution of gradually deforming deep-seated rock-slope instabilities?

This topic combines the challenging approach of dating near-vertical outcropping sliding surfaces with climate and permafrost analyses. The approximation of pre-historical temporal movement patterns additionally allows for an estimation of the

potential timing of initial failure. Accelerating or decelerating sliding rates may reflect a climatic shift and a subsequent change of internal stresses. In order to understand potential conditioning factors for slide initiation, local and regional deglaciation patterns and significant changes in temperature and precipitation throughout the Holocene provide pertinent information.

1.2 Outline

This thesis focuses on the temporal distribution of CRSF and the evolution of rock-slope instabilities in northern and western Norway. In order to identify potential destabilising events, an integrative understanding of pre-historical local, regional and national geographic characteristics is critical.

The thesis is structured as follows:

Rock-slope instabilities and failures

After a short definition of the term CRSF and an introduction into potential failure mechanisms of rock-slopes, this section discusses some of the most important factors affecting rock-slope stability in general and in Norway specifically. A short review of research and mapping projects connected to rock-slope failures in Norway places this study in the context of previous and ongoing work.

Principles of terrestrial cosmogenic nuclide (TCN) dating

TCN dating is an increasingly popular technique to directly determine the time, a rock surface has been exposed at the Earth's surface. Most of this thesis' work is based on this technique, wherefore the theory and its application is described in detail. Shielding and inheritance considerations are outlined, as two of the main factors to be considered when calculating surface exposure ages. The popularity of TCN dating for the age determination of landslides has increased significantly since the early 2000s, which is pointed out at the beginning of a brief review about dating landslides.

Geographic settings

This chapter is divided into two sections, whereof the first one focuses on the main study area Norway. Because of the importance of the geographic settings and their temporal evolution for the main objectives of this thesis, detailed information about the geology

1 Introduction

and glacial history of Norway, the Holocene climate and recent climate, and the present and past permafrost distribution are synthesised. After a short update on the status of a systematic mapping approach for rock-slope instabilities in Norway, each study site of this thesis is presented.

Methods

In order to follow, understand and discuss the results of this study, it is important to comprehend the contributing methods and their study-specific applications. This section demonstrates the Quaternary geological mapping approach before providing a detailed description of the age determination of CRSFs and sliding surfaces with ^{10}Be and ^{36}Cl . Discussed topics include sampling and sample processing, particular and innovative shielding analyses, and the final data reduction and age calculations.

Results

The results, which have been described in the three journal publications are summarised briefly in this chapter. Additional data that has been analysed during the period of this PhD study is presented in more detail. This encompasses age determinations of CRSF deposits at two study sites in northern and western Norway.

Discussion

The most prominent challenges connected to the TCN dating method for the direct age determination of CRSFs and slowly deforming rockslides are taken up again in this chapter. In the second section results, that have been presented in the previous chapter are interpreted and discussed. This is followed by a general discussion about the temporal distribution of CRSFs and rock-slope instabilities in Norway and around the world, in relation to potential driving factors. Finally, the impact and role of rock-slope failure activity on landscape development in a paraglacial environment are discussed before recommendations for further research are given and the value of potential results is discussed.

Conclusions

In this short chapter the main implications of the presented doctoral study are highlighted and summarised.

2 Rock-slope instabilities and failures

Mountain areas with a high relief are often characterised by high landslide activity. After a classification by Hungr et al. (2013), landslide processes in bedrock can be divided into six categories: Rock fall, rock topple, rockslide, rock-slope spread, rock avalanche and rock-slope deformation. Hereof, the term CRSF comprises the rock-slope failure processes with extremely rapid velocities, excluding rock-slope spread and deformation. The main focus of this doctoral study lies on processes of volumes $>50.000 \text{ m}^3$. Rock-fall processes of smaller volume are therefore explicitly defined as rock fall, while CRSF is used for rock avalanches and extremely rapid rockslide events. Gradually deforming rock-slope instabilities in Norway comprises rockslides of extremely slow sliding velocities, that may precede catastrophic failures. CRSFs are hence often the consequence of previously active rock-slope instabilities (Braathen et al., 2004; Stead and Wolter, 2015; Ostermann and Sanders, 2017).

2.1 General failure mechanisms

The failure and deformation processes for gradual and catastrophic rock-slope failures in crystalline bedrock are primarily controlled by geological structures and discontinuities (Stead and Wolter, 2015). The opening of vertical joints or extension fractures in near-vertical rock walls will likely lead to rock-fall events by toppling of small volumes, whereas slope parallel unconformities often result in failure by sliding along shear fractures (Braathen et al., 2004; Geertsema et al., 2006). Rock slopes with slope parallel structures are thus generally less stable than slopes with structures oriented normal to the slope (Badger, 2002). However, natural rock-slope instabilities often feature a complex combination of faults, folds, joints, extension fractures and shear zones. First order control of rock-slope stability is hence the geometry of the bedding or foliation and their orientation in relation to the slope (Figure 2.1). But additional stresses (cf. Sec. 2.2) can reactivate or generate unconformities, which can result in complex stress fields and compound failure mechanisms (Glastonbury and Fell, 2010).

2 Rock-slope instabilities and failures

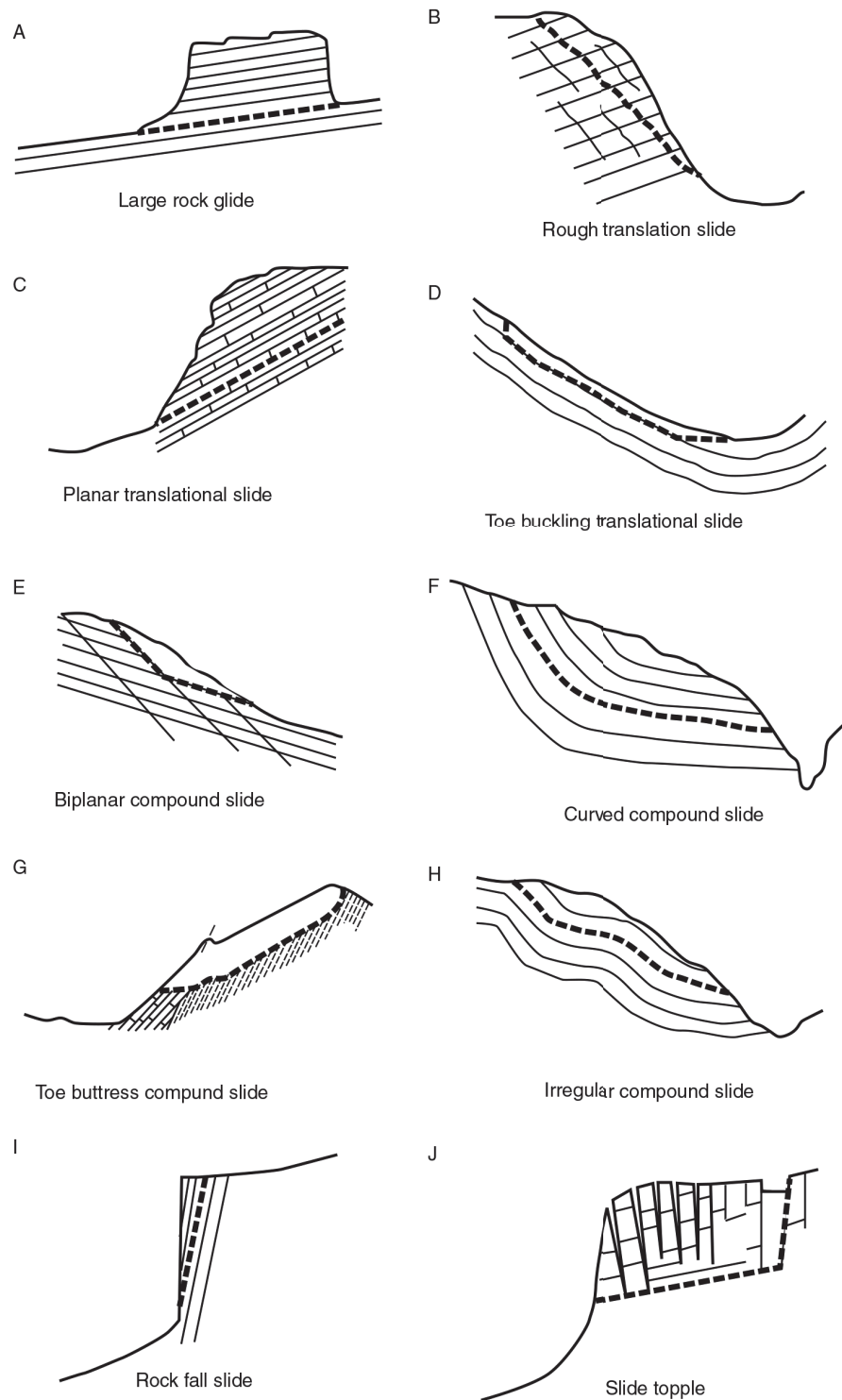


Figure 2.1: Schematic illustration of different systems of geological structures in a slope and corresponding potential failure mechanisms (Hermanns and Longva, 2012, Fig. 6.2).

2.2 Governing factors on rock-slope stability

The spatial and temporal distribution of unstable rock slopes and rock-slope failures are not random but determined by a number of environmental parameters and forces. Mechanically, rock-slope stability is controlled by the ratio of driving forces to resisting forces, which defines the factor of safety for a slope (e.g. Eberhardt et al., 2004; Gunzburger et al., 2005). The governing factors affecting both can roughly be divided into internal and external elements, with close interaction between the two. The internal factors characterise the slope and include topography, rock type, geological structures and the connected permeability and groundwater conditions (grey labels, Fig. 2.2). The external factors originate from outside of the slope and alter the internal factors over time. External or driving factors include gravity, tectonic activity, climatic parameters (e.g. precipitation, temperature), and anthropogenic impacts (italic labels, Fig. 2.2; Jaboyedoff et al., 2005; Raghuvanshi, 2017). Sudden extreme events, such as earthquakes or heavy rainfall, may

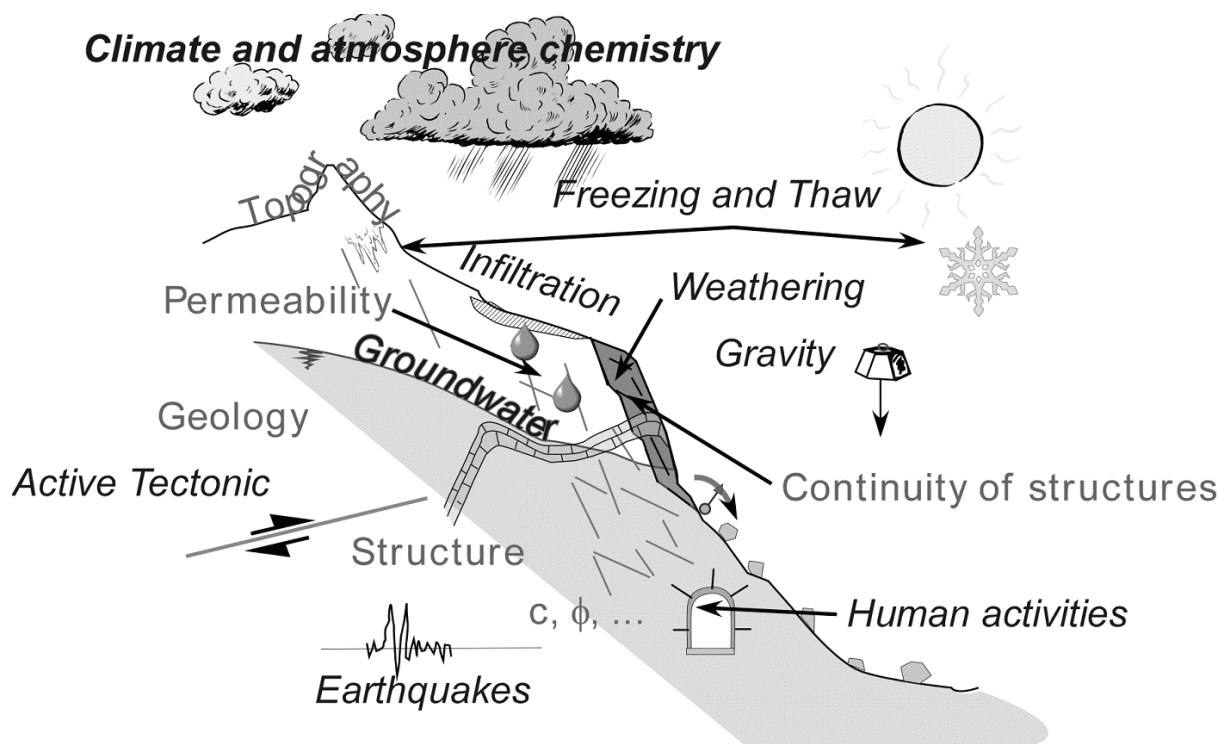


Figure 2.2: Illustration of internal (grey) and external (italic) factors and the driving factors (bold) that may influence the stability of a rock slope over time (modified from Jaboyedoff and Derron, 2005, Fig. 5).

2 Rock-slope instabilities and failures

affect both shear stress and resisting forces in such a great extent to finally trigger a CRSF (Gunzburger et al., 2005).

2.2.1 Internal factors

Slope geometry, geological structures and rock type - These three parameters are the principle controlling internal factors for the occurrence of CRSFs. They define the factor of safety, representing the ratio of the driving forces to resisting forces. The inclination angle of the slope and/or geological structures determines, together with the unstable rock mass (m), the gravitational force acting on the slope (Barton and Choubey, 1977). In the simple Mohr-Coulomb failure criterion, this vertical force is divided into two components: normal stress (σ), acting normal to the slope, and shear stress (τ), acting slope parallel (Fig. 2.3). A general lower threshold for a critical slope gradient in rock slopes is suggested to be between 40 and 45° (Fischer et al., 2012).

The characteristics defining the resisting forces of a potentially unstable rock mass are determined by the mechanical parameters friction angle (ϕ) and cohesion (c) (Barton and Choubey, 1977). They are properties of both intact rock and potential failure planes and define the critical shear stress of the rock slope by (Ahnert, 2003):

$$\tau_f = c + \sigma \tan(\phi) \quad (2.1)$$

The friction angle describes the threshold for a structural inclination angle, where gravitational stress exceeds the resisting forces (De Blasio, 2011). Because of this, the before mentioned direction of internal structures and discontinuities is the first order control on

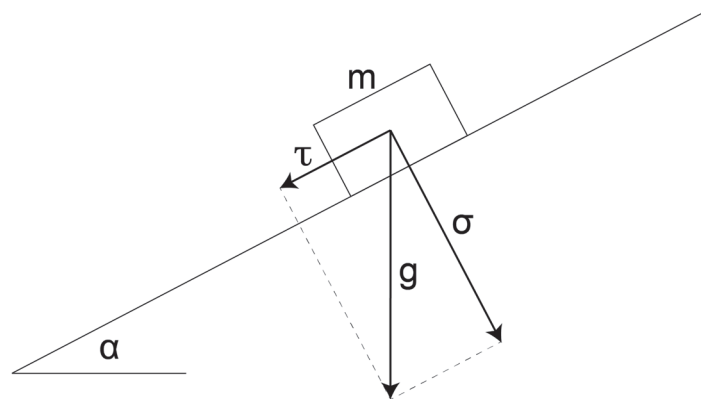


Figure 2.3: Theoretical illustration of the forces acting on a rock mass in on inclined slope (after Ahnert, 2003, Fig. 8.1).

2.2 Governing factors on rock-slope stability

slope stability. The friction angle along a potential sliding plane is then determined by its continuity and roughness, which can be altered significantly by external factors (Barton, 2013; Raghuvanshi, 2017).

Cohesion describes the resisting strength of the rock itself or material and surface characteristics along geological structures. It determines fracturing processes and is thus significant for the evolution of discontinuities. In order to destabilise a rock mass along internal discontinuous structures, brittle intact rock bridges along the potential failure plane need to be fractured. Cohesion significantly affects potential fracture initiation and propagation along structures, and the coherent progressive decrease of shear strength (Eberhardt et al., 2004).

Permeability and permafrost - The internal structures' characteristics of continuity, roughness and aperture add significantly to the permeability of the rock mass, which in turn determines the infiltration of precipitation and snow-melt, as well as groundwater flow (Brown, 1987). Open fractures can therefore lead to an increased water volume and subsequent effective hydrostatic pressure at depth (Clark and Phillips, 2003), reducing the shear strength along potential basal sliding surfaces (Pantelidis, 2009). The effect of hydrostatic pressure in rock walls can be increased if water passages are shut by ice at depth or superficial ice formation reduces potential space and water escape (Fischer et al., 2010). In cold environments, the occurrence of permafrost is thus a significant factor for slope stability. The nowadays widely accepted definition of permafrost is based on the thermal ground conditions and defines ground where the temperatures remain at or below 0°C for at least two consecutive years as permafrost. This applies for dry ground as well as for saturated ground, where the occurrence of ice is the physical consequence of temperatures below 0°C.

A typical feature of permafrost environments is the active layer, comprising the sub-surface zone between the ground surface and the permafrost table. In this area, due to the ground heat flux from the surface, ground temperatures fluctuate seasonally reaching positive temperatures and subsequently thawing during warm seasons. As a consequence, the area just above and below the permafrost table is especially susceptible to seasonal ice-segregation, reducing its tensile strength over time. With increasing freeze-thaw cycles, fractures may form in soft porous rocks (Murton et al., 2001, 2006; Jia et al., 2015). In low porosity bedrocks, permafrost processes have the greatest effect in fractures and joints (Gruber and Haeberli, 2007; Hasler et al., 2012). Matsuoka (1995) and Jia et al.

2 Rock-slope instabilities and failures

(2017) demonstrated with laboratory tests, and later field observations (Matsuoka, 2001), that annual temperature changes can lead to effective frost wedging in granites.

In cold permafrost conditions, where the active layer is shallow and ground temperatures remain below -2°C , the presence of ice in fractures and joints enhances rock-slope stability by increased shear resistance (Davies et al., 2001). However, close to the melting point, ice becomes weak and deformable, reducing shear resistance allowing for ice creep, fracture of ice and breaking of rock-ice contacts (Figure 2.4). An increasing depth of unfrozen ground alters the shear force at the same time by hydrostatic pressure above the non-permeable permafrost table. This eventually leads to the critical point where the shear forces exceed the resisting forces, leading to failure (Krautblatter et al., 2013). Changes in the thermal regime of a rock wall are attributed to be one of the main driving factors for an increasing number of CRSF in high-altitude or -latitude rock slopes (e.g. Fischer et al., 2006; Frauenfelder et al., 2016; Huggel et al., 2010).

2.2.2 External factors

Tectonic activity - Processes related to active tectonics are a significant conditioning factor for CRSFs in tectonically active regions such as the Andes (Hermanns and Strecker, 1999; Penna et al., 2011; Moreiras et al., 2015), the Himalaya (Korup et al., 2006; Hewitt,

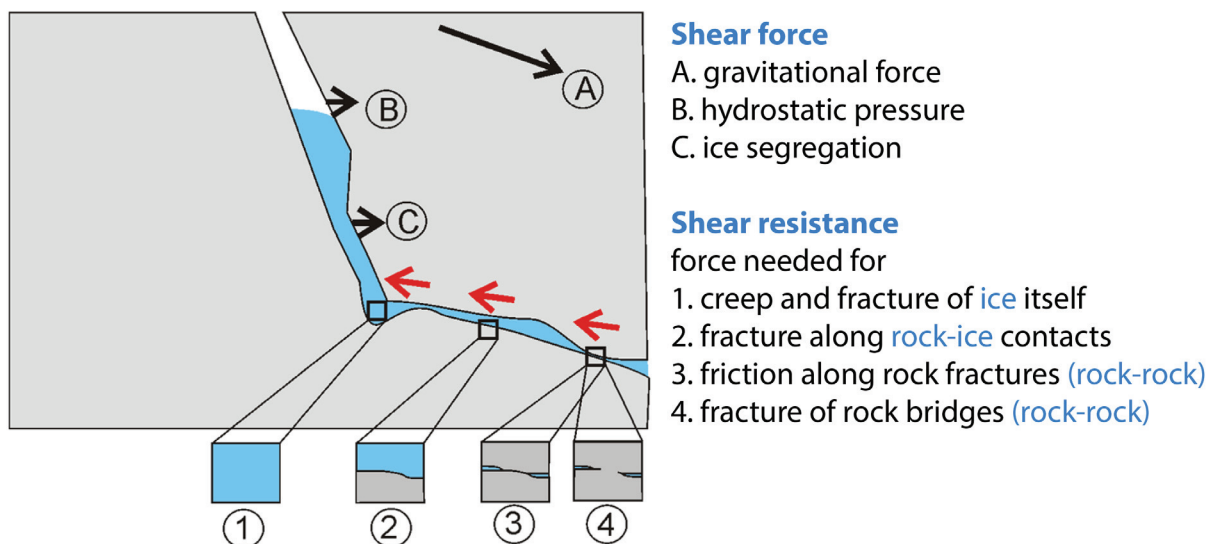


Figure 2.4: Illustration of the mechanical forces acting on an ice-filled fracture (Krautblatter et al., 2013, Fig. 1).

2.2 Governing factors on rock-slope stability

2006; Hewitt et al., 2011), the Southern Alps of New Zealand (Korup, 2004; Hewitt et al., 2008), the Tien Shan (Strom, 2006) and although of limited significance, the Alps (Agliardi et al., 2009). In such settings, the internal complex system of structures in a rock slope is often affected by tectonic faults, folds and/or shear zones (Brideau et al., 2009). The degree of tectonic damage, the re-orientation of pre-existing geological structures and the creation of discontinuities again define the internal ratio of driving forces to resisting forces. CRSFs associated to active tectonic faults and folds are often rock avalanches of large volumes (Penna et al., 2011).

Deglaciation and debuttreassing - The deeply incised valleys and steep slopes in previously glaciated mountain ranges are a product of glacial erosion by warm based ice streams along glacial troughs (Ballantyne, 2002b). Previously fluviially developed V-shaped valleys are typically transformed into U-shaped valleys with an increased slope gradient, affecting the internal shear stress (Fig. 2.3; MacGregor et al., 2009). This generally unstable condition leads to a rapid paraglacial response modifying the landscape towards a natural equilibrium. Different mass wasting processes acting on different spatial scales control the timescale of this relaxation process, which ranges from less than a century to several millennia (Ballantyne, 2002b).

A contributing factor to the unstable paraglacial landscape is glacial debuttreassing, which is effective when the load of thick glacier ice is removed from glacially oversteepened rock slopes. As a consequence, increased internal stress and stress redistribution preferentially leads to the reactivation of pre-existing joints but may also form new zones of weakness (Evans and Clague, 1994). Debuttreassing thus adds to the slope destabilisation and may lead to the collapse of previously activated rock masses (Geertsema et al., 2006). This is supported by several studies using numerical modeling to simulate the stress and strain distribution in a slope during deglaciation (e.g. Agliardi et al., 2001; Ambrosi and Crosta, 2011; Ghirotti et al., 2011).

However, it is discussed controversially if the mass of glacier ice and its mechanical characteristics are sufficient to provide lateral compressive stress onto the rock slopes (Wyrwoll, 1977; Cossart et al., 2008). McColl and Davies (2013) argue that under constant low strain, ice behaves in a ductile manner and may accommodate active slope deformations. Debuttreassing may therefore have a limited effect on slopes with moderate strength conditions but may cause significant damage under repeated glacial cycles. However, high joint densities in weaker rock slopes results in an increased sensitivity to debuttreassing (Grämiger et al., 2017) conditioning rock-slope failures during and shortly

2 Rock-slope instabilities and failures

after deglaciation. The reactivation and development of fractures and joints is subsequently important for the hydrology of the rock section adding to the stress regime.

Climate and weather variability - Climate is the main driver for permafrost distribution and its variability. Because of the purely thermal definition of permafrost, its occurrence is determined by seasonal, yearly and long term temperature characteristics. Ground temperatures at shallow depths are closely related to air temperatures and follow their daily, seasonal and annual fluctuations closely. However, the time lag of response and the effect of air temperatures increase with depth. A general long-term shift in air temperature is necessary to change ground temperatures and permafrost conditions at great depths. The decreasing dependency of ground temperatures to air temperatures with depth is clearly visible in most deep boreholes with associated temperature measurements. Here, short term fluctuations quickly diminish with depth, where only general temperature trends are visible (e.g. Haeberli et al., 2010; Isaksen et al., 2011). Thus, a climatic shift with a long-term temperature increase can result in permafrost degradation at depth, with potential rock-slope destabilisation as a consequence.

Another factor influencing the internal hydrology of a rock slope, and thus the shear resistance along potential failure surfaces, is the distribution and its variability of rainfall and snow. The infiltration of rainfall directly affects the friction angle along fractures. Repeated long lasting or heavy rainfall events alter groundwater and potential permafrost characteristics. The temporal and spatial distribution of snow cover has a significant effect on the grounds thermal regime. The presence of a snow cover during cold seasons with cold air temperatures has an insulating effect, preventing the otherwise effective cooling of the subsurface (Goodrich, 1982). Changes in snow cover thus have an impact on the general evolution of sub-surface temperatures and potentially associated permafrost changes (Stieglitz et al., 2003). Conversely, during snow-melt seasons the amount of previous snow precipitation adds significantly to the sub-surface discharge, and thus to the hydrostatic pressure and decrease of friction along fractures.

Weathering - Weathering processes are the physical and chemical impact of atmospheric characteristics, and vary in their intensity depending on rock type and climate (Ahnert, 2003). In karstic rock types, chemical weathering by water can weaken and destroy intact rock bridges directly and progressively lead to failure. Additionally, sequences of weathering zones in igneous and metamorphic rocks can become critical (Abramson et al., 2002). Deep weathering in any rock type generally reduces its cohesion and tensile

strength and can play a significant role in slope destabilisation (Regmi et al., 2013). In crystalline rock types, products of weathering processes can result in fine grained soil-like infill of joints and fractures (e.g. Ehlen, 2002). When saturated, cohesion and friction angle along these planes are reduced significantly. In the Swiss Alps, CRSFs have been linked to precipitation events, that should not have produced excess pore water pressure within the rock slope (Jaboyedoff et al., 2004).

In cold regions, internal long-term frost weathering adds to rock-slope destabilisation by weakening the rock mass. It has been shown, that the presence of permafrost leads to mechanical rock damage around the permafrost table due to repeated cycles of seasonal ice segregation (e.g. Murton et al., 2006; Hales and Roering, 2007). Thus fluctuating thermal gradients and related permafrost processes increase fracturing and irreversible rock fatigue in rock slopes affected by repeated stadials and interstadials (Weber et al., 2017; Mamot et al., 2018).

2.2.3 Triggering events

Earthquakes - Earthquakes as trigger for rock-slope failures often have a strong regional impact, resulting in spatial and temporal clustering of CRSFs (e.g. Hermanns et al., 2000; Redfield and Osmundsen, 2009; Sepúlveda et al., 2010). However, for a rock slope to fail due to an earthquake, it must have been pre-conditioned by driving factors (Figure 2.2) reducing the rock-slope stability prior to the catastrophic failure (Wang et al., 2003; Fischer et al., 2012; Kumar et al., 2018). Earthquake induced CRSFs are often connected to tectonically conditioned unstable rock-slopes. The 2008 Wenchuan earthquake in China triggered several CRSFs, creating more than 30 landslide dams and killing more than 69,000 people in this tectonically active mountain region (Chigira et al., 2010). However, seismic motion does not always directly trigger a catastrophic failure, but can reactivate inherited tectonic structures, and thus increase the failure susceptibility of a rock slope by opening fractures and breaking brittle intact rock bridges (Redfield and Osmundsen, 2009; Moore et al., 2012). Although tectonic activity plays an important role for conditioning and triggering CRSFs, in Norway this factor generally plays minor role as triggering factor for CRSFs due to very limited seismic activity. However, several studies suggest an increased seismic activity related to glacial isostatic uplift following the late-Pleistocene deglaciation (e.g. Lagerbäck, 1990; Olesen et al., 2004).

Extreme rainfall events - It has been observed in several cases that CRSFs occurred after a period or an event of extremely heavy rain fall (e.g. Crosta et al., 2007; Evans et

2 Rock-slope instabilities and failures

al., 2007; Xing et al., 2016). This can be associated to hydrostatic pressure from the water discharge, which is confined to open joints and fractures, to excess pore water pressure in rock and fine material and to the lubrication of fracture infill. An additional factor contributing to water (over-)saturation of rock walls are the snow conditions and connected snow-melt seasons. Intense snow melt releases large amounts of water in a short period of time that contributes significantly to the groundwater conditions. The contribution of water pressure to the destabilisation of rock slopes can be high in generally wet climate periods, while seasonal snow melt and weather events with heavy rainfall are possible trigger for CRSFs (Crosta and Agliardi, 2003). However, it is most likely that several of the previously described factors combine to pre-condition the rock wall, and finally trigger a catastrophic detachment.

2.3 Mapping and research activities on rock-slope instabilities in Norway

The naturally unstable paraglacial landscape condition due to glacially oversteepened valleys and fjords resulted in a high rock-slope failure activity in Norway throughout the Holocene with a peak shortly after deglaciation (e.g. Blikra et al., 2006b; Böhme et al., 2015a; Hermanns et al., 2017). Historical events with catastrophic consequences made CRSFs to one of the most deadly natural hazards of Norway (Reusch, 1907; Grimstad and Nesdal, 1990; Hermanns et al., 2006). But it is not CRSFs which testify to the landscape's pursuit of natural equilibrium; actively deforming unstable rock-slopes demonstrate the ongoing landscape adjustment and indicate locations of potential CRSFs.

Based on the background of historical rock-avalanche events with deadly consequences, several projects have been initiated since 1995 to map and analyse potentially unstable rock-slopes and the temporal and spatial distribution of rock-slope failure deposits in Norway (Blikra et al., 2002). Mapping activities were often combined with research projects, in order to increase knowledge about dominating factors which decrease slope stability and finally lead to failure in specific areas (e.g. Bøe et al., 2004; Fenton et al., 2011; Böhme et al., 2015a). First research reports in Norway present results of relative age determinations, using (1) geophysical methods to map the stratigraphic relation of the sediments and (2) numeric age determinations, using radiocarbon dating of organic material (Blikra, 1999; Blikra et al., 2000). For rock avalanches that cluster regionally in northern Norway and temporally shortly after deglaciation, they discuss potential occurrence of major earthquakes in addition to the short time lag after deglaciation. Age

2.3 Mapping and research activities on rock-slope instabilities in Norway

bracketing of pre-historical rock avalanches in Møre og Romsdal, however, revealed several much younger and temporally spread events, emphasising the importance of local factors affecting rock-slope stability (Blikra and Anda, 1997; Blikra, 1999; Blikra et al., 2006b).

Bathymetric data allowed localised extension of subaerial information pertaining to rock-avalanche and rockslide deposits, with rock masses deposited off-shore into the fjords (e.g. Blikra et al., 2002; Böhme et al., 2015a). A constantly increasing number of surface exposure age datings provides a more comprehensive understanding of the temporal distribution of CRSF events (cf. Sec. 3.4), which illustrates the peak of rock-slope failure activity shortly after deglaciation (Fenton et al., 2011; Böhme et al., 2015a; Schleier et al., 2017; Hermanns et al., 2017).

During early field campaigns, several signs of unstable rock-slopes were identified in areas with high concentrations of rock-avalanche deposits, featuring valley-parallel fractures on the mountain plateaus and outcropping sliding surfaces, indicating past and/or present gravitational deformation (e.g. Blikra, 1999; Braathen et al., 2004). Recognising the potential risk these rock-slope instabilities represent to infrastructure and inhabitants, the mapping became more systematic, initially in Møre og Romsdal and Sogn og Fjordane in western Norway (Henderson and Saintot, 2007; Henderson et al., 2008; Hermanns et al., 2011) and in Troms county in northern Norway (Henderson et al., 2010; Bunkholt et al., 2013b). The main objective of the mapping projects, is to develop a hazard and risk classification for the identified rock-slope instabilities. For this, periodic surveys are conducted, with detailed structural geologic and geomorphologic mapping for the identification of discontinuities and failure mechanisms, combined with deformation measurements in order to analyse displacement rates. Detailed integrative analyses at several sites indicate, that there is a strong structural control on the majority of unstable rock-slopes (e.g. Saintot et al., 2012; Böhme et al., 2013; Booth et al., 2015).

The potential consequences of a CRSF from the unstable rock-slopes are assessed using run-out analyses and models for potential impact areas of subsequent displacement waves (Oppikofer et al., 2018). The systematic mapping and classification approach in Norway (Hermanns et al., 2013c) with episodic, periodic and continuous monitoring techniques, is complemented by nationwide interferometric synthetic-aperture radar (InSAR) coverage, detecting relative sub-centimetre surface changes on a weekly basis (cf. Eriksen et al., 2017).

The modern approach of the Geological survey of Norway (NGU) to map and classify unstable rock-slopes in Norway is very systematic and includes the development of a national database for unstable rock slopes (Hermanns et al., 2012a; Bunkholt et al.,

2 Rock-slope instabilities and failures

2013a). It synthesises the increased understanding from both earlier mapping activities and specific research projects (Hermanns et al., 2012a; Bunkholt et al., 2013a). So far, more than 300 potentially unstable rock slopes with recent and/or previous deformation have been identified. 23 objects are classified according to their hazard and, combined with the potential consequences, the risk they depict (Oppikofer et al., 2015). Severe potential consequences can thus result in a high risk classification for instabilities in low or middle hazard classes (Hermanns et al., 2013b). The volume of rock-slope instabilities in the database are commonly in excess of $>10^5$ m³.

Owing to structural geological pre-conditioning, observed deformation and sliding rates and their potential impact on infrastructure and human life, the risk of several unstable rock-slopes is classified as 'high'. As a consequence, seven rock slopes are monitored continuously (Blikra and Kristensen, 2013; Blikra et al., 2013b) in order to detect unusual deformation processes and sudden acceleration.

3 Principles of terrestrial cosmogenic nuclide (TCN) dating

Terrestrial cosmogenic nuclide (TCN) dating is a surface exposure and burial dating technique that allows the determination of the cumulative time a rock or sediments have been at or near the Earth's surface. It is a unique chronology tool for a series of research fields within geology, geomorphology and archaeology, filling the gaps where other dating techniques are unsuitable. While glacial chronologies are one of the most common application fields for TCN dating, it is used in a large variety of landscapes and processes to reveal the story of landscape evolution in different scales of space and time (Fig. 3.1). The potential time range of chronologies depends on the addressed nuclide's characteristics and the current measurement capabilities, and vary from several million years for stable noble gasses to a few hundred years for some radionuclides (Gosse and Phillips, 2001; Ivy-Ochs and Kober, 2008). The most commonly used cosmogenic nuclides are the stable noble gasses ^3He and ^{21}Ne , and the radionuclides ^{10}Be , ^{26}Al , ^{36}Cl and ^{14}C .

3.1 Theory

The Earth is constantly bombarded by a flux of galactic cosmic rays composed of mostly fast moving high energetic protons and α -particles. The intensity of this particle flux when reaching the Earth's atmosphere is affected by the geomagnetic field. While fast particles with high kinetic energy are more likely to penetrate the magnetic field, incoming low-energy particles are deflected by it resulting in intricate individual trajectories. The effect of deflection is determined by the angle of incidence and the resistance of a particle to being deflected, expressed as *rigidity* (momentum per unit charge) (Wagner et al., 2000). The strength of the geomagnetic field can be expressed as *cut-off rigidity*, defining the minimum rigidity required for a particle to penetrate it. As a consequence, the flux of primary cosmic rays close to the equator consists of primarily high energetic fast particles travelling perpendicularly to the magnetic field, whereas low energetic particles

3 Principles of terrestrial cosmogenic nuclide (TCN) dating

are deflected by the geomagnetic field and will essentially approach the Earth at the poles (Dunai, 2010).

When entering the atmosphere the primary cosmic radiation initiates a cascade of reactions with a range of target elements, producing secondary particles. For instance, spallation impacts on atomic nuclei release nucleons, that in turn collide with other target nuclides while maintaining a general downward direction (Dorman et al., 1999). The successive number of reactions with penetration depth causes a decrease in individual particle energy and an increasing dominance of neutrons, because unlike protons, neutrons are resistant to ionization. Finally, the secondary cosmic radiation finally reaching the Earth's surface consists mainly of neutrons and muons (Gosse and Phillips, 2001).

In rock or sediments, the secondary cosmic particles react in a variety of minerals with one of many potential target elements to produce cosmogenic nuclides in the upper metres of the Earth's surface. The energetic neutron flux interacts strongly with matter, resulting in a much shorter *attenuation length* (penetration depth) than that of only weakly interacting muons. The attenuation length for a specific particle flux is controlled by the

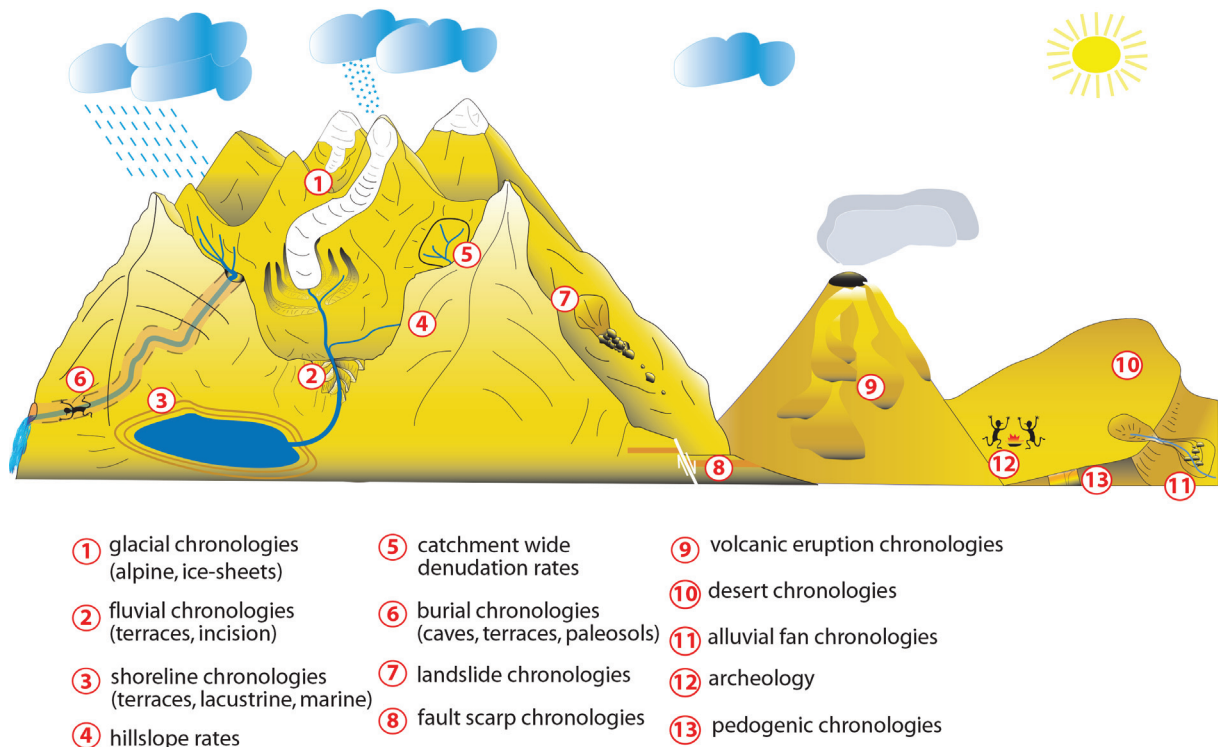


Figure 3.1: Illustration of the variety of application fields for TCN dating (Ivy-Ochs and Kober, 2008, Fig. 1).

density of penetrated matter and describes the maximum interaction depth in g cm^{-2} . Typical attenuation lengths for energetic neutron fluxes range from 121 to $>170 \text{ g cm}^{-2}$ and imply that the greatest part of neutrons is absorbed in less than one meter in most rocks ($>2.3 \text{ g cm}^{-3}$ density) (Gosse and Phillips, 2001; Colgan et al., 2002). This is where the largest portion ($\sim 98\%$) of TCN are produced due to spallation reactions with an exponential decrease with depth. However, TCN production continues at depth, where it is dominated by fast muons and negative muon capture (Fig. 3.2).

The surface production rate of each nuclide in rock is proportional to the incoming flux of secondary cosmic particles, and is thus a function of geomagnetic latitude and altitude/atmospheric pressure (Lal, 1991; Stone, 2000). However, the two factors are not only variable in space but also in time. Apart from geomagnetic reversals, the intensity and position of the Earth's magnetic field alters constantly (e.g. Dunai, 2001). The atmospheric pressure is sensitive to climatic effects, such as temperature changes, glaciations and ice-mass distribution, resulting in an irregular variability in atmospheric pressure distribution (Staiger et al., 2007).

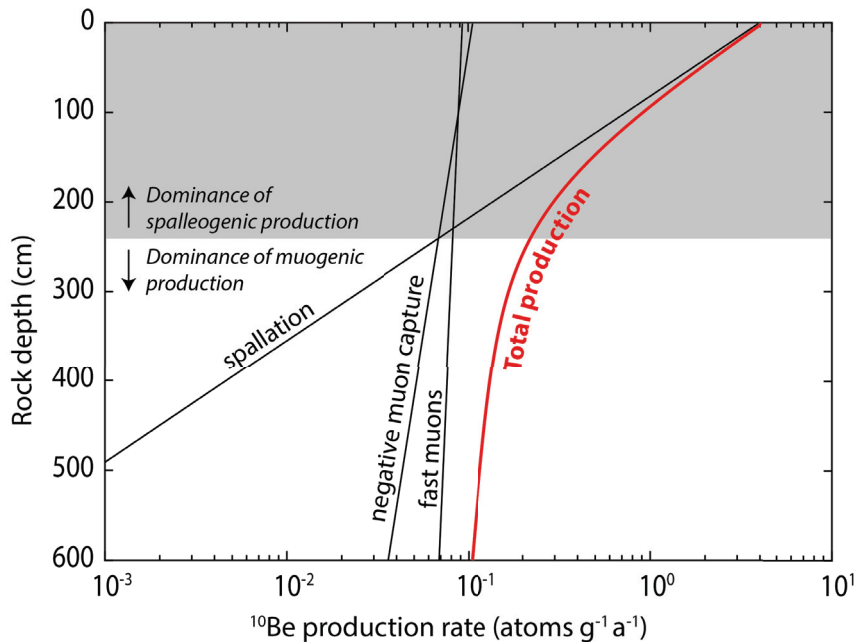


Figure 3.2: Production of ^{10}Be atoms due to spallation and muons with depth. Values for surface production rates and attenuation lengths for the spallogenic, negative muon capture and fast muons are taken from Borchers et al. (2016), Heisinger et al. (2002a) and Heisinger et al. (2002b), respectively.

3 Principles of terrestrial cosmogenic nuclide (TCN) dating

Global or regional production rates are thus reported representing the production rate at sea level and high latitude (SLHL) and must subsequently be corrected according to the sample location. For this, a series of scaling frameworks has been developed and improved over time (Gosse and Phillips, 2001; Marrero et al., 2016). The most recent scaling frameworks are the time- and nuclide dependent LSD and LSDn models, which consider dipole and non-dipole magnetic field fluctuations and solar modulation. The scaling is based on analytical approximations to Monte Carlo simulations of cosmic ray flux, which seem to be robust in comparison with measured values (Lifton et al., 2014).

3.2 Shielding

Online calculators that are available for apparent exposure age calculations, typically have a variety of scaling schemes incorporated and calculate the ages based on locally scaled production rates. However, if not stated otherwise, the calculations will be made on the assumption that the sample was taken on a flat, horizontal and completely unobstructed surface, that has not experienced any erosion, type of cover or obstruction during the entire exposure time. For any settings that naturally differ from this scenario, the user has to add a factor including all shielding effects. In the simple first case, the total incoming flux of secondary cosmic radiation F_{tot} for any point P is given by (e.g. Dunne et al., 1999):

$$F_{tot} = \int_{\phi=0}^{2\pi} \int_{\theta=0}^{\pi/2} I_0 \sin^m(\theta) \cos\theta d(\theta) d(\phi) \quad (3.1)$$

where ϕ (degrees) is the angle of azimuth, θ (degrees) is the inclination angle of incoming cosmic rays measured up from the horizontal, I_0 (particles $\text{cm}^{-2}\text{sr}^{-1}\text{s}^{-1}$) is the maximum intensity and m (unitless) is a constant defining the angular dependency of the intensity on θ . The most commonly used value for m is 2.3 ± 0.5 introduced by Lal (1958) (cited in (Nishiizumi et al., 1989)) and subsequently used by others (Dunai, 2010). Because of the energy-dependency of the inclination angle the intensity distribution at any point P varies slightly with geomagnetic latitude (Dorman et al., 2000). But the potential uncertainties of m are insignificant for most surface exposure dating studies in geosciences (Dunai, 2010). The non-linear angle dependency implies that the radiation coming from inclination angles $>45^\circ$ contribute to more than 75% of the cosmogenic nuclide production at the surface (Argento et al., 2015; Sato, 2016).

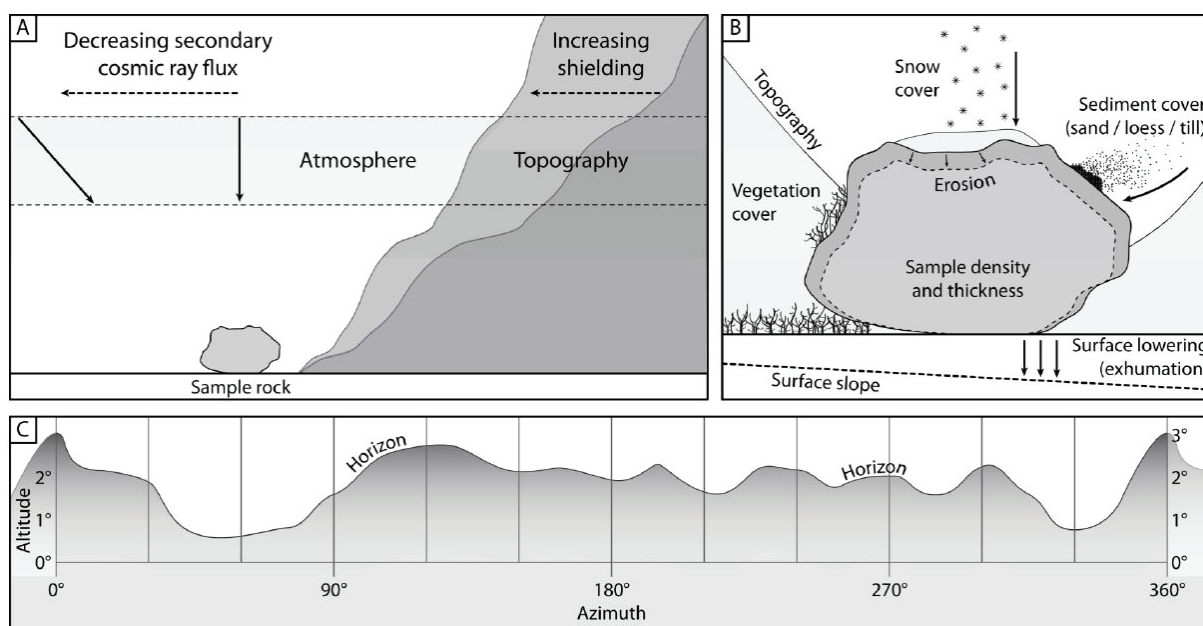


Figure 3.3: Site characteristics that potentially affect the shielding factor and thus the local production rate at a sample site (Darvill, 2013, Fig. 4).

However, most real sampling points are on irregular surfaces and do not have an unobstructed view of the sky during the entire exposure time. Typically they are affected by shielding of one or several of the following factors: surrounding topography (Fig. 3.3 A and C), sloping surface and snow, vegetation or sediment cover (Fig. 3.3 B). An additional factor reducing the production rate is the exponentially decreasing production at depth, and the effect of sample thickness and gradual or sudden erosion. Topographic shielding and self-shielding due to complex shapes are rather stable over time. In the majority of cases, the topographic conditions at the time of sampling are representative for the duration of exposure. The topographic shielding for a point P can then be calculated and potential uncertainties quantified (e.g. Gosse and Phillips, 2001; Codilean, 2006; Balco, 2014; Tikhomirov et al., 2014), whereas the other mentioned effects are dynamic over time and often connected to uncertainties of largely unknown extent (e.g. Schildgen et al., 2005; Plug et al., 2007; Delunel et al., 2014).

3.3 Inheritance

In order to avoid misinterpretations and ‘translate’ the concentration of a specific cosmogenic nuclide in a sample to an apparent exposure age which is as close as possible to the real exposure age, the local time-dependent production rate has to be determined for each sample position and thickness. The effect of inheritance is a common source for exposure-age overestimation, while the omission of shielding or erosion effects result in an overestimation of production rates and thus an underestimation of exposure age. Inherited cosmogenic nuclide concentrations are atoms that are already present when an event (e.g. deglaciation of bedrock, stabilisation of a moraine or fluvial fan, rock-slope failure) initialises the last exposure period (e.g. Ivy-Ochs and Kober, 2008). This is possible if the sampled sediments, boulder or bedrock have been exposed or positioned close enough to the surface to produce TCN at depth before final deposition.

To date the exposure time of a glacially eroded bedrock surface it is therefore necessary to know the erosion depth (Davis et al., 1999). Boulders, pebbles and sediments from unconsolidated depositional landforms might have accumulated cosmogenic nuclides at their source (in a rock wall previous to being released by a rock-fall event) or along their travel path (temporary storage in the sediment cascade). A landslide boulder might originate from a relatively shallow depth in the pre-failure rock slope.

3.4 Dating landslides

There are numerous different methods to determine either a minimum, a maximum or a numeric age (range) of a landslide event. They range from contextualising (pre-)historical remains and records and dendrochronology for relatively young events, over relative age determinations with lichenometry, pollen and geomorphic analyses, to numeric age determinations with radiometric, luminescence and surface exposure dating techniques (Jibson, 2009). However, TCN dating is the only method where the landslide material is dated directly, whereas other dating techniques are applied to related deposits or processes (Fig. 3.4 B). While landslide studies were long dominated by ^{14}C dating, the application of TCN techniques for landslide chronology has increased exponentially from a fraction of $\sim 0.01\%$ before the year 2000 to 25 - $>50\%$ throughout the last decades (Figure 3.4 A; Pánek, 2015).

The continuous improvement of production rate approximations and analytical techniques resulted in a general constant increase in TCN sample sites and studies world wide,

3.4 Dating landslides

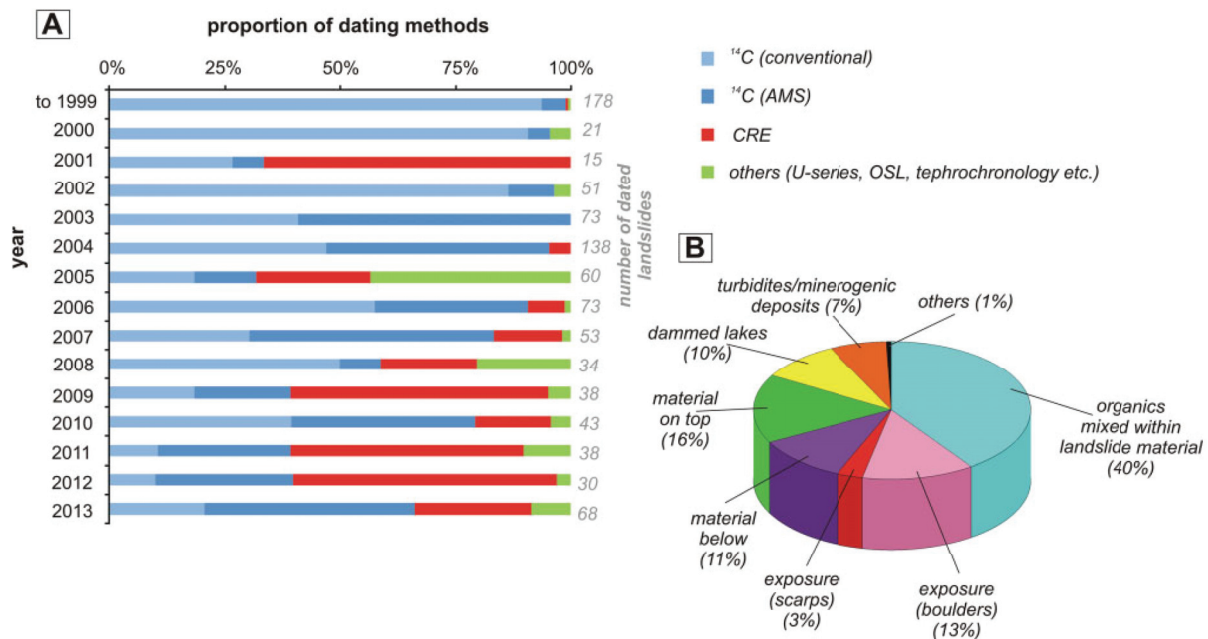


Figure 3.4: Recent development in landslide dating with a compilation of applied dating methods in relation to the total number of dated landslide events per year from before 1999 to 2013 (A) and the proportion of targeted landslide elements and associated features and materials for numeric age determinations of landslide events (B) (Pánek, 2015, Fig. 2).

and vice versa. However, a large part of these studies focus on glacial chronologies (e.g. Kaplan et al., 2004; Bentley et al., 2006; Hughes et al., 2016) or catchment erosion (e.g. Von Blanckenburg, 2006; Tofelde et al., 2018; Codilean et al., 2018). Despite the strongly increasing number of landslide-chronology studies using the TCN technique, the world wide spacial distribution remains asymmetric with most studies concentrated in some of the major mountain belts and regions, such as the Andean cordillera (e.g. Hermanns et al., 2001, 2004; Penna et al., 2011; Moreiras et al., 2015), the Scottish highlands (e.g. Ballantyne et al., 1998; Ballantyne and Stone, 2013; Ballantyne et al., 2014), the European Alps (e.g. Ivy-Ochs et al., 2009; Zerathe et al., 2014; Köpfler et al., 2018), the Norwegian Scandes (e.g. Fenton et al., 2011; Schleier et al., 2015; Hermanns et al., 2017) and the Himalaya (e.g. Dortch et al., 2009; Hewitt et al., 2011; Peng et al., 2018). However, studies exist from other alpine regions, including the Carpathians (Pánek and Klimeš, 2016; Břežný et al., 2018), the Rocky Mountains (Sturzenegger et al., 2015), the Southern Alps of New Zealand (Putnam et al., 2010; Sweeney et al., 2013) and the Crimean mountains (Pánek et al., 2018).

3 Principles of terrestrial cosmogenic nuclide (TCN) dating

Most rock-avalanche and rockslide chronologies are published as case studies being part of an integrative geological and morphological analysis (e.g. Mitchell et al., 2007; Böhme et al., 2013; Ostermann et al., 2016). However, the main objective of landslide chronologies and regional studies is to link the failure timing to potentially controlling factors, such as debuttressing (Cossart et al., 2008; Ballantyne et al., 2014; Hermanns et al., 2017), tectonic activity (Hermanns et al., 2001; Sanchez et al., 2010) and various climatic stresses (Dortch et al., 2009; Nagelisen et al., 2015) (cf. Sec. 2.2). But no matter if case study or regional study, an increasing number of landslide chronologies, ideally using a variety of dating techniques, allows for the contextualisation of (newly) dated landslide events and an enhanced understanding of potential regional trigger events versus local or internal destabilisation processes.

To date rock-avalanche or rockslide events using surface exposure dating techniques, the most common strategy is to sample large boulders sitting on top of the deposits (Figure 3.4B; e.g. Ballantyne and Stone, 2004; Hewitt et al., 2011; Hermanns et al., 2017). While the landslide deposits are usually well accessible, a number of potential sources of error have to be considered in order to produce reliable results. In addition to the shielding considerations, the boulders must have been stable during their entire exposure time to ensure constant conditions in relation to production rates. Production rates are also influenced by the size and shape of the boulders wherefore preferably several meter large and flat boulder surfaces are targeted (Masarik and Wieler, 2003). To address the uncertainty of potential inherited nuclide concentrations in the boulders of unknown pre-failure depth (cf. Sec. 3.3 and 6.1) some studies include surface exposure ages from failure surfaces, representing the maximum pre-failure depth and thus the location with minimal pre-failure TCN production (Hermanns et al., 2004; Ivy-Ochs et al., 2009). However, failure surfaces are often undefined or inaccessible restricting this approach to a limited number of applicable sites.

More studies exist, where outcropping sliding planes of deep seated gravitational slope deformations (DSGSDs) and slow moving rock slides are dated and analysed (e.g. Le Roux et al., 2009; Sanchez et al., 2010; Hermanns et al., 2012b; Pánek et al., 2018). The sampling strategy for such localities is similar to the approach for age and slip rate determination on fault scarps (e.g. Tikhomirov et al., 2014; Pousse-Beltran et al., 2017). Analysing vertical transects over the scarps allows for the calculation of potential sliding rates in between two sample points and the potential timing of initial failure. The results of two slowly deforming rockslides in the French Alps and two rock-slope instabilities in Norway indicate progressive slope deformation over several thousands of years (Le Roux et al.,

2009; Sanchez et al., 2010; Hermanns et al., 2012b, 2013c). In contrast, a sampled sliding surface of a large DSGSD in the French Pyrenees suggests a rather sudden gravitational deformation (Lebourg et al., 2014). However, potential uncertainties connected to post-exposure rock fall and the build-up of large debris cones can lead to non-chronological results and make interpretations challenging (Le Roux et al., 2009).

4 Geographic setting

The study areas of this thesis are mostly in Norway with an additional study site in Patagonia, Chile. The geographic background of the study sites and their surrounding regions is highly relevant for the results of this thesis and following interpretations and discussions. This chapter provides therefore an extensive overview over the geological and glacial history of Norway, its climate since the last glaciation and related variations in the past and present permafrost distribution. In this context, the systematic mapping of rock-slope instabilities in Norway is briefly presented, which provides valuable information about each study site.

4.1 Norway

Norway is part of the Scandinavian Peninsula and is characterised by an extensive fjord- and valley system shaping a coastline over 25,000 km in length including the islands of Jan Mayen and the Svalbard archipelago (>58,000 km with all island coastlines) (Worldatlas, 2018). Almost 75% of the Norwegian population lives along the coast, especially in the south and the southwest, while most of the inland and northern communities have a population density of 0-10 inhabitants/km². And although this uneven distribution is reasonable due to economics and climate, many of the coastal regions are prone to natural hazards, such as avalanches, debris flows and CRSFs. The latter can trigger subsequent displacement waves in fjords and lakes reaching large parts of the coast with potential high economic and life consequences.

4.1.1 Geology and glacial history

The geology of Norway is dominated by the Scandinavian Caledonides stretching from southern Norway over >1500 km to the Barents Sea region in northern Norway (Corfu et al., 2014). With a maximum width of 300 km the mountain range reaches into Sweden in the east (Roberts and Gee, 1985), while the highest peaks are located in the

4 Geographic setting

Jotunheimen region in western Norway with up to 2469 m asl. (Galdhøpiggen). The oldest autochthonous Archaean and Proterozoic crystalline basement rocks only crop out in southern Norway (and in the east of the Caledonides in Sweden). During the Caledonian orogeny and a general NW-SE crustal shortening in the early Palaeozoic, several allochthonous nappes were thrust up to several 100 km eastwards, over the Fennoscandian Shield (Roberts, 2003). Today the main rock type groups in Norway are (1) the Western Gneiss Region, which consists of metamorphosed pre-cambrian basement rocks, (2) the lower and middle Allochthons with dominantly sedimentary and metasedimentary nappe complexes and (3) the heterogeneous upper (high-grade shists to granulite and eclogite facies) and uppermost Allochthons (mainly gneiss) forming the largest part of the Caledonides (Roberts and Gee, 1985). The Caledonide structural fabrics and mineralogical banding add to the post-glacial rock slope stability by inherent critical weaknesses along the glacially oversteepened valley sides.

The present topography is the result of landscape modulation by several glaciations. Early Weichselian glaciations transformed a fluvial mountain system into a softer glacial landscape, which subsequently was modified by additional glacial erosion during early and middle Quaternary glaciations (MIS 2) to the characteristic u-shaped fjord- and valley system (Mangerud et al., 2011). The simultaneous removal of pre-Quaternary moraines inhibits the determination of earlier ice-extents in most areas. However, on high elevations surfaces from the Palaeogene and Cretaceous (MIS 5-3) are preserved due to cold-based non-erosive ice conditions during the most recent glaciations (Mangerud, 2004). Often they are covered by autochthonous pre-glacial blockfields of a few meters thickness (e.g. Nesje et al., 1988; Brook et al., 1996) and are lacking erratics, striation or moraine deposits (Sollid and Sørbel, 1979).

Deglaciation of the Scandinavian Ice Sheet began by thinning during the Bølling-Allerød interstadial (ca. 15-13 ka ago) at the end of the late Weichselian glacial (MIS 2). While the following cold Younger Dryas (YD) stadial led to widespread glacial re-advance, reaching the recent fjord heads in many valleys, the outer coast of Norway remained ice-free after initial deglaciation (Longva et al., 2009; Mangerud, 1987; Stroeven et al., 2016). The YD period was followed by rapid deglaciation, where ice streams in valleys remained only a few hundred years longer than the ice sheets on mountain plateaus. The timing of glacial advance and deglaciation was spatially variable along the Scandinavian Ice Sheet, but most major valleys were ice free 12-11 ka ago, with a slightly later deglaciation in south western and central Norway (Hughes et al., 2016).

Late Weichselian glacial fluctuations were accompanied by relative sea-level changes following the glacial load alterations of the Scandinavian Ice Sheet (Lohne et al., 2007). While during early deglaciation, the valleys in the coastal regions were inundated by the sea up to 220 m asl. (Oslo area), the relative sea-level lowered approximately exponentially with the glacio-isostatic uplift (Svendsen and Mangerud, 1987; Høgaas et al., 2012). However, because of the simultaneous global sea-level rise due to melt water, the total glacio-isostatic uplift exceeds the elevation difference between the maximum post-glacial marine limit and today's coastline (Høgaas et al., 2012). In many valleys, the marine limit can be reconstructed by elevated beach ridges and marine shells. The latter allow time constraints on different sea levels and thus the approximation of sea-level functions with time for single locations (Svendsen and Mangerud, 1987). Because of the overlap of deglacial processes with the relative sea-level fall and mass wasting processes, the Quaternary geology of Norwegian valleys is characterised by a combination of Pleistocene supraglacial, subglacial and proglacial subaerial and submarine deposits, post-glacial mostly Holocene near-shore marine, beach, alluvial and colluvial sediments, and rock-slope failure deposits (Corner, 2006; Eilertsen et al., 2006; Hilger et al., 2018).

4.1.2 Holocene and recent climate

Natural climate fluctuations over time are a global phenomenon but with significant spatial variability. Stable oxygen isotopes in deep ice-cores from large and thick ice sheets (e.g. Greenland ice sheet or Antarctic ice sheet) allow for long-term climate reconstructions, representing general climate trends in the northern or southern hemisphere (Masson-Delmotte et al., 2006). And while many distinct climatic signals of the ice cores can be observed in local climate reconstructions in large parts of the world, they may vary in intensity and concurrence. Climatic changes in Norway generally follow the fluctuations of the Greenland ice-core data (Andersen et al., 2004), but exhibit significant regional variations (Lilleøren et al., 2012).

An abrupt increase of temperature terminated the YD cold period (which followed the Bølling-Allerød interstadial) from about 12 ka (Severinghaus et al., 1998). The warming was interrupted by several cooling events, whereof the last one, between 8.4 and 8 ka, was the most short-lived but strongest (Alley et al., 1997). Glacial re-advances during these events were recorded for several regions of southern Norway (e.g. Bakke et al., 2005; Dahl and Nesje, 1994; Dahl et al., 2002; Nesje et al., 2001; Nesje, 2009), while the impact in northern Norway seemed to be minor (Lilleøren et al., 2012). The general warming trend

4 Geographic setting

culminated in the period of the Holocene thermal maximum (HTM) with a maximum c. 8-5 ka ago, where temperatures were significantly higher than today.

Lilleøren et al. (2012) compiled a large climate-proxy dataset of several regional and local studies to generate climate reconstructions representative for northern and southern Norway, including summer and winter temperature anomalies (Fig. 4.1). In addition to a shift of the HTM, temperature fluctuations after 5 ka seem to differ spatially, which is in agreement with a Europe wide climate reconstruction by Mauri et al. (2015). While in northern Norway relative summer temperatures stay above recent summer temperatures almost until today, summer temperatures in southern Norway drop relatively quickly after the HTM being slightly cooler than today during the last 2000 years. After a pronounced cooling event between 5 and 4.5 ka, temperatures in southern Norway seemed to have decreased with minor fluctuations, while post-HTM temperature fluctuations in northern Norway show larger amplitudes, especially during the winter season.

A similar north-south gradient can be observed for precipitation changes. Post YD summer precipitation in northern Norway was generally similar or slightly higher than today, whereas the south and especially the coastal regions received slightly higher summer precipitations compared to today. However, the Holocene pattern of winter precipitation is more complex. Northern Norway reaches a maximum of winter precipitation around the HTM with relatively low winter-precipitation rates throughout the Holocene. Initially high winter precipitation in southern Norway is interrupted by relatively dry winter seasons from 7 to 6 ka, followed by a precipitation increase, which fluctuates back to low winter precipitation from 3 ka (Mauri et al., 2015).

The Little Ice Age (LIA), a pronounced cooling event from the early 14th century to the mid-19th century affected most of the northern Hemisphere, including both, northern and southern Norway. During this time period mean annual air temperature (MAAT) were almost 1° colder than today and glaciers reached a maximum expansion since the last glacial (e.g. Nesje et al., 2001; Lilleøren et al., 2012). Nesje et al. (2008) argue, that the glacial advance during the LIA was not only driven by generally cold temperatures, but that mild and humid winters, related to increased snow precipitation onto the glaciers, was the main cause.

The high topographic variation and long south-east extension results in a not only temporally but spatially variable climate throughout mainland Norway. MAAT during the last normal period (1971-2000) ranges from below -6°C in the Jotunheimen region, the highest part of the Scandes, to 6-8°C along the southern and western coast. And while MAATs below 0°C are restricted to the high mountain areas in southern Norway, they

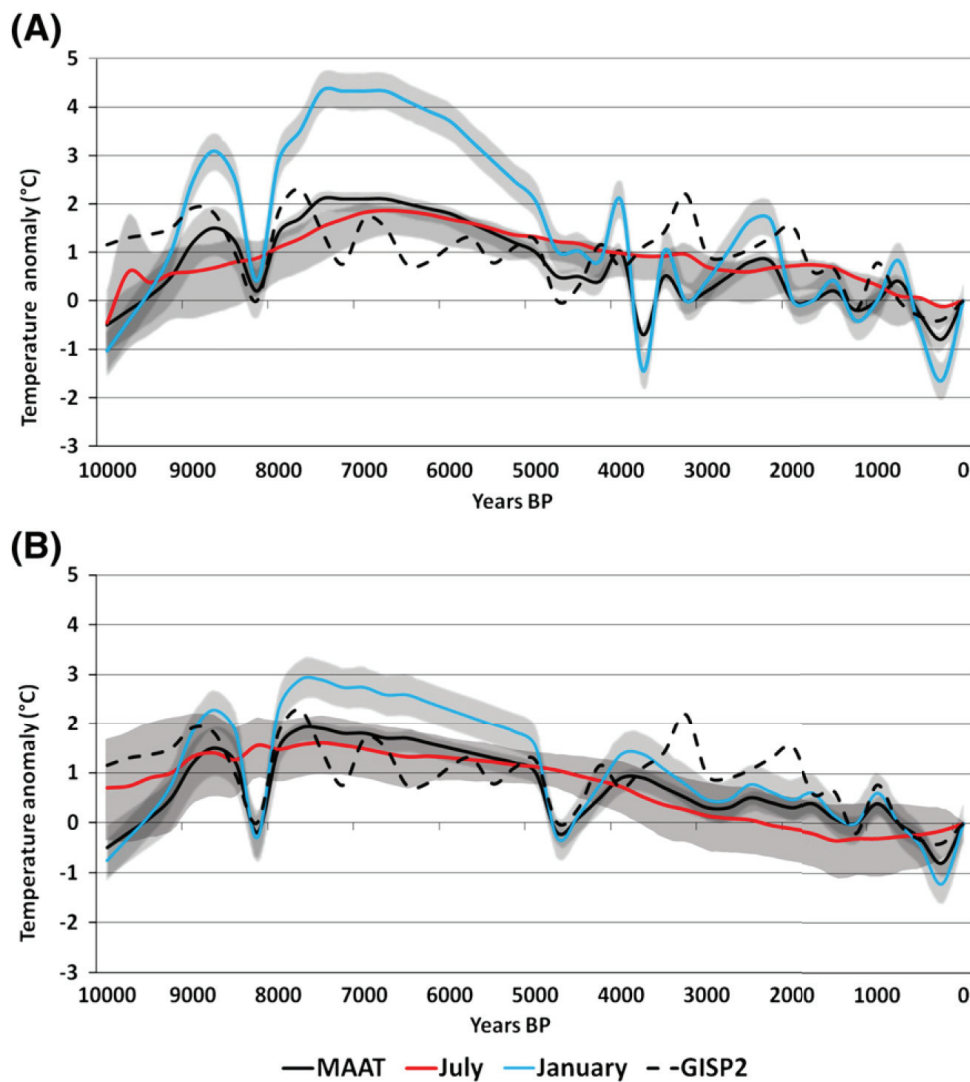


Figure 4.1: Temperature anomalies of today's (1961-90) mean annual air temperature (MAAT) throughout the Holocene for northern Norway (A) and southern Norway (B) (Lilleøren et al., 2012, Fig. 4).

are common in northern Norway, where only the coastal parts reach a MAAT of 0-4°C (seNorge.no, 2018).

Precipitation patterns over Norway show a strong west-east gradient. Because most of the precipitation results from western winds from north Atlantic cyclones and convective systems, the S-N orientated Scandes represent a significant orographic barrier. While the mean annual precipitation along the western coast lies between 2000 and >3500 mm for the period 1981-2010, south eastern valleys and large parts of northern Norway receive less than 750 mm precipitation annually (Dyrørdal et al., 2016).

4.1.3 Present and past permafrost distribution

Strongly connected to the MAAT and its variability is the mean annual ground temperature (MAGT), which defines the distribution of permafrost. Sporadic permafrost with a MAGT close to but below 0°C can be found in palsa mires down to c. 1000 m asl. in southern Norway and down to sea-level in northern Norway. While Finnmark county, especially the Finnmarksvidda plateau, is characterised by the most extensive palsa mires (Sollid and Sørbel, 1998; Farbrot et al., 2013; Borge et al., 2017), mires with sporadic permafrost occur along most of the Norwegian-Swedish border (Figure 4.2; Gisnås et al., 2017).

Both in northern Norway and southern Norway the alpine regions are affected by mountain permafrost. In southern Norway alpine permafrost is restricted to areas above 1300-1400m asl. in the east and 1600m asl. in the west, where the maritime climate effect increases with coastal proximity (Figure 4.2; Etzelmüller et al., 2003; Lilleøren et al., 2012). A similar east-west gradient is observed in northern Norway, where the lower boundary of alpine permafrost lies between 600-700 m asl. in the east and 1000-1200 m asl. in the west (Christiansen et al., 2010; Lilleøren et al., 2012; Gisnås et al., 2013). However, permafrost (most likely sporadic or discontinuous) has been observed in open fractures and steep rock walls down to 600 m asl. in the coastal area of Troms county (Blikra and Christiansen, 2014; Frauenfelder et al., 2016). A systematic statistical approach, modelling permafrost in steep rock walls, illustrates that the lower boundary of mountain permafrost is strongly dependent on the aspect of the rockwalls, with an altitudinal difference of 350-400 m between south- and north-facing rock walls in southern Norway and a difference of 200-250 m in northern Norway (Magnin et al., 2019). The results of this model suggest, that permafrost in steep rock slopes may exist outside of the previously modelled permafrost distributions, with a lower limit of discontinuous permafrost (permafrost probability $\geq 50\%$) at ~ 1200 m asl. in southern Norway and 700 m asl. in northern Norway, where sparse discontinuous permafrost can be found down to elevations of 50 m asl. at the highest latitudes.

It has been suggested by Berthling and Etzelmüller (2011) that pre-existing permafrost in high altitude areas in Norway could have persisted throughout the last glacial maximum (LGM). The presence of blockfields on mountain plateaus especially is an indicator for cold-based non-erosive glacial conditions during the late-Weichselian stadial, where permafrost conditions were preserved under the glacier ice (Figure 4.2; e.g. Nesje et al., 1988; Kleman and Borgström, 1990; Ballantyne and Stone, 2015).

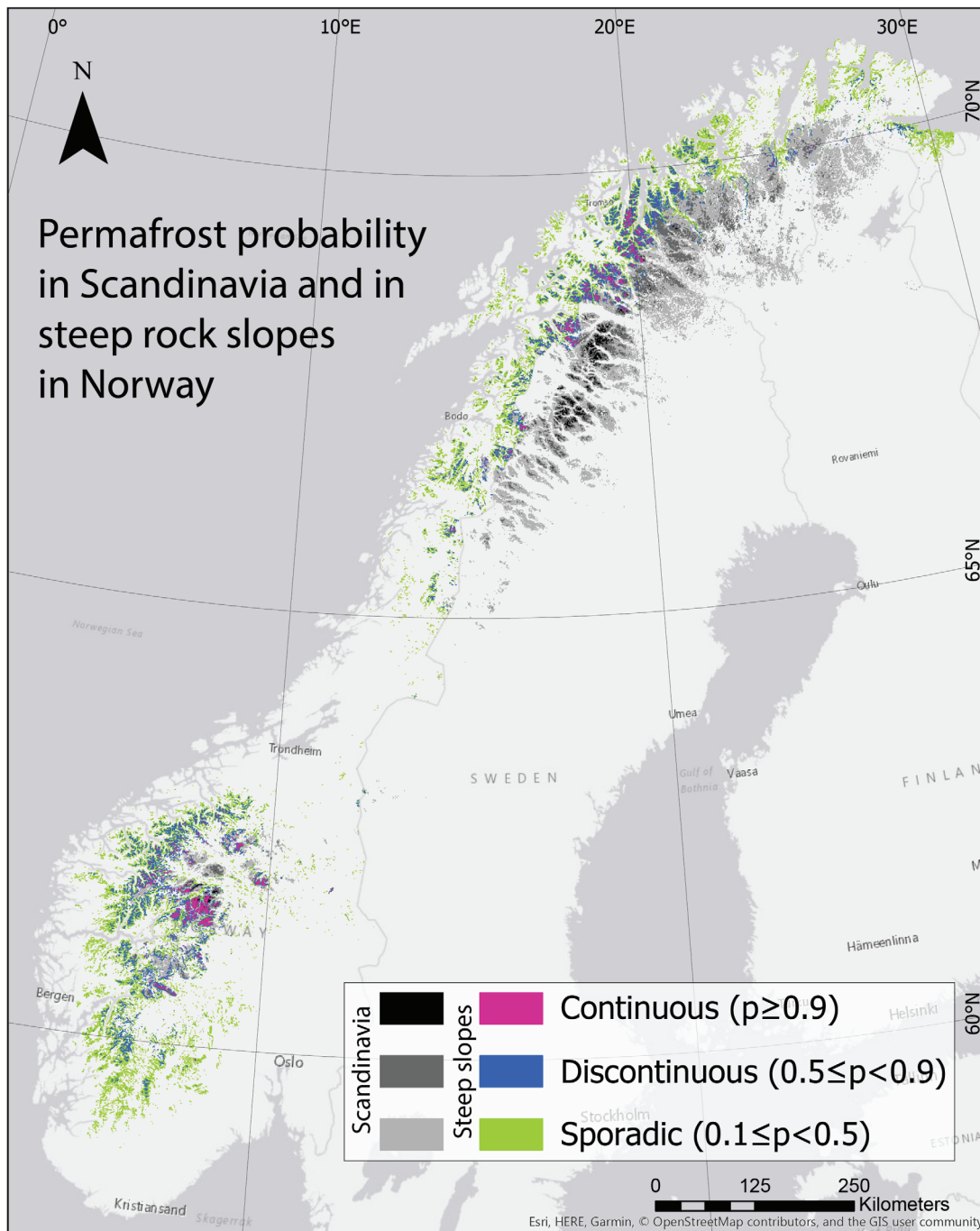


Figure 4.2: Permafrost probability distribution over Scandinavia (greyscales; Gislås et al., 2017) and in steep slopes ($>40^\circ$) in Norway (colour scale; Magnin et al., 2019). The permafrost probability (p) is classified after Brown et al. (1997). Note the occurrence of discontinuous and sporadic permafrost in steep slopes along the coast, outside of the general permafrost distribution by Gislås et al. (2017).

4 Geographic setting

Because of the thermal conditions of warm-based glaciers, the ground in valley settings and close to the ice-sheet margins was insulated from the cold air temperatures during the Pleistocene, resulting in unfrozen conditions during glaciation. But areas, that became ice-free during early stages of the Pleistocene deglaciation, experienced deep penetrating permafrost conditions throughout the Pleistocene. Although post-glacial permafrost propagation following deglaciation continued during the late Pleistocene, the depth of permafrost conditions was limited by the strongly increasing temperatures and the onset of widespread permafrost degradation at the beginning of the Holocene (Myhra, 2016). The spatial variability of deglaciation patterns in Norway thus resulted in a strong variability of permafrost conditions.

However, considerable permafrost degradation and MAATs up to 2°C higher than the 1961-90 normal period enabled only the highest locations in Norway to maintain frozen-ground conditions throughout the HTM (Lilleøren et al., 2012). The most extensive Holocene permafrost distribution occurred during the LIA (Figure 4.1; Lilleøren et al., 2012). Generally, permafrost dynamics in northern Norway seem to be more sensitive to climatic changes than in southern Norway. A deeper permafrost penetration in high elevations in southern Norway could be the reason for a more persistent thermal signal at depth, while permafrost aggradation during cold periods in northern Norway was restricted to shallower depths due to the generally lower topography (Lilleøren et al., 2012; Myhra, 2016).

4.1.4 Study sites

All the study sites in Norway have been selected in agreement with project partners according to the research objectives of the CryoWALL project (cf. Ch. 1). Each site is connected to a rock-slope instability, the upper part generally located at the topographical transition from a plateau(like) surface to a steep rock slope. Potential consequences of a catastrophic rock-slope failure from the instabilities include destruction of infrastructure and loss of life, either by direct hit or through landslide induced displacement waves. The study sites cover a latitudinal transect from western Norway (four sites) to northern Norway (four sites) (Figure 4.3). Four of the sites are part of an extensive network of temperature loggers installed in rock walls with different aspects providing valuable information for the analysis of permafrost distribution in steep rock walls on a local, regional and national scale (Magnin et al., 2019).

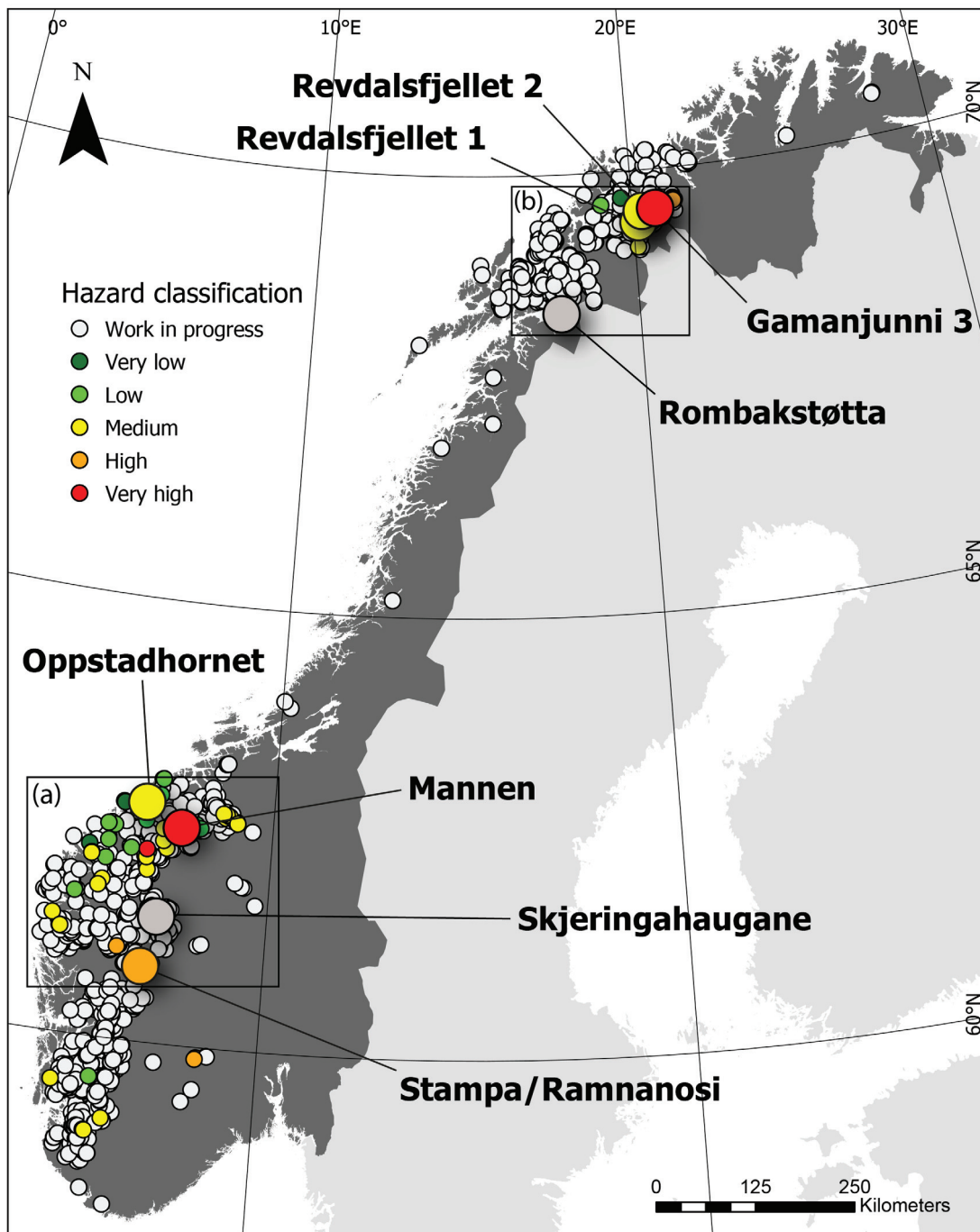


Figure 4.3: Location and hazard classification of the unstable rock-slopes at the study sites. The study site Ramnanosi is connected to the rock-slope instability Stampa. Black boxes indicate the areas of Figure 4.4 (a) and Figure 4.9 (b); Data: NGU (2018).

Mannen, Møre og Romsdal - The rock-slope instability at Mannen is situated along a north-facing slope of Romsdal Valley in the Rauma municipality, western Norway

4 Geographic setting

(Fig. 4.4b and 4.5). It is one of four active rock-slope instabilities along the valley, which features one of the highest density of pre-historic rock-slope failure deposits in Norway (Saintot et al., 2012). Romsdal Valley cuts southeast-northwest through the Western Gneiss Complex, dominated by reworked Precambrian crystalline basement rocks (Roberts, 2003; Corfu et al., 2014). The main rock types around the Mannen rock-slope instability are dioritic-granitic gneiss with local transitions to quartz-rich gneiss with sillimanite and kyanite, coarse granitic gneiss and intermittent amphibolite (Tveten et al., 1998). The Caledonide structural fabrics and mineralogical banding impart critical weaknesses inherent along the glacially oversteepened valley sides.

Post-Weichselian deglaciation in this region began by thinning during the Bølling/Allerød interstadial (c. 15-13 ka), as the outer coast of western Norway became ice-free (Longva et al., 2009). Ice marginal retreat up Romsdal Valley is believed to have been completed between 12.8 and 11.7 ka, following the YD cold period (Hughes et al., 2016; Stroeven et al., 2016; Hermanns et al., 2017). During deglaciation, the landscape was inundated by the

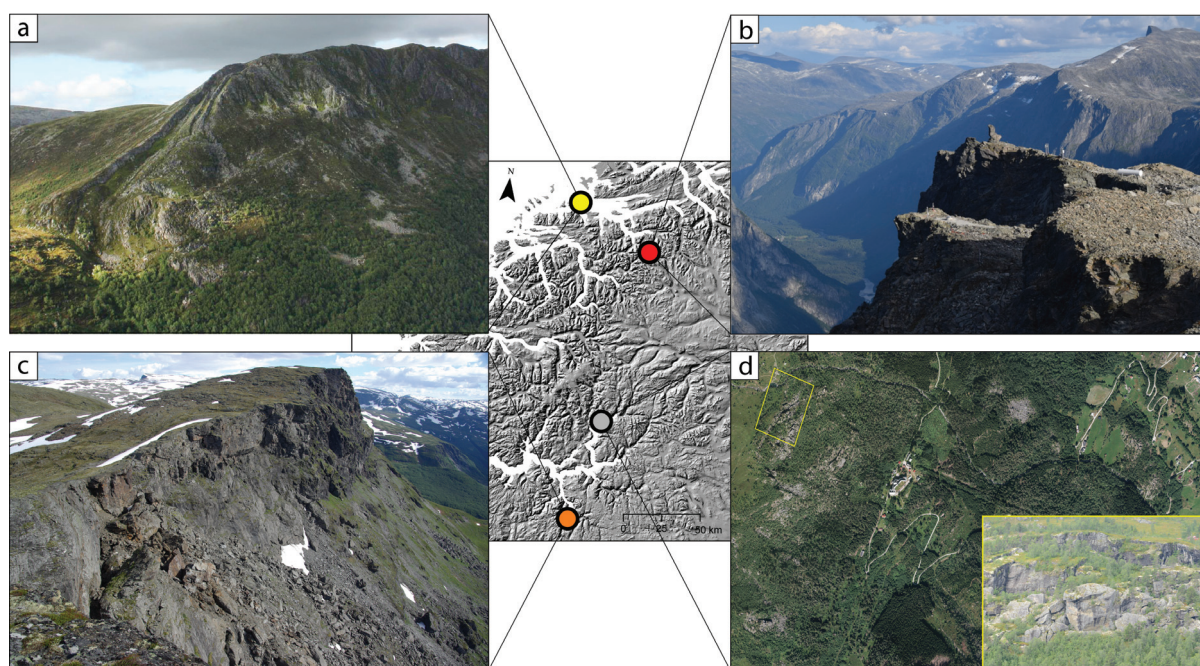


Figure 4.4: Detail hillshade from western Norway (location in figure 4.3) with the location and hazard classification of four study sites: Opptadhornet (a), Photo: T. Oppikofer, Mannen (b), Ramnanosi (c), note that this is a rather stable part of the whole rock-slope instability, Photo: M. Böhme and Skjeringahaugane (d), Orthophoto 'Luster 2012', Source: Kartverket (2018c), Photo: R.L. Hermanns.

sea, which reached a marine limit of 120 m above modern sea level in the Romsdal Valley (i.e. 60 m above the Rauma river at Mannen; Høgaas et al., 2012). Subsequently the relative sea level lowered approximately exponentially with glacio-isostatic uplift, reaching close to today's sea level about 1000 years ago (Svendsen and Mangerud, 1987).

Today, the climate at the site is dominated by maritime humid conditions, with MAAT of 0-2°C and mean annual precipitation (MAP) of 2000-3000 mm (seNorge.no, 2018). At the backscarp of the instability, rock wall temperatures are measured recently, indicating that permafrost was probably present under slightly cooler conditions than today. The Mannen rock-slope instability lies today at the regional permafrost limit in northerly-exposed steep slopes, with a permafrost probability >0.5 in the highest section of the slope (Fig. 4.5a; Magnin et al., 2019).

The Mannen rock-slope instability is located in the upper part of a more than 1200 m high rock slope where the presence of rock-slope failure deposits of up to nine distinct events at the bottom of the valley are evidence for high Holocene rock-slope failure activity (Hilger et al., 2018). The most active part, with deformation rates of $>2 \text{ cm a}^{-1}$, is well delimited by a 20 m high near-vertical backscarp at the top of the slope and a partly

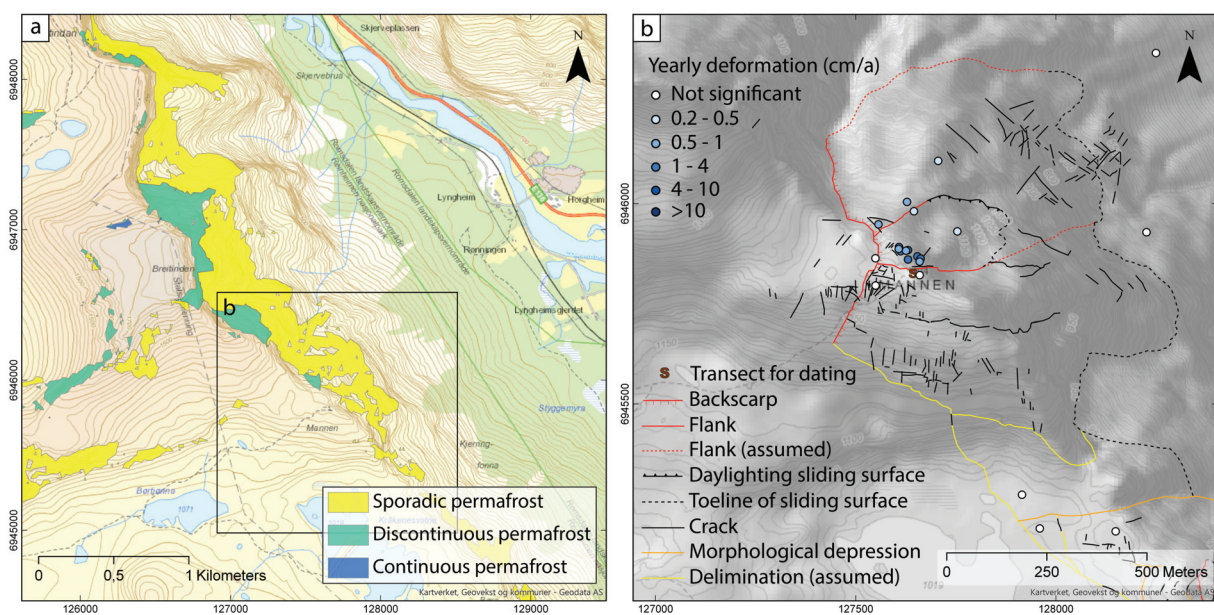


Figure 4.5: Location of the Mannen rock-slope instability in Romsdal valley with the permafrost probability in steep slopes (Magnin et al., 2019) (a). Classification of permafrost probability as in Fig. 4.2. Morphological features of the instability with a fully developed 5 to 20 m high backscarp (NGU, 2018) (b).

4 Geographic setting

outcropping sliding surface in the lower parts (Fig. 4.4b and 4.5b). The estimated yearly likelihood of failure for a 2-4 Mm³ rock mass is 1/100 to 1/1000 (Blikra et al., 2016).

The instability is classified as a high-risk object resulting from a high hazard (deformation rates, structural precondition etc.) and medium consequence class (NGU, 2018). After and during intensive mapping and research activities since 2000 (e.g. Dahle et al., 2010; Henderson and Saintot, 2007; Saintot et al., 2012) a continuous observation and monitoring system was established and expanded since 2009 (Kristensen and Blikra, 2011; NVE, 2017).

Ramnanosi, Sogn og Fjordane - The mountain Ramnanosi is connected to the unstable rock-slope Stampa located in the central part of the Aurland municipality at the fjord head of Aurlandsfjorden (Fig. 4.4c). The latter is part of the inner Sognefjord, the largest fjord in western Norway. The bedrock in the area is characterised by Late Precambrian to Paleozoic metamorphic rock of the lower Allochton (cf. Sec. 4.1.1). While the study site is located completely within phyllites, a thrust plane marks the proximal contact to crystalline bedrock of the overlying Jotun nappe (Corfu et al., 2014). The foliation at Ramnanosi dips moderately towards the valley (west) (Böhme et al., 2013). After the YD the area was deglaciated between 12 ka (on the plateaus; Hughes et al., 2016; Andersen et al., 2018) and 10.8 ka (valleys assumed to be ice-free; Mangerud et al., 2011). However, exposure ages of bedrock from the plateau in the Aurland region indicate that either high elevations have been ice-free before the YD glacial re-advance, or glacial erosion has been limited. While two sampled boulders indicate deglaciation between 11 and 12 ka on the plateaus, three bedrock exposure ages above 20 ka affirm that glacial erosion was not sufficient to reset TCN concentrations (Andersen et al., 2018).

Today, the climate at the site is dominated by maritime humid conditions, with MAAT of -1-2°C and MAP of 2000-3000 mm (seNorge.no, 2018). The steep rock-slope at Ramnanosi lies today within the regional permafrost limit for sporadic permafrost in steep slopes. The probability for permafrost occurrence within the slope is mostly 0.1-0.5, with a permafrost probability >0.5 in the highest section of the slope (Fig. 4.6a; Magnin et al., 2019).

The Stampa rock-slope instability, including Joasete, Furekamben and Ramnanosi was first described in the early 2000s (Domaas et al., 2002; Braathen et al., 2004) and later in detail analysed by Böhme et al. (2013) and Blikra et al. (2013a). The most active part is Stampa, where maximum deformation rates are up to 0.5 cm a⁻¹. In this study the southernmost part of the instability around Ramnanosi (1421 m asl.) is relevant, which is

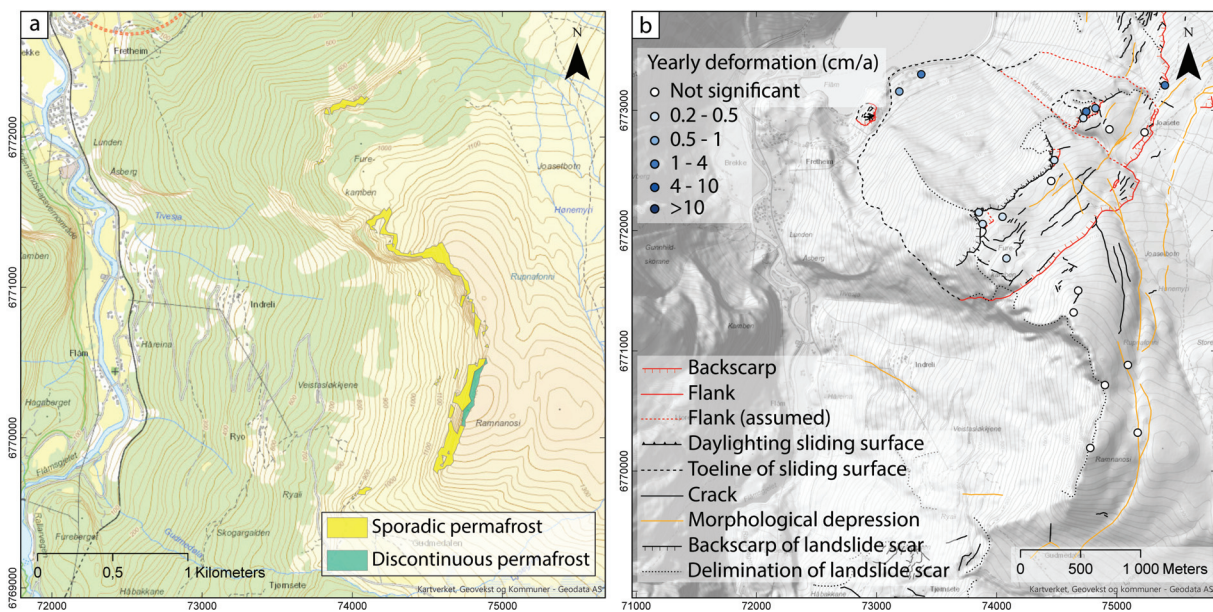


Figure 4.6: Location of Ramnanosi and its west-facing steep rock slope with a permafrost probability of 0.1-0.5, and higher in the highest section (Magnin et al., 2019) (a). Morphological features of the Stampa instability, including Ramnanosi as a relatively stable part (NGU, 2018) (b). Note, that the scale of (b) is with 1:30,000 larger than the scale of (a) with 1:20,000.

characterised by an up to 200 m high west facing rock wall and slope-parallel depressions indicating gravitational faults east of the rock wall (Fig. 4.6b). Extensive unvegetated rock-fall deposits demonstrate the recent activity of the rock wall and partly cover several deposits from rockslides and/or creeping processes reaching down to the valley bottom (Blikra et al., 2002; Böhme et al., 2013). Two samples representing the northern most lobate landform have earlier been analysed for cosmogenic nuclide exposure dating. One gives a late-Pleistocene age within the estimated period of deglaciation, while the other one seems to represent a late-Holocene rock fall over 2000 years ago (Böhme et al., 2013).

Skjeringahaugane, Sogn og Fjordane - The Skjeringahaugane slope instability is located in Lustrafjorden, a northern arm of inner Sognefjord (North east of Ramnanosi) and part of the Luster municipality (Fig. 4.4d). The bedrock at Skjeringahaugane is similar to the Ramnanosi site, with predominantly phyllites and mica shists from the relatively thin (1 km) lower Allochthon (cf. Sec. 4.1.1) with the contact to the granitic gneiss of the overlying Jotun nappe in direct vicinity (Henderson et al., 2008; Corfu et al., 2014). The foliation dips with 15-20° towards the fjord (SE) (Hermanns et al., 2012b). The

4 Geographic setting

area has been deglaciated around 11 ka (Hughes et al., 2016). Because of the relatively low elevation of the slope instability (600-750 m asl.), the timing of local deglaciation probably indicates the time when the site first became ice free after the LGM.

Today, the climate at the site is dominated by maritime humid conditions, with MAAT of 2-4 °C and MAP of 1500-2000 mm (seNorge.no, 2018). The modern regional permafrost limit in steep slopes lies several hundred meters above the Skjeringahaugane rock-slope instability (Fig. 4.7a; Steiger et al., 2016; Magnin et al., 2019).

The unstable slope area is divided into three segments with a total volume of 80 to 200 Mm³. The upper ~10,000 m² large part is delimited by an open back fracture, mapped as morphological depression in Fig. 4.7b. The fracture is covered with soil and vegetation, suggesting no recent deformation, as opposed to the sparsely vegetated ~46,000 m² middle part, which is broken up into large blocks with 10 to 500 m² surface area separated by deep open cracks (Hermanns et al., 2011). The largest and lowest part of the instability is characterised by some large open cracks in an otherwise vegetated area. The lack of soil and vegetation in the cracks indicates recent deformation in

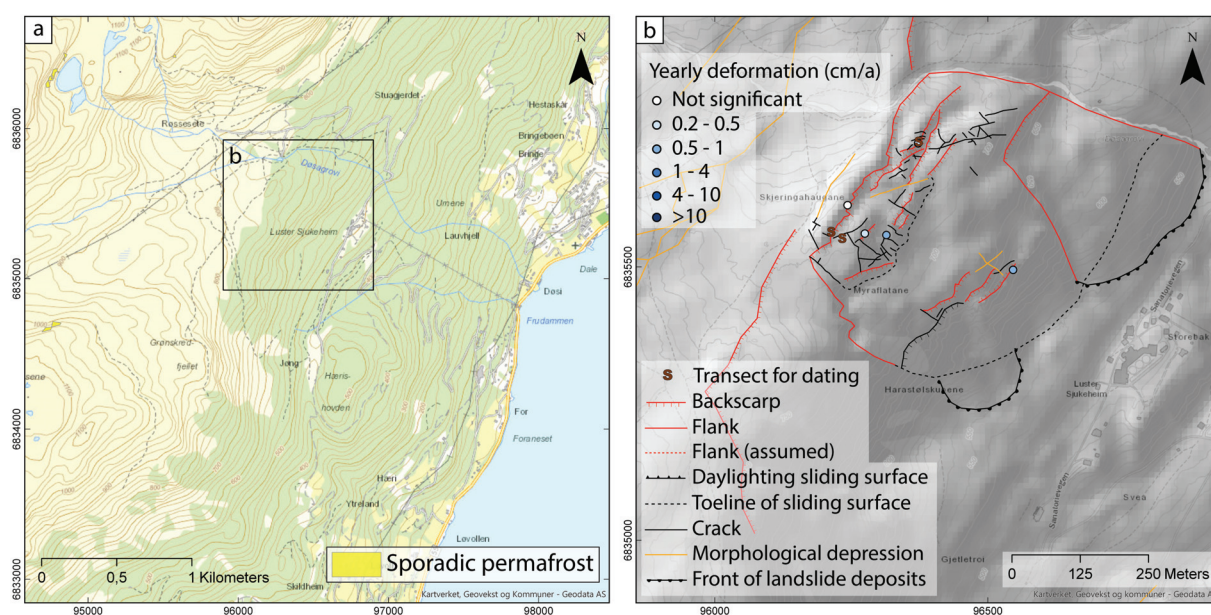


Figure 4.7: The low-elevation Skjeringahaugane rock-slope instability located several hundred meters below the regional permafrost limit in steep slopes after Magnin et al. (2019) (a). The oldest and inactive part of the instability is delimited by a morphological depression, while the more active middle and lower parts are characterised by open cracks and fractures (b). Data in (b) from NGU (2018).

both the middle and the lower part of the instability, which is supported by deformation measurements (Fig. 4.7b).

The Skjeringahaugane slope instability is periodically monitored but not yet classified after the hazard and risk classification, but recent deformation rates are $<0.5 \text{ cm a}^{-1}$ for all three sub-blocks. Revised and re-calculated data of three vertical transects in the middle part of the Skjeringahaugane instability, previously published by Hermanns et al. (2012b) are presented in this thesis.

Oppstadhornet, Møre og Romsdal - The Oppstadhornet slope instability is situated on the coast of Møre og Romsdal county at the southern slope of Otrøya island (Fig. 4.4 and 4.8a). It is located in the Western Gneiss Complex c. 45 km northwest of the Mannen instability and is characterised by locally well foliated dioritic to granitic gneiss dipping steep to moderately towards the fjord (S) (Derron et al., 2005). This part of the western coast of Norway has been deglaciated around 15 ka and has been ice-free throughout the late Pleistocene and Holocene (Hughes et al., 2016).

Today, the climate at the site is dominated by maritime humid conditions, with MAAT of $4-6^\circ\text{C}$ and MAP of 2000-3000 mm. The Oppstadhornet rock-slope instability lies today

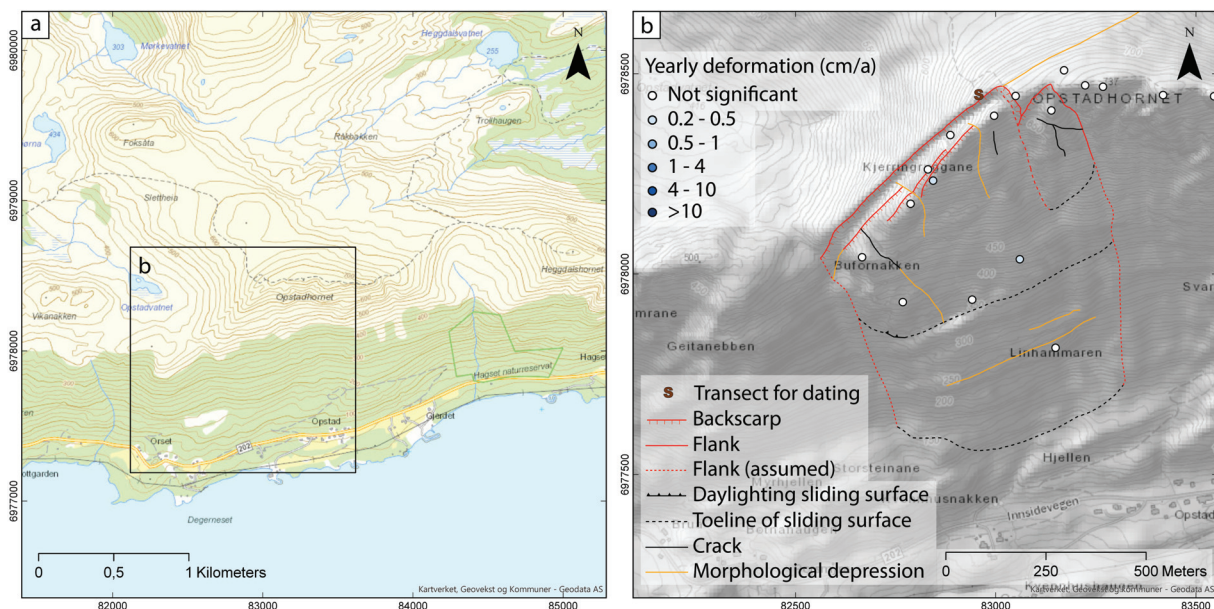


Figure 4.8: Location of the Oppstadhornet rock-slope instability on the southern coast of Otrøya island, above Midfjorden (a). Morphological features of the instability with a fully developed 5 to 20 m high backscarp (NGU, 2018) (b).

4 Geographic setting

well below the regional permafrost limit for steep slopes in Norway (Fig. 4.8a; Steiger et al., 2016; Magnin et al., 2019).

A fully developed backscarp along the foliation delimits the $\sim 20 \text{ Mm}^3$ large instability between 700 and 750 m asl. and demonstrates 5 to 20 m deformation over $>500 \text{ m}$ since initial failure. Several less developed backscarps and open cracks indicate internal deformation of the unstable rock mass (Fig. 4.8b; Braathen et al., 2004). Hermanns et al. (2013c) took a transect of five samples for exposure dating over the main head scarp (Fig. 4.8b) and set them into the context of initial failure and the development of sliding rates. In this thesis, the exposure ages were revised and re-calculated.

Because of the potentially extremely severe consequences, the Oppstadhornet slope instability is classified as a high risk object. However, the hazard for potential failure remains low to medium, i.a. because of low recent deformation rates of $<0.5 \text{ cm a}^{-1}$ (NGU, 2018).

Revdalsfjellet 1+2, Troms - In the Kåfjord municipality in northern Norway, two adjacent rock-slope instabilities are located at 650-670 m asl. above the Lyngen fjord on a west facing slope below the mountain Revdalsfjellet (Fig. 4.9a+b), only seven kilometres south of a continuously monitored high-risk instability at Nordnesfjellet (e.g. Blikra et al., 2009; Blikra and Christiansen, 2014; NGU, 2018). Garnet-mica schist and quartz-mica schist of the upper allochthon Kåfjord nappe are the main rock types on this side of the fjord (Boyd et al., 1984; Augland et al., 2014). The main direction of the locally very variable foliation is sub horizontal falling towards northwest and southeast (NGU, 2018).

The Revdalsfjellet instabilities are located at a clear topographic change in the slope, where a flat plateau like slope goes over into a steep glacially eroded valley flank. Moraine ridges that are related to the YD glacial extent are mapped almost continuously along the eastern flank of Lyngen fjord with a set of marginal moraines at c. 700 m asl. just above the instabilities (Corner, 2004; Blikra and Christiansen, 2014). While higher areas remained nunataks during the YD glaciation and might have been ice-free for 13 ka, both plateaus and valleys in the area were ice-free 11 ka ago (Hughes et al., 2016), which is in agreement with two local exposure age determinations (cf. Sec. 6.4).

Today, the local climate is dominated by maritime humid conditions, with MAAT of -2.0°C and MAP of 1000-1500 mm at the unstable site. The modern regional permafrost limit in steep slopes lies close to the top of the instabilities, with a probability of permafrost occurrence in the Revdalsfjellet instabilities of 0.1-0.5 (Fig. 4.10a; Magnin et al., 2019).

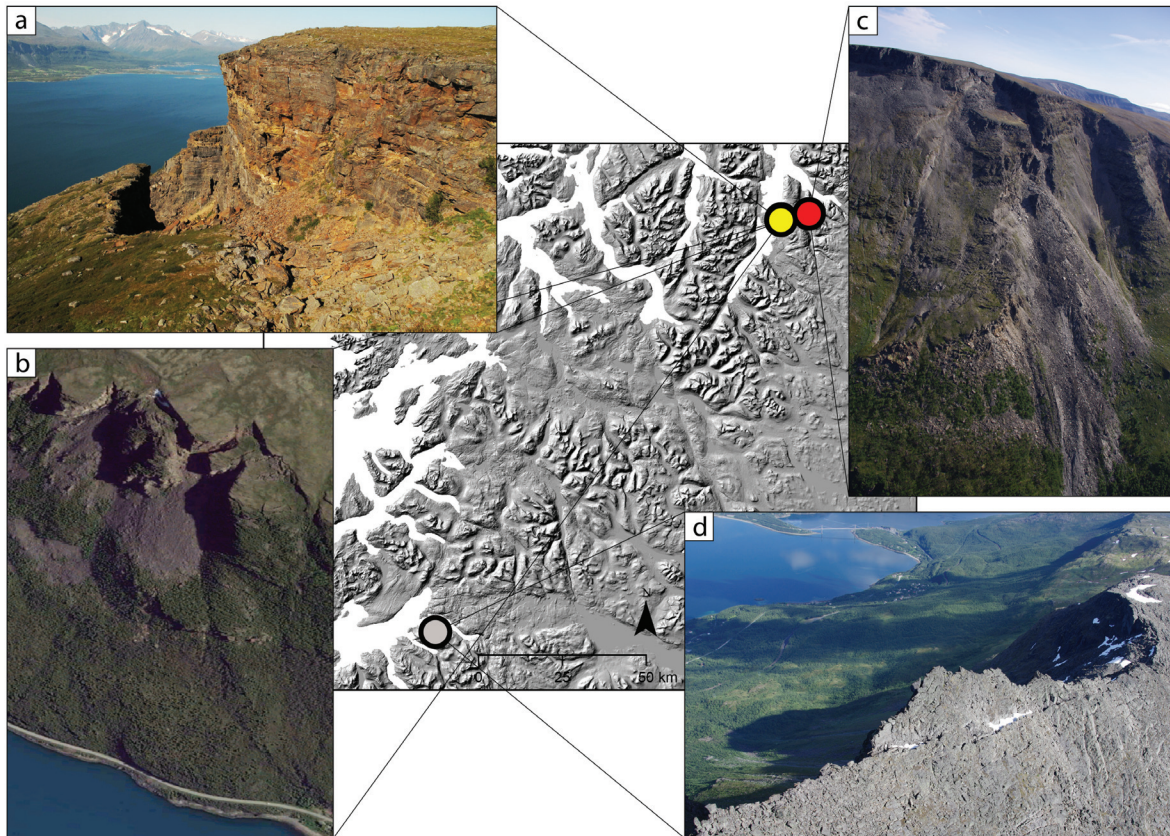


Figure 4.9: Detail hillshade from northern Norway (location in figure 4.3) with the location and hazard classification of four study sites: Revdalsfjellet 1 (a), Photo: H. Bunkholt, Revdalsfjellet 1 (right) and Revdalsfjellet 2 (left) (b), Aerial photograph from 2015, Source: GoogleEarth, Gamanjunni 3 (c), Photo: H. Bunkholt and Rombakstøtta (d), Photo: M. Böhme.

The Revdalsfjell instabilities 1 and 2 are wedge failures (cf. Stead and Wolter, 2015) with fully developed back scarps (Fig. 4.9b) cutting the foliation and manifesting 15 and 20 m near vertical displacement, respectively. The surfaces of the displaced blocks have the same characteristics as the plateau surfaces around the instabilities and are c. 250x150 m and 200x100 m large (Blikra et al., 2006a; Henderson et al., 2010). Estimated volumes for Revdalsfjellet 1 are two scenarios with 7 Mm³ and 800,000 m³, respectively. At Revdalsfjellet 2 a potential sudden failure could incorporate a volume of 5 Mm³. The slope below both instabilities is characterised by valley parallel cracks, indicating deformation almost down to the fjord. Deformation rates measured with differential global positioning system (GPS) are 0.2-0.3 cm a⁻¹ (Henderson et al., 2010) and 0.4-0.6 cm a⁻¹ respectively (Fig. 4.10b), and <0.8 cm a⁻¹ and <0.9 cm a⁻¹ measured with InSAR (NGU, 2018).

4 Geographic setting

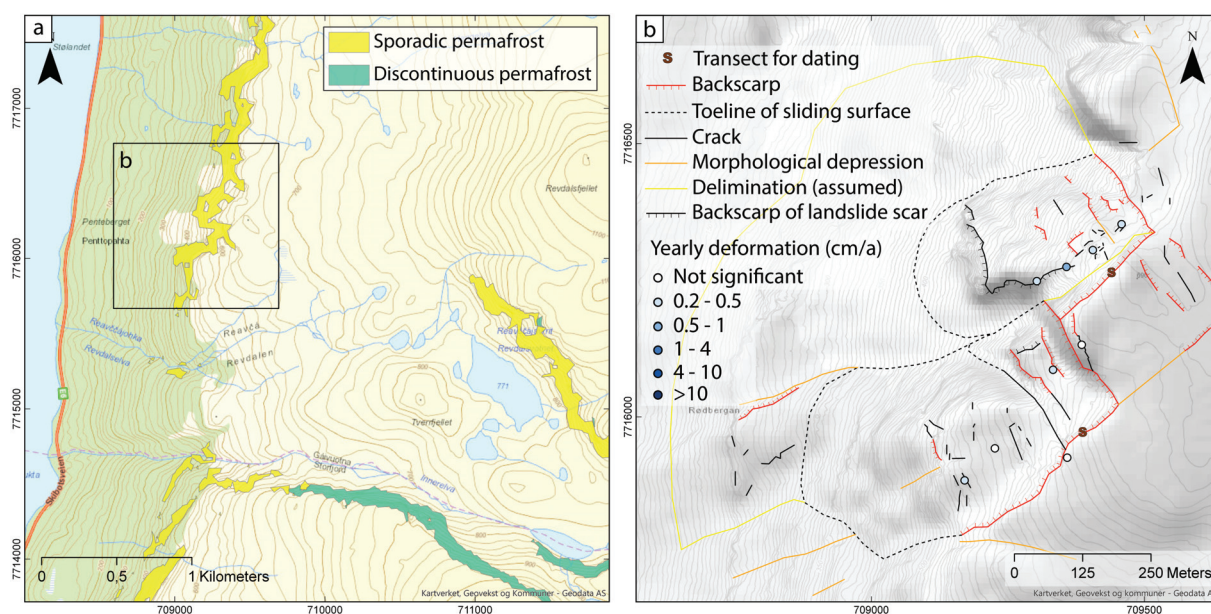


Figure 4.10: Location of the Revdalsfjellet rock-slope instabilities along a west-facing slope with the permafrost probability for steep slopes after Magnin et al. (2019) (a). Morphological features of the instabilities with fully developed wedge-shaped backscarps (NGU, 2018) (b).

Potential consequences in case of a sudden failure are classified to be high for both instabilities. However, because of a low likelihood of failure of $<1/5000$ years, the unstable rock mass Revdalsfjellet 1 is classified as an instability with medium to high risk (Blikra et al., 2016). Unlike Revdalsfjellet 1, Revdalsfjellet 2 is classified as a high risk object, which is the result of a medium failure probability of $1/1000$ to $1/5000$ years together with the severe potential consequences (Blikra et al., 2016).

Gamanjuni 3, Troms - The rock-slope instability Gamanjuni 3 is situated only 8.5 km east-northeast from the Revdalsfjellet instabilities along a west-facing slope of Manndalen valley in the Kåfjord municipality (Fig. 4.9c). As part of the Kåfjord nappe the bedrock of this region is also dominated by mica shists with a generally sub-horizontal foliation (Quenardel and Zwaan, 2008; Böhme et al., 2016).

Because of the proximity to Revdalsfjellet, the two sites share the same general deglacial history. Consequently, Manndalen was deglaciaded after the YD between 12 and 11 ka (Hughes et al., 2016; Stroeven et al., 2016). However, with an elevation of ~ 1200 m asl. Gamanjuni 3 exceeds the mapped YD marginal moraine at Revdalsfjellet by several hundred metres. It is therefore unlikely that the upper part of the unstable rock slope

has been glaciated during the YD and has been ice-free since ~ 14 ka. This allowed for deep permafrost penetration during the cold YD period. Today, the upper part of the instability lies within the limit of discontinuous permafrost in steep slopes and sporadic permafrost is possible almost down to the toe of the instability (Fig. 4.11a; Magnin et al., 2019). Today's climate at the site is also dominated by maritime humid conditions, with MAAT of -3 - -1°C and MAP of 1000-1500 mm.

The unstable rock slope Gamanjunki 3 is, although highly fractured, a coherent sliding block with a well defined wedge shaped backscarp cutting the foliation (Fig. 4.11b). The up to 150 m long daylighting sliding surface separates the sliding block and its intact palaeo-surface from the original plateau surface at ~ 1200 m asl. (Böhme et al., 2016).

Yearly deformation measured with terrestrial radar and differential GPS is with 6 cm a^{-1} high in the upper parts and show decreasing velocities down to $\sim 2\text{ cm a}^{-1}$ at the toe of the instability (Fig. 4.11b). The yearly likelihood of a sudden failure of this c. 26 Mm^3 large block is subsequently estimated to be $>1/100$ (Blikra et al., 2016). The hazard of the instability is classified to be very high, resulting in a high risk classification when combined with the medium potential consequences (NGU, 2018). As a consequence, the instability has been continuously monitored since 2017 (NVE, 2017).

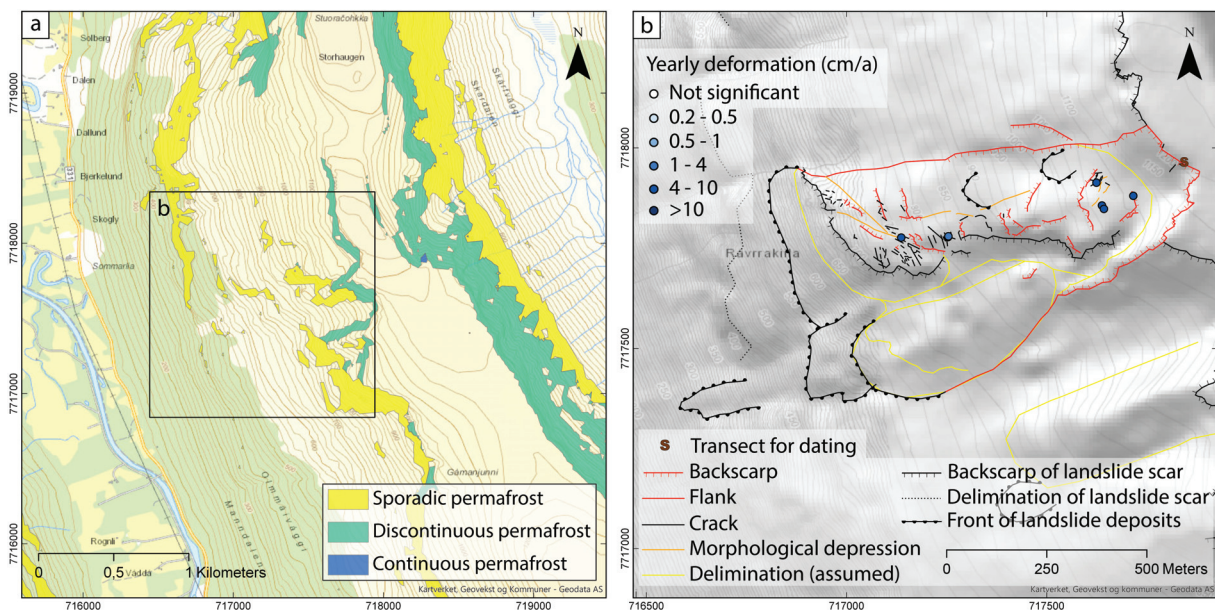


Figure 4.11: Location of the Gamanjunki 3 rock-slope instability along a west-facing slope with the permafrost probability for steep slopes after Magnin et al. (2019) (a). Morphological features of the instability with a fully developed wedge-shaped backscarp (NGU, 2018) (b).

4 Geographic setting

Rombakstøtta, Nordland - Rombakstøtta (local: Tøttatoppen) is a 1230 m high mountain a few kilometres east of the city Narvik in Nordland, northern Norway. On the eastern side of the summit a north facing unstable rock slope has been identified at about 1000-1100 m above the fjord Rombaken (Fig. 4.9d; NGU, 2018). The rock types in the area are characterised by the amphibolitic Narvik nappe complex (Augland et al., 2014; Corfu et al., 2014), which is part of the Caledonian upper Allochthon (cf. Sec. 4.1.1; Roberts, 2003). The area around the slope instability is dominated by quartz-rich garnet mica-shist with a sub-horizontal foliation (Karlsen, 1991).

Several regional studies about the YD ice-sheet extent agree that the glacial re-advance around 12 ka reached beyond Narvik (Bargel, 2003). Post-YD deglaciation of the Rombaken fjord is placed in a time frame between 11 and 10 ka (Andersen et al., 1981). It is however not clear if the mountain section, where the instability is located, has been deglaciated earlier, and whether Rombakstøtta was a nunatak during YD glaciation (Bargel et al., 1995; Hughes et al., 2016). Today, the north-facing slope at Rombakstøtta remains cold with a permafrost probability >0.5 (Fig. 4.12a; Magnin et al., 2019). The local climate, however, is dominated by maritime humid conditions, with MAAT of $0-2^{\circ}\text{C}$ and MAP of 1500-2000 mm.

After a $50-100\text{ m}^3$ large rock-fall event in 1996 caused damage to the frequently used railway running over the large debris cone below the Rombakstøtta instability, a first assessment for potential large scale rock-slope failures was conducted (Larsen, 1997). Valley parallel open tension cracks on the mountain plateau with a few meters to several tens of metres distance define unstable sections of the rock slope. Based on these observations a potential rock-slope failure volume of $100,000\text{ m}^3$ was discussed and the chance that rock-fall events will reach the infrastructure (two transmission lines, railway and E6/overland road) was estimated to be 1/10-20 years (Larsen, 1999). Recent run-out analyses for several rock-slope failure scenarios have shown, that depending on the location of its source area, a CRSF with a minimum volume of 10^6 m^3 may reach the fjord, affecting large areas of the infrastructure, including houses and cabins. Rock-slope failure scenarios of volumes smaller than 10^4 m^3 are unlikely to reach the fjord (Morken, 2017).

Below the steep north facing rock slope between 900 and 1100m asl. an extensive debris cone covers the underlying bedrock and overlies chaotic boulder fields from rock-slope failures exceeding the run-out lengths of recent rock-fall, debris-flow and snow avalanche processes, reaching the fjord in two sections.

4.2 Aysén Fjord, Patagonia (Chile)

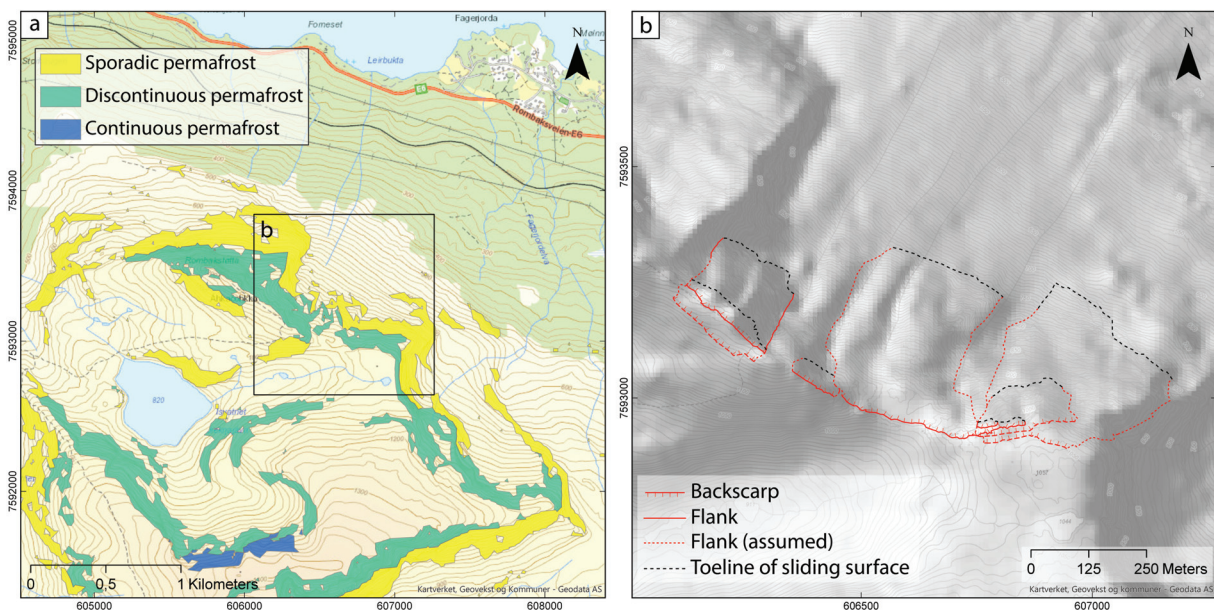


Figure 4.12: Location of the Rombakstøtta rock-slope instability along a north-facing slope with the permafrost probability for steep slopes after Magnin et al. (2019) (a). Morphological features of the instability, which can be divided into several unstable rock-masses along the steep rock slope (NGU, 2018) (b).

4.2 Aysén Fjord, Patagonia (Chile)

Chile stretches over 4000 km north-south along the Pacific coast of South America from the Atacama desert at 18°S to the tip of Patagonia at 56°S (Fig. 4.13a). The western border to Argentina runs along the summits of the Andes resulting in a topographic gradient from sea level in the west to almost 7000 m asl. in the east within ~200 km (Pankhurst and Hervé, 2007). South of c. 40°S the Andean cordillera is dominated by the plutonic complex of the Mesozoic-Cenozoic Patagonian batholith. Aysén Fjord cuts SE-NW (Fig. 4.13b) through late Jurassic to late Paleogene dioritic to granitic intrusions of the North Patagonian batholith, which is the product of the sequential subduction of the Phoenix, Farallon and Nazca plates under the westward-drifting South American plate (Pankhurst et al., 1999; Cembrano et al., 2002). A major NNE-SSW striking fault system has developed over 1000 km within this Cenozoic magmatic arc. Aysén Fjord is located within and crossed by the central part of the active Liquiñe Ofqui Fault Zone (LOFZ) (Cembrano et al., 2002).

During the LGM the southern Andes were covered by the Patagonian ice sheet extending over the entire Patagonian batholith (e.g. Caldenius, 1932; Hollin and Schilling, 1981;

4 Geographic setting

Hulton et al., 2002) with a maximum ice extension in most regions occurring between 27 and 22 ka (Denton et al., 1999). This resulted in a topography similar to the Norwegian coastal morphology, dominated by deeply incised glacial fjords and valleys with oversteepened rock walls. Major post-LGM deglaciation most likely took place from around 16 ka resulting in disconnected ice fields in the central part of the Andes (Kaplan et al., 2004). Glacial dynamical reconstructions by McCulloch et al. (2000) indicate that the study area became ice free by 15 ka. The existence of a later cooling period with glacial re-advance, equivalent to the Younger Dryas in the Northern Hemisphere, is controversially discussed in the literature and is so far not unequivocally supported by data (Glasser et al., 2004).

The present day lower limit of altitudinal permafrost in the Patagonian Andes is based on an inventory of cryogenic processes, periglacial landforms and rock glaciers estimated to be located between 1600-1700 m asl. (Trombotta Liaudat, 2008). However, the altitude of the present day 0° MAAT isotherm seems to be located at ~1700 m asl. (Falaschi et al., 2015). The volcano Macá is, at 2300 m asl., the highest peak in the Aysén Fjord region. The topography around the study site in a tributary valley of Aysén Fjord does not reach above 1400 m asl. and remains thus significantly below the estimated lower permafrost limit.

4.2.1 The Punta Cola rock avalanche

On April 21, 2007, after a series of shallow earthquakes that were potentially connected to the LOFZ, a Mw 6.2 earthquake ($D < 10$ km) struck the Aysén region (Legrand et al., 2011). Around 500 landslides were triggered, including two large-volume rock avalanches (Fig. 4.13c) (Sepúlveda et al., 2010). The rock avalanches entered the fjord generating displacement waves which impacted the coastal morphology, the regional economy, and the population (Naranjo et al., 2009; Sepúlveda and Serey, 2009). The second largest mass movement with a volume of 20.9 Mm³ is the Punta Cola rock avalanche. Here, the displaced rock mass produced a maximum run-up height of 150 m on the opposite slope of the failure before it turned 90 degrees and propagated 1-1.5 km along the valley and entered into the fjord. Approximately half of the total volume was deposited offshore causing a coastal erosional retreat of up to 100 m in the delta area (Oppikofer et al., 2012). Offshore, it caused massive fjord deposit deformation extending the aerial size of the rock slope failure depletion, transport and depositional area, causing fjord bottom erosion of the same magnitude as the rock avalanche volume itself (Lastras et al., 2013; Hermanns et al., 2014).

4.2 Aysén Fjord, Patagonia (Chile)

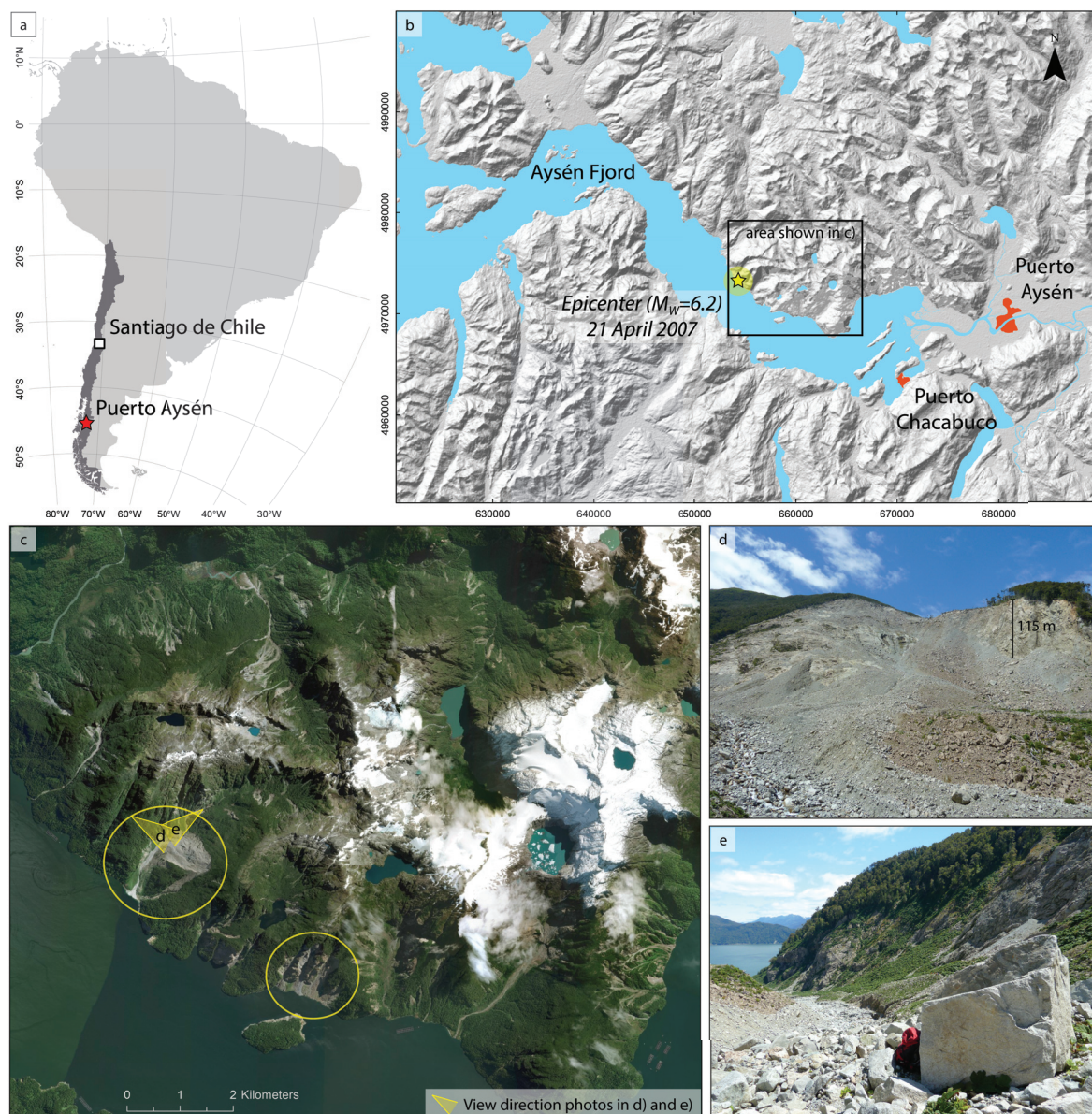


Figure 4.13: Overview over the study site: a) Location map of the Aysén fjord in Patagonia, Chile; b) The Aysén fjord area with the epicenter of the 2007 earthquake (Hillshade created from 17 m ASTER GDEM 2, METI and NASA); c) Orthophoto from 2015 showing high landslide activity triggered by the 2007 earthquake and two large scale rock avalanches in yellow circles (Imagery source: DigitalGlobe); d) Photo with view as indicated in c) looking towards the Punta Cola rock avalanche source area with a 115 m high rock wall for scale; e) Photo with view as indicated in c) looking down the run-out area towards the fjord from the foot of the source area, backpack in foreground for scale

4 Geographic setting

The main scar of the Punta Cola rock avalanche is about 1 km long and up to 760 m wide and mostly covered by debris (Fig. 4.13d). It stretches over an elevation difference of >500 m up to 730 m asl, which is more than 1 km below potential permafrost conditions (Falaschi et al., 2015). A topographic break-line across the scar, and a set of faults and fractures in the lateral release surface, are indicators for a potential active branch of the LOFZ, crossing the basal sliding surface (Redfield et al., 2011; Oppikofer et al., 2012). The depth of the detached rock mass was up to 110 m and >25 m in most places (Oppikofer et al., 2012). As evident from aerial photographs, the pre-failure slope has been forested before failure and probably throughout most of the Holocene, according to climate records (Glasser et al., 2004).

5 Methods and data acquisition

The methodological focus of this doctoral study was on terrestrial cosmogenic nuclide dating, which was not only applied in order to directly determine the failure timing of rock-slope failures, but was also assessed critically (Hilger et al., 2019). Laboratory procedures for sample processing were introduced at the NGU and computational shielding analyses developed. However, it is crucial to combine different methods in order to understand the exposure ages of landforms and their role in the landscape development of an area. The exposure dating was therefore complemented by detailed Quaternary geological mapping, geophysical surveys, and the compilation of relevant climate data for direct analysis or as input for a thermal model reconstructing the potential permafrost distribution in rock-slopes.

5.1 Quaternary geological mapping

In the context of investigations in the area at and around Mannen, a detailed Quaternary geological map was produced. The mapping activities not only enabled the characterisation of the Quaternary sediment cover, but were essential to determine a relative rock-slope failure chronology, where the exposure dating technique was not applicable. This was especially true for all landforms below the highest post-glacial sea-level, when the sedimentation or deposition was expected to be of older age and shielded by water for a period of time. In order to best understand the Quaternary history of the study area, intensive mapping, both in the field and based on high-resolution digital elevation models (DEMs), was carried out. This was complemented by geophysical applications, which added depth to complete the third dimension, where outcrops were absent and manual digging of trenches limited.

5.1.1 Field mapping and digital relief analyses

Data acquisition - To best prepare for the field work, digital resources were analysed for landcover and landforms, maps produced and points of interest marked. For most

5 Methods and data acquisition

study sites digital datasets were available, including aerial photographs, orthophotos and airborne Light detection and ranging (LiDAR) data. A 10 m DEM over entire Norway, based on airborne LiDAR data with varying point density, is freely available (Kartverket, 2018c). High-resolution LiDAR data and DEM (5 and 1 m) have been accessible for all of the study sites with variations in coverage and extent (Kartverket, 2018b). If not already included and accessible from the local NGU database, orthophotos were acquired from Kartverket (2018a).

Field mapping - The generally systematic mapping approach in the field was complemented by visiting previously marked points of interest, to clarify, verify, query or falsify prior assumptions. For the characterisation of sediments, field mapping included small-scaled trenching and sampling of sediments for particle-size analyses. Dialogs with farmers and residents generated valuable additional information about local observations, both recent and historic, of mass wasting activity, sediment characteristics (e.g. the occurrence of shells) and human activity in the mapping area.

Digital relief analyses - Digital relief analyses in geographical information systems (GISs) and (3D) orthophoto interpretation allow for enhanced visibility and information extraction compared to field studies only. One of the first steps in the recognition of a new study area is getting an overview from a high perspective. This can be achieved by 2D and 3D visualisations of the orthophotos. And while vegetation cover often limits the visibility of surface characteristics, a change in vegetation can give valuable information about a change in the underlying substrate.

One of the most fundamental resources for Quaternary geology and landform mapping, is the display of bare-earth DEM as hillshades with variable azimuths and inclination angles of the light source (exceeding the natural positions of the sun). Like this, different landforms and objects are visible from a birds-eye view, even if covered with vegetation on the orthophotos and in the field. A change of the position of the light source shifts the focus in between contrasting topographic features, highlighting or toning them down. For a complete survey of topographic features, slope maps, featuring slope angles independent of their aspect, were created. Together with a classified colour map of the DEM, a dataset of the described maps was produced for each study area and available throughout the entire study.

At the Mannen study site the volume of six CRSF was estimated. For this, the potential pre-failure surface was reconstructed from the most recent high-resolution (1 m) DEM.

Because of a relatively simple topography and flat, terraced surfaces, 5 m contour lines could be interpolated and modified manually and a new pre-failure DEM created. To extract the elevation differences, the pre-failure elevations were then subtracted from the post-failure elevations, resulting in a DEM of difference (DoD). With the DoD values, the volumes could be calculated on a pixel basis.

5.1.2 Geophysical methods

Many in-situ geophysical methods are relatively non-invasive techniques to measure, either directly or indirectly, physical properties of the subsurface (Perrone et al., 2014). Geophysical surveys are commonly conducted to complement Quaternary geological mapping (e.g. Jørgensen et al., 2003; Eilertsen et al., 2011), landslide investigations (e.g. Jongmans and Garambois, 2007; Ganerød et al., 2008; Falae et al., 2019) and permafrost and ground-ice studies (e.g. Hauck et al., 2004; De Pascale et al., 2008; Kneisel et al., 2008). In this study, we conducted two electrical resistivity tomography (ERT) surveys on the Quaternary sediments and rockslide deposits below the Mannen instability in order to map stratigraphic relationships. This was complemented by ground penetrating radar (GPR) surveys, which were also extended along the Romsdal Valley to set the local valley-fill sediments into a wider context.

Electrical resistivity tomography (ERT) - ERT applications allow for the imaging of two or three-dimensional direct current (DC) resistivity distributions of subsurface material. The apparent resistivity values are mainly connected to the mineralogy, porosity, ground water or ice content and the nature of electrolyte (Perrone et al., 2014). The principle of the method comprises the injection of DC into the ground through pairs of electrodes while measuring the potential between another pair along an array of regularly spaced steel electrodes (Dahlin, 2001). A variety of electrode configurations with complex combinations of potential electrode pairs define the geometrical coefficient, which is used to calculate the apparent resistivity at several pseudo-subsurface positions. In order to illustrate a pseudo-section, representing the approximate distribution of subsurface DC resistivities, the measured connectivity values must be inverted using inversion routines. The measurement depth is proportional to the electrode spacing along the multi-electrode cables (Perrone et al., 2014).

The two 2D ERT profiles below Mannen were obtained using an ABEM Terrameter LS employing the Schlumberger protocol (e.g. Aizebeokhai, 2010). Applying the roll-along method (Dahlin, 2001) with four 100 m long cables and 5 m electrode spacing, generated

5 Methods and data acquisition

tomographies representing several hundred metre long and up to 60 m deep profiles were generated. Several bad data points were excluded manually, before the data was inverted in RES2DINV (©M.H. Loke, 1995-2015) using a robust L1-norm.

Ground-penetrating radar (GPR) - GPR is one of the most commonly applied geophysical techniques in geological and geomorphological studies. The principle of GPR measurements is to transmit electromagnetic radiation into the ground and measure the signals from reflecting structures in the subsurface with a receiver. For this, a transmitter and receiver in a fixed geometry are moved over the ground, while measuring regularly (Annan, 2009). Depending on the targeted material and measurement scale, a suitable frequency for the emitted radio waves has to be chosen. A variety of GPR apertures provide a range of frequencies and field techniques.

In this study, a snake antenna with a frequency of 100 MHz was towed behind the surveyor. It allowed measurements in uneven blocky and forested terrain. A distance-based measurement frequency of 0.5 m (an alternative option is a time dependent measurement frequency), was met using a cotton thread, which is tied to a fixed point measuring the distance by the length of unreel thread. Post-processing of the GPR data was conducted with RadExplorer (©MALÅ Geoscience) where the following processing routines were applied: (1) time-zero adjustment, setting the zero-point of the vertical time scale, (2) background removal, to reduce undesired signals, such as direct waves from the transmitting antenna, (3) amplitude correction using automatic gain control, in order to visualise low amplitude signals (4) migration velocity determination with the Hyperbola tool, and finally (5) topography, correcting the surface topography according to the real topography, which was previously extracted from a 1 m-resolution DEM.

5.2 Terrestrial cosmogenic nuclide (TCN) dating

In the framework of this study, 44 samples of rockslide deposits for TCN dating were collected and processed by the author and complemented by 11 samples that were collected and partly processed earlier by R.L. Hermanns and colleagues (Table A.1). The majority of the samples were analysed for the ^{10}Be nuclide, which is, because of its relatively simple laboratory procedures, the most popular TCN in geosciences. Until today, the range of ages for ^{10}Be , lies between a few hundred years (Akçar et al., 2012; Hilger et al., 2019) and >1.8 Ma (desert pavement) (Matmon et al., 2009; Guralnik et al., 2010). The ^{10}Be dataset has been complemented with three ^{36}Cl samples, where the mineral fraction

of quartz was too small to extract enough ^{10}Be . For ^{36}Cl the whole rock (all minerals) was used.

5.2.1 Sampling and sample processing

Before going out into the field for sampling, orthophotos and DEMs correspondent to the study site were analysed (cf. Sec. 5.1.1). Because of the ongoing small scale mass-wasting activity from the steep rock walls above the CRSF deposits, sampling had to take place outside of their typical reach. The generated set of digital data allowed to map rock-fall and debris-flow tracks, with focus on their run-out length and extent of recent colluvium. The reconstructed maximum post glacial sea-level represented the lower limit of sampling in most cases.

When the foliation of the sampled boulders was favourable, the samples were taken with hammer and chisel. For other samples a handheld angle grinder was used to cut c. 2x2x2 cm cubes, that were then detached with hammer and chisel. While the latter gave best results in even thickness of 2 cm and allowed for quartz rich samples, the battery supply and cutting discs were limiting factors. For safety reasons, samples from steep rock slopes were taken on ropes using hammer and chisel. Samples in general had a minimum size of 20x20 cm and a thickness of 1-6 cm, typically closer to 1-2 cm (Table A.1).

In the course of this doctoral study, a total of four batches of samples were processed in two cycles of laboratory work. The first batch included 17 samples from the Mannen study area; 13 from CRSF deposits, three from the main sliding surface of the instability, and one from the plateau surface. In the second cycle, three batches including six samples from the Punta-Cola rock avalanche (Chile), nine samples from deposits below Rombakstøtta (Nordland) and 12 samples from below Ramnanosi (Sogn og Fjordane), were processed. An additional 11 samples were processed by the Cosmic Ray Isotope Sciences at Dalhousie University (CRISDal) laboratory in Halifax, Canada, where generally most of the sample processing was carried out.

The samples were first cleaned by brushing, then crushed with a jaw breaker, ground with a disc pulveriser and finally sieved, optimising the 250–355 μm fraction (Fig. 5.1a-e). For all the 44 samples that were processed by the author, this procedure occurred in the laboratory of NGU. Subsequently, the quartz was concentrated using magnetic separation (belt type and Frantz), Aqua Regia, heavy liquid separation and froth flotation (Fig. 5.1f-i), before purifying the quartz (Fig. 5.1j) with chemical leaching. Before further processing, the abundance of selected cations including Be was measured with ICP-OES

5 Methods and data acquisition

to ensure purity (<100 ppm Al and Ti). During the second cycle of sample processing, the most steps for quartz concentration were done at NGU, while CRISDal provided the facilities (and support) for quartz purification, the connected ICP-OES measurements, following chemical procedures and target preparation.

In order to concentrate Beryllium with a number of chemical procedures, 240 mg of ^9Be carrier was added to mostly 30 g of pure quartz from each sample (Fig. 5.1k). During this procedure a process blank without sample material was added to each sample batch, which would be processed the same way as the other samples, in order to capture potential contaminations during the following processes. The samples were subsequently digested in a mixture of concentrated trace-metal grade perchloric, hydrofluoric, and aqua regia acids (Figure 5.1l). After successive hydrochlorid acid evaporations, anion exchange columns remove mainly Fe before sulfate conversion using cation columns separates Be from Al and Ti (Fig. 5.1m). The results of the following pH-controlled precipitations with ammonia gas were then calcinated to BeO over a Bunsen burner flame (Fig. 5.1n+o). Finally, the BeO was pulverised in its low-boron quartz vial, mixed with niobium powder (1:1.5 BeO:Nb by volume) and packed (Fig. 5.1p). The prepared targets were measured by AMS at Lawrence Livermore National Laboratory, Livermore (USA).

5.2.2 Shielding considerations

Before the final calculation of an apparent exposure age for a rock surface, a unitless factor describing the reduction of the local total production rate (F_{tot} ; Sec. 3.2) due to shielding has to be calculated for each analysed sample.

Topographic shielding - As the nature of CRSF processes postulates, the generated deposits are usually located within deep valleys and/or at the foot of steep rock-slopes. Rock surfaces of boulders that are used for the determination of the timing of failure, are therefore partly shielded by the surrounding topography. In order to approximate the most accurate topographic shielding factor for each sample, the corresponding skylines were derived based on a high-resolution (5 m) DEM and the horizon angle (measured from the horizontal) for each 1° azimuth extracted. For this, the elevation for each sample was corrected using the LiDAR data. The final unitless topographic shielding factor was then calculated with the CRONUS-Earth topographic shielding calculator version 2.0 (Marrero et al., 2016), including the dip angle and dip direction of the sampled rock surface. The results were validated with field measurements using an inclinometer, which were often affected by low-level clouds and vegetation. The digitally derived horizon angles overesti-



Figure 5.1: Workflow for the extraction of Be from quartz with three main steps: 1. Breaking the samples (a) using a jaw crusher (b), a disc pulveriser (c) and sieves of different mesh densities (d) in order to produce the desired grain size fraction (e); 2. Mineral separation in order to concentrate quartz including magnetic separation (f) aqua regia digestion (g), heavy liquid separation (h), froth flotation (i) and final chemical leaching resulting in purified quartz (j); 3. Chemistry procedures comprise ^9Be spiking (k), sample digestion (l), column chemistry (m), pH-controlled precipitation (n) and calcination (o) before the final AMS target preparation (p). Photos k and o by G. Yang.

5 Methods and data acquisition

mate the measured values on average by 1.3° . However, because of the high resolution of 1° azimuth steps and zero obstruction by clouds and vegetation the values should overall be more accurate and complete.

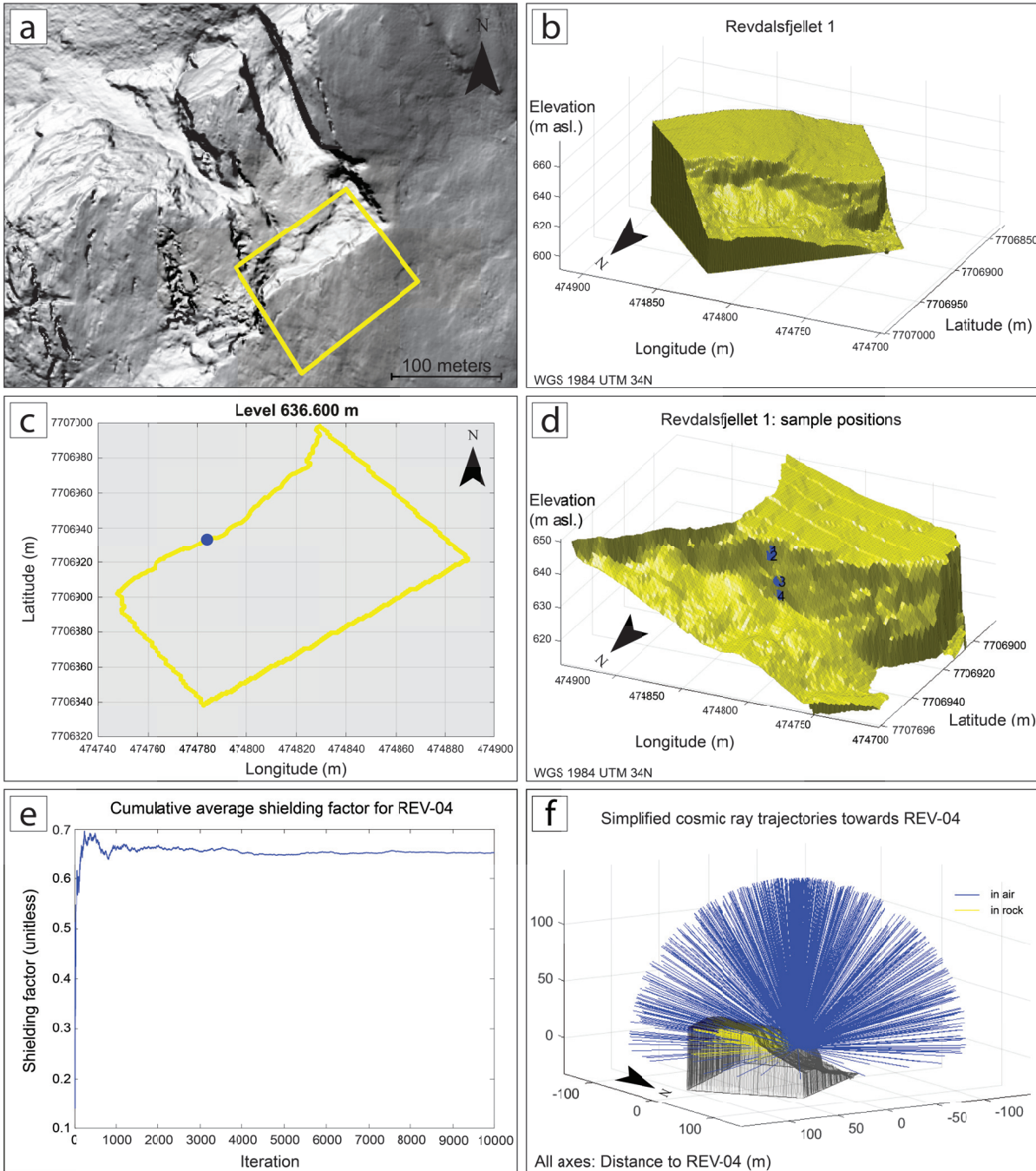
Shielding on cliff faces - On the near-vertical sliding surfaces of the rock-slope instabilities, shielding by snow and vegetation is negligible. However, calculating the topographic shielding can be challenging due to the surrounding rock-walls and irregular surfaces. Field measurements can be compromised owing to the conditions when working whilst suspended by a rope. Nevertheless, for most rock-wall samples the topographic shielding has been measured and was used to develop a semi-automated approach for most reliable results using a MATLAB code developed to estimate shielding for oddly shaped objects (Balco, 2014).

For this, an area of interest (AOI) around the cliff face with the sampled profile, with a minimum size of 100x100 m, was extracted from a high-resolution (0.5, 1, 2 or 5 m) DEM (Fig. 5.2a) to create a 3D block as triangular irregular network (TIN), with artificially closed sides (Fig. 5.2b). The TINs were created in the open source GIS SAGA (Conrad et al., 2015) using the module ‘Grid to TIN’, which uses all data points for the TIN derivation. Prior to the triangulation a buffer was created around the grid, with elevation values corresponding to the lowest point resulting in vertical walls after the triangulation. Using the MATLAB code by Balco (2014) the sample position for each sample is then determined precisely, based on the waterline of their corresponding elevation (Fig. 5.2c). It is possible to place the samples at the depth (horizontally behind the rock wall) according to the average sample thickness (Fig. 5.2d). The shielding is then calculated based on the rock density, the particle attenuation length and optionally the topographic shielding of the horizon (Balco, 2014).

The final value is the result of a Monte Carlo simulation over the attenuation of n single cosmic ray trajectories (Fig. 5.2e). In this thesis, 10,000 iterations were calculated for each sample, representing 10,000 cosmic ray trajectories distributed uniformly in zenith and azimuth angles. When a vector, representing a trajectory, hits a surface of the 3D block for the first time, a phase change from atmosphere (blue) to rock (yellow) is assumed and the corresponding attenuation applied (Fig. 5.2f). The most accurate shielding values could be calculated at the Mannen site, where a DEM based on photogrammetry including oblique views was created. The samples locations were marked in the rock wall and could thus be extracted very precisely from the coloured point cloud.

5.2 Terrestrial cosmogenic nuclide (TCN) dating

Snow shielding - Correction for shielding by snow cover was only done for the samples taken below the Mannen instability in Romsdal Valley, Norway. Here, the snow shielding was derived after Gosse and Phillips (2001) using historic and modern climate data to estimate the local seasonal snow cover. The average snow depth and duration of the snow



5 Methods and data acquisition

Figure 5.2: Semi-automated approach to derive the topographic shielding on a steep rock face using a MATLAB code developed to estimate shielding for oddly shaped objects (Balco, 2014): Definition and clip of an area of interest (AOI) around the sampled transect (a). 3D visualisation of the AOI as a triangular irregular network (TIN) block (b). Waterline plot (horizontal 'slice' of 3D block) of a specific elevation. This plot is used interactively to place the sample accurately (c). 3D visualisation of the AOI (close up) including the sample locations (d). Final plot of the cumulative average shielding factor for sample REV-04, assembled over 10,000 Monte Carlo iterations (e). 3D plot of the generated cosmic rays towards sample REV-04 indicating the attenuating matter that is passed. For better visualisation only 1000 iterations are plotted (f).

season for several decades was extracted from the interpolated gridded snow depth data from seNorge.no (2018) while the snow density was estimated after Færevåg (2013). This method only represents the snow conditions for the last decades and does not include local effects such as vegetation and wind drift. However, since temperatures during most of the Holocene were warmer than today (Fig. 4.1; Lilleøren et al., 2012), it can be expected that this is a rather conservative approach. Because of the limited snow fall in Puerto Aysén, Chile, with 0.5-7.7 cm snow cover (Romsdal 37 cm) over a winter season of 3-5 months (Romsdal 7 months), shielding by snow was ignored.

Shielding by forest - The shielding effect of vegetation on a sample location throughout the Holocene can roughly be estimated. A detailed study by Plug et al. (2007) shows that the shielding effect in forests is dependent on stem thickness and tree height, sample location, succession rate and age. In their study, the authors estimate the effect of Arcadian and rainforest on the attenuation length of cosmic radiation. In this study, we presume that the light birch tree forest with small stem diameters that covers large parts of the sampled CRSF deposits has a smaller shielding effect than the Arcadian forest.

5.2.3 Data reduction and age calculation

All 53 exposure ages analysed with the ^{10}Be nuclide for this thesis are calculated with version 3 of the online exposure age calculator formerly known as the CRONUS Earth online exposure age calculator written by G. Balco, 2017. As input, the calculator requires a text file with information about each sample, including sample ID, latitude (dd), longitude (dd), elevation (m asl.) or alternatively pressure (hPa), sample thickness (cm), sample density (g cm^{-3}), shielding factor (unitless), erosion rate (cm a^{-1}), date of sample

5.2 Terrestrial cosmogenic nuclide (TCN) dating

collection, targeted nuclide and mineral, corrected nuclide concentration and uncertainty (atoms g^{-1}) and finally the name of the standardisation that was used for the AMS measurements. The relevant parameters for the samples analysed within this thesis are compiled in Tab. A.1 and A.2.

Three samples had previously been processed targeting the ^{36}Cl nuclide. The data for these samples only had to be checked and re-calculated with the CRONUS-Earth ^{36}Cl exposure age calculator v2.0 (Marrero et al., 2016).

In order to obtain a ^{10}Be concentration representing the apparent exposure age of a rock surface, results of the AMS measurements first have to be transformed from a $^{10}\text{Be}/^9\text{Be}$ ratio to ^{10}Be counts (atoms). From this value, estimated contaminations are subtracted. In order to estimate ^{10}Be contaminations, a blank sample was processed with each sample batch of 6-12 samples, applying all chemical procedures in the same way as for the regular samples. The process blank does not contain any material in the beginning, and thus only represents contamination from the processing. After this correction, the amount of ^{10}Be atoms is converted into ^{10}Be concentrations (atoms g^{-1}) for each sample. For samples from boulder surfaces, these obtained values are used for the age calculations. However, samples taken from vertical and near-vertical sliding surfaces have to be corrected respectively for ^{10}Be or ^{36}Cl production at depth prior to direct exposure through vertical displacement of an unstable rock slope (Fig. 5.3).

A progressively moving rockslide at the edge of a mountain plateau gradually exposes the upper part of its sliding surface. Sampling along a vertical transect can thus offer valuable information about the position of the moving rock mass at pre-historical times (cf. Sec. 3.4). Although the samples only offer a snapshot of the time frame a specific location has been first exposed, a number of values along the sliding surface may constitute a general picture about potential changes of sliding rates.

At most locations the plateau surface has been exposed to cosmic radiation prior to and during the progressive failure, producing ^{10}Be and ^{36}Cl at the surface and at depth. Cosmogenic nuclide concentrations in such samples thus have to be corrected for inherited cosmogenic nuclide concentrations. In order to determine the time span a plateau surface has been exposed, we sampled the surfaces proximate to the rock-slope instabilities and the corresponding transects. Because of the limited production rates at depth, small uncertainties in those age determinations have a minor impact on the data corrections. However, if glacial erosion was limited during the last glaciation, ^{10}Be and ^{36}Cl could have accumulated at depth for several tens of thousands of years, building up a substantial amount of ^{10}Be and ^{36}Cl atoms.

5 Methods and data acquisition

In two cases, Oppstadhornet and Skjeringahaugane, we are lacking reference samples from the plateaus. The two sites have been sampled and analysed previously to this study (Hermanns et al., 2012b, 2013c). In order to integrate the sites into this study, generating a wider range of locations, the complex topographic shielding was recalculated according to the newly developed approach (cf. Sec. 5.2.2), and the exposure ages are updated using the latest production rates. In these two cases the pre-failure exposure was estimated according to the timing of deglaciation presuming deep glacial erosion (cf. Andersen et al., 2018).

Initially, approximate exposure ages for each sample along the sliding plane are calculated using ^{10}Be or ^{36}Cl concentrations, that are not yet corrected for pre-exposure production at depth. This allows for the estimation of pre-failure exposure time, subtracting the individual approximate exposure ages from the exposure age of the plateau. The pre-exposure concentration (C_{inh}) for each sample can then be approximated empirically with the following equation (after e.g. Gosse and Phillips (2001)):

$$C_{inh} = S \left[\frac{P_n}{\lambda} e^{-\frac{\rho d_i}{\Lambda_n}} (1 - e^{-\lambda(t_t - t_s)}) + P_{\mu_n}/\dots + P_{\mu_f}/\dots \right] \quad (5.1)$$

where S represents the dimensionless shielding factor at the surface, P_{n,μ_n,μ_f} (atoms $\text{g}^{-1} \text{a}^{-1}$) are the production rates for the three different path ways, spallation by fast nucleons (n), negative muon capture (μ_n) and fast muon reactions (μ_f), respectively, λ (a^{-1}) is the decay constant, ρ (g cm^{-3}) is the bulk density of the penetrated rock (in this study usually 2.6 g cm^{-3}), d_i (cm) is depth, Λ_{n,μ_n,μ_f} (g cm^{-2}) represent the attenuation lengths for each pathway, t_t (a) is the exposure age of the top surface and t_s (a) is the approximated post-failure exposure time of each sample.

The individual sample depth is determined by the vertical distance between the sample and the reconstructed pre-failure surface (Fig. 5.3b). In most cases the latter is presumed to be similar to the elevation of the modern plateau surface. The effect of a gradually decreasing depth due to the progressive rock-slope failure instead of a constant value was insignificant for tested sites, but the calculations are significantly more complex. Because of the unknown sliding rates and complexity of the calculations, constant depth values are used for the inheritance corrections. The production rates were obtained by averaging the values of the time-dependent LSD scaling scheme for each time frame (Lifton et al., 2014; Lifton, 2016). Finally, the obtained pre-failure concentrations (C_{inh}) are subtracted from the measured concentrations (C_{rw}) and exposure ages calculated with the corrected concentrations (Fig. 5.3a+c).

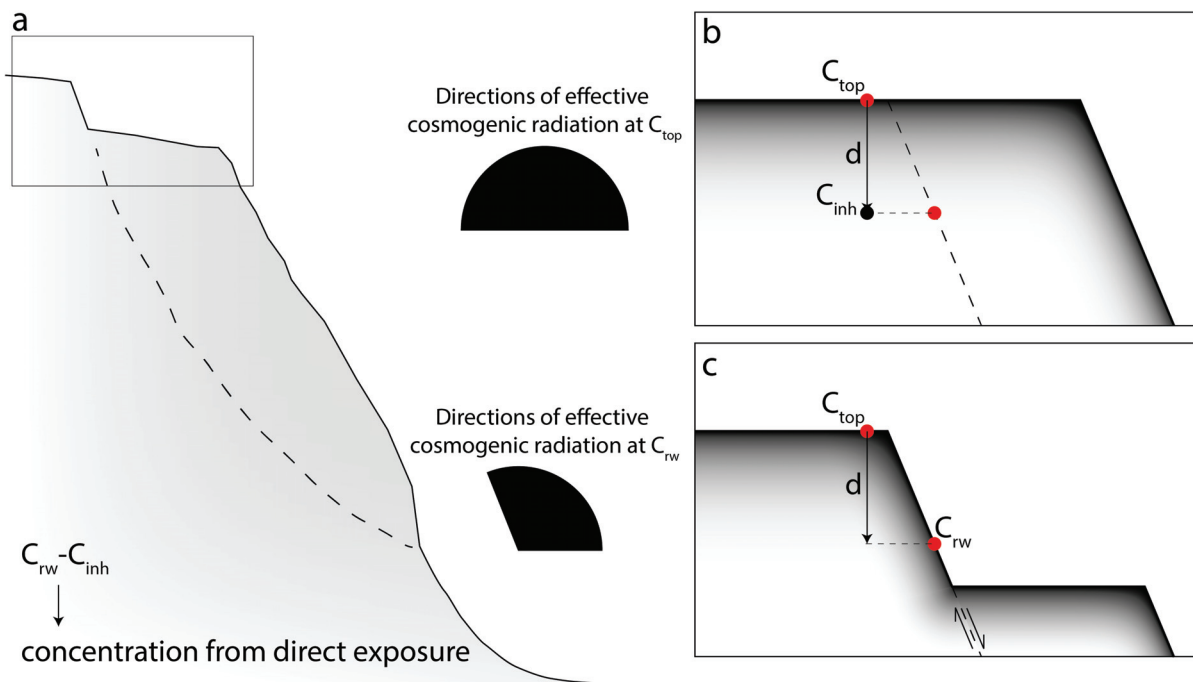


Figure 5.3: Illustration of a rock-slope instability at the transition of a plateau surface into a steep rock wall (a), schematic of the position of a top sample (C_{top}) and a sample location along the (potential) sliding surface (b-c). Black/White scaling represents the exponential TCN production at depth, resulting from the effective incoming cosmogenic radiation at the surfaces (center of figure).

5.3 Climate data acquisition

For assessing a possible climate signal in the timing of CRSFs at Mannen and sliding patterns of rock-slope instabilities in Norway, long-term climate reconstructions for the Late Glacial and the Holocene were collected, analysed and either plotted for visual comparison or used as forcing for a long-term thermal model (CryoGRID 2D, Myhra, 2016).

The first dataset was produced by Lilleøren et al. (2012) and represents Holocene temperature anomalies compared to the normal period 1961-90 in 250 year steps. Reconstructions of both summer and winter temperatures, as well as MAAT, were made for northern and southern Norway, respectively. In order to compile the time series of July temperatures, five proxy datasets from previously published data were used. The MAAT anomalies represent a compilation of speleothem data, GISP2 data (e.g. Alley, 2000) and glacial signals, while mean January temperatures were calculated from linear regressions of

5 Methods and data acquisition

relationships to modern temperature measurements. These temperature reconstructions were adopted unchanged as presented by Lilleøren et al. (2012).

A second dataset was extracted from climate reconstructions by Mauri et al. (2015). Here, both temperature and precipitation anomalies were reconstructed for Europe over a time period from 12 ka until the pre-industrial (~ 1850 AD). The dataset is based on various pollen data from all over Europe, which has been calibrated and interpolated to produce $1^\circ \times 1^\circ$ gridded maps. From this dataset, available data over Norway was extracted and analysed to produce 2D time series for northern and western Norway. For this, the time series of MAAT, summer temperatures and winter temperatures, as well as the mean and seasonal precipitation data, were extracted for each grid cell. The single time series were then grouped into climate regions, for which finally the individual time series were combined by averaging. To make the results of this reconstruction comparable to the dataset by (Lilleøren et al., 2012), the temperature data from Mauri et al. (2015) was corrected, to represent the temperature anomalies according to the normal period 1961-90.

The third dataset was extracted from the TraCE-21k climate dataset, reconstructed using the Community Climate System Model version 3 (CCSM3) (<http://www.cgd.ucar.edu/ccr/TraCE/>; He, 2011). The model is forced with transient greenhouse gas concentrations and orbitally-driven insolation changes, along with a transient scenario of meltwater forcing to the oceans from the retreating ice sheets. Because of the resolution of the model ($\sim 3.75^\circ \times 3.75^\circ$), northern and southern Norway are represented by one cell each, for which the respective temperature and precipitation series were extracted. A comparison with the NGRIP Greenland ice-core data (North Greenland Ice Core Project members (NGRIP), 2004) revealed a poor performance of the TraCE-21ka dataset for the Holocene thermal maximum, which was subsequently corrected based on the NGRIP dataset. The final TraCE-21k time series for northern and southern Norway were then adjusted linearly to the climatic situation at three of the rock-slope instabilities, under the assumption of consistence between the general temperature patterns in Norway and Greenland (Lilleøren et al., 2012). The results were used as forcing for the long-term thermal model GryoGRID 2D, which was provided and executed by K. S. Myhra (cf. Sec. 5.4).

5.4 Long-term thermal modelling with CryoGRID 2D

The CryoGRID 2D model was used to evaluate the thermal regime at Mannen, Revdalsfjellet and Gamanjunni 3. The process-based permafrost model solves the heat conduction

5.4 Long-term thermal modelling with CryoGRID 2D

equation with material and temperature dependent thermal parameters by the finite element solver MILAMIN (Dabrowski et al., 2008). For this, 2D geometries are produced as triangular mesh (Shewchuck, 1996), representing the individual slopes and their transitions to plateau surfaces. Along these geometries, air temperature forcing was derived for each node along the slopes and the flat plateau surfaces, through a linear interpolation using a mean altitudinal lapse rate of $0.005^{\circ}\text{C}^{-1}$ (Farbrot et al., 2011). While the work scheme for CryoGRID 2D is described in more detail in Myhra (2016); Myhra et al. (2017), the modelling steps are summarised as follows:

First, the site-specific deglaciation dynamics were derived from a time-slice reconstruction of the Eurasian ice sheet (Hughes et al., 2016) combined with a simplified model of the glacier surface profile following (Paterson, 1994) and the assumption of perfect-plastic ice flow. For each time slice of 1000 years (Hughes et al., 2016), the glacier thickness h_x (m) was calculated for each site located x (m) from the coast, and interpolated to yearly thickness estimates:

$$h_x - h_{margin} = C\sqrt{x - x_{margin}} \quad (5.2)$$

where h_{margin} (m) represents the glacier thickness at the ice margin x_{margin} (m) with the coastal position $x_{coast} = 0$ used as the reference position. C is a constant, determined from assumptions regarding shear stress at the glacier bed. Below the ice sheet a ground forcing temperature of 0°C was assumed.

The geometry of the model domain represents a 2D slice through the mentioned instabilities. The triangular mesh was constructed with a depth dependent resolution and the simulations were run with yearly time steps. The bedrock conditions were defined after the characteristics of granite dominated rock, which is typical for Norwegian basement rocks. The bedrock porosity was hence defined as 1% with water saturated conditions and a thermal conductivity of $k_m = 3.5 \text{ W}/^{\circ}\text{C}$ (e.g. Clauser and Huenges, 1995). The model was constructed with zero flux boundary conditions along vertical boundaries at elevations below the slope geometry and along the backside of the domain while a geothermal heat flux of 50 mW m^{-2} (Slagstad et al., 2009) was implemented along the bottom of the numerical domain (5000 m asl.).

Along the slope and top of the domain temperature forcing data was implemented through both glaciated (0°C) and glacier-free periods by means of Dirichlet boundary conditions. Glacier-free areas were forced by temperature series derived from a combination of the TraCE-21ka modelling data and the NGRIP data (cf. Sec. 5.3). During glacier-free periods, snow accumulation outside steep rock walls and on mountain plateaus

5 Methods and data acquisition

was assumed, and an insulating effect from cold air temperatures below 0°C, was implemented. An n-factor of 0.5 was chosen, which corresponds to an annual mean height of snow of approximately 20-30 cm (Gisnås et al., 2013). The initial ground temperature conditions were obtained through a steady state simulation of the simplified rock wall geometry forced with surface temperature conditions of 0°C, reflecting the ground temperature conditions in the late Weichselian when the Norwegian mainland was completely covered with glacial ice (Hughes et al., 2016). Under the assumption of temperate glaciers, this corresponds to initially unfrozen ground conditions, which means that the modelled ground temperatures represent a minimum estimate of the permafrost extent as the Scandinavian ice-sheet may have been mainly cold-based in high-mountain environments in central southern Norway (e.g. Kleman, 1994).

6 Results

The main results of this PhD thesis are provided in this chapter. For previously published results and prepared manuscripts, brief summaries of the main findings and conclusions are provided in the respective sections, which are ordered thematically. The results are complemented by additional unpublished data that have been produced within the doctoral studies.

6.1 The role of inheritance when dating rock-slope failures with ^{10}Be (Paper I)

This methodological study illustrates the potential effect of inherited ^{10}Be concentrations in boulders when dating rockslides and rock avalanches. When a rock slope is unshielded (e.g. not covered by a glacier) and thus exposed to cosmic radiation, ^{10}Be produced mainly at the surface but also at depth (Fig. 6.1a). The nuclide concentration within a slope prior to failure is strongly dependent on the exposure duration. After the event of a CRSF new surfaces, such as the failure scar and boulders on top of the deposits, are exposed. Depending on their pre-failure position, the amount of inherited ^{10}Be in the rockslide boulders varies (Fig. 6.1b). However, large boulders sitting on top of the deposits are typically targeted for age determination through surface exposure dating. As a consequence, inherited ^{10}Be concentrations may lead to significant and/or systematic age overestimations.

In order to quantify the inheritance in rock-avalanche boulders, a rock avalanche of known age has been sampled. The 20.9 Mm³ large Punta Cola rock avalanche in Patagonia, Chile, was triggered by an earthquake in 2007 and was thus nine years old by the time of sampling. In relation to the reconstructed pre-failure topography, the failure plane was between 25 and 110 m below the surface (Oppikofer et al., 2012).

Six rock-avalanche boulders from the deposits were dated using ^{10}Be , revealing apparent exposure ages between 200 and 1800 years. The results exceed the real failure time significantly and suggest the presence of ^{10}Be concentrations inherited from pre-failure

6 Results

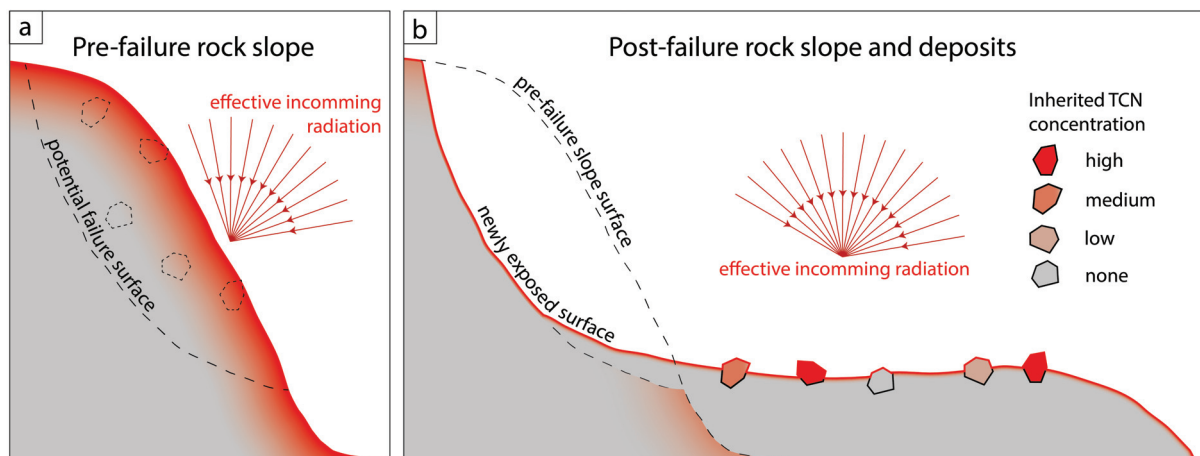


Figure 6.1: Schematic illustration of ^{10}Be concentrations in a pre- and post-failure rock slope. (a) Pre-failure rock slope, that has been exposed to cosmogenic radiation for a long time, building up ^{10}Be at the surface and at depth (red shading). (b) New surfaces are exposed to cosmic radiation along the failure surface and the deposits. The boulders, sitting on top of the deposition body, are affected by varying ^{10}Be concentrations, depending on their pre-failure position indicated in (a). (Hilger et al., 2019, Fig. 1).

production at depth. The boulder with the highest concentration was sampled below the scar of a secondary failure, where it was most likely derived from a depth <2 m. An approximation of the distribution of subsurface ^{10}Be concentrations along a 2D transect allowed for the analysis of possible pre-failure boulder positions (Fig. 6.2).

According to the analysis all boulders seem to originate from depth <13 m despite the large volume and great depth of the failure mass. The apparent exposure ages of three of the six boulders cluster within their uncertainties, which is commonly defined as a reliable dating result. In this case, however, it would still significantly overestimate the real exposure time. These results support previous studies, demonstrating that large exposure ages from rockslide deposits may generally overestimate the failure timing compared to results from failure surfaces or known historical ages (e.g. Hermanns et al., 2004; Sewell et al., 2006; Akçar et al., 2012). Tying in with early observations by McSaveney (1978) and Hadley (1978), the study supports the theory that large boulders on top of rock-avalanche deposits preferentially originate from rather shallow (<20 m) depth, even if the maximum depth of a rock avalanche is >100 m.

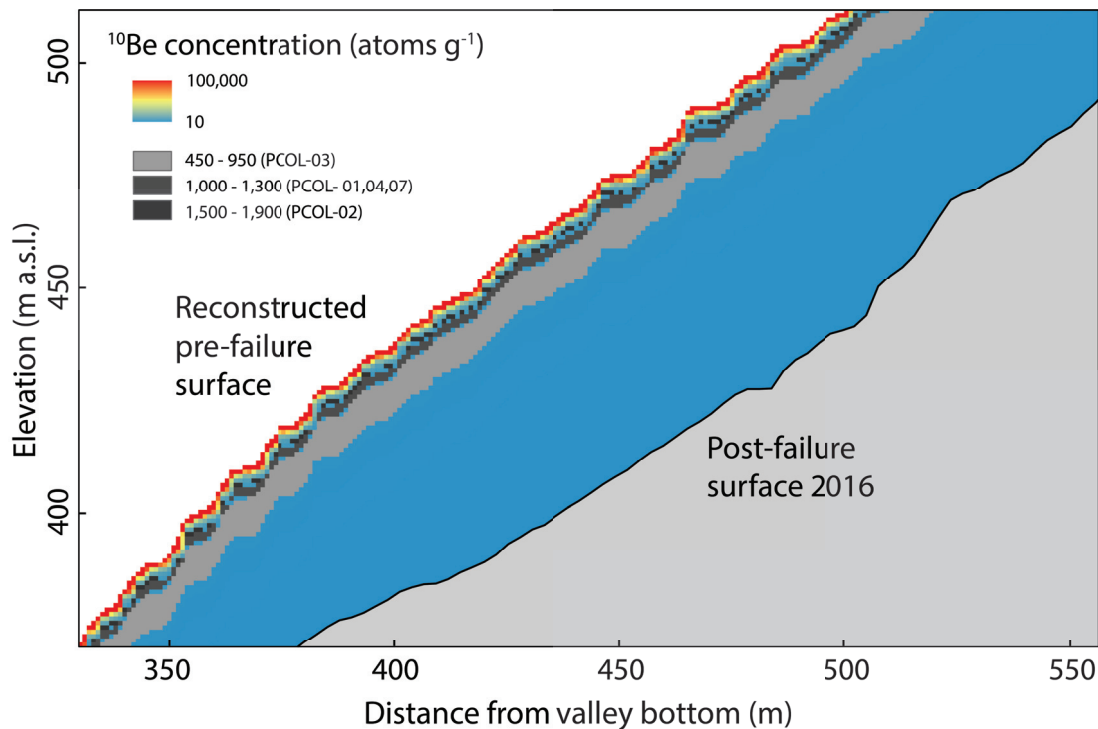


Figure 6.2: Potential ^{10}Be concentration distribution in a cutout of the pre-failure slope of the Punta Cola rock avalanche. The potential pre-failure depth for five sampled boulders is indicated in gray (Hilger et al., 2019, Fig. 6).

6.2 Mapping and exposure dating reveal multiple rock-slope failures at Mannen, Romsdal valley (Paper II)

The publication of this study presents an integrative Quaternary geological study from below the Mannen rock-slope instability in Møre og Romsdal, western Norway. A combination of field mapping, digital relief analyses and geophysical surveys generated a detailed Quaternary geology map of the area (Fig. 6.3). The presented landforms are the result of the concurrence of sedimentation processes connected to deglaciation, isostatic rebound and sea-level drop and mass wasting from the slopes. The map demonstrates a clear dominance of colluvium and CRSF deposits overlying thick stratified drift. Young fluvial sediments cover the valley floor in lower elevations close to today's river level. The extensive colluvial and CRSF deposits are evidence of a long history of rock-slope failure activity along the steep valley flanks.

6 Results

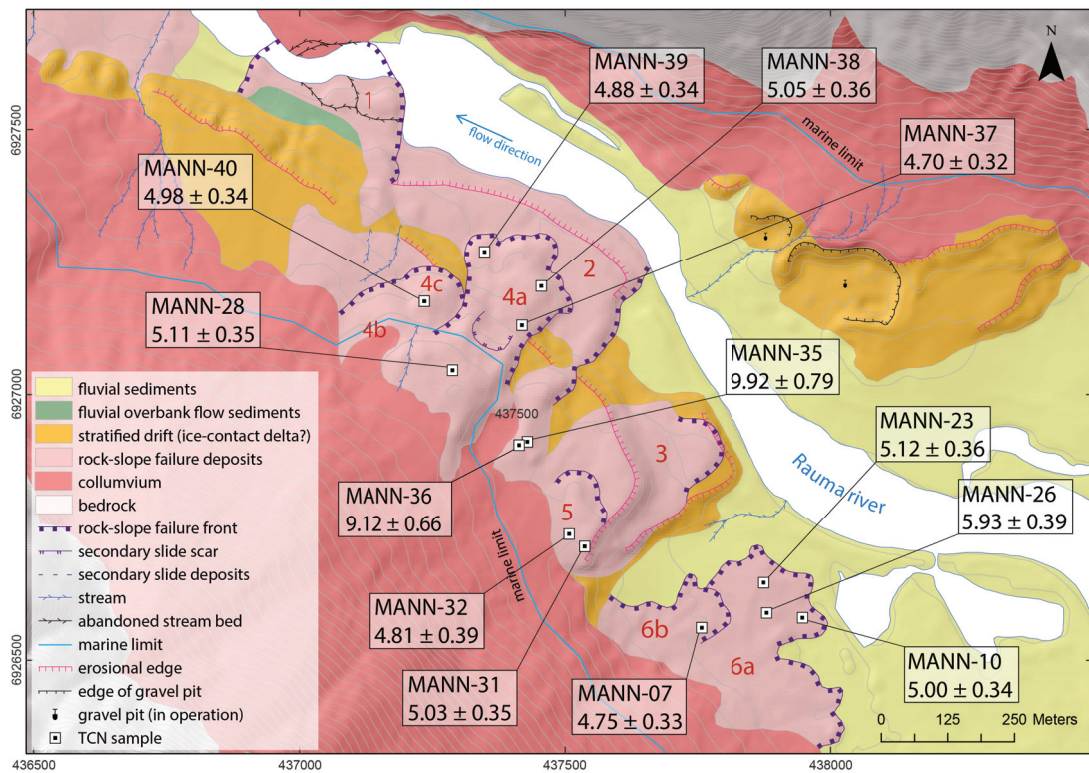


Figure 6.3: Quaternary geology map of the valley below the Mannen rock-slope instability with apparent exposure ages ($ka \pm 1\sigma$) of CRSF deposits (Hilger et al., 2018, Fig. 6).

Landforms of six to nine individual CRSF events were mapped below the Mannen rock-slope (numbered 1-6 in Fig. 6.3), which has been active since the post-YD deglaciation. Three of the CRSFs have mainly been determined by mapped stratigraphical relations and two surface exposure ages. They most likely failed shortly after deglaciation, when the sea level still reached this part of the valley (Fig. A+C). Stress release due to debuttressing effects following deglaciation may have been one of the main driving factors for the slope destabilisation of these three early failures. These early failures shortly after deglaciation coincide with a major peak in rock-avalanche activity in Norway.

A cluster of another three to nine CRSFs was dated to a time period between 4.7 and 5.1 ka ago, where several parts of the same slope failed within a few hundred years only. A possible conditioner for this mid-Holocene slope destabilisation is a strong climate deterioration at the end of the HTM (Fig. 6.4B) with increased precipitation and a strong seasonality, i.e. strong temperature fluctuations and high winter precipitation followed by intense snow melt. Rock fatigue and decreased discontinuity cohesion due to permafrost degradation may have played a role in addition.

6.3 Temporal distribution of rock-slope failures at two sites in northern and western Norway

Several consecutive failures from one slope within a few years or decades has already been observed in Norway in historical times (cf. Sec. 1). The results of this study substantiate the probability of similar scenarios in the future at slopes prone for CRSFs.

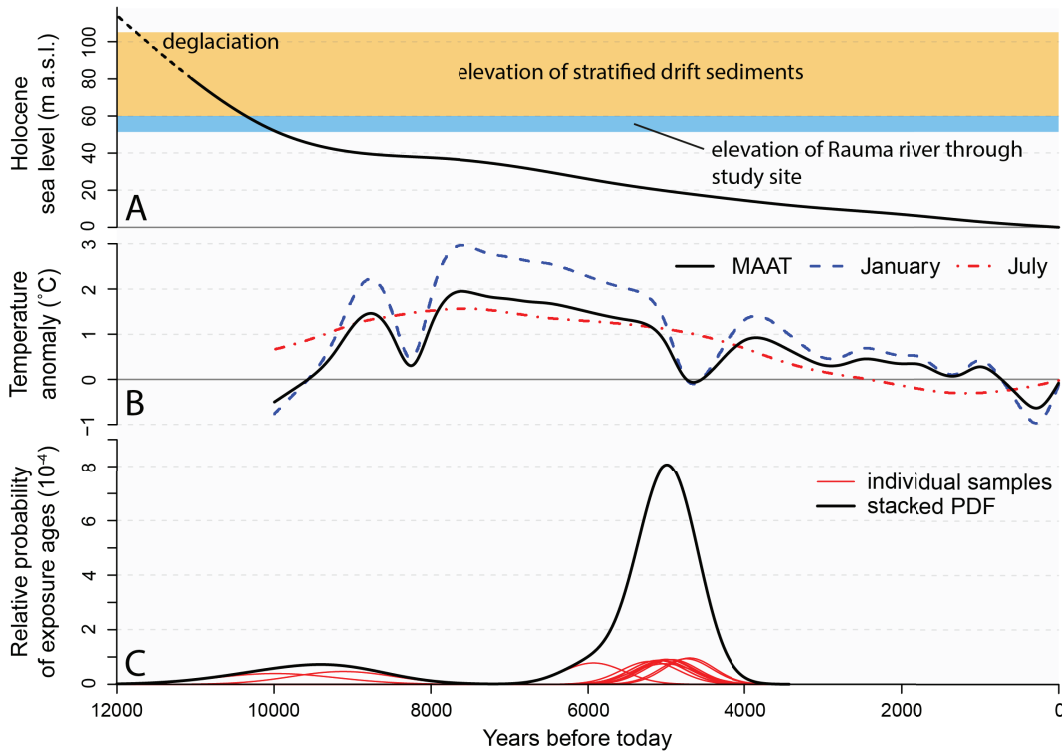


Figure 6.4: Local sea-level curve approximated after Svendsen and Mangerud (1987) (A) and approximated Holocene temperature anomalies for southern Norway (Lilleøren et al., 2012) (B) above apparent exposure ages as individual probability density functions (PDF) and the stacked PDF for all ages (C) (Hilger et al., 2018, Fig. 7).

6.3 Temporal distribution of rock-slope failures at two sites in northern and western Norway

In addition to the rock-slope failure deposits below Mannen (Sec. 6.2; Hilger et al., 2018) nine samples from Rombakstøtta in Nordland and 12 samples from below Ramnanosi in Sogn og Fjordane have been analysed for the ¹⁰Be nuclide. While some of the resulting apparent exposure ages from Rombakstøtta clearly cluster temporally, surface exposure ages from Ramnanosi are distributed over a time period from the late Pleistocene to the late Holocene (Tab. 6.1).

Table 6.1: Analytical data and results of the rock-slope failure deposits at Rombakstøtta, Nordland, and Rammanosi (Flåm), Sogn og Fjordane. Horizontal dashed lines indicate sample groups of different identified landforms.

Sample name	Lat.	Long.	Elev.	Thick-ness	Topogr. shielding	^{10}Be concentration	Exposure age	Error-weighted mean
Units	dd	dd	m asl.	cm	unitless	10^4 atoms g^{-1}	ka	ka
ROM-01	68.4431	17.6133	75	1.5	0.9705	4.74±0.14	9.7±0.3(0.6)	9.7±0.2(0.6)
ROM-03	68.4413	17.6129	116	1.5	0.9623	4.93±0.17	9.8±0.3(0.7)	
ROM-04	68.4415	17.6147	119	2.0	0.9619	3.54±0.11	7.1±0.2(0.5)	
ROM-05	68.4405	17.6152	174	1.5	0.9715	5.27±0.15	9.8±0.3(0.6)	9.8±0.2(0.6)
ROM-06	68.4403	17.6147	160	3.0	0.9659	5.10±0.19	9.8±0.4(0.7)	
ROM-08	68.4400	17.6143	170	1.5	0.9642	6.37±0.18	12.0±0.3(0.8)	
ROM-09	68.4436	17.6014	75	2.0	0.9579	4.37±0.13	9.1±0.3(0.6)	9.8±0.2(0.6)
ROM-12	68.4430	17.6024	102	3.0	0.9502	0.44±0.03	0.9±0.1(0.1)	
ROM-13	68.4427	17.6008	119	3.0	0.9225	1.55±0.06	3.2±0.1(0.2)	
FLAAM-01	60.8324	7.1304	262	2.0	0.9690	3.00±0.10	5.4±0.2(0.4)	7.9±0.2(0.5)
FLAAM-02	60.8323	7.1282	196	2.5	0.9576	3.95±0.13	7.6±0.2(0.5)	
FLAAM-03	60.8309	7.1258	153	1.0	0.9607	4.15±0.12	8.2±0.2(0.5)	
FLAAM-05	60.8403	7.1402	526	2.0	0.9383	9.64±0.26	13.9±0.4(0.9)	7.9±0.2(0.5)
FLAAM-06	60.8402	7.1416	560	3.0	0.9628	8.91±0.25	12.2±0.3(0.8)	
FLAAM-07	60.8418	7.1433	583	2.0	0.9538	5.58±0.17	7.5±0.2(0.5)	
FLAAM-09	60.8406	7.1272	154	2.0	0.9582	6.59±0.18	13.1±0.4(0.9)	7.9±0.2(0.5)
FLAAM-10	60.8401	7.1275	160	1.5	0.9541	5.12±0.14	10.1±0.3(0.7)	
FLAAM-11	60.8403	7.1268	145	4.0	0.9602	4.14±0.12	8.4±0.2(0.6)	
FLAAM-12	60.8369	7.1300	227	5.0	0.9649	1.92±0.10	3.6±0.2(0.3)	3.7±0.1(0.3)
FLAAM-13	60.8375	7.1294	211	2.0	0.9593	2.08±0.12	3.9±0.2(0.3)	
FLAAM-14	60.8371	7.1288	190	3.0	0.9586	2.86±0.11	5.6±0.2(0.4)	

6.3.1 Rombakstøtta, Nordland

High recent rock fall, debris flow and snow-avalanche activity at Rombakstøtta have resulted in a large debris cone below the periodically monitored unstable rock-slope (NGU, 2018). Mapping based on 1 m LiDAR data, aerial photographs and field observations allowed the identification of chaotic boulder fields that exceed the range of recent activity, reaching the fjord in places. The sampling area for dating pre-historical CRSFs was thus restricted to an area between the maximum marine limit, which lies close to the 100 m contour, and 200 m asl. Two samples originate from deposits below the marine limit, because the CRSFs may post date a high sea level at or close to the marine limit. If not, conclusions about the effect of sea-water shielding may be drawn. The results, however, suggest the first.

Based on the mapping the deposits were divided into three areas of potential individual CRSF events, for each of which a group of three samples were processed (Tab. 6.1, Fig. 6.5). The first sample group (a), ROM-01, -03 and -04, resulted in two nearly identical ages of 9.7 and 9.8 ± 0.3 ka, respectively, and 7.1 ± 0.2 ka. A very similar pattern appears for the next sample group (b), ROM-05, -06 and -08, where two boulders seem to have the same exposure age of 9.8 ± 0.3 and ± 0.4 ka, respectively, and the third exposure age is with 12.0 ± 0.3 ka more than two millennia older. Defining ROM-04 and ROM-08 as statistical outliers, the error-weighted mean of the four remaining boulders from groups a+b is 9.8 ± 0.2 ka. This is indistinguishable to the individual ages i.e. within their 1σ uncertainties.

The samples from three boulders on the western side of the deposits (group c), however, result in very diverse exposure ages. The apparent exposure ages of ROM-09, -12 and -13 are 9.1 ± 0.3 , 0.9 ± 0.1 and 3.2 ± 0.1 ka, respectively. While ROM-09 and the combined exposure age of the four indistinguishable ages overlap within their 2σ uncertainties (Fig. 6.6), ROM-12 and ROM-13 are six and more than eight thousand years younger, respectively.

6.3.2 Ramnanosi, Sogn og Fjordane

In earlier reports about the Stampa rock-slope instabilities Joasete, Furekamben and Ramnanosi, attempts were made to map individual rock-slope failure deposits below the steep rock wall of Ramnanosi (e.g. Hermanns et al., 2011; Blikra et al., 2013a). Here, a large area is characterised by a continuous thick colluvial mass of boulders and sediments (Fig. 6.7). The identification of single CRSF events, however, remains challenging. While

6 Results

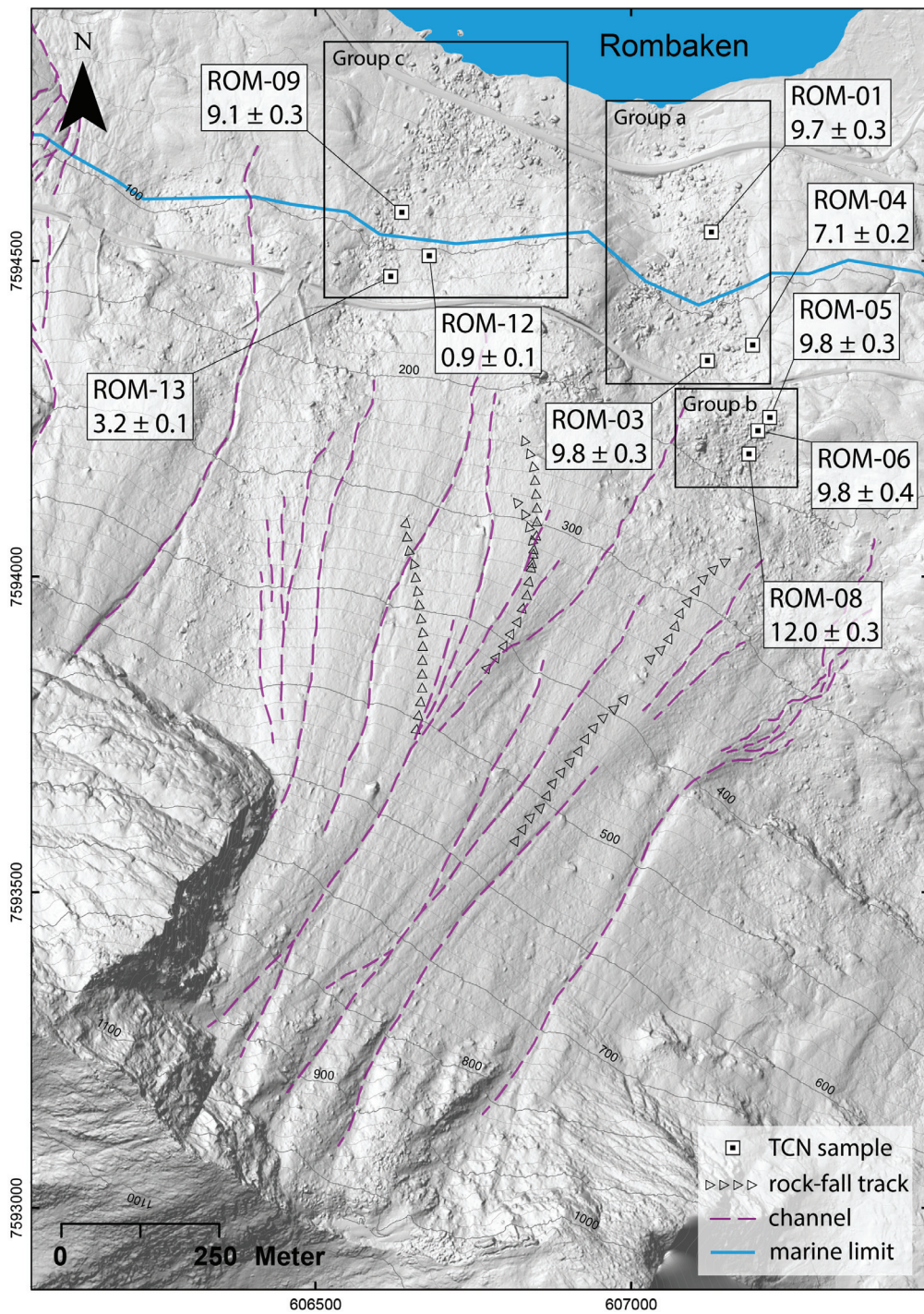


Figure 6.5: Hillshade of the Rombakstøtta study site with the locations and results of the dated boulders. Apparent exposure ages are given in ka. The mapped channels (dashed lines) represent debris flow, snow avalanche and discharge channels. For orientation and visualisation of the relative slope gradient, the 100 m and 20 m contour lines are printed.

6.3 Temporal distribution of rock-slope failures in northern and western Norway

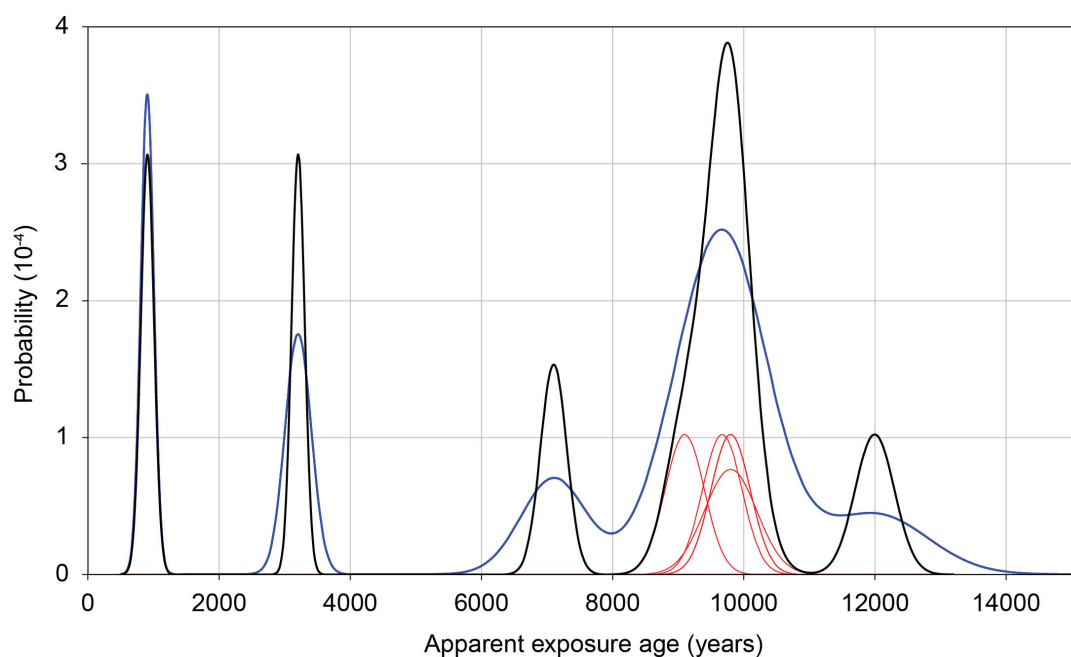


Figure 6.6: Probability density distributions of the apparent exposure ages at Rombakstøtta, based on internal errors. Red/thin functions are the Gaussian distributions of the individual samples, while the black/thick function represents the stacked probability of the dataset. The blue thick line is the stacked probability of the dataset based on external errors (Tab. 6.1).

steep fronts of lobate landforms are apparent in several places, further delimitation are not feasible, because of smooth transitions into the surrounding deposits. The lobate landforms are therefore not confidently assigned to one process. Alternatives of either CRSFs, creeping processes, or a combination of both, as shaping processes are mentioned by Blikra and Kristensen (2013). 12 new and two re-calculated exposure ages allow for a discussion about the genesis of the landforms (Tab. 6.1; Fig. 6.7).

At Ramnanosi 14 boulders were sampled within this study, whereof three samples per lobate landform (12 in total) were processed. For sampling, areas below the marine limit and beyond the estimated reach of historical large rock-fall processes were avoided. The youngest known large rock-fall event is 'Nystein', which occurred about 300 years ago, more than a kilometer downslope from the main rock-wall (Source: by word of mouth from a local farmer). A smaller rock-fall event ($<100 \text{ m}^3$) killed a local farmer in 1766. Several recent rock-fall events of small volumes have been registered at the railway close to the valley bottom (NVE, 2018). However, the source areas of these events are most likely the proximate steep fronts of the lobate landforms.

6 Results

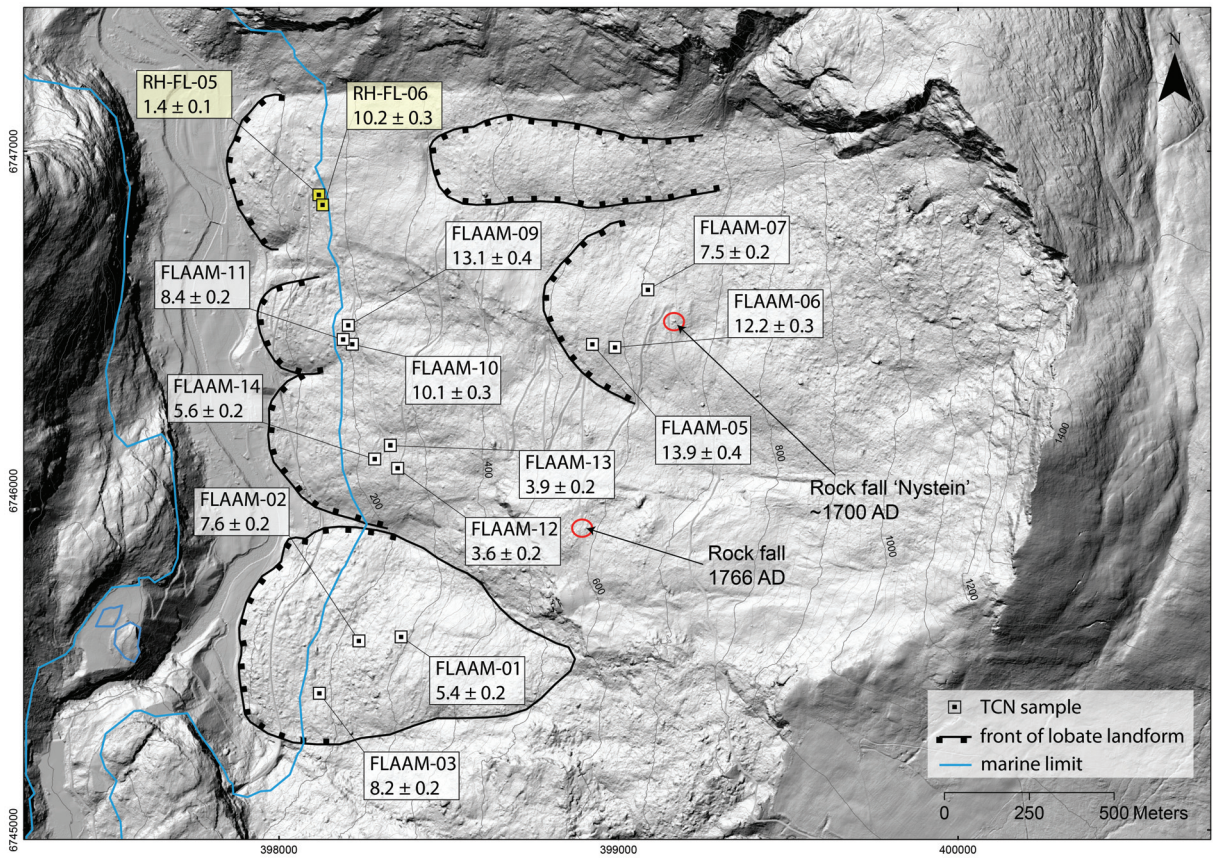


Figure 6.7: Hillshade of the Ramnanosi study site with the locations and results of the dated boulders. Apparent exposure ages are given in ka. ^{10}Be samples marked in yellow are recalculated exposure ages from previously published data (Böhme et al., 2013). The fronts of lobate landforms are mapped similarly to previous studies and mark deposits from CRSFs or creeping processes (Hermanns et al., 2011; Blikra et al., 2013a). For orientation and visualisation of the relative slope gradient, the 100 m and 20 m contour lines are printed.

Apparent exposure ages of the 12 analysed boulders are spread over the entire Holocene and late Pleistocene (Fig. 6.8). They range from 3.6 ± 0.2 ka to 13.9 ± 0.4 ka. There are only two sample couples that originate from one landform and overlap within their 2σ uncertainties. The error-weighted mean for FLAAM-02 and -03, with 7.6 ± 0.2 and 8.2 ± 0.2 ka (1σ uncertainties), respectively, is 7.9 ± 0.2 ka (Tab. 6.1). For FLAAM-12 and -13, with 3.6 ± 0.2 and 3.9 ± 0.2 ka, respectively, the mean value results in 3.7 ± 0.1 ka. These exposure ages represent the two southernmost adjacent lobate landforms (Fig. 6.7).

When focussing on the total distribution of apparent exposure ages at the Ramnanosi study site, leaving the individual landform characteristics out of consideration and including the two samples from Böhme et al. (2013), several groups or sample couples can be detected (Fig. 6.8). The oldest group ranges from 13.9 ± 0.4 ka, over 13.1 ± 0.4 ka to

6.4 Reconstructing the sliding and permafrost history of rockslides

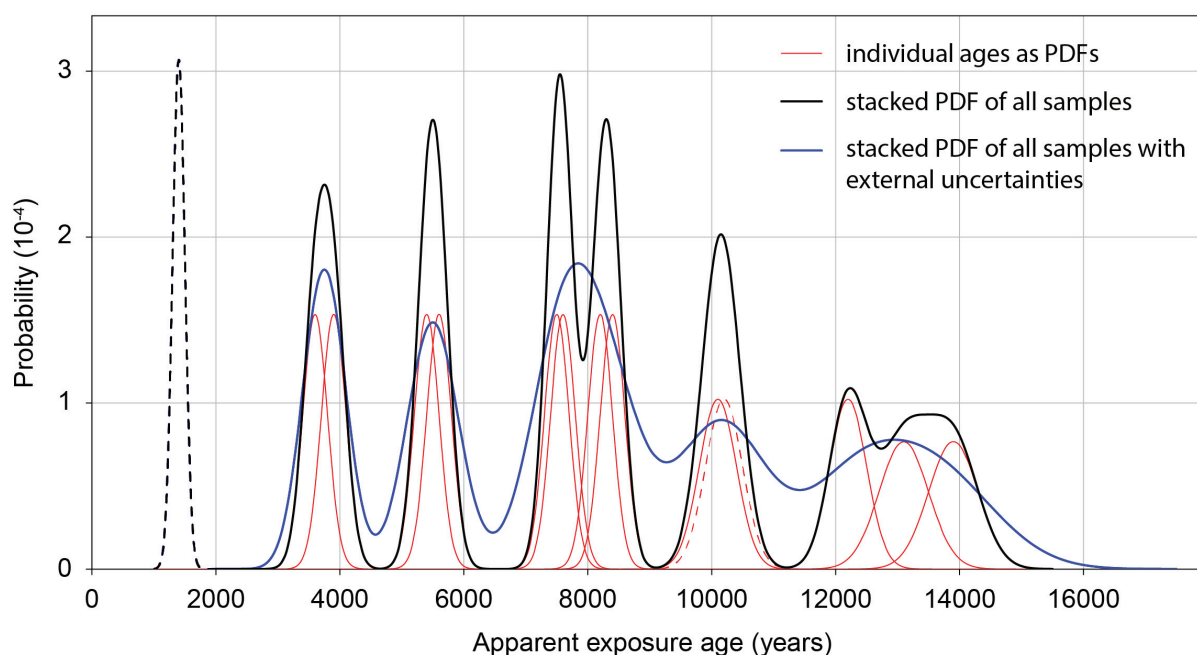


Figure 6.8: Probability density distributions of the apparent exposure ages at Ramnanosi, based on internal errors. Red/thin functions are the Gaussian distributions of the individual samples, while the black/thick function represents the stacked probability of the dataset. The blue thick line is the stacked probability of the dataset based on external errors and dashed lines represent samples from Böhme et al. (2013).

12.2 ± 0.3 ka, overlapping in both their external and 2σ uncertainties. Exposure ages of a couple of samples are indistinguishable within their internal uncertainties, with 10.2 ± 0.3 ka for RH-FL-06 and 10.1 ± 0.3 for FLAAM-10. A group of four samples cluster around 7.9 ka (± 0.4), with two samples averaging 8.3 ± 0.2 ka and two averaging 7.5 ± 0.2 ka. Two more sample couples result in 5.4 ± 0.1 ka (FLAAM-01 and -14) and the previously mentioned 3.7 ± 0.1 ka, respectively. The youngest sample is with 1.4 ± 0.1 ka the previously published sample RH-FL-05.

6.4 Reconstructing the sliding and permafrost history of rockslides (Paper III)

Only a few studies have applied the surface exposure dating technique using TCNs on steeply dipping sliding surfaces of relic or actively deforming rockslides (Le Roux et al., 2009; Sanchez et al., 2010; Hermanns et al., 2012b; Zerathe et al., 2014) due to logisti-

6 Results

cal, morphological and computing challenges. In Norway however, this approach seems suitable to estimate the timing of potential initial deformation and to analyse the pre-historical development of a rockslide (Hermanns et al., 2012b, 2013c). In this study a compiled dataset of surface exposure age determinations of six slowly deforming rockslides in Norway is presented. Potential uncertainties due to inherited ^{10}Be or ^{36}Cl concentrations at depth were approximated using the age information of the plateau surface around the rockslides (cf. Sec. 5.2.3, Fig. 5.3).

In order to consider the results in the context of a changing climate and related variations in the permafrost distribution, unrelated climate reconstructions have been analysed and partly used as input for the permafrost model CryoGRID 2D. The model reconstructs long-term fluctuations of ground temperatures along a 2D transect over selected sites (Myhra et al., 2017).

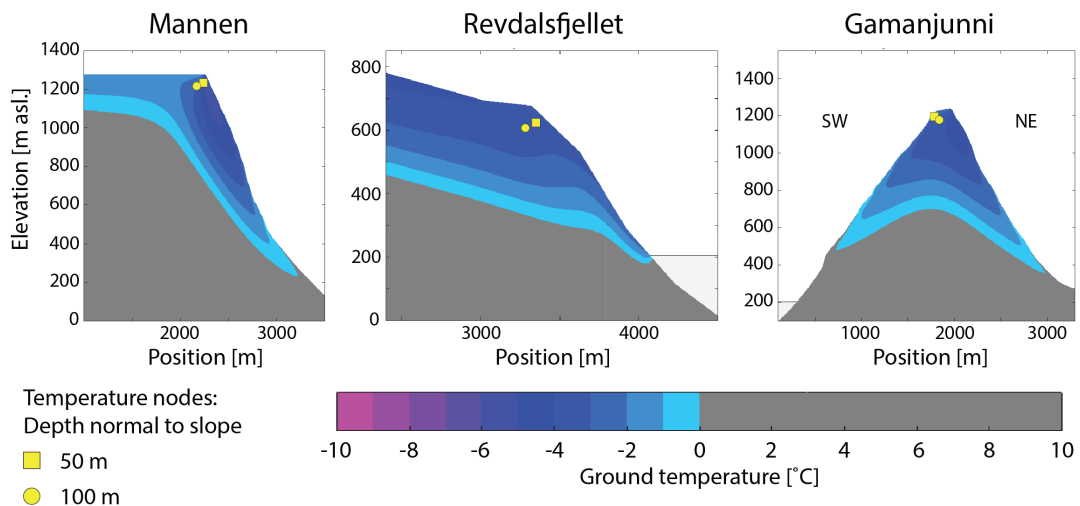


Figure 6.9: Permafrost distribution in the rock slopes of Mannen Revdalsfjellet and Gamanjunni 11.5 ka ago. The temperature nodes indicate the approximate location of the upper most active parts of the rockslides.

At the three rock-slope instabilities Mannen, Revdalsfjellet and Gamanjunni cold permafrost reached deep into the mountain shortly after deglaciation about 11.5 ka ago (Fig. 6.9). Strongly increasing temperatures led subsequently to rapid permafrost degradation reaching a minimum distribution during the HTM. However, it is likely that permafrost remained at depth, at least in the Gamanjunni mountain. During the LIA, the permafrost distribution in the rock-slopes reached a Holocene maximum and is degrading

6.4 Reconstructing the sliding and permafrost history of rockslides

strongly since. At the high elevation rock-slope instability Gamanjunni permafrost is still present today, while at Mannen and Revdalsfjellet sporadic or deep permafrost is possible.

The dating results suggest that the timing of initial deformation at the two rock-slope instabilities Skjeringahaugane (Fig. 6.10) and Oppstadhornet most likely coincided with deglaciation. Due to their low elevation it is unlikely that they have been influenced by cold permafrost conditions, which could have a stabilising effect. It is therefore likely that debuttressing effects during deglaciation may have contributed to initial deformation at these slopes.

However, most of the analysed rockslides, such as Mannen, were initiated during the HTM and were affected by strongly degrading permafrost (Fig. 6.9 and 6.10). The time-

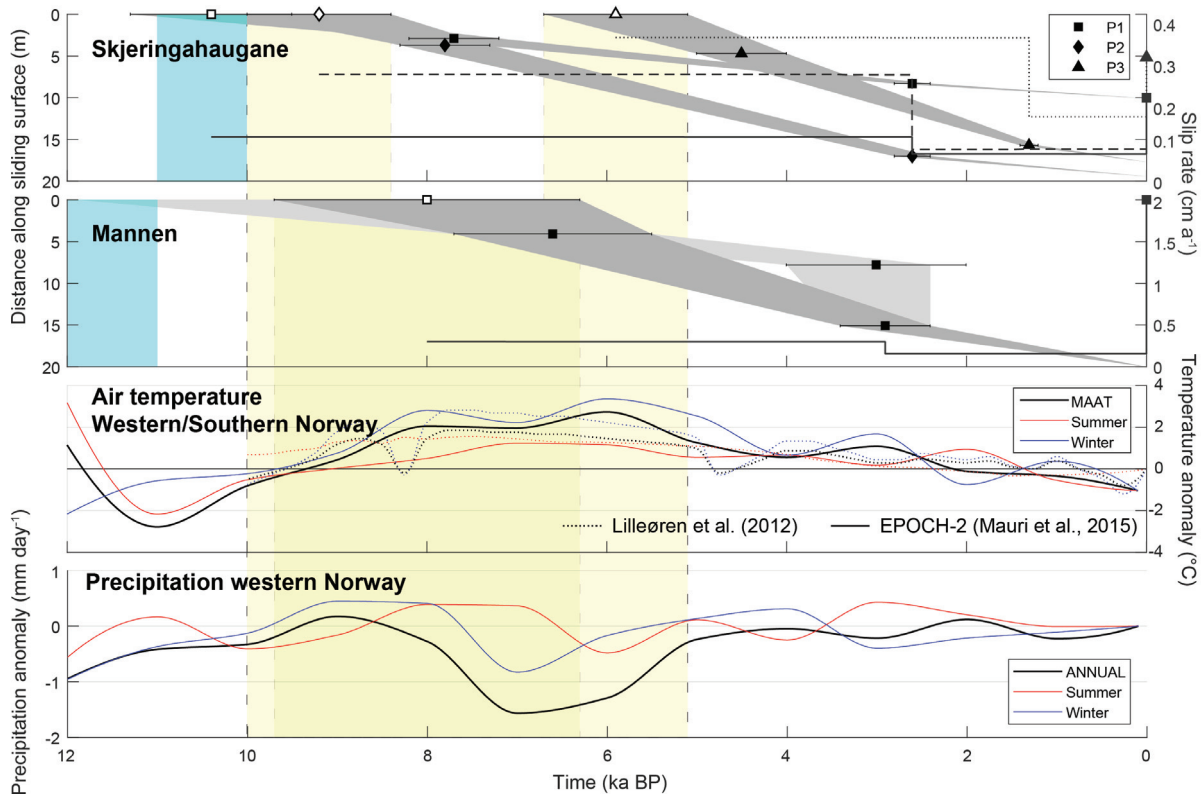


Figure 6.10: Results of TCN-dating along the sliding surfaces at the rock-slope instabilities Skjeringahaugane and Mannen above reconstructed series of temperature anomalies and precipitation changes. Note that summer and winter anomalies from Lilleøren et al. (2012) represent data from July and January, respectively, whereas Mauri et al. (2015) combine June, July and August and December, January and February, to represent the seasons.

6 Results

lag between local deglaciation and initial deformation therefore suggests climatic factors and permafrost degradation as major drivers for slope destabilisation.

In addition to the timing of initial deformation, sliding velocities and their change in time have been analysed. Generally, the sliding patterns of all rockslides follow a similar pattern, with initially high sliding rates decreasing over time. This is in contrast to the often observed pattern of continuously increasing sliding velocities of progressive rock-slope failures in the Alps (e.g. Le Roux et al., 2009; Zerathe et al., 2014). However, it reflects the theory of progressive rock-slope failure, where strain rates are specially high during initial deformation.

Recent measurements of sliding rates suggest that deformation has increased significantly, compared to the Holocene sliding rates, at Mannen (Fig. 6.10) and Gamanjunni. Recent sliding rates at one of two adjacent rockslides at Revdalsfjellet and a relatively young part of the Skjeringahaugane instability suggest moderate acceleration (Fig. 6.10). The unstable rock slopes at Mannen, Gamanjunni and Revdalsfjellet are located at or above the altitudinal permafrost limit. The ongoing temperature increase and related permafrost degradation may therefore add to slope destabilisation at these sites, where the increased sliding rates may indicate a potential catastrophic failure (Crosta and Agliardi, 2003).

7 Discussion

Surface exposure dating with ^{10}Be and ^{36}Cl proved to be a valuable tool in determining the timing and development of rock-slope failures. However, despite continuous improvement of the measurement precision and better approximations of the production rates, the method is still connected to uncertainties that are challenging to address. In the following section the most important error sources, especially within this doctoral study, but also for other fields of application are assessed. The ensuing section focuses on the opportunities and drawbacks of setting the dated processes into a climatic context and the main discussion points emerging from the results and implications.

7.1 Uncertainties when dating CRSFs and rock-slope instabilities with cosmogenic nuclides

During this study challenges connected to three main error sources were faced: inheritance, shielding considerations, and post-failure processes. While efforts were made to reduce the uncertainties related to inherited nuclide concentrations and shielding, post-failure processes could not be predicted and therefore had to be dealt with within data interpretations (Sec. 7.2.2).

7.1.1 Inherited cosmogenic nuclides

For analysing both CRSFs and active rock-slope instabilities, cosmogenic nuclide production at depth, prior to direct exposure, may lead to age overestimations. Inherited cosmogenic nuclides are also a common source of error when determining the timing of glacial fluctuations, when using boulders on moraine ridges (e.g Cockburn and Summerfield, 2004; Matthews et al., 2017). However, the inheritance-causing processes in this case are different and are rather related to potential exposure of the boulders prior to final deposition.

7 Discussion

The study about a young rock avalanche in Chile (Sec. 6.1) illustrates that the distribution of inherited ^{10}Be concentrations may be estimated based on the pre-failure topography and exposure time. Due to the lack of knowledge about the pre-failure position of each boulder however, this distribution cannot be used to define the amount of inheritance on the individual boulder surfaces. From the maximum pre-failure depth of either the whole rock mass or a shallower zone, where the boulders most likely originate from, a minimum amount of inherited cosmogenic nuclides may be defined. But if the break-out area and pre-failure geometry are unknown, inheritance may only be identified by statistical outliers. Several studies, where both failure scarps and deposits have been dated, or the time of failure is known, result in generally older ages on the deposits, for both young and old events (Sewell et al., 2006; Akçar et al., 2012; Oppikofer et al., 2017). It is thus important to consider and discuss the potential effect of inheritance on rockslide boulders, even if no evidence is present.

The potential amount of inherited cosmogenic nuclides in samples from near-vertical sliding surfaces (Sec. 6.4), may be constrained if information about the exposure age of the stable surface above the instability is available. For this, this surface was sampled in addition to the transects over the sliding surface, where possible. One single sample, however, may not be reliable and could lead to errors within the correction calculation. In some cases, the reference sample may represent a complex burial, exposure and erosional history, which hinders an accurate correction. The impact of the correction is mostly significant for surfaces sampled only a few metres below the original pre-failure surface where the amount of inherited cosmogenic nuclides is largest. Consequently, it is the uppermost samples that have to be taken with care if the exposure age of the pre-failure surface is unclear. In this study, the effect was generally small, due to relatively short and well constrained pre-failure exposure times.

7.1.2 Topographic shielding along steep rock slopes

The topographic shielding along steep and near-vertical rock slopes is relatively high and has hence a significant affect on exposure ages. On flat and open areas, a sample position can have a full view of the sky. Because the most effective cosmic radiation for TCN production comes from medium to high inclination angles (measured from the horizontal up), a horizon that shields the incoming radiation in relatively low angles has a limited effect on the total production rate (cf. Sec. 3.2). Along steep rock slopes, a large fraction of azimuths is obstructed completely, affecting local production rates significantly. Correction for inherited cosmogenic nuclides could thus become irrelevant, when outweighed by

7.1 Uncertainties when dating CRSFs and rock-slope instabilities with cosmogenic nuclides

the uncertainty related to imprecise derivations of topographic shielding. A conscientious and systematic derivation of the shielding factor is hence crucial, and related uncertainties must be included within the exposure age calculations.

In order to establish a reliable approach for estimating the topographic shielding along steep rock slopes several procedures were tested: (1) Shielding calculations using field measurements, (2) deriving the skyline from each point based on a 1 m-DEM, (3) using the calculator for oddly shaped objects by Balco (2014) with a 5 m-DEM and a (4) 1 m-DEM. The local shielding was measured in the field at every sample location with an inclinometer. The resolution of these measurements is variable, depending on personal judgment, obstruction by clouds and vegetation and situation at the sample location. Incorporating small scale obstructions along the rock wall is also challenging, when working on a rope. It was therefore necessary to develop a numerical approach, allowing for the complementation or replacement of field measurements (cf. Sec. 5.2.2).

A sensitivity test conducted at a locality, which is not included in this study, illustrates the uncertainties and challenges connected to the different approaches. The substantial workload for such a test does not justify a repetition for each study site. However, resulting uncertainties may be incorporated within the age calculations of other sites. Shielding values for five samples along a vertical transect over a sliding surface include two calculations with the CRONUS-Earth topographic shielding calculator version 2.0 (Marrero et al., 2016). For one of these computations, the field measurements were used, while for the second one, the azimuth and inclination angles were derived digitally from the skyline for each sample based on a 1m-DEM. Two additional approaches use the shielding calculator for oddly shaped objects by Balco (2014). Following the procedure described in section 5.2.2, shielding values were obtained using a 5 m- and a 1 m-DEM.

The largest discrepancies are observed for SPL-01, where the absolute differences between the 5 m-DEM and the other shielding calculations are between 0.05 and 0.08. Differences to the field measurements of SPL-04 lie between 0.04 and 0.06. The standard deviations for all five samples are between 0.01 and 0.04 (Tab. 7.1).

In general, the values calculated with the CRONUS-Earth calculator, agree relatively well within ± 0.03 , except for SPL-04, where the difference is 0.06. The calculations with G. Balco's calculator results in discrepancies < 0.03 for three, and close to 0.05 for two sample locations. The fact that there is no clear pattern, pointing out one method that generally disagrees with the others, and that individual discrepancies are presumably dependent on the local topographic characteristics around the sample location. For each

7 Discussion

Table 7.1: Sensitivity test comparing different approaches to derive topographic shielding values along steep rock walls.

Sample	CRONUS-Earth v2.0		Balco (2014)		SD
	Inclinometer	Skyline 1 m-DEM	5 m-DEM	1 m-DEM	σ
SPL-01	0.7165	0.7214	0.8005	0.7462	0.0379
SPL-02	0.6840	0.6861	0.7134	0.6893	0.0137
SPL-03	0.7309	0.7375	0.7584	0.7097	0.0201
SPL-04	0.7715	0.7103	0.7364	0.7286	0.0258
SPL-05	0.7858	0.7556	0.7945	0.7924	0.0181

numerical approach, the sample locations have to be adjusted manually, fitting the three dimensional surfaces.

Shielding values derived with the 1 m-DEM and G. Balco’s calculator, are all smaller (representing more shielding) than the values derived with the 5 m-DEM. This indicates that local small topographic features affecting the shielding at the sample location are either not or less represented by the generally smoother 5 m-DEM. While this may mean that the shielding might be underestimated with a coarse DEM, it can also lead to shielding overestimations, when the sample is placed slightly inaccurately on a high-resolution DEM. Note, that high values mean low shielding and vice versa.

The knowledge about the exact sample location along the rock wall is thus crucial. Well visible marks at the sample scars could help to precisely determine the sample location on a photogrammetric model. It is, however, advisable to always conduct field measurements, in order to compare the results of at least two approaches. If only one method for the derivation of shielding along steep rock walls is applied, a conservative uncertainty value of 0.04 (according to this sensitivity analysis) could be added to the exposure age calculations.

Although an effort was made to locate the samples as precisely as possible within this study, errors connected to this may occur. However, a higher accuracy is only necessary if the triggering events are dated by another geochronological method. In order to identify general patterns in the context of climatic variability, certain uncertainties may be accepted.

7.2 Post-glacial processes at Rombakstøtta and Ramnanosi

The results of the exposure ages at Rombakstøtta give relatively clear picture over the Holocene rock-slope failure activity at this site. The distribution of exposure ages at Ramnanosi in contrast, is complex. However, both study sites allow for a comprehensive interpretation and discussion about landscape development in such settings.

7.2.1 CRSF activity following deglaciation at Rombakstøtta

Four out of the nine sampled boulders below the Rombakstøtta rock-slope instability are represented by indistinguishable, almost identical, apparent exposure ages averaging 9.8 ± 0.2 ka. The distances between these boulders are <300 m and they are all located in the northwest of the depositional area. The strong agreement and proximity suggests that they represent one CRSF event (Fig. 7.1).

The area of the fjord Rombaken has most likely been glaciated during the YD cold period (Bargel, 2003) and the local post-YD deglaciation was completed more than 10 ka ago (cf. Sec. 4.1.4; Andersen et al., 1981; Hughes et al., 2016). The apparent exposure age of 12.0 ± 0.3 ka, representing one of the statistical outliers, exceeds the post-YD deglaciation by up to 2 ka. The relatively high ^{10}Be concentration in the boulder surface is most likely the result of inherited cosmogenic nuclides from ^{10}Be production before failure. This suggests, that Rombakstøtta may have been a nunatak during YD glaciation, allowing for the production of TCNs in the rock surface prior to the deglaciation of the valley. The boulder presumably originates from a shallower pre-failure depth than the remaining sampled boulders. It is, however, not possible to determine if this concentration represents the exposure age of the pre-failure surface and thus the timing of deglaciation, or if it defines only a minimum age for the latter.

The second outlier in the same depositional area underestimates the potential failure timing by over 2 ka. This may be caused by a series of factors. Physical erosion by frost wedging or roots may have removed several centimetres of the boulder surface, though morphological signs related to such processes generally not observed at the study site. It is therefore likely, that rock-fall processes or post-depositional activity, such as toppling of the boulder, are the cause for a ^{10}Be concentration lower than the surrounding average. Four small (<100 m³) rock-fall events reaching the railway have been registered below Rombakstøtta in 1996 (Larsen, 1997), 2005, 2010 and 2012 (Fig. 7.1) (NVE, 2018). Not

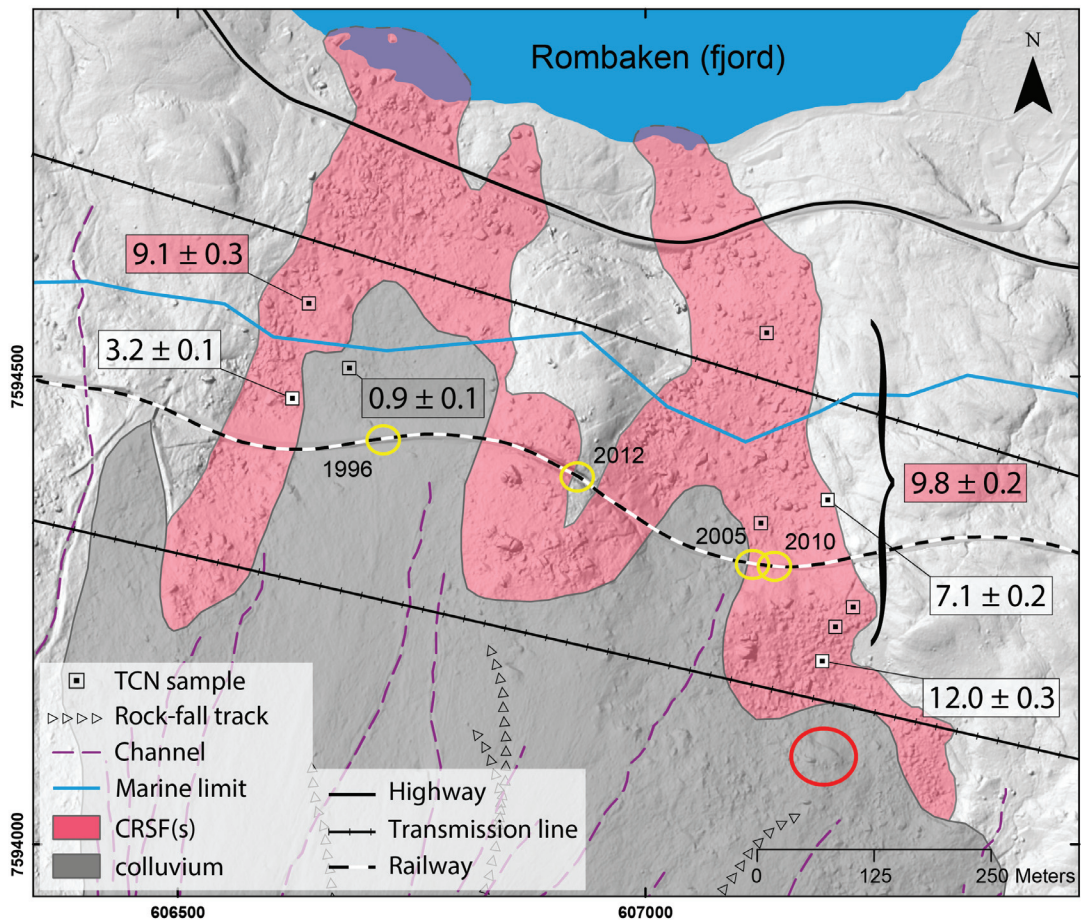


Figure 7.1: Detail map of the lower depositional area of Rombakstøtta with the apparent exposure ages of individual boulders. Note that the delimitations of the CRSF deposits are not based on detailed geomorphological mapping and are therefore not necessarily accurate. The delimitation of the recently active colluvium is based on a qualitative assessment and may be exceeded by single events (Morken, 2017). It represents mainly debris-flow and snow avalanches, filling the coarse boulder fields with finer material. Yellow circles mark recently registered small rock-fall events, that affected the railway. Infrastructure and the block in the red circle are marked for orientation and comparison with Fig. 7.2.

much is known about the source of the latter three, but due to the topography, they could be blocks and boulders that originated from the proximate steep slope. Destabilisation could have been induced by large rock-fall boulders impacting the slope above (Fig. 7.2) and setting some of the deposits in motion. A similar scenario is plausible for the young dated boulder, though it can not be excluded that it represents a rock-fall event originating from the Rombakstøtta rock slope.

7.2 Post-glacial processes at Rombakstøtta and Ramnanosi

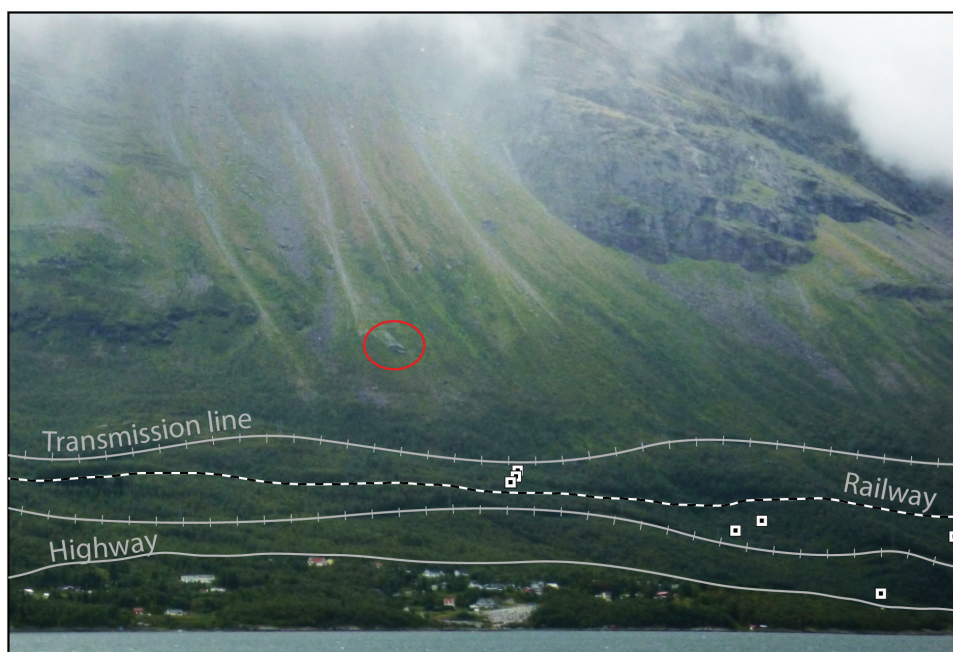


Figure 7.2: Photo of a large part of the depositional area below Rombakstøtta. The picture was taken from northeast, looking towards southwest. The approximate sample locations of seven sampled boulders are marked (the remaining two are not visible in the photo). The large boulder in the red circle (cf. Fig. 7.1), marks the end of a relatively unvegetated track, indicating a relatively recent deposition.

The roughly estimated reach of modern slope processes along the Rombakstøtta coluvium crosses both a higher elevated transmission line and the railway in two sections (Fig. 7.1). It was mapped according to relatively clear transitions in surface roughness, vegetation and morphology. The range agrees well with the modelled run-out for rock-fall blocks $>10 \text{ m}^3$ originating from different positions in the steep rock slope at Rombakstøtta (Morken, 2017, Fig. 4.16). Larsen (1997) suggest that the 1996 rock-fall event was triggered by frost-weathering processes and that such rock-fall events may have a re-occurrence interval of 10-20 years at Rombakstøtta. According to the statistically mapped permafrost occurrence in steep rock walls in Norway (Magnin et al., 2019), almost the entire unstable rock-slope at Rombakstøtta lies within discontinuous permafrost. This supports the conclusion of Larsen (1997) and is a reasonable explanation for local ongoing rock-fall activity (e.g. Arosio et al., 2013; Jia et al., 2017).

Additional processes with a long reach at this site are debris flows and snow avalanches (NVE, 2018), filling and covering potentially blocky CRSF deposits with sediment. Larger rock-fall events, however, may have longer potential run-lengths and may affect previous

7 Discussion

boulder fields. The two apparent exposure ages of 0.9 ± 0.1 and 3.2 ± 0.1 ka on the north-western side of the colluvium may represent such large sized rock-fall events. It is well possible that the youngest boulder was part of the 1996 rock-fall event, originating from the slope surface and thus containing inherited ^{10}Be concentrations equivalent to 900 years exposure (cf. Sec. 6.1).

One boulder with an apparent exposure age of 9.1 ± 0.3 ka outside of the mapped modern colluvium is likely not representative in defining the timing of a larger CRSF event. The temporal proximity to the failure timing 9.8 ka ago, which is represented by four boulders, allows for speculations that this part of the deposit is connected to the northeastern CRSF deposits. The mapped CRSF deposits could therefore represent one large rock-avalanche event that failed between 8.8 and 10 ka ago. Alternatively, the deposits represent two or more CRSF events in the same time range, with an initial event c. 9.8 ka ago. Based on run-out analyses for potential rock-avalanche scenarios it is more likely, that the deposits belong to one larger event (Morken, 2017).

This failure timing follows the post-YD deglaciation closely, with a time lag of less than or about one millennium. The debuitressing effect is therefore likely to have played a major role in the destabilisation of the slope. If Rombakstøtta remained a nunatak during the YD glaciation, the mountain was presumably affected by deep cold permafrost during this period of low temperatures (Myhra et al., 2017), which likely had a stabilising effect on the rock-slope (e.g. Davies et al., 2001; Krautblatter et al., 2013). The YD cold period was followed by a strong temperature increase, leading to widespread deglaciation and permafrost degradation, when ground temperatures reached above 0° . At Rombakstøtta both factors i.e. the removal of glacier ice as counterweight from the slope and permafrost degradation, may have conditioned one or several CRSFs shortly after deglaciation.

7.2.2 Mass-movement processes at Ramnanosi

The apparent exposure ages from boulders below Ramnanosi in western Norway are spread throughout the entire Holocene (Sec. 6.3; Fig. 6.8). It is therefore not possible to assign failure timings to single CRSF events. But the results provide valuable information about (1) the deglaciation history, (2) the potential nature of rock-slope failure activity from the Ramnanosi rock slope, and (3) post-failure processes.

The first peculiarity in the dataset is the relatively old exposure ages of three boulders, ranging from 13.9 ± 0.4 ka, over 13.1 ± 0.4 ka to 12.2 ± 0.3 ka. The ages exceed the timing of local deglaciation on the plateaus by almost 2 ka. They are thus evidence for the previous postulation: the pre-failure surface contained inherited ^{10}Be concentrations, produced in

7.2 Post-glacial processes at Rombakstøtta and Ramnanosi

the rock surface prior to the presence of an ice cover. This means that glacial erosion was not sufficient to reset the ^{10}Be concentration on the mountain plateau.

The second observation is the fact that couples or groups of boulders exist with similar apparent exposure ages. One group of four samples clusters between 7.5 and 8.4 ka ago. This coincides with the HTM, where air temperatures reached a maximum and permafrost was most likely absent in Ramnanosi (Myhra, 2016). This could have increased rock-slope instability, leading to one or several CRSFs. The latter may also be supported by the spread in the exposure ages, suggesting several failure periods. One potential scenario is therefore, that the deposits below Ramnanosi are the result of successive rock-slope failure activity throughout the Holocene, with individual volumes far below the total volume of the entire potential break-out niche. The spatial spread of agreeing exposure ages calls for further interpretations, however.

Since the general climatic and geographic conditions are the same for all sampled boulders, a variety in erosion or vegetational shielding, large enough for such differences in exposure age, is unlikely. Hence, when assuming that the boulders do not represent many single rock-fall events, the disagreeing exposure ages on single landforms must be explained by either inheritance or post-depositional motion. It has been suggested previously that the lobate landforms at Ramnanosi might be the result of creeping processes or the combination of both CRSFs and creeping processes (Blikra et al., 2002, 2013a; NGU, 2019). On the northern slope below the Stampa instability and in the upper part of the deposits below Ramnanosi, recent deformation of $<0.5 \text{ cm a}^{-1}$ are observed (Böhme et al., 2019). The movement in the upper parts below Ramnanosi becomes very clear in InSAR data, where a yearly negative displacement of $<4 \text{ cm a}^{-1}$ is observed (NGU, 2019). The vegetation cover in lower elevations prohibits reliable InSAR measurements. However, the presence of the vegetation cover suggests that deformation rates are significantly smaller than in the upper depositional area, where vegetation is absent.

A potential evolution of the rock slope below Ramnanosi could thus include one big or several CRSFs shortly after deglaciation, conditioned by the debuttressing effect. This was most likely followed by a period of creeping activity with decreasing deformation rates after the HTM, marked by the apparent exposure ages of four boulders. The two adjacent boulders FLAAM-12 and -13, with almost identical exposure ages of 3.6 and 3.9 ka, respectively, could represent a large rock-fall event. The two sampled boulders are relatively large (a-axis $>10 \text{ m}$), and are surrounded by several similarly large boulders. Finally, two unrelated boulders result in ages of 5.4 and 5.6 ka, respectively. If not explained by slope creeping and related boulder toppling, bio-mechanical erosion might have

removed the upper centimetres of the boulder surfaces. This process has been observed on some single boulders in the area, which have been avoided for sampling. However, it cannot be excluded that similar processes have been affecting the sampled boulders. Because of the many factors potentially resulting in exposure ages underestimating the real failure timing, it is likely that Ramnanosi has not been affected by CRSFs of larger volume than rock-fall events after the HTM.

7.3 Temporal distribution and evolution of CRSFs and unstable rock-slopes in Norway

It is generally accepted that internal structural pre-conditions are one of the most important factors controlling slope stability, especially in crystalline bedrock (Saintot et al., 2012; Böhme et al., 2013; Booth et al., 2015), even though several internal and external factors add to slope destabilisation (cf. Sec. 2.2). The focus of this thesis was the timing of rock-slope failure activity, in the context of potential climatic drivers and related phenomena, such as deglaciation and permafrost distribution. While individual failure timings have been discussed in detail in the presented publications, this following discussion focusses on the general distribution of rock-slope failures in Norway.

In a data compilation 29 CRSF events in Norway that have been dated either directly with ^{10}Be and ^{36}Cl dating or indirectly with ^{14}C in organic material are represented (Table 7.2). 22 events have been dated in western and southern Norway, while seven events were recorded in northern Norway. Events and their corresponding failure timings are only represented in this dataset if at least two exposure ages agree within their uncertainties, or if the age of a single sample is verified stratigraphically or by another dating method. Several failures from the same slope with indistinguishable apparent exposure ages are counted as one event since the activation of the slope is relevant, and multiple failures from the same slope, such as at Mannen could bias the distribution. Relative age determinations based on stratigraphical relations (e.g. Böhme et al., 2015a) or sea-level curves (e.g. Blikra et al., 2006b) only and undefined mass movement events (e.g. Bøe et al., 2004) are not included within the compilation and allow for comparison. Finally, the dataset is complemented by the estimated timing of initial deformation for eight rock-slope instabilities in western and northern Norway (Sec. 6.4) and three historical events, adding to a total number of 39 events (Fig. 7.3).

The temporal distribution of all events in both northern and southern Norway shows a clear peak of rock-slope failure activity between 12 and 9 ka ago and two periods with

7.3 Temporal distribution and evolution of CRSFs and unstable rock-slopes in Norway

Table 7.2: Compilation of rock-slope failures in Norway, directly dated using ^{10}Be or ^{36}Cl or indirectly dated, using radiocarbon (^{14}C) in organic material. For slow moving rockslides the ages represent the estimated timing of initial deformation

	Name	RSF element*	Age (ka) [†]	Method	Reference
Southern/Western Norway	Oppstadhornet	3	14.9+5.5 -3.5	^{10}Be	this study
	Mannen 1	1	9.5±0.6	^{10}Be	this study
	Mannen 2	3	8.0±1.7	^{36}Cl	this study
	Mannen 3	1	4.9±0.4	^{10}Be	this study
	Skjeringahaugane P1	3	10.4±0.9	^{10}Be	this study
	Skjeringahaugane P2	3	9.2±0.8	^{10}Be	this study
	Skjeringahaugane P3	3	5.9±0.8	^{10}Be	this study
	Gråura	1	13.8±0.9	^{10}Be	Hermanns et al. (2017)
	Vora a+b	1	12.6±0.9	^{10}Be	Hermanns et al. (2017)
	Kallen	1	11.4±1.0	^{10}Be	Hermanns et al. (2017)
	Skiri	1	11.2±0.6	^{10}Be	Hermanns et al. (2017)
	Vora d	1	10.8±1.4	^{10}Be	Hermanns et al. (2017)
	Alstadfjellet	1	9.3±0.7	^{10}Be	Hermanns et al. (2017)
	Innfjorddalen	1	14.3±1.4	^{10}Be	Schleier et al. (2017)
	Digerura	1			Austigard (2016)
	Kjøttåfjellet	1	2.8±0.7	$^{10}\text{Be}/^{14}\text{C}$	Oppikofer et al. (2013)
	Innerdalen 1	1	14.4±0.8	^{10}Be	Schleier et al. (2015)
	Innerdalen 2	1	7.4±0.6	^{10}Be	Schleier et al. (2015)
	Nokkenibba	2	7.1±0.9	^{10}Be	Böhme et al. (2015a)
	Nakkeneset	2	6.7±0.9	^{10}Be	Böhme et al. (2015a)
	Blåhornet	2	2.2±0.4	^{10}Be	Böhme et al. (2015a)
	Stampa	1	3.7±0.4	^{10}Be	Böhme et al. (2013)
	Oldedalen	1	6.0±0.1	^{14}C	Goehring et al. (2012)
	Fjærlandfjorden 1	1	10.0±0.8	^{10}Be	Hermanns et al. (2011)
	Fjærlandfjorden 2	1	10.0±0.8	^{10}Be	Hermanns et al. (2011)
	Fjærlandfjorden 3	1	3.5±0.5	^{10}Be	Hermanns et al. (2011)
Venje	1	1.6±?	^{14}C	Blikra et al. (2006b)	
Northern Norway	Rombakstøtta	1	9.8±0.6	^{10}Be	this study
	Revdalsfjelelt 2	3	7.5±0.7	^{10}Be	this study
	Revdalsfjelelt 1	3	4.4±0.4	^{10}Be	this study
	Gamanjunni 3	3	5.3±1.4	^{10}Be	Böhme et al. (2019)
	Storhaugen 1	1	10.5±0.5	^{10}Be	Böhme et al. (2015b)
	Storhaugen 2	1	4.1±0.3	^{10}Be	Böhme et al. (2015b)
	Grøtlandsura	1	11.4±0.1	^{14}C	Fenton et al. (2011)
	Russenes	1	10.9±0.1	^{14}C	Fenton et al. (2011)
	Hølen	1	7.5±0.3	^{10}Be	Fenton et al. (2011)
	Balsfjord	1	10.8±?	^{14}C	Blikra et al. (2006b)

*1 = Landslide deposits, 2 = Failure surface, 3 = Active sliding surface

[†]*Deposits*: weighted average ± 1σ uncertainty or as stated in literature. *Active sliding surfaces*: estimated timing of initial deformation based on vertical sample transect along the sliding surfaces.

7 Discussion

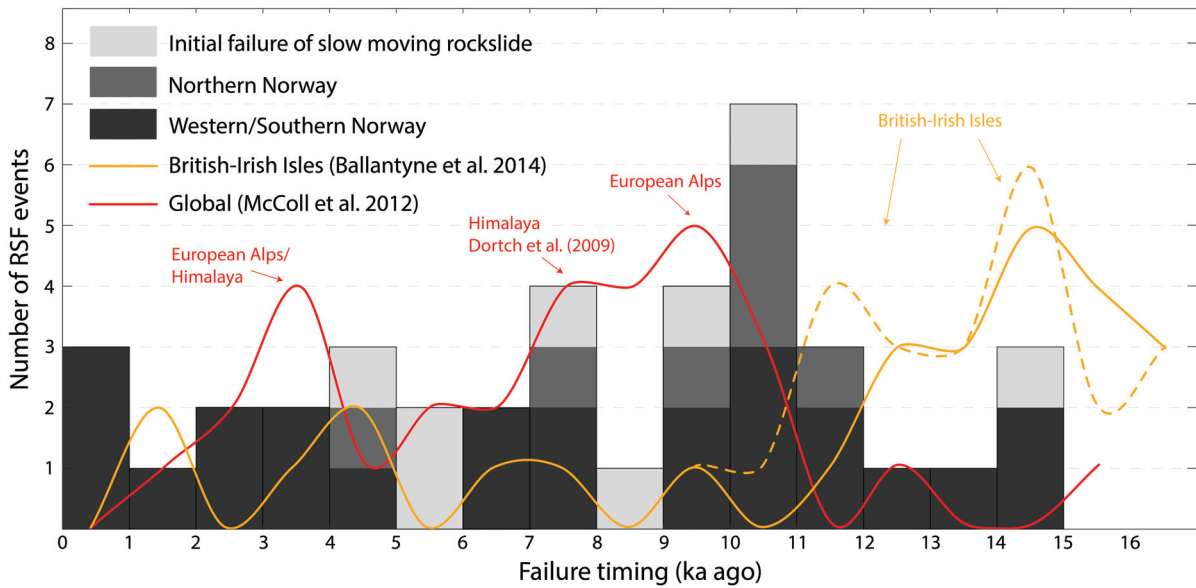


Figure 7.3: Temporal distribution (frequency per millennium) of CRSFs (Tab. 7.2) and the initial failure of rock-slope instabilities (Sec. 6.4) in Norway. For comparison, the data of a compilation from the British-Irish Isles (Ballantyne et al., 2014) and a global dataset (McColl, 2012) are added. The dashed line represents the same exposure age dataset from Ballantyne et al. (2014), calculated with a different local production rate.

slightly increased CRSF activity between 8 and 6 ka and 5 and 2 ka ago. Looking at the events from southern/western Norway only, the early peak becomes rather insignificant, but the activity can still be curtailed to these three main phases. Five of the seven events in northern Norway fall into the early peak, while only two failures have been registered during the rest of the Holocene. The initial failure timing of slow moving rockslides seems almost evenly distributed throughout the Holocene.

A similar distribution with an early Holocene peak and increased activity during the mid-late Holocene has been observed for the reconstructed rock-slope failure frequency in the Storfjord area, and specifically in the small area of Tafjorden (Böhme et al., 2015a). And although the number of events in this compilation may not be statistically representative, the peaks and periods of increased CRSF activity coincide with and include the three time periods (11,000-9700, 8300-7700 and <4200 cal. yrs BP) of increased submarine mass transport and deposition identified in several fjord systems and lakes in western and mid-Norway (Bellwald et al., 2018).

The early peak in sub-aerial rock-slope failure activity represents the first two millennia after post-YD deglaciation in most areas, while earlier events coincide with local deglaciation.

7.3 Temporal distribution and evolution of CRSFs and unstable rock-slopes in Norway

tion in the respective areas (Schleier et al., 2015, 2017; Hermanns et al., 2017). The Oppstadhornet rockslide remained ice-free after the first deglaciation following the LGM with initial deformation between 15 and 14 ka ago. This early activity and the early peak in the failure-frequency pattern suggests that glacial debuitressing was effective in many oversteepened rock-slopes in Norway.

Bellwald et al. (2018) however, ascribe increased mass-movement activity to periods of enhanced seismic motion and a relation to continental isostatic uplift due to significant ice loss of the Scandinavian Ice Sheet during the late-Pleistocene and early Holocene. This agrees with Ballantyne et al. (2014), who conclude that debuitressing effects were a key factor for preconditioning early rock-slope failures on the British-Irish Isles, but that earthquakes related to the glacio-isostatic rebound are likely the trigger for many failures post-dating local deglaciation by a millennial-scale time lag.

A similar time lag of several thousand years since deglaciation can be observed in the European Alps and the Himalaya, where different reasons for this long endurance period of rock slopes are discussed (e.g. Dortch et al., 2009; Le Roux et al., 2009; McColl, 2012). While earthquakes related to seismic activity are frequently mentioned as a likely trigger for large-scale rock-slope failures, there is often limited evidence. In areas with generally low tectonic activity it is therefore often suggested that climatic factors have a significant effect on rock-slope stability and are likely to significantly pre-condition CRSFs (e.g. Dortch et al., 2009; Ivy-Ochs et al., 2009). Gasse et al. (1996) for example suggest that there have been three periods with specifically intense monsoon events, where especially the time period between 7 and 8 ka ago coincides with the failure of several large-scale rock avalanches (Dortch et al., 2009). This time period also coincides with the HTM and increased rock-slope failure activity in Norway. During the HTM temperatures and precipitation rates in Norway reached a maximum (Lilleøren et al., 2012; Mauri et al., 2015), while the distribution of mountain permafrost was minimal (Myhra et al., 2017; Gisnås et al., 2017). It is therefore likely that the combination of degrading permafrost with increased precipitation rates was a key factor for slope destabilisation during the HTM in high altitude areas.

The last period of increased rock-slope failure activity between 5 and 2 ka ago also coincides with a period of increased mass-movement activity in the fjords of western Norway (Bøe et al., 2004; Bellwald et al., 2018). Bøe et al. (2004) suggest that a cluster at about 3 cal. ka BP may be driven by climatic variability, while they ascribe the temporal clustering of spatially well distributed mass movements around 2 cal. ka BP to one or several earthquake events. The latter agrees with Bellwald et al. (2018), who hypothesise

that increased mass-movement activity generally indicates periods of enhanced seismic activity. However, preparatory and triggering factors of submarine sedimentary processes may differ to those of sub-aerial deep-seated and catastrophic rock-slope failures. In Norway, seismicity as main driving factor for late Holocene failure events seems unlikely due to (1) the temporal spread of sub-aerial CRSF events in western Norway and the absence of a well determined regional rock-slope failure cluster (e.g. Blikra et al., 2006b), and (2) due to the low frequency and magnitude of potential earthquakes in Norway (Olesen et al., 2004). Increased debris-flow activity and colluvial deposition within short time periods since 3.2 ka and around 2 ka ago (e.g. Blikra and Nemeč, 1998; Nesje et al., 1995; Sletten et al., 2003) may indicate periods of climatic deteriorations and increased precipitation and snow melt, which may also be a factor for increased submarine mass-movement activity.

7.4 Implications for paraglacial landscape development

Paraglacial landscapes that have been conditioned by glacial activity (Church and Ryder, 1972) are characterised by increased geomorphological activity, aiming for a natural stability equilibrium (Ballantyne, 2002a). An important element of paraglacial systems are sediment cascades, acting on various temporal and spatial scales (e.g. Ballantyne, 2003; Schrott et al., 2006; Heckmann et al., 2008). However, paraglacial geomorphological activity is not restricted to hillslope-channel processes, but includes a wide range of mass wasting and erosional processes and process scales. CRSFs displace and accumulate large amounts of material within minutes, but can affect the landscape development for millennia, interfering with other factors, such as tectonics, climate, channel incision and lowering of the erosional basis (e.g. Korup, 2005; Korup and Schlunegger, 2007; Korup et al., 2010).

In the valley below the Mannen rock-slope instability, the Quaternary geological and geomorphological observations allow the reconstruction of the landscape development in this typical fjord valley setting. Here, the interplay of an initially high but rapidly lowering sea-level, a high availability of glaciogenic sediments and mass wasting activity from the valley slopes, demonstrate the paraglacial landscape response to oversteepened rock walls, and the impact of rocksliding on the landscape evolution. The Romsdal valley was influenced by late (YD) deglaciation, a high marine limit and a quick post-glacial sea-level drop. The Quaternary geology is dominated by glacial and marine sediments modified by a high mass wasting activity and fluvial erosion and deposition.

7.4 Implications for paraglacial landscape development

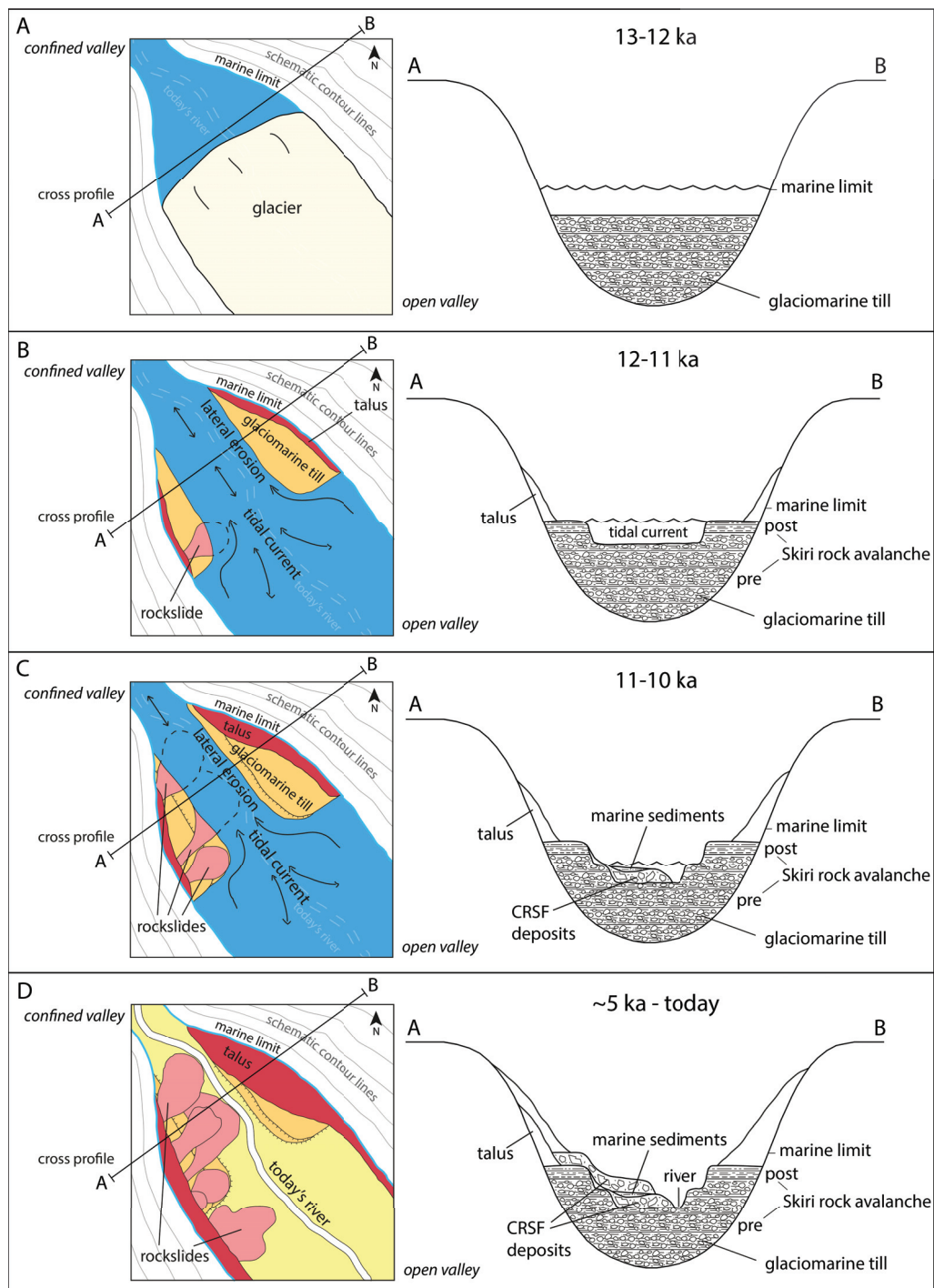


Figure 7.4: Schematic illustration of a Holocene landscape evolution model in Romsdal valley below Mannen. The section is characterised by an increasing valley confinement downstream which enhanced currents during tidal reversals while the sea level was dropping. The cross section A-B indicates the sedimentology with depth for each time step.

7 Discussion

Several tens of meter thick layered glacial deposits below Mannen are suggested to be older than the Skiri rock-avalanche deposits, that have apparent ^{10}Be ages of 10.5-11.7 ka (Hermanns et al., 2017). The rock masses of this event dammed the valley c. 5 km upriver, and must have retained at least large parts of the coarse glacio-fluvial sediments (Fig. 7.4A). The rock-avalanche dam was never completely eroded and still represents a barrier across the Rauma valley (Hermanns et al., 2013a).

Deposition processes at the glacial front in this section could have been similar to those of a submarine fan or ice-contact underwater fan (Lønne, 1995; Winsemann et al., 2009). A confined section of the valley, which connects downriver to the wide basin like valley below Mannen, probably led to a quick build-up of 20-30 m thick glacio-marine till layers with a sharp ice-contact line valley upwards (cf. Hilger et al., 2018). While fine sediments were evacuated, coarser till deposits persisted behind this choke point. The sharp transition from the glacio-marine till to fine-grained marine sediments on top (Hilger et al., 2018) could be an indicator for the timing of the Skiri rock-avalanche, retaining the coarse grain size fraction (Fig. 7.4B). The top surface of these sediments reaches an elevation from 90 m asl. in the northwest to 100 m asl. in the southeast. These elevations coincide with the sea level 11-12 ka ago, when wave and tidal activity must have produced flat erosional surfaces and steep longitudinal erosional edges (Fig. 7.4B). The velocities of the currents connected to the tide reversals were most likely increased by the strong convergence in valley width in this section (Ross et al., 2017) and led to incision and strong lateral erosion in the central part.

12-10 ka ago three CRSFs covered glacio-marine and marine sediments and reached, at least partly, into the fjord environment (Fig. 7.4C). Erosional modification of the deposits can be connected to the continued strong tidal activity and valley parallel currents during the following rapid sea level drop. The height of the erosional slopes suggests that tidal currents have been effective from deglaciation to about 10 ka ago when the sea level dropped close to the modern river level (Fig. 7.4D).

Subsequently, fluvial processes took over, modifying the cross section by fluvial deposition and erosion processes. Since c. 5 ka lobate landforms from three to six CRSF events overlie the stratified drift. Today, large talus slopes and debris cones characterise both sides of the valley's morphology, which probably started to form during an early stage of deglaciation and built up continuously throughout the Holocene. Although the CRSF deposits have been partly modified by erosional processes, large parts of the landforms are located outside of the modern range of the Rauma river, and of many of the hillslope

processes from the valley sides. They may persist for many millennia more, conditioning and characterising the landscape evolution of Romsdal valley.

This landscape evolution model and today's morphology at the Mannen (and many other) sites in Norway represent several elements of the paraglacial geomorphological processes and landforms presented by Ballantyne (2002b), including (1) catastrophic rock-slope failures following the downwasting glacier surface, (2) paraglacial rock-slope deformation, (3) paraglacial rockfall and talus slope accumulation, and (4) recent paraglacial reworking of sediment-mantled slopes.

7.5 Recommendations for future research

The results presented in this thesis suggest that climatic factors most likely play an important role in rock-slope stability in Norway. Processes related to both permafrost degradation and alterations in groundwater conditions are likely to have a significant effect. However, it has been suggested in previous reports and studies (e.g. Böhme et al., 2013; Booth et al., 2015) that the structural geological pre-condition is one of the most important controlling factors for rock-slope instabilities in Norway. In order to better assess the effect of climatic factors it would therefore be beneficial to include detailed models of the geological setting at a local scale and general rock-mechanical characteristics and the main direction of discontinuities at the regional scale. These could be incorporated in multi-stage mechanical models (e.g. Krautblatter et al., 2013; Grämiger et al., 2017) and be extended regionally. The information about rock-fatigue due repeated glaciations or permafrost fluctuations depending on the rock-type and regional geological setting can then be used as valuable information for more detailed local studies.

A good test site for a local study could be the Revdalsfjellet instabilities. The proximity of the two rockslides suggest a similar general geological setting, while the results of this study and recent deformation rates suggest local disparities and a different sensitivity to climatic changes. A detailed geological study including structural measurements, geophysical surveys and the analysis of spacial variations in deformation could be the basis for a more detailed reconstruction of the potential permafrost distribution in the slope. This could be extended by a hydro-geological assessment, which ideally could incorporate different permafrost conditions. Data from the well studied and continuously monitored rock-slope instability at Nordnesfjellet, which is located in a similar setting only a few kilometres north of Revdalsfjellet, could be used for comparison. More detailed permafrost modelling at the Gamanjunni 3 rockslide could stand in contrast to

7 Discussion

warmer ground temperatures at Revdalsfjellet and may be a useful addition to such a project.

Such a case study at Revdalsfjellet or other adjacent test sites should include a more extensive collection of samples for ^{10}Be dating along the outcropping backscarps. A vertical transect with an increased sample density would result in a higher resolution of potential pre-historical movement patterns, and may uncover the hypothesised discrepancy in climate sensitivity.

The latter could be extended to a methodological study testing the applicability of TCN dating along failure and sliding surfaces. Sampling a regular grid over a stable failure surface is one approach, which would require significant economical resources but may uncover uncertainties and challenges that have been overseen so far. On the other hand, if the study site is chosen carefully and uncertainties are low, it could give a more complete picture about deformation patterns of progressive rock-slope deformation followed by catastrophic failure.

Using cosmogenic ^{10}Be in order to date CRSF events has become increasingly popular during the last decades. However, the challenge of inherited pre-failure ^{10}Be concentrations in boulders is often not discussed or ruled out due to the presence of statistical outliers. The first paper of this thesis shows the likelihood of inheritance when dating landslide boulders. It would be beneficial for many researchers to extend this study by theoretical geometrical sensitivity analyses. For this, the potential distribution of production rates in different landslide geometries and sizes could be approximated. The probability and intensity of inherited nuclide concentrations can then be tested with different failure models.

Finally, this thesis discusses the role of CRSFs in paraglacial landscape development. The detailed study at Mannen in Romsdal valley illustrates the significant impact of repeated rock-slope failures on the pre-historical valley evolution and today's landscape. In the presented model for the local landscape evolution it is suggested that the several metre high stratified drift may have formed as a contact delta. However, no clear evidence for this was found, wherefore it is uncertain how the steep slope on the up-stream side of the several metre high stratified drift was formed. In order to assess this further it could be valuable to find similar settings in other valleys in Norway. A regional analysis of digital data could be supported by field visits to find similarities and differences that may help to reconstruct the genesis of such landforms and the potential impact of CRSFs.

8 Conclusions

The main achievements and conclusions of the research and discussions in this thesis are summarised as follows:

- ^{10}Be dating is a powerful tool for the direct age determination of CRSFs. However, earlier discussed uncertainties of different sources have to be considered when applying this technique.

One significant potentially systematic error source when dating CRSF boulders are inherited ^{10}Be concentrations from pre-failure ^{10}Be production at the surface and at depth. Large rock-avalanche boulders targeted for surface exposure dating are likely to originate from relatively shallow pre-failure depths entailing inherited ^{10}Be concentrations whose dimensions are strongly dependent on the pre-failure exposure and erosional history of the slope. The investigated site in Aysén Fjord, Patagonia, shows that the commonly applied approach of defining inheritance as insignificant when at least three samples of one landform agree within their internal uncertainties is too simplistic. It may result in age overestimations of unknown extent. Largest offsets can be expected for young CRSF events in previously unglaciated areas with low erosion rates.

- Along outcropping sliding surfaces of rock-slope instabilities, TCN dating allows for the reconstruction of sliding histories and an estimation of deformation initiation. For this approach, the computation of shielding and the effect of rock-fall processes are the most significant challenges, while the TCN concentrations at each sample location along such vertical transects can be corrected for pre-exposure production at depth. However, in Norway, the backscarps of most rock-slope instabilities are little affected by rock-fall processes and, as such, produce reliable data.
- The results of age determinations of CRSFs at one site in northern Norway (Rombakstøtta) and two sites in western Norway (Ramnanosi and Mannen) fit well into a previously observed temporal pattern, with a peak of CRSF activity following

8 Conclusions

deglaciation closely. A second period of increased activity can be observed during the mid-late Holocene (Mannen). One of the major factors for the early destabilisation of rock slopes in Norway is likely the debuttreassing effect, while slope destabilisation during the Holocene may be driven by strong climatic and permafrost alterations.

- At Mannen, three to six CRSF events fall into a short time period of a few hundred years about 5 ka ago. After the HTM, permafrost was most likely absent in the Mannen mountain. A climate deterioration connected to high precipitation rates may have added to slope destabilisation, while subsequent failures may be the result of internal stress re-organisation due to first failure(s). Consecutive CRSFs from one slope within a short period of time have been observed in Norway following deglaciation and in historical times. This indicates that extensive post-failure monitoring and stability assessments are mandatory in the future, acknowledging that one failure may be followed by several more.
- The sliding history of actively deforming rock slopes can be determined by TCN dating. In this approach the location of a sample in relation to the pre-slide surface is known, which allows the determination of pre-failure TCN concentrations by sampling the original surface above the sliding scar. At the Revdalsfjellet sites these exposure ages indicate a temporal agreement with the deglaciation history, while at Gamanjunni the surface predates deglaciation by several tens of millennia and at Mannen it postdates general deglaciation by some millennia. This demonstrates the importance of concentration measurements at the pre-failure surface for accurate inheritance corrections along the slope.
- The estimated timing of initial deformation indicates that at Oppstadhornet and Skjeringahaugane P1 sliding started during or shortly after deglaciation, while the rest initiated during or shortly after the HTM. This suggests that the significant increase of ground temperatures and related permafrost degradation may have had an effect on initial slope destabilisation, while glacial debuttreassing and the activation of pre-glacial geological structures lead to late-Pleistocene and early Holocene sliding initiations.
- The sliding patterns along eight analysed slip surfaces in Norway show a similar trend. Initially high sliding rates are generally followed by slower rates. These

patterns may represent the typical strain development connected to progressive rock-slope failure.

Today, the Mannen and Gamanjunni rockslides show a significant increase in sliding rates compared to the Holocene rates, while Revdalsfjellet 2 and Skjeringahaugane P2 accelerated moderately. The instabilities at Mannen, Revdalsfjellet and Gamanjunni are located at or above the lower boundary of alpine permafrost and may therefore be most affected by the ongoing climate change today. At these sites, increased sliding rates could be an indicator for strongly degrading permafrost wherefore special attention should to be given to continued changes in ground temperatures and potentially ice-filled cracks and fractures.

- The results of this thesis illustrate the significance of rock-slope failures for the paraglacial landscape development in Norway. The susceptibility of CRSF deposits to fluvial erosion is limited, wherefore the landforms can be preserved over tens of thousands of years, characterising the landscape. The high density of such deposits together with active rock-slope instabilities in the high relief areas of western and northern Norway testify to the high late-Pleistocene, Holocene and ongoing rock-slope failure activity.
- The Mannen site in Romsdal valley represents a complex post-glacial rock-slope failure history comprising most of the components discussed in this thesis. Here, post-YD deglaciation along the valley was closely followed by several CRSFs coinciding with high rates of isostatic rebound and related relative sea-level lowering. After a time lag of several thousand years and a strong increase in air and ground temperatures, sliding at the Mannen rock-slope instability initiated at about 8 ka. Shortly after the HTM during a climate deterioration with increased precipitation rates, the rock-slope at Mannen failed up to six times within a few hundred years. The deposits of the CRSFs characterise the valley's morphology up to today. This second period of rock-slope failure activity, however, is not visible in the sliding history of the active rock-slope instability. Here, increased sliding may have occurred between 4 and 3 ka, followed by relatively low sliding rates. Measured sliding rates today suggest a strong acceleration compared to Holocene sliding rates and may predict a new period of catastrophic failures, possibly connected to strongly degrading permafrost in the rock slope.

References

- Abramson LW, Lee TS, Sharma S and Boyce GM (2002) *Slope stability and stabilization methods*. John Wiley & Sons, second edition
- Agliardi F, Crosta G and Zanchi A (2001) Structural constraints on deep-seated slope deformation kinematics. *Engineering Geology*, **59**(1-2), 83–102
- Agliardi F, Zanchi A and Crosta GB (2009) Tectonic vs. gravitational morphostructures in the central Eastern Alps (Italy): Constraints on the recent evolution of the mountain range. *Tectonophysics*, **474**(1-2), 250–270
- Ahnert F (2003) *Einführung in die Geomorphologie (Introduction to Geomorphology)*. Verlag Eugen Ulmer (UTB), Stuttgart, third edition, [in German]
- Aizebeokhai AP (2010) 2D and 3D geoelectrical resistivity imaging: Theory and field design. *Scientific Research and Essays*, **5**(23), 3592–3605
- Akçar N, Deline P, Ivy-Ochs S, Alifimov V, Hajdas I, Kubik PW, Christl M and Schlüchter C (2012) The AD 1717 rock avalanche deposits in the upper Ferret Valley (Italy): a dating approach with cosmogenic ^{10}Be . *Journal of Quaternary Science*, **27**(4), 383–392
- Allen SK, Gruber S and Owens IF (2009) Exploring steep bedrock permafrost and its relationship with recent slope failures in the Southern Alps of New Zealand. *Permafrost and Periglacial Processes*, **20**(4), 345–356
- Alley RB (2000) The Younger Dryas cold interval as viewed from central Greenland. *Quaternary science reviews*, **19**(1-5), 213–226
- Alley RB, Mayewski PA, Sowers T, Stuiver M, Taylor KC and Clark PU (1997) Holocene climate instability: A prominent widespread event 8200 years ago. *Geology*, **25**(6), 483–486
- Ambrosi C and Crosta GB (2011) Valley shape influence on deformation mechanisms of rock slopes. In M Jaboyedoff (ed.), *Slope Tectonics*, volume 351, 215–233, Geological Society, London, Special Publications (doi: 10.1144/sp351.12)
- Andersen BG, Bøen F, Nydal R, Rasmussen A and Vallevik PN (1981) Radiocarbon dates of marginal moraines in Nordland, North Norway. *Geografiska Annaler: Series A, Physical Geography*, **63**(3-4), 155–160

References

- Andersen JL, Egholm DL, Knudsen MF, Linge H, Jansen JD, Pedersen VK, Nielsen SB, Tikhomirov D, Olsen J, Fabel D and Xu S (2018) Widespread erosion on high plateaus during recent glaciations in Scandinavia. *Nature Communications*, **9**(1)
- Andersen KK, Azuma N, Barnola JM, Bigler M, Biscaye P, Caillon N, Chappellaz J, Clausen HB, Dahl-Jensen D, Fischer H et al. (2004) High-resolution record of Northern Hemisphere climate extending into the last interglacial period. *Nature*, **431**, 147–151
- Annan AP (2009) Electromagnetic principles of ground penetrating radar. In HM Jol (ed.), *Ground penetrating radar. Theory and applications*, volume 1, 3–40, Elsevier Science: Amsterdam
- Argento DC, Stone JO, Reedy RC and O'Brien K (2015) Physics-based modeling of cosmogenic nuclides part II—key aspects of in-situ cosmogenic nuclide production. *Quaternary Geochronology*, **26**, 44–55
- Arosio D, Longoni L, Mazza F, Papini M and Zanzi L (2013) Freeze-thaw cycle and rockfall monitoring. In *Landslide science and practice*, 385–390, Springer, Berlin-Heidelberg
- Augland LE, Andresen A, Gasser D and Steltenpohl MG (2014) Early Ordovician to Silurian evolution of exotic terranes in the Scandinavian Caledonides of the Ofoten–Troms area—terrane characterization and correlation based on new U–Pb zircon ages and Lu–Hf isotopic data. *Geological Society, London, Special Publications*, **390**(1), 655–678
- Austigard B (2016) *Årbok 2016: Naturkatastrofer*, chapter Digerura i Eikesdalen - Omkring ei datering, 120–143. Romsdalsmuseet, [in Norwegian]
- Badger TC (2002) Fracturing within anticlines and its kinematic control on slope stability. *Environmental & Engineering Geoscience*, **8**(1), 19–33
- Bakke J, Dahl SO and Nesje A (2005) Lateglacial and early Holocene palaeoclimatic reconstruction based on glacier fluctuations and equilibrium-line altitudes at northern Folgefonna, Hardanger, western Norway. *Journal of Quaternary Science: Published for the Quaternary Research Association*, **20**(2), 179–198
- Balco G (2014) Simple computer code for estimating cosmic-ray shielding by oddly shaped objects. *Quaternary Geochronology*, **22**, 175–182
- Ballantyne CK (2002a) A general model of paraglacial landscape response. *The Holocene*, **12**(3), 371–376
- Ballantyne CK (2002b) Paraglacial geomorphology. *Quaternary Science Reviews*, **21**(18–19), 1935–2017
- Ballantyne CK (2003) Paraglacial landform succession and sediment storage in deglaciated mountain valleys: theory and approaches to calibration (with 6 figures). *Zeitschrift für Geomorphologie, Supplementbände*, **132**, 1–18

- Ballantyne CK and Stone JO (2004) The Beinn Alligin rock avalanche, NW Scotland: cosmogenic ^{10}Be dating, interpretation and significance. *The Holocene*, **14**(3), 448–453
- Ballantyne CK and Stone JO (2013) Timing and periodicity of paraglacial rock-slope failures in the Scottish Highlands. *Geomorphology*, **186**, 150–161
- Ballantyne CK and Stone JO (2015) Trimlines, blockfields and the vertical extent of the last ice sheet in southern Ireland. *Boreas*, **44**(2), 277–287
- Ballantyne CK, Stone JO and Fifield LK (1998) Cosmogenic Cl-36 dating of postglacial landsliding at the Storr, Isle of Skye, Scotland. *The Holocene*, **8**(3), 347–351
- Ballantyne CK, Sandeman GF, Stone JO and Wilson P (2014) Rock-slope failure following Late Pleistocene deglaciation on tectonically stable mountainous terrain. *Quaternary Science Reviews*, **86**, 144–157
- Bargel TH (2003) *Quaternary geological mapping of Central Fennoscandia and Nordland: deglaciation, deposition, stratigraphy and applications*. Ph.D. thesis, Norwegian University of Science and Technology (NTNU)
- Bargel TH, Boyd R and Dahl R (1995) *Geologien i Narvik - en vandring i tid og rom (The geology of the Narvik district - a journey in time and space)*. Norges Geologiske Undersøkelse, Trondheim
- Barton N (2013) Shear strength criteria for rock, rock joints, rockfill and rock masses: Problems and some solutions. *Journal of Rock Mechanics and Geotechnical Engineering*, **5**(4), 249–261
- Barton N and Choubey V (1977) The shear strength of rock joints in theory and practice. *Rock mechanics*, **10**(1-2), 1–54
- Bellwald B, Hjelstuen BO, Sejrup HP, Stokowy T and Kuvås J (2018) Holocene mass movements in west and mid-Norwegian fjords and lakes. *Marine Geology*, **407**, 192–212
- Bentley MJ, Fogwill CJ, Kubik PW and Sugden DE (2006) Geomorphological evidence and cosmogenic $^{10}\text{Be}/^{26}\text{Al}$ exposure ages for the Last Glacial Maximum and deglaciation of the Antarctic Peninsula Ice Sheet. *Geological Society of America Bulletin*, **118**(9-10), 1149–1159
- Berthling I and Etzelmüller B (2011) The concept of cryo-conditioning in landscape evolution. *Quaternary Research*, **75**(2), 378–384
- Blikra LH (1999) Rock avalanches, gravitational faulting and its potential palaeoseismic cause. In J Dehls and O Olesen (eds.), *Neotectonics in Norway, Annual Technical Report 1998*, Norges Geologiske Undersøkelse, NGU Report 99.007
- Blikra LH and Anda E (1997) Large rock avalanches in Møre og Romsdal, western Norway. *NGU Bulletin*, **433**, 44–45

References

- Blikra LH and Christiansen HH (2014) A field-based model of permafrost-controlled rock-slide deformation in northern Norway. *Geomorphology*, **208**, 34–49
- Blikra LH and Kristensen L (2013) Monitoring concepts and requirements for large rock-slides in Norway. In C Margottini, P Canuti and K Sassa (eds.), *Landslide Science and Practice*, 193–200, Springer, Berlin, Heidelberg
- Blikra LH and Nemeč W (1998) Postglacial colluvium in western Norway: depositional processes, facies and palaeoclimatic record. *Sedimentology*, **45**(5), 909–959
- Blikra LH, Longva O and Sletten K (2000) Palaeoseismic activity and gravitational-slope failures. In O Olesen (ed.), *Neotectonics in Norway, Final report*, Norges Geologiske Undersøkelse, NGU Report 2000.02
- Blikra LH, Braathen A, Anda E, Stalsberg K and Longva O (2002) Rock avalanches, gravitational bedrock fractures and neotectonic faults onshore northern West Norway: Examples, regional distribution and triggering mechanisms. NGU Report 2002.016, Norges Geologiske Undersøkelse
- Blikra LH, Eiken T, Henderson I and Venvik-Ganerød G (2006a) Forprosjekt fjellskred i Troms - Status 2005. NGU Report 2006.040, Norges Geologiske Undersøkelse, [in Norwegian]
- Blikra LH, Longva O, Braathen A, Anda E, Dehls JF and Stalsberg K (2006b) Rock slope failures in Norwegian fjord areas: examples, spatial distribution and temporal pattern. In SG Evans, GS Mugnozza, A Strom and RL Hermanns (eds.), *Landslides from Massive Rock Slope Failure*, volume 49 of *NATO Science Series*, 475–496, Springer, Dordrecht
- Blikra LH, Henderson I and Nordvik T (2009) Faren for fjellskred fra Nordnesfjellet i Lyn-genfjorden, Troms. NGU Report 2009.026, Norges Geologiske Undersøkelse, [in Norwegian]
- Blikra LH, Hermanns R and Berg H (2013a) De ustabile fjellsidene i Stampa - Flåm, Aurland kommune: Sammenstilling, scenario, risiko og anbefalinger. NVE Report 30.2013, Norges vassdrags- og energidirektorat, [in Norwegian]
- Blikra LH, Kristensen L and Lovisolo M (2013b) Subsurface monitoring of large rockslides in Norway: a key requirement for early warning. *Ital. J. Eng. Geol. Environ*, **6**, 307–314
- Blikra LH, Majala G, Anda E, Berg H, Eikenæs O, Helgås G, Oppikofer T, Hermanns RL and Böhme M (2016) Fare- og risikoklassifisering av ustabile fjellparti - Faresoner, arealhåndtering og tiltak. NVE Report 77-2016, Norges Energi og Vassdrags direktoratet, [in Norwegian]
- Bøe R, Longva O, Lepland A, Blikra LH, Sonstegaard E, Hadlidason H, Bryn P and Lien R (2004) Postglacial mass movements and their causes in fjords and lakes in western Norway. *Norsk Geologisk Tidsskrift*, **84**(1), 35–56

- Böhme M, Hermanns RL, Oppikofer T, Fischer L, Bunkholt HSS, Eiken T, Pedrazzini A, Derron MH, Jaboyedoff M, Blikra LH and Nilsen B (2013) Analyzing complex rock slope deformation at Stampa, western Norway, by integrating geomorphology, kinematics and numerical modeling. *Engineering Geology*, **154**, 116–130
- Böhme M, Oppikofer T, Longva O, Jaboyedoff M, Hermanns RL and Derron MH (2015a) Analyses of past and present rock slope instabilities in a fjord valley: Implications for hazard estimations. *Geomorphology*, **248**, 464–474
- Böhme M, Yugsi Molina F, Dehls J and Hermanns RL (2015b) Fare- og risikoklassifisering av det ustabile fjellpartiet Storhaugen block i Manndalen, Troms. NGU Report 2015.050, Norges Geologiske Undersøkelse, Trondheim, [in Norwegian]
- Böhme M, Bunkholt H, Dehls J, Oppikofer T, Hermanns RL, Dalsegg E, Kristensen L, Lauknes TR and Eriksen HØ (2016) Geologisk modell og fare- og risikoklassifisering av det ustabile fjellpartiet Gamanjunni 3 i Manndalen, Troms. NGU report 2016.031, Norges Geologiske Undersøkelse, Trondheim, [in Norwegian]
- Böhme M, Hermanns RL, Gosse J, Hilger P, Eiken T, Lauknes TR and Dehls JF (2019) Comparison of monitoring data with paleo-slip rates: Cosmogenic nuclide dating detects acceleration of a rockslide. *Geology*
- Booth AM, Dehls J, Eiken T, Fischer L, Hermanns RL and Oppikofer T (2015) Integrating diverse geologic and geodetic observations to determine failure mechanisms and deformation rates across a large bedrock landslide complex: the Osmundneset landslide, Sogn og Fjordane, Norway. *Landslides*, **12**(4), 745–756
- Borchers B, Marrero S, Balco G, Caffee M, Goehring B, Lifton N, Nishiizumi K, Phillips F, Schaefer J and Stone J (2016) Geological calibration of spallation production rates in the CRONUS-Earth project. *Quaternary Geochronology*, **31**, 188–198
- Borge AF, Westermann S, Solheim I and Etzelmüller B (2017) Strong degradation of palsas and peat plateaus in Northern Norway during the last 60 years. *The Cryosphere*, **11**, 1–16
- Boyd R, Mikalsen T, Minsaas O and Zwaan KB (1984) Storfjord. Berggrunnskart; Storfjord; 16334; 1:50 000; sort/hvitt;. Norges geologiske undersøkelse (NGU)-distribution, [in Norwegian]
- Braathen A, Blikra LH, Berg SS and Karlsen F (2004) Rock-slope failures of Norway, type, geometry deformation mechanisms and stability. *Norsk Geologisk Tidsskrift*, **84**(1), 67–88
- Břežný M, Pánek T, Lenart J, Zondervan A and Braucher R (2018) ^{10}Be dating reveals pronounced Mid-to Late Holocene activity of deep-seated landslides in the highest part of the Czech Flysch Carpathians. *Quaternary Science Reviews*, **195**, 180–194

References

- Brideau MA, Yan M and Stead D (2009) The role of tectonic damage and brittle rock fracture in the development of large rock slope failures. *Geomorphology*, **103**(1), 30–49
- Brook EJ, Nesje A, Lehman SJ, Raisbeck GM and Yiou F (1996) Cosmogenic nuclide exposure ages along a vertical transect in western Norway: implications for the height of the Fennoscandian ice sheet. *Geology*, **24**(3), 207–210
- Brown J, Ferrians Jr OJ, Heginbottom JA and Melnikov ES (1997) *Circum-Arctic map of permafrost and ground-ice conditions*. US Geological Survey, Reston
- Brown SR (1987) Fluid flow through rock joints: the effect of surface roughness. *Journal of Geophysical Research: Solid Earth*, **92**(B2), 1337–1347
- Bunkholt H, Nordahl B, Hermanns RL, Oppikofer T, Fischer L, Blikra LH, Anda E, Dahle H and Sætre S (2013a) Database of unstable rock slopes of Norway. In C Margottini, P Canuti and K Sassa (eds.), *Landslide science and practice*, 423–428, Springer, Berlin, Heidelberg
- Bunkholt H, Otterå S, Yugsi Molina FX, Hermanns RL, Dehls J, Osmundsen PT, Redfield T, Eiken T and Böhme M (2013b) Undersøkelser av ustabile fjellpartier i Troms - Status og planer etter feltarbeid 2011 og 2012. NGU Report 2013.021, Norges Geologiske Underøkelse, Trondheim, [in Norwegian]
- Caldenius CC (1932) Las Glaciaciones Cuaternarias en la Patagonia y Tierra del Fuego. *Geographiska Annaler*, **14**, 1–164, ISSN 2001-4422
- Cembrano J, Lavenu A, Reynolds P, Arancibia G, López G and Sanhueza A (2002) Late Cenozoic transpressional ductile deformation north of the Nazca–South America–Antarctica triple junction. *Tectonophysics*, **354**(3-4), 289–314
- Chigira M, Wu X, Inokuchi T and Wang G (2010) Landslides induced by the 2008 Wenchuan earthquake, Sichuan, China. *Geomorphology*, **118**(3-4), 225–238
- Christiansen HH, Etzelmüller B, Isaksen K, Juliussen H, Farbrøt H, Humlum O, Johansson M, Ingeman-Nielsen T, Kristensen L, Hjort J et al. (2010) The thermal state of permafrost in the nordic area during the international polar year 2007–2009. *Permafrost and Periglacial Processes*, **21**(2), 156–181
- Church M and Ryder JM (1972) Paraglacial sedimentation: a consideration of fluvial processes conditioned by glaciation. *Geological Society of America Bulletin*, **83**(10), 3059–3072
- Clark JI and Phillips R (2003) Centrifuge modelling of frost heave of arctic gas pipelines. In *Proceedings of the 8th International Permafrost Conference, Zurich, Switzerland*, 21–24

- Clauser C and Huenges E (1995) Thermal conductivity of rocks and minerals. In TJ Ahrens (ed.), *Rock Physics & Phase Relations*, volume 3, 105–126, American Geophysical Union
- Cockburn HAP and Summerfield MA (2004) Geomorphological applications of cosmogenic isotope analysis. *Progress in Physical Geography*, **28**, 1–42
- Codilean AT (2006) Calculation of the cosmogenic nuclide production topographic shielding scaling factor for large areas using DEMs. *Earth Surface Processes and Landforms*, **31**(6), 785–794
- Codilean AT, Munack H, Cohen TJ, Saktura WM, Gray A and Mudd SM (2018) OCTOPUS: An open cosmogenic isotope and luminescence database. *Earth System Science Data Discussions*, **2018**, 1–23
- Colgan PM, Bierman PR, Mickelson DM and Caffee M (2002) Variation in glacial erosion near the southern margin of the Laurentide Ice Sheet, south-central Wisconsin, USA: Implications for cosmogenic dating of glacial terrains. *Geological Society of America Bulletin*, **114**(12), 1581–1591
- Conrad O, Bechtel B, Bock M, Dietrich H, Fischer E, Gerlitz L, Wehberg J, Wichmann V and Böhner J (2015) System for automated geoscientific analyses (SAGA) v.2.1.4. *Geoscientific Model Development*, **8**(7), 1991–2007
- Corfu F, Andersen TB and Gasser D (2014) The Scandinavian Caledonides: main features, conceptual advances and critical questions. *Geological Society, London, Special Publications*, **390**, 9–43
- Corner G (2004) Storfjord. Kwartærgeologisk kart. Norges Geologiske Undersøkelse (NGU)-distribution
- Corner GD (2006) A Transgressive-Regressive Model of Fjord-Valley Fill: Stratigraphy, Facies and Depositional Controls. In *Incised Valleys in Time and Space*, 85, SEPM Special Publication
- Cossart E, Braucher R, Fort M, Bourlès DL and Carcaillet J (2008) Slope instability in relation to glacial debuttressing in alpine areas (Upper Durance catchment, southeastern France): Evidence from field data and ^{10}Be cosmic ray exposure ages. *Geomorphology*, **95**(1-2), 3–26
- Crosta GB and Agliardi F (2003) Failure forecast for large rock slides by surface displacement measurements. *Canadian Geotechnical Journal*, **40**(1), 176–191
- Crosta GB, Frattini P and Fusi N (2007) Fragmentation in the Val Pola rock avalanche, Italian alps. *Journal of Geophysical Research: Earth Surface*, **112**(F1)

References

- Dabrowski M, Krotkiewski M and Schmid DW (2008) MILAMIN: MATLAB-based finite element method solver for large problems. *Geochemistry, Geophysics, Geosystems*, **9**(4), 1–24
- Dahl SO and Nesje A (1994) Holocene glacier fluctuations at hardangerjøkulen, central-southern Norway: a high-resolution composite chronology from lacustrine and terrestrial deposits. *The Holocene*, **4**(3), 269–277
- Dahl SO, Nesje A, Lie Ø, Fjordheim K and Matthews JA (2002) Timing, equilibrium-line altitudes and climatic implications of two early-Holocene glacier readvances during the Erdalen Event at Jostedalbreen, western Norway. *The Holocene*, **12**(1), 17–25
- Dahle H, Saintot A, Blikra LH and Anda E (2010) Geofagleg oppfølging av ustabil fjellparti ved Mannen i Romsdalen. NGU Report 2010.022, Norges Geologiske Undersøkelse, [in Norwegian]
- Dahlin T (2001) The development of DC resistivity imaging techniques. *Computers & Geosciences*, **27**(9), 1019–1029
- Darvill CM (2013) Cosmogenic nuclide analysis. In SJ Cook, LE Clarke and JM Nield (eds.), *Geomorphological Techniques*, chapter 4.2.10, British Society for Geomorphology, London, UK
- Davies MCR, Hamza O and Harris C (2001) The effect of rise in mean annual temperature on the stability of rock slopes containing ice-filled discontinuities. *Permafrost and Periglacial Processes*, **12**(1), 137–144
- Davis PT, Bierman PR, Marsella KA, Caffee MW and Southon JR (1999) Cosmogenic analysis of glacial terrains in the eastern Canadian Arctic: a test for inherited nuclides and the effectiveness of glacial erosion. *Annals of Glaciology*, **28**, 181–188
- De Blasio FV (2011) Friction, cohesion, and slope stability. In *Introduction to the Physics of Landslides*, chapter 2, 23–52, Springer, Dordrecht
- De Pascale GP, Pollard WH and Williams KK (2008) Geophysical mapping of ground ice using a combination of capacitive coupled resistivity and ground-penetrating radar, Northwest Territories, Canada. *Journal of Geophysical Research: Earth Surface*, **113**(F2)
- Delunel R, Bourlès DL, van der Beek PA, Schlunegger F, Leya I, Masarik J and Paquet E (2014) Snow shielding factors for cosmogenic nuclide dating inferred from long-term neutron detector monitoring. *Quaternary Geochronology*, **24**, 16–26
- Denton GH, Lowell TV, Heusser CJ, Schluchter C, Andersen BG, Heusser LE, Moreno PI and Marchant DR (1999) Geomorphology, Stratigraphy, and Radiocarbon Chronology of Llanquihue Drift in the Area of the Southern Lake District, Seno Reloncavi, and Isla Grande de Chiloe, Chile. In BG Andersen, GH Denton and VL Lowell (eds.),

- Glacial and Vegetational History of the Southern Lake District of Chile*, volume 81 of *Geographiska Annaler*, 167–229, Taylor & Francis, on behalf of the Swedish Society for Anthropology and Geography
- Derron MH, Jaboyedoff M and Blikra LH (2005) Preliminary assessment of rockslide and rockfall hazards using a DEM (Oppstadhornet, Norway). *Natural Hazards and Earth System Science*, **5**(2), 285–292
- Domaas U, Rosenvold BS, Blikra LH, Johansen H, Grimstad E, Sørli JE, Gunleiksrud O, Engen A and Lægveid O (2002) Studie av fjellskred og dalsidestabilitet i fyllittområder (Study of rockslides and valley-side-stability in phyllite regions). NRF Report 20001132–2, Norges Forskningsråd, [in Norwegian]
- Dorman LI, Valdés-Galicia JF and Dorman IV (1999) Numerical simulation and analytical description of solar neutron transport in the Earth's atmosphere. *Journal of Geophysical Research: Space Physics*, **104**(A10), 22417–22426
- Dorman LI, Villaresi G, Iucci N, Parisi M, Tyasto MI, Danilova OA and Ptitsyna NG (2000) Cosmic ray survey to Antarctica and coupling functions for neutron component near solar minimum (1996–1997): 3. Geomagnetic effects and coupling functions. *Journal of Geophysical Research: Space Physics*, **105**(A9), 21047–21056
- Dortch JM, Owen LA, Haneberg WC, Caffee MW, Dietsch C and Kamp U (2009) Nature and timing of large landslides in the Himalaya and Transhimalaya of northern India. *Quaternary Science Reviews*, **28**(11-12), 1037–1054
- Dunai T (2001) Influence of secular variation of the geomagnetic field on production rates of in situ produced cosmogenic nuclides. *Earth and Planetary Science Letters*, **193**(1-2), 197–212
- Dunai TJ (2010) *Cosmogenic nuclides: principles, concepts and applications in the earth surface sciences*. Cambridge University Press
- Dunne J, Elmore D and Muzikar P (1999) Scaling factors for the rates of production of cosmogenic nuclides for geometric shielding and attenuation at depth on sloped surfaces. *Geomorphology*, **27**(1-2), 3–11
- Dyrrdal AV, Skaugen T, Stordal F and Førland EJ (2016) Estimating extreme areal precipitation in Norway from a gridded dataset. *Hydrological Sciences Journal*, **61**(3), 483–494
- Easterling DR, Evans JL, Groisman PY, Karl TR, Kunkel KE and Ambenje P (2000) Observed variability and trends in extreme climate events: A brief review. *Bulletin of the American Meteorological Society*, **81**, 417–425
- Eberhardt E, Stead D and Coggan JS (2004) Numerical analysis of initiation and progressive failure in natural rock slopes—the 1991 Randa rockslide. *International Journal of Rock Mechanics and Mining Sciences*, **41**, 69–87

References

- Ehlen J (2002) Some effects of weathering on joints in granitic rocks. *Catena*, **49**(1-2), 91–109
- Eidsvig UM, Medina-Cetina Z, Kveldsvik V, Glimsdal S, Harbitz CB and Sandersen F (2011) Risk assessment of a tsunamigenic rockslide at Åknes. *Natural hazards*, **56**(2), 529–545
- Eilertsen R, Corner GD, Aasheim O, Andreassen K, Kristofferson Y and Ystborg H (2006) Valley-fill Stratigraphy and Evolution of the Målselv Fjord Valley, Northern Norway. In *Incised valleys in time and space*, number 85 in Special publication / Society for Sedimentary Geology, SEPM, Tulsa, Okla
- Eilertsen RS, Corner GD, Aasheim O and Hansen L (2011) Facies characteristics and architecture related to palaeodepth of Holocene fjord-delta sediments: Facies characteristics and architecture. *Sedimentology*, **58**(7), 1784–1809
- Eriksen HØ, Lauknes TR, Larsen Y, Corner GD, Bergh SG, Dehls J and Kierulf HP (2017) Visualizing and interpreting surface displacement patterns on unstable slopes using multi-geometry satellite sar interferometry (2d insar). *Remote sensing of environment*, **191**, 297–312
- Etzelmüller B, Berthling I and Sollid JL (2003) Aspects and concepts on the geomorphological significance of Holocene permafrost in southern Norway. *Geomorphology*, **52**(1-2), 87–104
- Etzelmüller B, Westermann S, Hermanns RL, Larsen JO and Krautblatter M (2014) CryoWALL - Steep permafrost slopes in Norway, unpublished project proposal for a researcher project in the program KLIMAFORSK (Research Council of Norway)
- Evans SG (2006) Single-event landslides resulting from massive rock slope failure: characterising their frequency and impact on society. In SG Evans, G Scarascia Mugnozza, A Strom and RL Hermanns (eds.), *Landslides from Massive Rock Slope Failure*, 53–73, Springer, Dordrecht
- Evans SG and Clague JJ (1994) Recent climatic change and catastrophic geomorphic processes in mountain environments. *Geomorphology*, **10**(1-4), 107–128
- Evans SG and DeGraff JV (2002) *Catastrophic landslides: effects, occurrence, and mechanisms*, volume 15. Geological Society of America
- Evans SG, Mugnozza GS, Strom A, R H, Ischuk A and Vinnichenko S (2006) Landslides from Massive Rock Slope Failure and Associated Phenomena. In SG Evans, GS Mugnozza, A Strom and RL Hermanns (eds.), *Landslides from Massive Rock Slope Failure*, 53–73, Springer, Dordrecht
- Evans SG, Guthrie RH, Roberts NJ and Bishop NF (2007) The disastrous 17 February 2006 rockslide-debris avalanche on Leyte Island, Philippines: a catastrophic landslide in tropical mountain terrain. *Natural Hazards and Earth System Science*, **7**(1), 89–101

- Færevåg Å (2013) *Predicting Snow Density*. Master's thesis, Norwegian University of Science and Technology, Trondheim
- Falae PO, Kanungo DP, Chauhan PKS and Dash RK (2019) Recent trends in application of electrical resistivity tomography for landslide study. In J Chattopadhyay, R Singh and O Prakash (eds.), *Renewable Energy and its Innovative Technologies*, 195–204, Springer, Singapore
- Falaschi D, Tadono T and Masiokas M (2015) Rock glaciers in the Patagonian Andes: an inventory for the Monte San Lorenzo (Cerro Cochrane) Massif, 47° S. *Geografiska Annaler: Series A, Physical Geography*, **97**(4), 769–777
- Farbrot H, Hipp TF, Etzelmüller B, Isaksen K, Ødegård RS, Schuler TV and Humlum O (2011) Air and ground temperature variations observed along elevation and continentality gradients in southern Norway. *Permafrost and Periglacial Processes*, **22**(4), 343–360
- Farbrot H, Isaksen K, Etzelmüller B and Gislås K (2013) Ground thermal regime and permafrost distribution under a changing climate in northern Norway. *Permafrost and Periglacial Processes*, **24**(1), 20–38
- Fenton CR, Hermanns RL, Blikra LH, Kubik PW, Bryant C, Niedermann S, Meixner A and Goethals MM (2011) Regional ¹⁰Be production rate calibration for the past 12ka deduced from the radiocarbon-dated Grøtlandsura and Russenes rock avalanches at 69° N, Norway. *Quaternary Geochronology*, **6**(5), 437–452
- Fischer L, Kääh A, Huggel C and Noetzli J (2006) Geology, glacier retreat and permafrost degradation as controlling factors of slope instabilities in a high-mountain rock wall: the Monte Rosa east face. *Natural Hazards and Earth System Science*, **6**(5), 761–772
- Fischer L, Amann F, Moore JR and Huggel C (2010) Assessment of periglacial slope stability for the 1988 Tschierwa rock avalanche (Piz Morteratsch, Switzerland). *Engineering Geology*, **116**(1-2), 32–43
- Fischer L, Purves RS, Huggel C, Noetzli J and Haeberli W (2012) On the influence of topographic, geological and cryospheric factors on rock avalanches and rockfalls in high-mountain areas. *Natural Hazards and Earth System Science*, **12**(1), 241–254
- Frauenfelder R, Isaksen K, Nötzli J and Lato MJ (2016) Ground thermal and geomechanical conditions in a permafrost-affected high-latitude rockslide site (Polvartinden, Northern Norway). *The Cryosphere Discussions*, 1–31
- Fukui K, Fujii Y, Ageta Y and Asahi K (2007) Changes in the lower limit of mountain permafrost between 1973 and 2004 in the Khumbu Himal, the Nepal Himalayas. *Global and Planetary Change*, **55**(4), 251–256
- Furseth A (1985) *Dommedagsfjellet - Tafjord 1934*. Gyldendal Norsk Forlag A/S, [in Norwegian]

References

- Ganerød GV, Grøneng G, Rønning JS, Dalsegg E, Elvebakk H, Tønnesen JF, Kveldsvik V, Eiken T, Blikra LH and Braathen A (2008) Geological model of the Åknes rockslide, western Norway. *Engineering Geology*, **102**(1-2), 1–18
- Gasse F, Fontes JC, Van Campo E and Wei K (1996) Holocene environmental changes in Bangong Co basin (Western Tibet). Part 4: discussion and conclusions. *Palaeogeography, Palaeoclimatology, Palaeoecology*, **120**(1-2), 79–92
- Geertsema M, Clague JJ, Schwab JW and Evans SG (2006) An overview of recent large catastrophic landslides in northern British Columbia, Canada. *Engineering Geology*, **83**(1-3), 120–143
- Ghirotti M, Martin S and Genevois R (2011) The Celentino deep-seated gravitational slope deformation (DSGSD): structural and geomechanical analyses (Peio Valley, NE Italy). In M Jaboyedoff (ed.), *Slope Tectonics*, volume 351, 235–251, Geological Society, London, Special publications
- Gisnås K, Etzelmüller B, Lussana C, Hjort J, Sannel ABK, Isaksen K, Westermann S, Kuhry P, Christiansen HH, Frampton A et al. (2017) Permafrost map for Norway, Sweden and Finland. *Permafrost and Periglacial Processes*, **28**(2), 359–378
- Gisnås K, Etzelmüller B, Farbroth H, Schuler TV and Westermann S (2013) CryoGRID 1.0: Permafrost Distribution in Norway estimated by a Spatial Numerical Model. *Permafrost and Periglacial Processes*, **24**(1), 2–19
- Glasser NF, Harrison S, Winchester V and Aniya M (2004) Late Pleistocene and Holocene palaeoclimate and glacier fluctuations in Patagonia. *Global and planetary change*, **43**(1-2), 79–101
- Glastonbury J and Fell R (2010) Geotechnical characteristics of large rapid rock slides. *Canadian Geotechnical Journal*, **47**(1), 116–132
- Goehring BM, Lohne ØS, Mangerud J, Svendsen JI, Gyllencreutz R, Schaefer J and Finkel R (2012) Late glacial and holocene ¹⁰Be production rates for western Norway. *Journal of Quaternary Science*, **27**(1), 89–96
- Goodrich LE (1982) The influence of snow cover on the ground thermal regime. *Canadian geotechnical journal*, **19**(4), 421–432
- Gosse JC and Phillips F (2001) Terrestrial in situ cosmogenic nuclides: theory and application. *Quaternary Science Reviews*, **20**, 1475–1560
- Grimstad E and Nesdal S (1990) *Loen rockslides. A historical review*, volume 182. Norwegian Geotechnical Institute (NGI) Publication
- Grämiger LM, Moore JR, Gischig VS, Ivy-Ochs S and Loew S (2017) Beyond debuttressing: Mechanics of paraglacial rock slope damage during repeat glacial cycles. *Journal of Geophysical Research: Earth Surface*, **122**(4), 1004–1036

- Gruber S and Haeberli W (2007) Permafrost in steep bedrock slopes and its temperature-related destabilization following climate change. *Journal of Geophysical Research*, **112**(F2)
- Guhathakurta P, Pai DS and Rajeevan MN (2017) Variability and trends of extreme rainfall and rainstorms. In M Rajeevan and S Nayak (eds.), *Observed Climate Variability and Change over the Indian Region*, 37–49, Springer Geology. Springer, Singapore
- Gunzburger Y, Merrien-Soukatchoff V and Guglielmi Y (2005) Influence of daily surface temperature fluctuations on rock slope stability: case study of the Rochers de Valabres slope (France). *International Journal of Rock Mechanics and Mining Sciences*, **42**, 331–349
- Guralnik B, Matmon A, Avni Y and Fink D (2010) 10be exposure ages of ancient desert pavements reveal Quaternary evolution of the Dead Sea drainage basin and rift margin tilting. *Earth and Planetary Science Letters*, **290**(1-2), 132–141
- Hadley JB (1978) Madison Canyon rockslide, Montana, USA. In B Voight (ed.), *Rockslides and avalanches*, volume 14, 167–180, Elsevier, Amsterdam
- Haerberli W (1992) Construction, environmental problems and natural hazards in periglacial mountain belts. *Permafrost and periglacial processes*, **3**(2), 111–124
- Haerberli W, Noetzli J, Arenson L, Delaloye R, Gärtner-Roer I, Gruber S, Isaksen K, Kneisel C, Krautblatter M and Phillips M (2010) Mountain permafrost: development and challenges of a young research field. *Journal of Glaciology*, **56**(200), 1043–1058
- Hales T and Roering JJ (2007) Climatic controls on frost cracking and implications for the evolution of bedrock landscapes. *Journal of Geophysical Research: Earth Surface*, **112**(F2)
- Harris C, Arenson LU, Christiansen HH, Etzelmüller B, Frauenfelder R, Gruber S, Haerberli W, Hauck C, Hölzle M, Humlum O, Isaksen K, Kääb A, Kern-Lütschg MA, Lehnig M, Matsuoka N, Murton JB, Nötzli J, Phillips M, Ross N, Seppälä M, Springman SM and Vonder Mühll D (2009) Permafrost and climate in Europe: Monitoring and modelling thermal, geomorphological and geotechnical responses. *Earth-Science Reviews*, **92**(3-4), 117–171
- Hasler A, Gruber S and Beutel J (2012) Kinematics of steep bedrock permafrost. *Journal of Geophysical Research: Earth Surface*, **117**(F1)
- Hauck C, Isaksen K, Vonder Mühll D and Sollid JL (2004) Geophysical surveys designed to delineate the altitudinal limit of mountain permafrost: an example from Jotunheimen, Norway. *Permafrost and Periglacial Processes*, **15**(3), 191–205
- He F (2011) *Simulating transient climate evolution of the last deglaciation with CCSM3*. Ph.D. thesis, University of Wisconsin-Madison

References

- Heckmann T, Haas F, Wichmann V and Morche D (2008) Sediment budget and morphodynamics of an alpine talus cone on different timescales. *Zeitschrift für Geomorphologie, Supplementary Issues*, **52**(1), 103–121
- Heisinger B, Lal D, Jull A, Kubik P, Ivy-Ochs S, Knie K and Nolte E (2002a) Production of selected cosmogenic radionuclides by muons: 2. capture of negative muons. *Earth and Planetary Science Letters*, **200**(3-4), 357–369
- Heisinger B, Lal D, Jull A, Kubik P, Ivy-Ochs S, Neumaier S, Knie K, Lazarev V and Nolte E (2002b) Production of selected cosmogenic radionuclides by muons. *Earth and Planetary Science Letters*, **200**(3-4), 345–355
- Henderson I and Saintot A (2007) Fjellskred undersøkelser i Møre og Romsdal. NGU Report 2007.043, Norges Geologiske Undersøkelse, Trondheim, [in Norwegian]
- Henderson I, Saintot A, Böhme M and Henriksen H (2008) Kartlegging av mulig ustabile fjellpartier, Sogn og Fjordane. NGU Report 2008.026, Norges Geologiske Undersøkelse, Trondheim, [in Norwegian]
- Henderson I, Osmundsen PT and Redfield T (2010) ROS Fjellskred i Troms: Status og planer 2010. NGU Report 2010.021, Norges Geologiske Undersøkelse, Trondheim, [in Norwegian]
- Hermanns RL and Longva O (2012) Rapid rock-slope failures. In JJ Clague and D Stead (eds.), *Landslides*, 59–70, Cambridge University Press, Cambridge
- Hermanns RL and Strecker MR (1999) Structural and lithological controls on large Quaternary rock avalanches (sturzstroms) in arid northwestern Argentina. *Geological Society of America Bulletin*, **111**(6), 934–948
- Hermanns RL, Trauth MH, Niedermann S, McWilliams M and Strecker MR (2000) Tephrochronologic constraints on temporal distribution of large landslides in northwest Argentina. *The Journal of Geology*, **108**(1), 35–52
- Hermanns RL, Niedermann S, Garcia AV, Sosa Gomez J and Strecker MR (2001) Neotectonics and catastrophic failure of mountain fronts in the southern intra-Andean Puna Plateau, Argentina. *Geology*, **29**(7), 619–622
- Hermanns RL, Niedermann S, Ivy-Ochs S and Kubik PW (2004) Rock avalanching into a landslide-dammed lake causing multiple dam failure in Las Conchas valley (NW Argentina)? Evidence from surface exposure dating and stratigraphic analyses. *Landslides*, **1**(2), 113–122
- Hermanns RL, Blikra LH, Naumann M, Nilsen B, Panthi KK, Stromeyer D and Longva O (2006) Examples of multiple rock-slope collapses from Köfels (Ötz valley, Austria) and western Norway. *Engineering Geology*, **83**(1-3), 94–108

- Hermanns RL, Fischer L, Oppikofer T, Böhme M, Dehls JF, Henriksen H, Booth A, Eilertsen R, Longva O and Eiken T (2011) Mapping of unstable and potentially unstable rock slopes in Sogn og Fjordane (work report 2008-2010). NGU Report 2011.055, Norges Geologiske Undersøkelse, Trondheim
- Hermanns RL, Hansen L, Sletten K, Böhme M, Bunkholt HSS, Dehls JF, Eilertsen RS, Fischer L, L'Heureux JS, Høgaas F, Nordahl B, Oppikofer T, Rubensdotter L, Solberg IL, Stalsberg K and Yugsi Molina FX (2012a) Systematic geological mapping for landslide understanding in the Norwegian context. In E Eberhardt, C Froese, K Turner and S Leroueil (eds.), *Landslides and Engineered Slopes: Protecting Society through Improved Understanding*, 2050, Taylor & Francis Group, London
- Hermanns RL, Redfield TF, Bunkholt HSS, Fischer L and Oppikofer T (2012b) Cosmogenic nuclide dating of slow moving rockslides in Norway in order to assess long-term slide velocities. In EB Eberhardt, C Froese, AK Turner and S Leroueil (eds.), *Landslides and engineered slopes: protecting society through improved understanding: Proceedings of the 11th International and 2nd North American Symposium on Landslides and Engineered Slopes, Banff, Canada, 3-8 June 2012*, 849–854, Taylor & Francis, London
- Hermanns RL, Dahle H, Bjerke PL, Crosta GB, Anda E, Blikra LH, Saintot A and Longva O (2013a) Rockslide Dams in Møre og Romsdal County, Norway. In C Margottini, P Canuti and K Sassa (eds.), *Landslide Science and Practice: Volume 6: Risk Assessment, Management and Mitigation*, 3–12, Springer Berlin Heidelberg, Berlin, Heidelberg
- Hermanns RL, Oppikofer T, Anda E, Blikra LH, Böhme M, Bunkholt H, Crosta G, Dahle H, Devoli G, Fischer L and others (2013b) Hazard and risk classification for large unstable rock slopes in Norway. In , *International Conference Vajont 1963-2013. Thoughts and analyses after 50 years since the catastrophic landslide, Padua, Italy - 8-10 October 2013*, Book Series (6), 245–254, Italian Journal of Engineering Geology and Environment, Sapienza Università Editrice
- Hermanns RL, Oppikofer T, Dahle H, Eiken T, Ivy-Ochs S and Blikra LH (2013c) Understanding long-term slope deformation for stability assessment of rock slopes: the case of the Oppstadhornet rockslide, Norway. In *Proceedings of the International Conference Vajont 1963–2013, Padua, Italy, 8–10 October 2013*
- Hermanns RL, Sepúlveda SA, Lastras G, Amblas D, Canals M, Azpiroz M, Bascuñán I, Calafat AM, Duhart P, Frigola J, Iglesias O, Kempf P, Lafuerza S, Longva O, Micallef A, Oppikofer T, Rayo X, Vargas G and Molina FY (2014) Earthquake-triggered subaerial landslides that caused large scale fjord sediment deformation: Combined subaerial and submarine studies of the 2007 Aysén fjord event, Chile. In G Lollino, A Manconi, J Locat, Y Huang and M Canals Artigas (eds.), *Engineering Geology for Society and Territory - Volume 4*, 67–70, Springer International Publishing, Cham

References

- Hermanns RL, Schleier M, Böhme M, Blikra LH, Gosse J, Ivy-Ochs S and Hilger P (2017) Rock-avalanche activity in W and S Norway peaks after the retreat of the Scandinavian Ice Sheet. In M Mikoš, V Vilímek, Y Yin and K Sassa (eds.), *Advancing Culture of Living with Landslides*, 331–338, Springer International Publishing, Cham
- Hewitt K (2006) Disturbance regime landscapes: mountain drainage systems interrupted by large rockslides. *Progress in Physical Geography*, **30**(3), 365–393
- Hewitt K, Clague JJ and Orwin JF (2008) Legacies of catastrophic rock slope failures in mountain landscapes. *Earth-Science Reviews*, **87**(1-2), 1–38
- Hewitt K, Gosse J and Clague JJ (2011) Rock avalanches and the pace of late Quaternary development of river valleys in the Karakoram Himalaya. *Geological Society of America Bulletin*, **123**(9-10), 1836–1850
- Høgaas F, Hansen L, Rinstad BI, Sveian H and Olsen L (2012) Database for registrering av marin grense (MG) i Norge. NGU Report 2012.063, Norges Geologiske Undersøkelse, [in Norwegian]
- Hilger P, Hermanns RL, Gosse JC, Jacobs B, Etzelmüller B and Krautblatter M (2018) Multiple rock-slope failures at Mannen in Romsdal Valley, western Norway, revealed from Quaternary geological mapping and ^{10}Be exposure dating. *The Holocene*, **28**(12), 1841–1854
- Hilger P, Gosse JC and Hermanns RL (2019) How significant is inheritance when dating rockslide boulders with terrestrial cosmogenic nuclide dating?—a case study of an historic event. *Landslides*
- Hollin JT and Schilling DH (1981) Late Wisconsin-Weichselian mountain glaciers and small ice caps. In GH Denton and TJ Hugues (eds.), *The Last Great Ice Sheets*, 179–220, Wiley, New York
- Huang S, Pollack HN and Shen PY (2000) Temperature trends over the past five centuries reconstructed from borehole temperatures. *Nature*, **403**, 756–758
- Huggel C, Salzmann N, Allen S, Caplan-Auerbach J, Fischer L, Haeberli W, Larsen C, Schneider D and Wessels R (2010) Recent and future warm extreme events and high-mountain slope stability. *Philosophical Transactions of the Royal Society A: Mathematical, Physical and Engineering Sciences*, **368**(1919), 2435–2459
- Hughes ALC, Gyllencreutz R, Lohne ØS, Mangerud J and Svendsen JI (2016) The last Eurasian ice sheets - a chronological database and time-slice reconstruction, DATED-1. *Boreas*, **45**(1), 1–45
- Hulton NRJ, Purves RS, McCulloch RD, Sugden DE and Bentley MJ (2002) The Last Glacial Maximum and deglaciation in southern South America. *Quaternary Science Reviews*, **21**(1), 233–241

- Hungr O, Leroueil S and Picarelli L (2013) The Varnes classification of landslide types, an update. *Landslides*, **11**(2), 167–194
- Isaksen K, Ødegård RS, Etzelmüller B, Hilbich C, Hauck C, Farbrot H, Eiken T, Hygen HO and Hipp TF (2011) Degrading mountain permafrost in southern Norway: spatial and temporal variability of mean ground temperatures, 1999–2009. *Permafrost and Periglacial Processes*, **22**(4), 361–377
- Ivy-Ochs S and Kober F (2008) Surface exposure dating with cosmogenic nuclides. *Quaternary Science Journal*, **57**(1-2), 179–209
- Ivy-Ochs S, Poschinger A, Synal HA and Maisch M (2009) Surface exposure dating of the Flims landslide, Graubünden, Switzerland. *Geomorphology*, **103**(1), 104–112
- Jaboyedoff M and Derron MH (2005) Hazard assessment within an integrated risk assessment process for landslides (IRAPL). In *Proc., International Conference on Landslide Risk Management, Vancouver, Balkema*
- Jaboyedoff M, Baillifard F, Bardou E and Girod F (2004) The effect of weathering on Alpine rock instability. *Quarterly Journal of Engineering Geology and Hydrogeology*, **37**(2), 95–103
- Jaboyedoff M, Baillifard F, Derron MH, Couture R, Locat J and Locat P (2005) Modular and evolving rock slope hazard assessment methods. In K Senneset, K Flaate and JO Larsen (eds.), *Landslides and avalanches, ICFL 2005 Norway: proceedings of the 11th International Conference and Field Trip on Landslides, Norway, 1 - 10 September 2005*, Balkema proceedings and monographs in engineering Water and earth sciences, 366, Taylor & Francis, London
- Jia H, Xiang W and Krautblatter M (2015) Quantifying rock fatigue and decreasing compressive and tensile strength after repeated freeze-thaw cycles. *Permafrost and Periglacial Processes*, **26**(4), 368–377
- Jia H, Leith K and Krautblatter M (2017) Path-dependent frost-wedging experiments in fractured, low-permeability granite. *Permafrost and Periglacial Processes*, **28**(4), 698–709
- Jibson RW (2009) *Paleoseismology*, volume 95 of *International Geophysics*, chapter 8 Using Landslides for Paleoseismic Analysis, 565–601. Elsevier
- Jongmans D and Garambois S (2007) Geophysical investigation of landslides: a review. *Bulletin de la Société géologique de France*, **178**(2), 101–112
- Jørgensen F, Lykke-Andersen H, Sandersen PBE, Auken E and Nørmark E (2003) Geophysical investigations of buried Quaternary valleys in Denmark: an integrated application of transient electromagnetic soundings, reflection seismic surveys and exploratory drillings. *Journal of Applied Geophysics*, **53**(4), 215–228

References

- Jorgenson MT, Shur YL and Pullman ER (2006) Abrupt increase in permafrost degradation in Arctic Alaska. *Geophysical Research Letters*, **33**
- Kaplan MR, Ackert Jr RP, Singer BS, Douglass DC and Kurz MD (2004) Cosmogenic nuclide chronology of millennial-scale glacial advances during O-isotope stage 2 in Patagonia. *Geological Society of America Bulletin*, **116**(3-4), 308–321
- Karlsen TA (1991) Narvik. Berggrunnskart; Narvik; 14314; 1:50 000; sort/hvitt. Norges geologiske undersøkelse (NGU)-distribution
- Kartverket (2018a) <http://norgebilder.no>. online, last accessed 06. September 2018
- Kartverket (2018b) <https://høydedata.no/LaserInnsyn/>. online, last accessed 06. September 2018
- Kartverket (2018c) <https://kartkatalog.geonorge.no/>. online, last accessed 06. September 2018
- Kleman J (1994) Preservation of landforms under ice sheets and ice caps. *Geomorphology*, **9**(1), 19–32
- Kleman J and Borgström I (1990) The boulder fields of Mt. Fulufjället, west-central Sweden: Late Weichselian boulder blankets and interstadial periglacial phenomena. *Geografiska Annaler: Series A, Physical Geography*, **72**(1), 63–78
- Kneisel C, Hauck C, Fortier R and Moorman B (2008) Advances in geophysical methods for permafrost investigations. *Permafrost and Periglacial Processes*, **19**(2), 157–178
- Korup O (2004) Geomorphometric characteristics of New Zealand landslide dams. *Engineering Geology*, **73**(1-2), 13–35
- Korup O (2005) Geomorphic imprint of landslides on alpine river systems, southwest New Zealand. *Earth Surface Processes and Landforms*, **30**(7), 783–800
- Korup O and Schlunegger F (2007) Bedrock landsliding, river incision, and transience of geomorphic hillslope-channel coupling: Evidence from inner gorges in the Swiss Alps. *Journal of Geophysical Research: Earth Surface*, **112**(F3)
- Korup O, Strom AL and Weidinger JT (2006) Fluvial response to large rock-slope failures: Examples from the Himalayas, the Tien Shan, and the Southern Alps in New Zealand. *Geomorphology*, **78**(1-2), 3–21
- Korup O, Densmore AL and Schlunegger F (2010) The role of landslides in mountain range evolution. *Geomorphology*, **120**(1-2), 77–90
- Köpfli P, Grämiger LM, Moore JR, Vockenhuber C and Ivy-Ochs S (2018) The Oeschinensee rock avalanche, Bernese Alps, Switzerland: a co-seismic failure 2300 years ago? *Swiss Journal of Geosciences*, **111**(1-2), 205–219

- Krautblatter M, Funk D and Günzel FK (2013) Why permafrost rocks become unstable: a rock-ice-mechanical model in time and space: a rock-ice-mechanical model for permafrost rocks. *Earth Surface Processes and Landforms*, **38**(8), 876–887
- Kristensen L and Blikra LH (2011) Monitoring displacement on the Mannen rockslide in Western Norway. In K Fletcher (ed.), *InSAR principles: guidelines for SAR interferometry processing and interpretation - proceedings of the Second World Landslide Forum - 3.-7. Oktober 2011, Rome*, 19, ESA Publications, ESTEC, Noordwijk, the Netherlands
- Kumar V, Gupta V and Sundriyal YP (2018) Spatial interrelationship of landslides, lithotectonics, and climate regime, Satluj valley, Northwest Himalaya. *Geological Journal*, **54**(1), 537–551
- Lagerbäck R (1990) Late Quaternary faulting and-paleoseismicity in northern Fennoscandia, with particular reference to the Lansjärv area, northern Sweden. *Geologiska Föreningen i Stockholm Förhandlingar*, **112**(4), 333–354
- Lal D (1991) Cosmic ray labeling of erosion surfaces: in situ nuclide production rates and erosion models. *Earth and Planetary Science Letters*, **104**, 424–439
- Larsen JO (1997) Rombakstøtta, Narvik - Vurdering av fare for fjellskred. NGI Report 964097-2, Norges Geoteknitske Institut, [in Norwegian]
- Larsen JO (1999) Rombakstøtta, Narvik - Vurdering av skredfare og bevegelse på tensjonsprekker. NGI Report 96/14408, Norges Geotekniske Institutt, [in Norwegian]
- Lastras G, Amblas D, Calafat AM, Canals M, Frigola J, Hermanns RL, Lafuerza S, Longva O, Micallef A, Sepúlveda SA et al. (2013) Landslides cause tsunami waves: insights from Aysén fjord, Chile. *Eos, Transactions American Geophysical Union*, **94**(34), 297–298
- Le Roux O, Schwartz S, Gamond JF, Jongmans D, Bourles D, Braucher R, Mahaney W, Carcaillet J and Leanni L (2009) CRE dating on the head scarp of a major landslide (Séchilienne, French Alps), age constraints on Holocene kinematics. *Earth and Planetary Science Letters*, **280**(1-4), 236–245
- Lebourg T, Zerathe S, Fabre R, Giuliano J and Vidal M (2014) A Late Holocene deep-seated landslide in the northern French Pyrenees. *Geomorphology*, **208**, 1–10
- Legrand D, Barrientos S, Bataille K, Cembrano J and Pavez A (2011) The fluid-driven tectonic swarm of Aysén Fjord, Chile (2007) associated with two earthquakes (Mw= 6.1 and Mw= 6.2) within the Liquiñe-Ofqui Fault Zone. *Continental Shelf Research*, **31**(3-4), 154–161
- Lifton N (2016) Implications of two Holocene time-dependent geomagnetic models for cosmogenic nuclide production rate scaling. *Earth and Planetary Science Letters*, **433**, 257–268

References

- Lifton N, Sato T and Dunai TJ (2014) Scaling in situ cosmogenic nuclide production rates using analytical approximations to atmospheric cosmic-ray fluxes. *Earth and Planetary Science Letters*, **386**, 149–160
- Lilleøren KS, Etzelmüller B, Schuler TV, Gislén K and Humlum O (2012) The relative age of mountain permafrost — estimation of Holocene permafrost limits in Norway. *Global and Planetary Change*, **92–93**, 209–223
- Lønne I (1995) Sedimentary facies and depositional architecture of ice-contact glaciomarine systems. *Sedimentary Geology*, **98**(1-4), 13–43
- Lohne ØS, Bondevik S, Mangerud J and Svendsen JI (2007) Sea-level fluctuations imply that the Younger Dryas ice-sheet expansion in western Norway commenced during the Allerød. *Quaternary Science Reviews*, **26**(17), 2128–2151
- Longva O, Blikra LH and Dehls JF (2009) Rock avalanches: distribution and frequencies in the inner part of Storfjorden, Møre og Romsdal County, Norway. NGU Report 2009.002, Norges Geologiske Undersøkelse, Trondheim
- MacGregor KR, Anderson RS and Waddington ED (2009) Numerical modeling of glacial erosion and headwall processes in alpine valleys. *Geomorphology*, **103**(2), 189–204
- Magnin F, Etzelmüller B, Westermann S, Isaksen K, Hilger P and Hermanns RL (2019) Permafrost distribution in steep slopes in Norway: measurements, statistical distribution modelling and geomorphological implications. *Earth Surf. Dynam. Discuss.*, in review
- Mamot P, Weber S, Schröder T and Krautblatter M (2018) A temperature- and stress-controlled failure criterion for ice-filled permafrost rock joints. *The Cryosphere*, **12**(10), 3333–3353
- Mangerud J (1987) The Allerød/Younger Dryas boundary. In WH Berger and LD Labeyrie (eds.), *Abrupt Climatic Change*, volume 216 of *NATO ASI Series (Series C: Mathematical and Physical Sciences)*, 163–171, Springer, Dordrecht
- Mangerud J (2004) Ice sheet limits on Norway and the Norwegian continental shelf. In J Ehlers and PL Gibbard (eds.), *Quaternary Glaciations - Extent and chronology - Part I: Europe*, volume 2 of *Developments in Quaternary Sciences*, 271–294, Elsevier Amsterdam
- Mangerud J, Gyllencreutz R, Lohne Ø and Svendsen JI (2011) Glacial history of Norway. In J Ehlers, PL Gibbard and PD Hughes (eds.), *Quaternary Glaciations - Extent and chronology - A closer look*, volume 15 of *Developments in Quaternary Sciences*, 279–298, Elsevier Amsterdam
- Marrero SM, Phillips FM, Borchers B, Lifton N, Aumer R and Balco G (2016) Cosmogenic nuclide systematics and the CRONUScale program. *Quaternary Geochronology*, **31**, 160–187

- Masarik J and Wieler R (2003) Production rates of cosmogenic nuclides in boulders. *Earth and Planetary Science Letters*, **216**(1-2), 201–208
- Masson-Delmotte V, Dreyfus G, Braconnot P, Johnsen S, Jouzel J, Kageyama M, Landais A, Loutre MF, Nouet J, Parrenin F et al. (2006) Past temperature reconstructions from deep ice cores: relevance for future climate change. *Climate of the Past Discussions*, **2**(4), 399–448
- Matmon A, Simhai O, Amit R, Haviv I, Porat N, McDonald E, Benedetti L and Finkel RC (2009) Desert pavement - coated surfaces in extreme deserts present the longest-lived landforms on Earth. *Geological Society of America Bulletin*, **121**(5/6), 688–697
- Matsuoka N (1995) A laboratory simulation on freezing expansion of a fractured rock: preliminary data. *Annual report of the Institute of Geoscience, the University of Tsukuba*, **21**, 5–8
- Matsuoka N (2001) Direct observation of frost wedging in alpine bedrock. *Earth Surface Processes and Landforms: The Journal of the British Geomorphological Research Group*, **26**(6), 601–614
- Matthews JA, Shakesby RA and Fabel D (2017) Very low inheritance in cosmogenic surface exposure ages of glacial deposits: A field experiment from two Norwegian glacier forelands. *The Holocene*, **27**, 1406–1414
- Mauri A, Davis BAS, Collins PM and Kaplan JO (2015) The climate of Europe during the Holocene: a gridded pollen-based reconstruction and its multi-proxy evaluation. *Quaternary Science Reviews*, **112**, 109–127
- McColl ST (2012) Paraglacial rock-slope stability. *Geomorphology*, **153-154**, 1–16
- McColl ST and Davies TRH (2013) Large ice-contact slope movements: glacial buttressing, deformation and erosion. *Earth Surface Processes and Landforms*, **38**(10), 1102–1115
- McCulloch RD, Bentley MJ, Purves RS, Hulton NRJ, Sugden DE and Clapperton CM (2000) Climatic inferences from glacial and palaeoecological evidence at the last glacial termination, southern South America. *Journal of Quaternary Science: Published for the Quaternary Research Association*, **15**(4), 409–417
- McSaveney MJ (1978) Sherman Glacier rock avalanche, Alaska, USA. In B Voight (ed.), *Rockslides and Avalanches*, volume 14, 197–258, Elsevier, Amsterdam
- Mitchell WA, McSaveney MJ, Zondervan A, Kim K, Dunning SA and Taylor PJ (2007) The Keylong Serai rock avalanche, NW Indian Himalaya: geomorphology and palaeoseismic implications. *Landslides*, **4**(3), 245–254

References

- Moore JR, Gischig V, Amann F, Hunziker M and Burjanek J (2012) Earthquake-triggered rock slope failures: Damage and site effects. In *Proceedings 11th International & 2nd North American Symposium on Landslides*
- Moreiras SM, Hermanns RL and Fauqué L (2015) Cosmogenic dating of rock avalanches constraining Quaternary stratigraphy and regional neotectonics in the Argentine Central Andes (32° S). *Quaternary Science Reviews*, **112**, 45–58
- Morken OA (2017) *Integrated analysis of past, and potential future rock slope failures of various size from Rombakstøtta, Nordland*. Master's thesis, NTNU
- Murton J, Coutard JP, Lautridou JP, Ozouf JC, Robinson D and Williams R (2001) Physical modelling of bedrock brecciation by ice segregation in permafrost. *Permafrost and Periglacial Processes*, **12**(3), 255–266
- Murton JB, Peterson R and Ozouf JC (2006) Bedrock fracture by ice segregation in cold regions. *Science*, **314**(5802), 1127–1129
- Myhra KS (2016) *Modelling Permafrost Conditions in Steep Mountain Environments*. Ph.D. thesis, University of Oslo
- Myhra KS, Westermann S and Etzelmüller B (2017) Modelled Distribution and Temporal Evolution of Permafrost in Steep Rock Walls Along a Latitudinal Transect in Norway by CryoGrid 2D. *Permafrost and Periglacial Processes*, **28**(1), 172–182
- Nagelisen J, Moore JR, Vockenhuber C and Ivy-Ochs S (2015) Post-glacial rock avalanches in the Obersee Valley, Glarner Alps, Switzerland. *Geomorphology*, **238**, 94–111
- Naranjo JA, Arenas M, Clavero J and Muñoz O (2009) Mass movement-induced tsunamis: main effects during the Patagonian Fjordland seismic crisis in Aisén (45° 25'S), Chile. *Andean Geology*, **36**(1), 137–145
- Nesje A (2009) Latest Pleistocene and Holocene alpine glacier fluctuations in Scandinavia. *Quaternary Science Reviews*, **28**(21-22), 2119–2136
- Nesje A, Dahl SO, Anda E and Rye N (1988) Block fields in southern Norway: Significance for the Late Weichselian ice sheet. *Norwegian Journal of Geology*, **68**(3), 149–169
- Nesje A, Dahl SO and Løvlie R (1995) Late Holocene glaciers and avalanche activity in the Ålfotbreen area, western Norway: evidence from a lacustrine sedimentary record. *Norwegian Journal of Geology*, **75**, 120–126
- Nesje A, Matthews JA, Dahl SO, Berrisford MS and Andersson C (2001) Holocene glacier fluctuations of Flatebreen and winter-precipitation changes in the Jostedalbreen region, western Norway, based on glaciolacustrine sediment records. *The Holocene*, **11**(3), 267–280

- Nesje A, Dahl SO, Thun T and Nordli Ø (2008) The ‘Little Ice Age’ glacial expansion in western Scandinavia: summer temperature or winter precipitation? *Climate Dynamics*, **30**(7-8), 789–801
- NGU (2018) Nasjonal database for ustabile fjellparti - national database for unstable rock-slopes (<http://geo.ngu.no/kart/ustabilefjellparti/>). online map service, last accessed: January, 17 2019
- NGU (2019) InSAR Norge - InSAR Norway (<http://insar.ngu.no>). online map service, last accessed: January, 17 2019
- Nishiizumi K, Winterer EL, Kohl CP, Klein J, Middleton R, Lal D and Arnold JR (1989) Cosmic ray production rates of ^{10}Be and ^{26}Al in quartz from glacially polished rocks. *Journal of Geophysical Research: Solid Earth*, **94**(B12), 17907–17915
- North Greenland Ice Core Project members (NGRIP) (2004) High-resolution record of Northern Hemisphere climate extending into the last interglacial period. *Nature*, **431**, 147
- NVE (2017) Fjellskretovervaking - NVE. online, last accessed: January, 17 2019, [in Norwegian]
- NVE (2018) NVE Atlas 3.0 (<https://atlas.nve.no/>). online map service, last accessed: November, 20 2018
- Olesen O, Blikra LH, Braathen A, Dehls JF, Olsen L, Rise L, Roberts D, Riis F, Faleide JJ and Anda E (2004) Neotectonic deformation in Norway and its implications: a review. *Norwegian Journal of Geology*, **84**(1), 3–34
- Oppikofer T, Hermanns RL, Redfield TF, Sepúlveda SA, Duhart P and Bascuñán I (2012) Morphologic description of the Punta Cola rock avalanche and associated minor rock-slides caused by the 21 April 2007 Aysén earthquake (Patagonia, southern Chile). *Revista de la Asociación Geológica Argentina*, **69**(3), 339–353
- Oppikofer T, Saintot A, Otterå S, Hermanns RL, Anda E, Dahle H and Eiken T (2013) Investigations on unstable rock slopes in Møre og Romsdal - status and plans after field surveys in 2012. NGU Report 2013.014, Norges Geologiske Undersøkelse, Trondheim
- Oppikofer T, Nordahl B, Bunkholt H, Nicolaisen M, Jarna A, Iversen S, Hermanns RL, Böhme M and Yugsi Molina FX (2015) Database and online map service on unstable rock slopes in Norway — From data perpetuation to public information. *Geomorphology*, **249**, 69–81
- Oppikofer T, Saintot A, Hermanns RL, Böhme M, Scheiber T, Gosse J and Dreiås GM (2017) From incipient slope instability through slope deformation to catastrophic failure—Different stages of failure development on the Ivasnasen and Vollan rock slopes (western Norway). *Geomorphology*, **289**, 96–116

References

- Oppikofer T, Hermanns RL, Roberts NJ and Böhme M (2018) SPLASH: semi-empirical prediction of landslide-generated displacement wave run-up heights. In DG Lintern, DC Mosher, LG Moscardelli, PT Bobrowsky, C Campbell, JD Chaytor, JJ Clague, A Georgiopoulou, P Lajeunesse, A Normandeau, DJW Piper, M Scherwath, C Stacey and D Turmel (eds.), *Subaqueous Mass Movements*, volume 477, Geological Society, London, Special Publications
- Ostermann M and Sanders D (2017) The Benner pass rock avalanche cluster suggests a close relation between long-term slope deformation (DSGSDs and translational rock slides) and catastrophic failure. *Geomorphology*, **289**, 44–59
- Ostermann M, Ivy-Ochs S, Sanders D and Prager C (2016) Multi-method (^{14}C , ^{36}Cl , $^{234}\text{U}/^{230}\text{Th}$) age bracketing of the Tschirgant rock avalanche (Eastern Alps): implications for absolute dating of catastrophic mass-wasting. *Earth Surface Processes and Landforms*, **42**(7), 1110–1118
- Pánek T (2015) Recent progress in landslide dating: A global overview. *Progress in Physical Geography*, **39**(2), 168–198
- Pánek T and Klimeš J (2016) Temporal behavior of deep-seated gravitational slope deformations: A review. *Earth-Science Reviews*, **156**, 14–38
- Pánek T, Lenart J, Hradecký J, Hercman H, Braucher R, Šilhán K and Škarpich V (2018) Coastal cliffs, rock-slope failures and Late Quaternary transgressions of the Black Sea along southern Crimea. *Quaternary Science Reviews*, **181**, 76–92
- Pankhurst RJ and Hervé F (2007) *The Geology of Chile*, chapter Introduction and overview. Geology of Series, The Geological Society, London
- Pankhurst RJ, Weaver SD, Hervé F and Larrondo P (1999) Mesozoic-Cenozoic evolution of the North Patagonian Batholith in Aysén, southern Chile. *Journal of the Geological Society*, **156**(4), 673–694
- Pantelidis L (2009) Rock slope stability assessment through rock mass classification systems. *International Journal of Rock Mechanics and Mining Sciences*, **46**(2), 315–325
- Paterson WSB (1994) *The physics of glaciers*. Elsevier, third edition
- Peng X, Chen Y, Liu B, Liu G, Liu Q and Liu J (2018) Timing and features of a late MIS 2 rock avalanche in the Eastern Himalayas, constrained by ^{10}Be exposure dating. *Geomorphology*, **318**, 58–68
- Penna IM, Hermanns RL, Niedermann S and Folguera A (2011) Multiple slope failures associated with neotectonic activity in the Southern Central Andes (37°–37°30'S), Patagonia, Argentina. *Geological Society of America Bulletin*, **123**(9–10), 1880–1895
- Perrone A, Lapenna V and Piscitelli S (2014) Electrical resistivity tomography technique for landslide investigation: A review. *Earth-Science Reviews*, **135**, 65–82

- Plug LJ, Gosse JC, McIntosh JJ and Bigley R (2007) Attenuation of cosmic ray flux in temperate forest. *Journal of Geophysical Research: Earth Surface*, **112**(F2)
- Pousse-Beltran L, Vassallo R, Audemard F, Jouanne F, Carcaillet J, Pathier E and Volat M (2017) Pleistocene slip rates on the Boconó Fault along the North Andean Block plate boundary, Venezuela. *Tectonics*, **36**, 1207–1231
- Putnam AE, Schaefer JM, Barrell DJA, Vandergoes M, Denton GH, Kaplan MR, Finkel RC, Schwartz R, Goehring BM and Kelley SE (2010) In situ cosmogenic ^{10}Be production-rate calibration from the Southern Alps, New Zealand. *Quaternary Geochronology*, **5**(4), 392–409
- Quenardel JM and Zwaan KB (2008) Manndalen. Berggrunnskart; Manndalen; 1:50 000; Foreløpig utgave plottversjon. Norges Geologiske Undersøkelse (NGU)-distribution, [in Norwegian]
- Raghuvanshi TK (2017) Plane failure in rock slopes – A review on stability analysis techniques. *Journal of King Saud University - Science*, **31**(1), 101–109
- Redfield T and Osmundsen P (2009) The tjellefonna fault system of western Norway: Linking late-caledonian extension, post-caledonian normal faulting, and tertiary rock column uplift with the landslide-generated tsunami event of 1756. *Tectonophysics*, **474**(1-2), 106–123
- Redfield T, Hermanns RL, Oppikofer T, Duhart P, Mella M, Derch P, Bascuñán I, Arenas M, Fernández J, Sepúlveda S et al. (2011) Analysis of the 2007 earthquake-induced Punta Cola rockslide and tsunami, Aysén fjord, Patagonia, Chile (45.3°S, 73.0°W). In *5th international conference on earthquake geotechnical engineering, January 2011, 10-13, Santiago, Chile*
- Regmi AD, Yoshida K, Nagata H, Pradhan AMS, Pradhan B and Pourghasemi HR (2013) The relationship between geology and rock weathering on the rock instability along Mugling–Narayanghat road corridor, Central Nepal Himalaya. *Natural hazards*, **66**(2), 501–532
- Reusch H (1907) *Skredet i Loen 15. Januar 1905. Norges Geologiske Undersøkelse, Aarbok 1907*. Aschehoug & Co, Kristiana
- Roberts D (2003) The Scandinavian Caledonides: event chronology, palaeogeographic settings and likely modern analogues. *Tectonophysics*, **365**(1-4), 283–299
- Roberts D and Gee DG (1985) An introduction to the structure of the Scandinavian Caledonides. *The Caledonide orogen–Scandinavia and related areas*, **1**, 55–68
- Ross L, de Swart H, Ensing E and Valle-Levinson A (2017) Three-dimensional tidal flow in a fjord-like basin with converging width: An analytical model. *Journal of Geophysical Research: Oceans*, **122**(9), 7558–7576

References

- Saintot A, Dahle H, Derron MH, Henderson I and Oppikofer T (2012) Large gravitational rock slope deformation in Romsdalen valley (Western Norway). *Revista de la Asociación Geológica Argentina*, **69**(3), 354–371
- Sanchez G, Rolland Y, Corsini M, Braucher R, Bourlès D, Arnold M and Aumaître G (2010) Relationships between tectonics, slope instability and climate change: Cosmic ray exposure dating of active faults, landslides and glacial surfaces in the SW Alps. *Geomorphology*, **117**(1-2), 1–13
- Sato T (2016) Analytical model for estimating the zenith angle dependence of terrestrial cosmic ray fluxes. *PloS ONE*, **11**(8), e0160390
- Schildgen T, Phillips W and Purves R (2005) Simulation of snow shielding corrections for cosmogenic nuclide surface exposure studies. *Geomorphology*, **64**(1-2), 67–85
- Schleier M, Hermanns RL, Rohn J and Gosse JC (2015) Diagnostic characteristics and paleodynamics of supraglacial rock avalanches, Innerdalen, Western Norway. *Geomorphology*, **245**, 23–39
- Schleier M, Hermanns RL, Gosse JC, Oppikofer T, Rohn J and Tønnesen JF (2017) Subaqueous rock-avalanche deposits exposed by post-glacial isostatic rebound, Innfjordalen, Western Norway. *Geomorphology*, **289**(15), 117–133
- Schrott L, Götz J, Geilhausen M and Morche D (2006) Spatial and temporal variability of sediment transfer and storage in an alpine basin (bavarian alps, germany). *Geographica Helvetica*, **3**, 191–201
- seNorgeno (2018) seNorge - online climate and weather service (<http://senorge.no/>). Last accessed: January, 17 2019
- Sepúlveda SA, Serey A, Lara M, Pavez A and Rebolledo S (2010) Landslides induced by the April 2007 Aysén Fjord earthquake, Chilean Patagonia. *Landslides*, **7**(4), 483–492
- Sepúlveda SA and Serey A (2009) Tsunamigenic, earthquake-triggered rock slope failures during the april 21, 2007 aiséen earthquake, southern chile (45.5 s). *Andean Geology*, **36**(1)
- Severinghaus JP, Sowers T, Brook EJ, Alley RB and Bender ML (1998) Timing of abrupt climate change at the end of the younger dryas interval from thermally fractionated gases in polar ice. *Nature*, **391**(6663), 141
- Sewell RJ, Barrows TT, Campbell SDG and Fifield LK (2006) Exposure dating (^{10}Be , ^{26}Al) of natural terrain landslides in Hong Kong, China. In AM Alonso-Zarza and LH Tanner (eds.), *In Situ-produced Cosmogenic Nuclides and Quantification of Geological Processes*, volume 415 of *Geological Society special publication*, 131–146, Geological Society of America

- Shewchuck JR (1996) Engineering a 2D quality mesh generator and Delaunay triangulator. In MC Lin and D Manocha (eds.), *Applied Computational Geometry: Towards Geometric Engineering*, 203–222, Springer, Berlin, Heidelberg
- Slagstad T, Balling N, Elvebakk H, Midttømme K, Olesen O, Olsen L and Pascal C (2009) *Component parts of the World Heat Flow Data Collection*. PANGAEA
- Sletten K, Blikra LH, Ballantyne C, Nesje A and Dahl SO (2003) Holocene debris flows recognized in a lacustrine sedimentary succession: sedimentology, chronostratigraphy and cause of triggering. *The Holocene*, **13**(6), 907–920
- Sollid JL and Sørbel L (1998) Palsa bogs as a climate indicator: examples from Dovrefjell, southern Norway. *Ambio*, **27**(4), 287–291
- Sollid JL and Sørbel L (1979) Deglaciation of western Central Norway. *Boreas*, **8**(2), 233–239
- Staiger J, Gosse J, Toracinta R, Oglesby B, Fastook J and Johnson JV (2007) Atmospheric scaling of cosmogenic nuclide production: Climate effect. *Journal of Geophysical Research*, **112**(B2)
- Stead D and Wolter A (2015) A critical review of rock slope failure mechanisms: The importance of structural geology. *Journal of Structural Geology*, **74**, 1–23
- Steiger C, Etzelmüller B, Westermann S and Myhra KS (2016) Modelling the permafrost distribution in steep rock walls. *Norwegian Journal of Geology*, **96**(4), 329–341
- Stieglitz M, Déry S, Romanovsky V and Osterkamp T (2003) The role of snow cover in the warming of arctic permafrost. *Geophysical Research Letters*, **30**(13)
- Stone JO (2000) Air pressure and cosmogenic isotope production. *Journal of Geophysical Research*, **105**(B10), 23,753–23,759
- Stroeven AP, Hättestrand C, Kleman J, Heyman J, Fabel D, Fredin O, Goodfellow BW, Harbor JM, Jansen JD, Olsen L, Caffee MW, Fink D, Lundqvist J, Rosqvist GC, Strömberg B and Jansson KN (2016) Deglaciation of Fennoscandia. *Quaternary Science Reviews*, **147**, 91–121
- Strom A (2006) Morphology and internal structure of rockslides and rock avalanches: grounds and constraints for their modelling. In SG Evans, GS Mugnozza, A Strom and RL Hermanns (eds.), *Landslides from Massive Rock Slope Failure*, volume 49 of *NATO Science Series*, 305–326, Springer, Dordrecht
- Sturzenegger M, Stead D, Gosse J, Ward B and Froese C (2015) Reconstruction of the history of the Palliser Rockslide based on ^{36}Cl terrestrial cosmogenic nuclide dating and debris volume estimations. *Landslides*, **12**(6), 1097–1106

References

- Svendsen JI and Mangerud J (1987) Late Weichselian and holocene sea-level history for a cross-section of western Norway. *Journal of Quaternary Science*, **2**(2), 113–132
- Sweeney CG, Brideau MA, Augustinus PC and Fink D (2013) Lochnagar landslides-dam - Central Otago, New Zealand: geomechanics and timing of the event. In CY Chin (ed.), *Hanging by a thread? Lifelines, infrastructure and natural disasters*, volume 38 of *Proceedings of the 19th NZGS Symposium*, 447–454, New Zealand Geotechnical Society, Queenstown
- Tikhomirov D, Akçar N, Ivy-Ochs S, Alfimov V and Schlüchter C (2014) Calculation of shielding factors for production of cosmogenic nuclides in fault scarps. *Quaternary Geochronology*, **19**, 181–193
- Tofelde S, Duesing W, Schildgen TF, Wickert AD, Wittmann H, Alonso RN and Strecker M (2018) Effects of deep-seated versus shallow hillslope processes on cosmogenic ^{10}Be concentrations in fluvial sand and gravel. *Earth Surface Processes and Landforms*, **43**(15), 3086–3098
- Trombotta Liaudat D (2008) Geocryology of Southern South America. In J Rabassa (ed.), *Late Cenozoic of Patagonia and Tierra del Fuego*, volume 11 of *Developments in Quaternary Sciences*, 255–268, Elsevier, The Netherlands
- Tveten E, Lutro O and Thorsnes T (1998) Geologisk kart over Norge, berggrunnskart Ålesund, 1:250,000
- Von Blanckenburg F (2006) The control mechanisms of erosion and weathering at basin scale from cosmogenic nuclides in river sediment. *Earth and Planetary Science Letters*, **242**(3-4), 224–239
- Wagner G, Masarik J, Beer J, Baumgartner S, Imboden D, Kubik PW, Synal HA and Suter M (2000) Reconstruction of the geomagnetic field between 20 and 60 kyr BP from cosmogenic radionuclides in the GRIP ice core. *Nuclear Instruments and Methods in Physics Research Section B: Beam Interactions with Materials and Atoms*, **172**(1-4), 597–604
- Wang WN, Chigira M and Furuya T (2003) Geological and geomorphological precursors of the Chiu-fen-erh-shan landslide triggered by the Chi-chi earthquake in central Taiwan. *Engineering geology*, **69**(1-2), 1–13
- Weber S, Beutel J, Faillettaz J, Hasler A, Krautblatter M and Vieli A (2017) Quantifying irreversible movement in steep, fractured bedrock permafrost on Matterhorn (CH). *The Cryosphere*, **11**(1), 567–583
- Winsemann J, Hornung JJ, Meinsen J, Asprion U, Polom U, Brandes C, Bußmann M and Weber C (2009) Anatomy of a subaqueous ice-contact fan and delta complex, Middle Pleistocene, North-west Germany. *Sedimentology*, **56**(4), 1041–1076

- Worldatlas (2018) worldatlas.com. Last accessed: 24.07.2018
- Wyrwoll KH (1977) Causes of rock-slope failure in a cold area: Labrador-ungava. *Geological Society of America Reviews in Engineering Geology*, **3**, 59–67
- Xing A, Wang G, Yin Y, Tang C, Xu Z and Li W (2016) Investigation and dynamic analysis of a catastrophic rock avalanche on September 23, 1991, Zhaotong, China. *Landslides*, **13**(5), 1035–1047
- Zerathe S, Lebourg T, Braucher R and Bourlès D (2014) Mid-Holocene cluster of large-scale landslides revealed in the Southwestern Alps by ^{36}Cl dating. Insight on an Alpine-scale landslide activity. *Quaternary Science Reviews*, **90**, 106–127

Part II

Journal publications

Paper I

Hilger, P., Gosse, J.C., Hermanns, R.L.:

How significant is inheritance when dating rockslide boulders with terrestrial cosmogenic nuclide dating? — a case study of an historic event

Landslides doi:10.1007/s10346-018-01132-0

Note on contributions

The candidate wrote the paper and carried out all field work and analyses, including sample preparation, sample analyses, calculation of exposure ages and theoretical pre-failure ^{10}Be concentration analysis. The second author advised the candidate during sample processing and theoretical analyses. The third author had the project idea and selected the field site. All authors contributed to finalising the manuscript.

Landslides

DOI 10.1007/s10346-018-01132-0

Received: 25 September 2018

Accepted: 27 December 2018

© Springer-Verlag GmbH Germany
part of Springer Nature 2019

Paula Hilger · John C. Gosse · Reginald L. Hermanns

How significant is inheritance when dating rockslide boulders with terrestrial cosmogenic nuclide dating?—a case study of an historic event

Abstract Terrestrial cosmogenic nuclide (TCN) exposure dating of boulders is frequently used for rockslide chronology. A well-recognized source of error that cannot be readily quantified is related to inheritance of TCN produced in the rock prior to failure. The effect of inheritance is not constant and will be greatest in the instance of a very recent shallow failure on a high-altitude surface with low event frequencies. We illustrate the effect by measuring ^{10}Be concentrations in six boulders exposed for only 9 years before sampling, on a rock avalanche in Puerto Aysén, Chile. Their apparent exposure ages range from 216 ± 76 to 1755 ± 436 years. The mean apparent exposure age of a statistical cluster of three samples exceeds the real exposure time by 345 ± 36 years (3800%), implying that all sampled rock surfaces experienced pre-failure TCN production. A reconstructed pre-failure topography enables the analysis of possible pre-failure boulder positions and an estimate of the range of possible inherited concentrations along a 2D transect. Despite a maximum failure-mass thickness of 110 m, the boulders seem to have originated from depths shallower than 14 m. Because of the likelihood that large boulders, prioritized for TCN sampling, originate from relatively shallow pre-failure depths owing to surface-near transport with minor turbation, it is necessary to consider potentially inherited TCN concentrations and their effect on the age determination, especially in cases of young rockslides, where the commonly adjusted effects of boulder erosion and snow, ash, or vegetation shielding are negligible in comparison.

Keywords Surface exposure dating · Rockslides · Rock avalanches · Inheritance

Introduction

In the last decade, terrestrial cosmogenic nuclide (TCN) exposure dating has become one of the most widely used techniques for rock avalanche and rockslide chronology (Pánek 2015). An increasing number of studies link the timing of rock-slope failures (RSF) to potential controlling factors, such as debuttressing (Cossart et al. 2008; Ballantyne et al. 2014; Hermanns et al. 2017), tectonic activity (Hermanns et al. 2001; Mitchell et al. 2007; Sanchez et al. 2010), and various climatic stresses (Dortch et al. 2009; Nagelisen et al. 2015). TCN exposure ages range from decades to tens of millions of years. While cosmogenic ^{10}Be produced in exposed quartz is the most widely used nuclide, other radionuclides and stable noble gases can be measured in a wide range of lithologies. For rockslide chronology, multiple exposed surfaces can be exploited, including boulders on the catastrophically failed deposits (Ballantyne and Stone 2004; Hewitt et al. 2011; Hermanns et al. 2017), a sliding surface (i.e., in the case of a gradually sliding block (Sanchez et al. 2010; Hermanns et al. 2013; Schwartz et al. 2017)), or breakaway surfaces (Ivy-Ochs et al. 2009; Zerathe et al. 2014).

Despite significant improvements in the sample preparation, measurement, and interpretation of TCN concentrations as exposure ages (Lifton et al. 2014; Borchers et al. 2016), the initial TCN concentration in a rockslide boulder prior to the failure event can contribute a significant error in the exposure age (Fig. 1). If not subtracted from the measured concentrations, the inherited concentration causes the calculated exposure age to overestimate the event age (Lal 1991; Akçar et al. 2012). The large number of measurements necessary to apply statistical or multi-nuclide approaches quantifying inheritance is prohibited by cost (most studies use less than ten measurements to date a deposit). An important exception is the utility of the depth profile method to simultaneously solve for inheritance and exposure age, but this requires that the mass-wasted material produced a homogeneous matrix-rich layer (Anderson et al. 1996; Hidy et al. 2013). In the rare case where a rockslide targeted for chronology can be selected on the basis of size, a low elevation deep-seated rockslide will on average have less inheritance than a shallower one sourced high above the deposit because the cosmic ray flux diminishes exponentially with depth in the atmosphere and below the mountain surface. Without the luxury of selecting the optimal rockslide for minimizing inheritance, or using multiple measurements, the effect of inheritance cannot be calculated. Therefore, published chronologies have not been explicitly adjusted for the inherited concentration, although statistical outliers have been interpreted to be the result of inheritance (Ballantyne et al. 2014; Ostermann et al. 2016; Hilger et al. 2018). Since it is unlikely that different boulders will have the same inheritance concentration, authors have argued that if exposure ages on three or more boulders on the deposit are within the reported 1-sigma analytical precision (typically 2 to 3%), the inheritance concentration is insignificant (Ivy-Ochs et al. 2009). Although the approach cannot be applied when sampling a contiguous rock surface such as a failure plane or breakaway surface, it may be a reasonable argument for rockslide deposits. However, the hypothesis has not been tested by empirical measurements, particularly on recent events where the effect of inheritance would be greatest.

In this experiment, cosmogenic ^{10}Be is measured in six boulders deposited by a recent large ($> 20 \text{ Mm}^3$) rock avalanche that took place in the Patagonian Andes in 2007 (Oppikofer et al. 2012), to resolve whether there is inheritance in any boulder and if so, how these inherited concentrations could influence the age determination. A cursory discussion of the relevant theory is provided to enable a simplified comparison between measured and expected concentration distributions. Owing to the wide range of complex geometric and exposure history first-order controls on the pre-event (subsurface) concentrations, it is not possible to provide an explicit solution that applies to all natural rockslides. Our results have implications for (i) rockslide risk analyses that incorporate

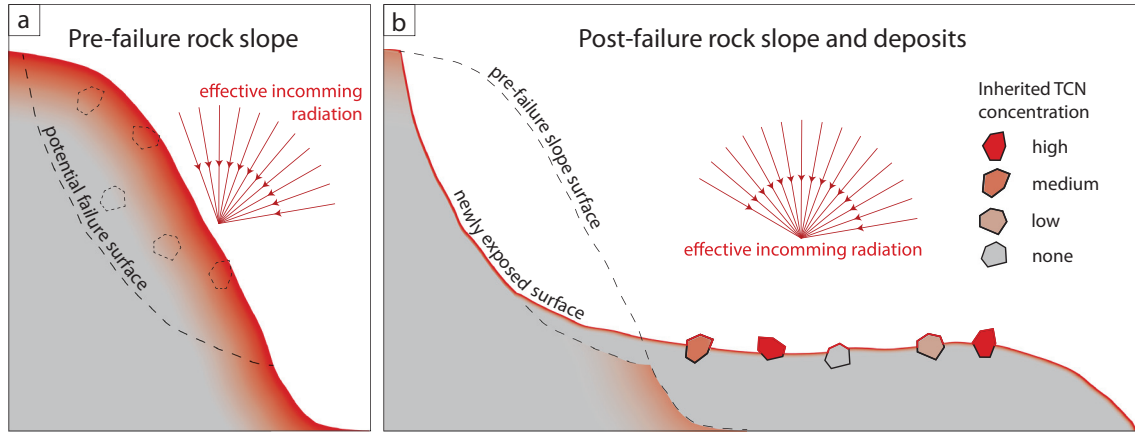


Fig. 1 Schematic illustration of TCN concentrations in a pre- and post-failure rock slope. **a** Pre-failure rock slope, that has been exposed to cosmic radiation for a long time, building up TCNs at the surface and at depth (red shading). **b** After failure, new surfaces are exposed to cosmic radiation along the failure surface and the deposits. The boulders, sitting on top of the deposition body, are affected by varying TCN concentrations, depending on their pre-failure position, indicated in (a). See discussion for more details about this simplified model

uncertainty in TCN exposure dating and (ii) the uncertainty of past and future attempts to improve knowledge of TCN production rate scaling by calibrating against independently dated rockslide deposits.

How to quantify TCN inheritance in rockslide deposits?

Exposed rock surfaces are constantly bombarded by a flux of secondary cosmic rays. When penetrating the rock, the incoming high-energy particles produce cosmogenic isotopes in a range of minerals, with an approximately exponential decrease through hundreds of meters of penetration. For instance, production of ^{10}Be in quartz-bearing rock types is primarily through spallation reactions by fast nucleons in the upper 4 m, decreasing with an e -folding length of approximately $\Lambda_n = 150 \text{ g cm}^{-2}$, while production by different muon interactions is significant at depths to at least hundreds of meters ($\Lambda_\mu > 1500 \text{ g cm}^{-2}$).

The amount of inherited cosmogenic nuclide concentrations in boulders of rockslide deposits is thus dependent on (1) the pre-failure topography (slope, other geometric factors) and source area height above the deposit, (2) the source depth of the sampled boulder, and (3) the exposure and erosion history of the pre-failure surface. The potential ^{10}Be concentration C (atoms g^{-1}), of the selected mineral in the pre-failure rock slope, can be approximated using the relationship proposed by Lal (1991):

$$C = \left[\frac{F_n S_n P_o}{\left(\lambda + \frac{\rho \varepsilon}{\Lambda_n} \right)} e^{-\frac{\rho d_i}{\Lambda_n}} \left(1 - e^{-\left(\lambda + \frac{\rho \varepsilon}{\Lambda_n} \right) t} \right) \right] + [F_{\mu_s} S_{\mu_s} P_o / \dots] + [F_{\mu_f} S_{\mu_f} P_o / \dots] \quad (1)$$

where F_{n,μ_f,μ_s} is the fraction of production rate for the three pathways, spallation by fast nucleons (n), slow negative muon capture (μ_s), and fast muon reactions (μ_f), respectively. S is the dimensionless shielding factor (defined by the pre-failure

geometry) and P_o is the production rate of, in this example, ^{10}Be in quartz (atoms $\text{g}^{-1} \text{ a}^{-1}$) considering the latitude, longitude, elevation of a rock mass, and time-dependent magnetic and solar effects on the cosmic ray flux. λ is the decay constant of ^{10}Be ($4.9 \times 10^{-7} \text{ a}^{-1}$), ρ (g cm^{-3}) is the rock bulk density, ε (cm ka^{-1}) is the erosion rate, and d_i (cm) is the depth. Λ_{n,μ_s,μ_f} (g cm^{-2}) represents the attenuation lengths for the three pathways, respectively.

Many rockslide and rock-avalanche studies are situated in areas glaciated during the last glaciation when glacial erosion incised and widened valleys and created freshly exposed steep slopes prone to rockslide activity, especially following unloading (e.g., the European Alps, Norway, Patagonia, Himalaya). We tested factors 1–3 with a simple Monte Carlo simulation using Eq. (1) and assuming deep glacial erosion before first exposure 13–16 ka ago. In this case, early Holocene rockslides are hardly affected by inherited cosmogenic nuclides. We evaluate the effect of inheritance for a hypothetical Holocene scenario (Table 1) of a 7-ka-old rockslide originating from a slope whose TCN concentration was reset to zero by the last glaciation, resulting in a total exposure time of ca. 14 ka.

The relative effect of inheritance can then be expressed as the fraction of inherited ^{10}Be concentrations in relation to the ^{10}Be concentration of the assumed 28,000 atoms g^{-1} expected for the actual event age. This effect is dependent on the apparent post-failure exposure age because with longer post-failure exposure, the post-depositional concentration will eventually exceed the decaying inheritance.

In this example, a decrease of slope will at most double the effect of inheritance (a point on an unlimited vertical wall is exposed to approximately half of the cosmic rays compared to a horizontal surface) (Fig. 2a). But depending on the source depth of the sampled boulder, the effect increases exponentially with decreasing source rock depth (Figs. 1 and 2). For this scenario of 7-ka-old rockslide deposits, the effect of inheritance is $< 5\%$ for boulders sourcing from at least 5-m depth for up to 14 ka pre-exposure time (Fig. 1b). For an increasing pre-failure exposure

Table 1 Compilation of the values used for the Monte Carlo simulation (Fig. 2) using Eq. (1)

Parameter	Symbol	Value	Units
Surface production rate (SLHL)	(P_0)	4	$\text{atoms g}^{-1} \text{a}^{-1}$
Rock density	(ρ)	2.6	g cm^{-3}
Attenuation length neutrons	(Λ_n)	160	g cm^{-2}
Attenuation length slow muons	(Λ_{μ_s})	1500	g cm^{-2}
Attenuation length fast muons	(Λ_{μ_f})	5300	g cm^{-2}
Pre-slide exposure time	(t_{pre})	14,000	a
Decay constant	(λ)	$4.56 \cdot 10^{-7}$	a^{-1}
Erosion rate	(ε)	0	cm a^{-1}

time, the slope angle of the pre-failure surface becomes increasingly important. If a sampled boulder originates from a relatively flat surface ($< 20^\circ$) near the top of the pre-failure slope, which experienced 14 ka pre-exposure, it could result in an age overestimation of more than 40% in the case of 7-ka-old rockslide deposits.

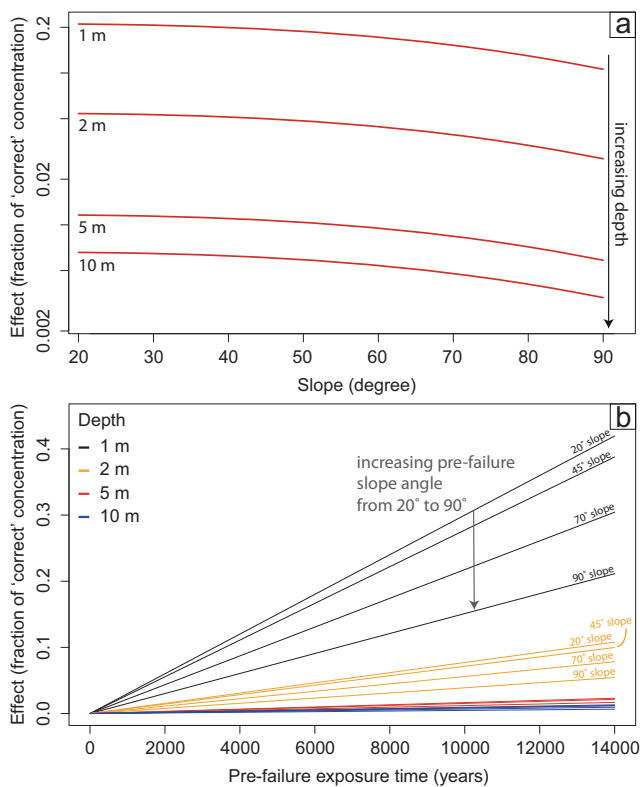


Fig. 2 Results of the Monte Carlo simulation using Eq. (1), showing the effect of inherited TCN concentrations on a 7-ka-old rockslide depending on pre-failure slope and depth with a 7 ka pre-exposure time (log-y-scale) and **b** increasing pre-failure exposure time, slope, and depth. Slope angles are defined in respect to a horizontal surface, so that 90° represent a vertical wall. The effect describes the fraction of inherited TCN concentrations in relation to the TCN concentration expected for 7-ka exposure of a boulder surface

This conceptual sensitivity test reveals that pre-exposure time and depth have a larger control on inherited TCN concentrations than the pre-failure slope angle. They are thus the main parameters to be considered when estimating the uncertainties owing to inheritance. The following case study of a young rock avalanche with known age and reasonably well constrained pre-failure geometry reveals a significant inheritance effect and that the approach of identifying statistical outliers may be deceptive, even for large-volume rock avalanches, and when no outlier can be detected.

Case study: the Punta Cola rock avalanche

Study site and background

The study site is located in the NW-SE trending Aysén fjord in southern Chile (Fig. 3). The fjord cuts the North Patagonian Batholith which is dominated by dioritic to granitic intrusions of Mesozoic to Paleogene age (Cembrano et al. 2002). The high (> 1000 m) relief is dominated by deeply incised glacial fjords and valleys with steep flanks. Glacial dynamic reconstructions by McCulloch et al. (2000) indicate that the study area became ice free ~ 15 ka ago. The existence of a later cooling period with glacial re-advance, equivalent to the Younger Dryas in the Northern Hemisphere, is controversially discussed in the literature and is so far not unequivocally supported by data (Glasser et al. 2004). At present, till and shallow volcanogenic soils cover the slopes in many places, which are mostly forested (Sepúlveda et al. 2010). A combination of long steep slopes and high monthly precipitation rate (> 200 mm/month on average) leads to high erosion rates and landslide activity in the area (Sepúlveda et al. 2010).

On April 21, 2007, after a series of shallow earthquakes, a Mw 6.2 earthquake (focal depth < 10 km) struck the Aysén region (Fig. 3b). The events were related to the activity of the NNE striking Liquiñe-Ofqui fault zone (LOFZ) which crosses the Aysén fjord, resulting in a high density of faults around the study site (Fig. 3c). Around 500 landslides were triggered, including two large-volume rock avalanches (Sepúlveda et al. 2010). The rock avalanches entered the fjord generating displacement waves which impacted the coastal morphology, the regional economy, and the population (Naranjo et al. 2009; Sepúlveda and Serey 2009). The second largest mass movement with a volume of 20.9 Mm^3 is the Punta Cola rock avalanche (Fig. 4). Here, the displaced rock mass produced a maximum run-up height of 150 m on the opposite slope of the failure before it turned 90° and propagated 1–1.5 km along the valley and entered into the fjord. Approximately half of the total volume was deposited offshore impacting the delta area (Oppikofer et al. 2012).

The main scar of the Punta Cola rock avalanche is about 1 km long and up to 760 m wide and mostly covered by debris. It stretches over 500 m of elevation, from c. 250 m a.s.l. to over 750 m a.s.l. It is located more than 1 km below potential permafrost conditions in this area (Falaschi et al. 2015). A topographic break-line across the scar and a set of faults and fractures in the lateral release surface are indicators for a potential active branch of the LOFZ, crossing the basal sliding surface (Figs. 3c and 4; Redfield et al. 2011; Oppikofer et al. 2012). The depth of the failure surface, in relation to the pre-failure slope, was down to 110 m and > 25 m in most places (Oppikofer et al. 2012). A smaller secondary rockslide failed within 10 days after the main rock avalanche

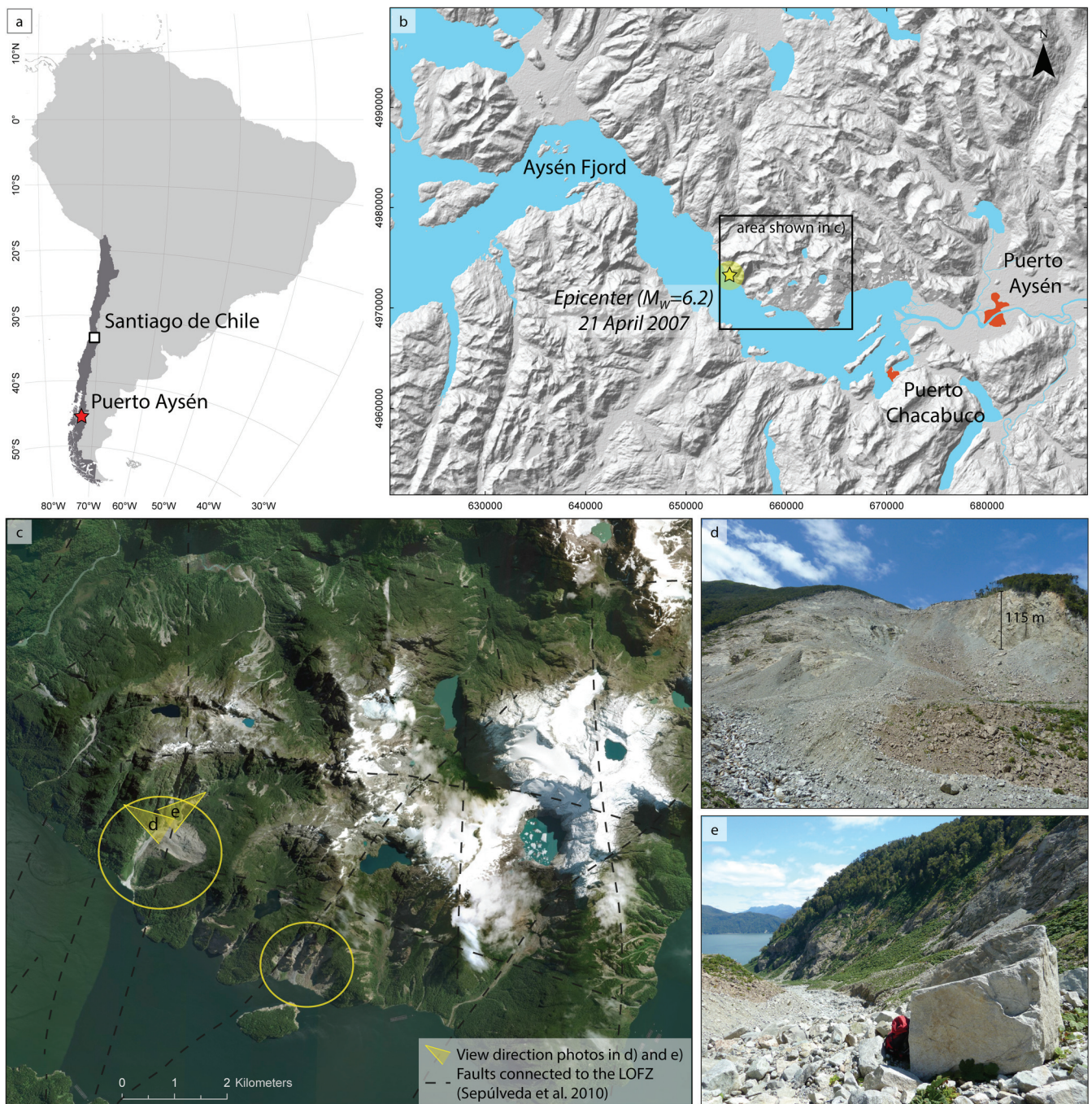


Fig. 3 Overview over the study site: **a** location map of the Aysén fjord in Patagonia, Chile; **b** the Aysén fjord area with the epicenter of the 2007 earthquake (Hillshade created from 17 m ASTER GDEM 2, METI, and NASA); **c** orthophoto from 2015 showing high landslide activity triggered by the 2007 earthquake and two large-scale rock avalanches in yellow circles (imagery source: DigitalGlobe); **d** photo with view as indicated in (c) looking towards the Punta Cola rock avalanche source area with a 115-m-high rock wall for scale; **e** photo with view as indicated in (c) looking down the run-out area towards the fjord from the foot of the source area, backpack in foreground for scale

(Sepúlveda and Serey 2009), where the failure surface was mostly 10–25 m deep (Oppikofer et al. 2012). As evident from aerial photographs (a figure showing an aerial photograph from 1974 and imagery from 2015 are provided in the electronic supplementary material (ESM) 1), the pre-failure slope has been forested before failure and probably throughout most of the Holocene, according to climate records (Glasser et al. 2004).

Methods

Exposure dating with ^{10}Be in quartz

We sampled the deposits of the Punta Cola rock avalanche in a tributary valley of the Aysén fjord in Patagonia, Chile. From the terrestrial portion of the deposits, we collected six samples from boulders higher and wider than 1.5 m using hammer and chisel

(Fig. 4). While sampling, we avoided steep erosional gullies in the deposit that formed since the event deposition. One of the samples (PCOL-08) is from a boulder close to the scar of a secondary failure (Fig. 4).

For best results during the mineral separation, we crushed the samples to a 250–355 μm grain-size fraction. At the Cosmic Ray Isotope Sciences at Dalhousie University (CRISDal) lab, Halifax, Canada, we concentrated and purified the quartz consecutively with magnetic separation at first, then froth flotation and heavy liquid separation and finally leaching with dilute hydrofluoric acid. Quartz purity and Be content in the quartz were verified with a Leeman Lab-Teledyne Prodigy ICP-OES at CRISDal Lab. We added 240 mg of ^9Be carrier to 20 g quartz of each sample and to a process blank without quartz, and the samples were then digested, the Be removed with column chemistry, and pH-controlled precipitations. The BeO was mixed with ultrapure Nb metal, loaded in stainless target holders, and sent to the Center for Accelerator Mass Spectrometry at Lawrence Livermore National Laboratory, USA, for AMS analysis of the $^{10}\text{Be}/^9\text{Be}$ against standard 07KNSTD-3110 (nominal $^{10}\text{Be}/^9\text{Be} = 2.85 \times 10^{-12}$). In order to capture potential contaminations during the chemical procedures, a process blank was added to the batch of six samples. The process blank does not contain any sample material and is processed the same way as the other samples. It thus represents only contamination from processing. After the AMS analysis and before final age calculations, the amount of ^{10}Be atoms in the blank is subtracted from the measured values of each sample.

The final ages were calculated with the version 3 of the online exposure age calculator formerly known as the CRONUS-Earth online exposure age calculator written by G. Balco (2017) and the LSDn scaling scheme. The topographic shielding was derived using inclinometer measurements from the field and the CRONUS-Earth topographic shielding calculator version 2.0 (Marrero et al. 2016). A table with the input parameters for the calculator is provided in the electronic supplementary material (ESM 2).

Approximation of potential pre-slide ^{10}Be concentrations

The goal of this study is to compare the measured ^{10}Be in a landslide with negligible post-depositional exposure, with the concentration distribution of ^{10}Be in the restored pre-failure rock geometry. Recognizing the methodological approach below is simplistic, it provides a first-order estimate of pre-slide concentration in the failed volume. A more accurate determination of 3D distribution of TCN concentration prior to failure with error analysis would need to consider the principal two error sources—i.e., the uncertainty in the paleo-surface geometry and uncertainties in the duration of the pre-failure exposure time (although we can estimate the timing of ice marginal retreat, we cannot estimate the history of previous failures on the slope). Secondary error sources include the angular dependence of the secondary cosmic ray flux, effective attenuation lengths for fast nucleons and muons, and bulk density.

In order to calculate potential ^{10}Be concentrations at and below the pre-failure surface, a 2D profile was extracted from a

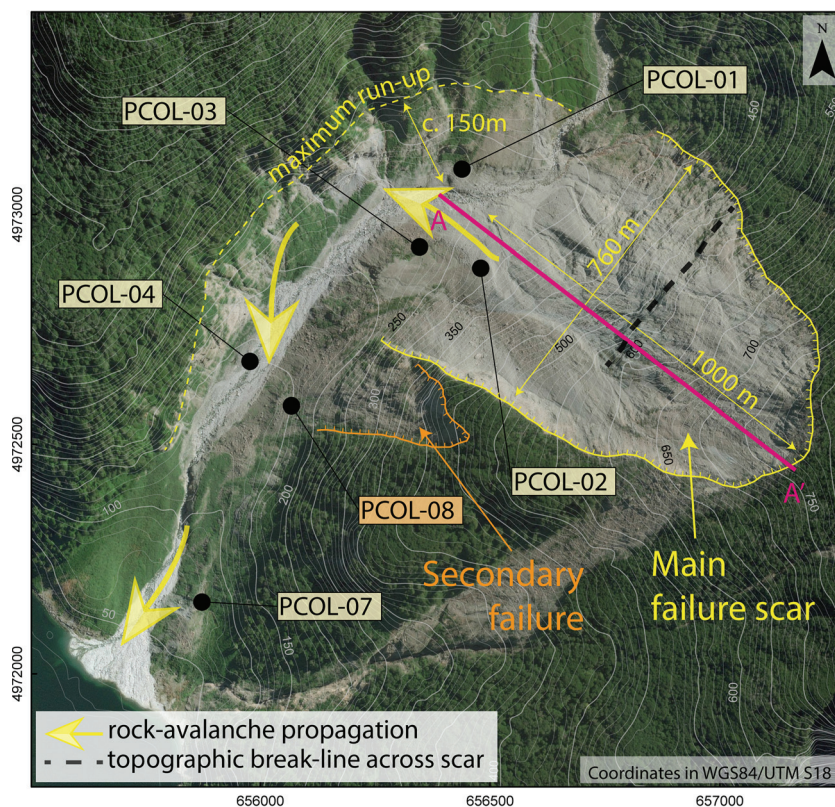


Fig. 4 Orthophoto of the Punta Cola rock avalanche in 2015 with TCN-sample locations and the head scarp of a secondary failure. The pink line A-A' shows the location of the profile section in the following figures (imagery source: DigitalGlobe)

reconstructed pre-failure digital elevation model (DEM). The pre-failure DEM was previously generated using digital photogrammetry techniques on the basis of 11 panchromatic aerial photographs taken in 1998 (Yugsi Molina et al. 2012). The surface production rates along this 2D profile were derived with the LSD scaling scheme (Lifton et al. 2014). Because of the large elevation change from 250 m a.s.l. at the bottom to 750 m a.s.l. at the top of the rockslide scar, the total surface production rate for ^{10}Be ranges from 4.78 to 7.38 atoms $\text{g}^{-1} \text{a}^{-1}$. The topographic shielding from distal objects (valley walls) was approximated based on azimuthal and gradient measurements at the bottom of the failure scar, where it was expected to be maximal. A gradual decrease in topographic shielding to zero is expected with increasing elevation along the slope. For the local geometric shielding, the gradient for each section between two points along the profile was derived. Based on the resolution of the reconstructed pre-failure surface (Yugsi Molina et al. 2012), the horizontal distance between two value points along the 2D profile is 2.7 m. To smooth topographic irregularities arising from the photogrammetric reconstruction (e.g., caused by vegetation), a linear one-point step moving window over nine values ($\sim 22\text{-m}$ horizontal distance) was applied along the 2D transect. Using these predicted slopes, the CRONUS Earth topographic shielding calculator v2 (Marrero et al. 2016) was used to calculate a shielding factor for the local (2.7 m) slopes which was then multiplied by the previously approximated topographic shielding factors to produce a total shielding factor for each point along the profile.

The ^{10}Be concentration at the surface and at depth below each point along the profile was then approximated with Eq. (1) for down to 100-m depth with 1-m increments. The input parameters are the values compiled in Table 1 but for an assumed pre-slide exposure time of 15 ka, according to the regional deglaciation history. For a complete 2D concentration distribution, the calculated values were then contoured in ArcGIS with the natural neighbor geostatistical fit.

Results

TCN-dating using ^{10}Be

A low ^{10}Be concentration was measured in all six samples, which when corrected for the process blank of 9.53×10^3 atoms allowed the calculation of apparent exposure ages of hundreds of years, not 9 years, the actual event age (Table 2). However, because of the low concentrations, measurement uncertainties were controlled by counting statistics and were 11–33%. The process blank correction resulted in the subtraction of 6–40% of the measured concentrations. The largest uncertainty is connected to a concentration of 2.39×10^4 atoms before correction, and 7.19×10^2 atoms after correction, resulting in a 40% effect in relation to the apparent age.

Although Savi et al. (2017) show that using one blank only leads to additional uncertainties, a compilation of blanks at CRISDal Lab measured during the last 2 years at the same accelerator facility, using the same phenacite-based carrier and sample preparation, demonstrates that the process blank lies well within 1σ of the arithmetic mean ($N=16$) of $9.24 \times 10^3 \pm 5.74 \times 10^3$ atoms (ESM 1), which is the commonly accepted statistical approach for validating the blank correction (Shakun et al. 2018).

Table 2 Apparent ^{10}Be concentrations and calculated ages (a table with all input parameters for the online calculator is provided in ESM 2)

Sample name	Elevation (m a.s.l.)	Quartz mass (g)	^{10}Be atoms before blank subtraction (atoms)	^{10}Be atoms after blank subtraction (atoms)	^{10}Be atoms uncertainty (atoms)	^{10}Be concentration (atoms g^{-1})	^{10}Be concentration uncertainty (atoms g^{-1})	Exposure age (years)
PCOL-01	240	20.0046	3.19×10^4	2.24×10^4	2.93×10^3	1.12×10^3	1.47×10^2	328 ± 43
PCOL-02	247	20.0077	4.28×10^4	3.33×10^4	4.43×10^3	1.66×10^3	2.22×10^2	458 ± 67
PCOL-03	224	20.0208	2.39×10^4	1.44×10^4	4.99×10^3	7.19×10^2	2.49×10^2	216 ± 76
PCOL-04	111	20.0085	3.21×10^4	2.26×10^4	3.61×10^3	1.13×10^3	1.81×10^2	370 ± 63
PCOL-07	65	20.0196	3.29×10^4	2.34×10^4	3.17×10^3	1.17×10^3	1.58×10^2	379 ± 56
PCOL-08	144	20.0091	1.49×10^5	1.39×10^5	3.36×10^4	6.97×10^3	1.68×10^3	1755 ± 436

All calculated surface exposure ages of the sampled boulders exceed the post-failure time of 9 years by several hundred years. The mean age of the three samples PCOL-01, PCOL-04, and PCOL-07 lies within 1σ uncertainty of the individual ages at 354 ± 36 (error-weighted mean). The average age of all samples, except for PCOL-08 is 356 ± 32 (error-weighted mean) and thus overestimates the real failure time by 347 ± 32 years (3856%). The apparent age of PCOL-08 is five times higher than the average of the rest and has a large error of 25%. As noted earlier, there is a possibility that this boulder had a different pre-failure history than the other five samples because it appears to have originated from a different source.

Approximation of potential pre-slide ^{10}Be concentrations

Using the available pre-failure geometry (Oppikofer et al. 2012), and the approximate duration of exposure, we estimated the TCN concentrations to the depth of the eventual slide plane along the 2D transect A-A' (Figs. 4 and 5). Concentrations at the surface are as high as $100,000 \text{ atoms g}^{-1}$, but diminish four orders of magnitude to the depth of the reconstructed failure plane. Meter scale topographic variations in the pre-slide geometry were not resolved and may influence the actual concentration with depth. Likewise, pre-event erosion, shielding by ash and snow, and the long-term history of exposure prior to the last glaciation would need to be known for a more realistic volumetric distribution of ^{10}Be concentration. Nevertheless, our 2D approximation enables an assessment of the potential pre-slide (inherited) concentration of the dated boulders. The concentration ranges of our measured boulder samples help to estimate their height-depth source region below the pre-slide cliff face (gray-scale ranges, Fig. 6). Because of its relatively high ^{10}Be concentration, the potential pre-failure depth of PCOL-08 cannot be visualized in this figure. The values, however, suggest that the sampled boulder surface originated from a depth $< 2 \text{ m}$, supporting the hypothesis, that it was part of the relatively shallow secondary failure (Fig. 4). It has therefore been

removed from the following analysis, concentrating on the main failure.

Two concentration-depth profiles visualize the difference between low-elevation locations with higher topographic shielding and lower surface production rates, and locations from the top of the pre-failure slope (Fig. 7). They demonstrate the expected increase of surface production and hence a higher penetration depth with increasing elevation and decreasing slope angle.

The depth profiles show that sample PCOL-02 most likely originated from a depth $< 5 \text{ m}$ for the approximated scenario of 15 ka pre-exposure, and both the lower or higher locations. The samples PCOL-01, PCOL-04, and PCOL-07 are very close and potentially originate from $\sim 5\text{-m}$ depth in the lower part of the slope or $\sim 8\text{-m}$ depth in the higher elevated locations. The apparently deepest sample is PCOL-03 with a depth between 10 and 13 m. None of the sampled boulders seem to originate from a greater pre-failure depth than 13 m, which is significantly shallower than the mean depth of the reconstructed pre-failure volume.

Discussion

The results of the sampled boulders overestimate the real failure timing by 207–1746 years, which due to the young real age results in 2400–19,500% relative overestimation. The magnitude of potential age overestimation due to inheritance depends strongly on the pre- and post-failure exposure durations, and pre-failure boulder depth. Therefore, inheritance is relatively low for old rock avalanches, and for shallow failures with short pre-exposure durations. However, for the age determination of young rockslides with a potentially long pre-exposure, the inheritance becomes increasingly significant (Fig. 2).

Three of our samples agree in age within their individual 1σ uncertainties, which would lead to the incorrect interpretation that inheritance is negligible, when dating rockslide deposits of an unknown age. Instead, these boulders, and two others from the same 9 years post-failure exposure, had a factor of 40× more

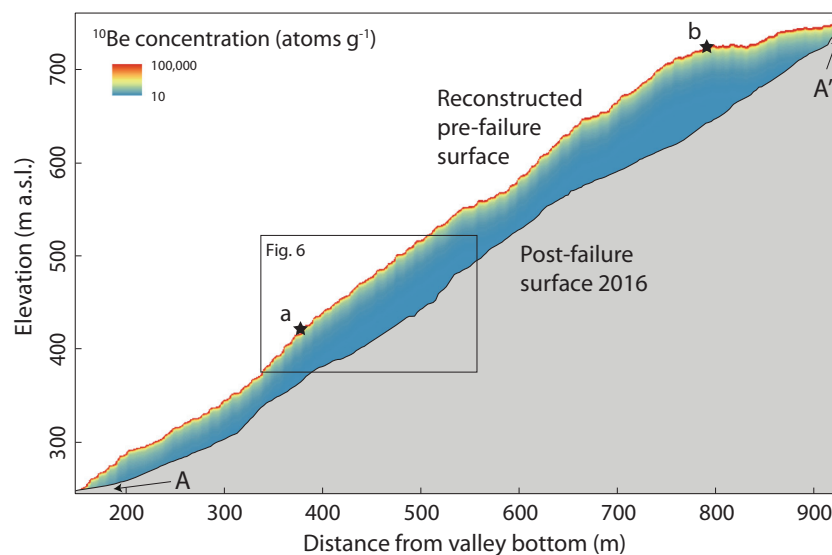


Fig. 5 Potential ^{10}Be concentration distribution in the pre-failure slope for an exposure time of 15,000 years. The location of the profile A-A' is marked in Fig. 4. Note that the color range is plotted with a stretch factor of 3 to make shallow high values visible

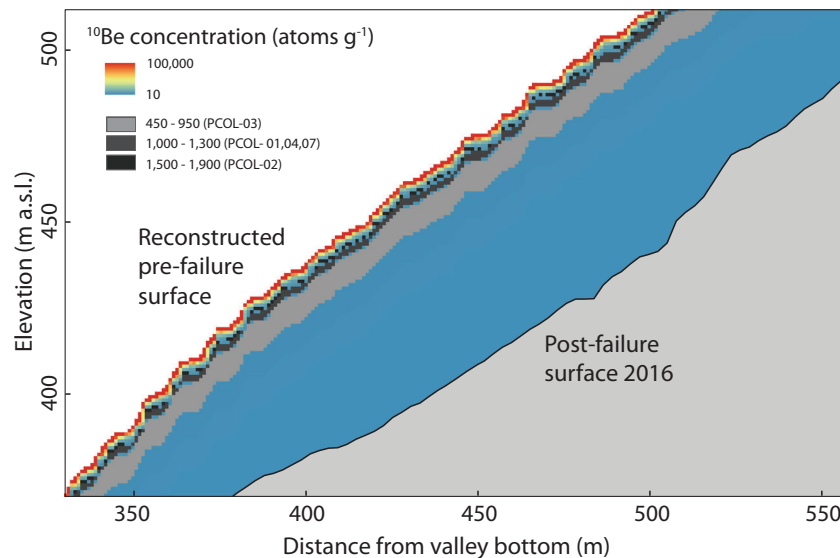


Fig. 6 Detailed plot as indicated in Fig. 5 (without stretch factor and hence linear coloring), with the location of the concentration ranges of the analyzed samples. The concentration range of PCOL-08 is not plotted

concentration than expected, even after process-blank subtraction. A similar result has been presented by Sewell et al. (2006) where the boulder ages generally seem to exceed the ages derived from a failure surface of known age. Although of smaller extent, the dating of a historic rock-avalanche event of known age (AD 1717) in Italy resulted in overestimations between 15 and 65% (Akçar et al. 2012).

While the depth of the detached rock mass at the Punta Cola rock avalanche was up to 110 m and > 25 m in most places (Oppikofer et al. 2012), the amount of inherited ^{10}Be atoms indicates that none of the sampled boulders originated from a greater depth than 13 m, with a cluster between 5 and 8-m depth. This assumes that we did not underestimate the blank correction, which would reduce the apparent ^{10}Be concentration in the samples and thus increase the depth of the potential pre-slide boulder positions. Even if the actual blank subtraction was a full standard deviation higher than the arithmetic mean of 16 process blanks, making the post-event concentrations subsequently lower, the concentrations would still be non-zero. Exposure ages would then lie between 134 ± 47 and 1690 ± 420 years and the boulders originate from not more than 18-m depth, still shallower than the estimated mean (Fig. 7; ESM 1). The number of boulder TCN concentrations needed to reliably estimate the failure volume would be significant given the low probability of achieving an average depth based on the six measurements.

It has been observed previously that boulders visibly originating from the pre-failure surface can settle on top of the rock-avalanche deposits (McSaveney 1978; Hadley 1978; Ivy-Ochs et al. 2009). Dufresne (2012) demonstrated that material, which has been entrained at the bottom of a rock avalanche, most likely stays at the bottom and therefore will comminute more rapidly than the near surface boulders. This also suggests that the rock-avalanche material does usually not get thoroughly mixed throughout the entire depth. One of the rockslide-body types first described by Shreve (1968) and later adapted by others (e.g., Strom 2006) supports this, where the rock mass “moves as a flexible sheet”, representing the original geological sequence after

deposition. The second model presented by Strom (2006) suggests a stratified deposition, in the order of superimposed lithologies along the slope. This second model implies that the top layer of the rock-avalanche deposits represents material from the uppermost often relatively shallow pre-failure rock mass. Furthermore, it has been shown that there is substantial disintegration of rock mass close to the sliding surface (Davies and McSaveney 2002, 2009), while the shallowest meters of rock-avalanche deposits is often coarse blocky material, transported at the surface (Dunning et al. 2005). Although we must also consider the potential for buoyancy forces that support the larger surface-area clasts, the TCN measurements and reconstructions at the Punta Cola combined with observations elsewhere suggest that the boulders that we normally target of exposure sampling at the surface of rock-avalanche deposits are likely to originate from a rather shallow section of the pre-failure mass. In other words, our sampling strategy optimizes the probability of significant inheritance.

In areas that have not been glaciated during the last glacial periods, the pre-exposure time can reach many tens of thousands of years, leading to significant amounts of inherited TCNs. For example, in the non-glaciated part of northwestern Argentina, the exposure age of c. 10 ka from a failure surface differs from the corresponding deposit ages by c. 5 ka (Hermanns et al. 2004). We therefore suggest that in such settings, the TCN exposure dating technique should be complemented by other dating methods in order to obtain reliable ages on rock-avalanche deposits. In regions that have been glaciated during the most recent glaciation, the potential error due to inherited TCN concentrations seems to lie within a few hundred years. Age determinations below 1000 years may therefore be challenging.

Conclusion

The apparent exposure ages of six boulders from the 9-year-old Punta Cola rock-avalanche deposit overestimate the real age by several hundred years. A similar pre-failure exposure history on a rock-avalanche that was several thousand years ago would be significantly less affected by inheritance. This study affirms the assumption that the source depth

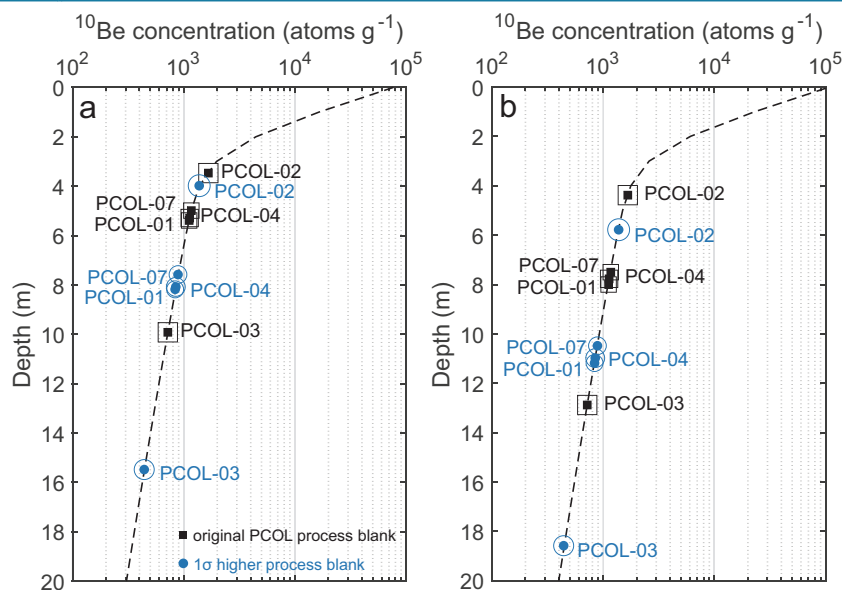


Fig. 7 Apparent ^{10}Be concentration depth profiles at locations **a** and **b** in Fig. 5 with potential pre-failure depth of our analyzed samples. Sample concentrations derived with the original PCOL process blank are plotted as black squares, and sample concentrations derived with blank subtraction one standard deviation higher than the according process blank (see “Discussion” and ESM 1) are plotted as blue circles. Uncertainties are plotted as black boxes and blue circles around the markers, respectively

of a sampled boulder is a first order control of the inherited TCN concentrations. This is true even if the pre-failure volume and geometry is reliably reconstructed, because the results suggest that all six of the large boulders sampled for exposure dating were derived from a depth much shallower than the average depth of the reconstructed volume. Our study also supports previous studies, demonstrating that large boulders on top of rockslide deposits may preferentially originate from rather shallow (< 20 m) depth, even if the maximum depth of a rock avalanche is > 100 m.

However, if the pre-failure history and geometry are unknown, other approaches to mitigate the effect of inherited TCN concentrations are necessary. For instance, exposure dating the rockslide scarp in addition to the deposits can reduce the uncertainty. The Punta Cola experiment suggests that more than three boulders may be required to apply the currently widely used premise that multiple boulders with TCN concentrations within one standard deviation of their mean implies that inheritance is negligible.

Acknowledgements

The authors acknowledge the support of S. Sepúlveda and his research team, giving the first author the opportunity to join the field campaign in January 2016 and collect the samples. The TCN sample preparation was completed by the first author at CRISDal at Dalhousie University under supervision of G. Yang. We thank two anonymous reviewers for their suggestions that allowed improving the former version of the manuscript.

Funding Information

The study is part of the project “CryoWALL – Permafrost slopes in Norway” (243784/CLE) funded by the Research Council of Norway (RCN). Additional funding was provided by the Norwegian Geological Survey, Trondheim, and the Department of Geosciences, University of Oslo. J. Gosse acknowledges support for the CRISDal Lab from Canada Foundation for Innovation (21305 and 36158), NSERC, and NSRIT grants.

References

- Akçar N, Deline P, Ivy-Ochs S, Alfimov V, Hajdas I, Kubik PW, Christl M, Schlüchter C (2012) The AD 1717 rock avalanche deposits in the upper Ferret Valley (Italy): a dating approach with cosmogenic ^{10}Be . *J Quat Sci* 27:383–392. <https://doi.org/10.1002/jqs.1558>
- Anderson RS, Repka JL, Dick GS (1996) Explicit treatment of inheritance in dating depositional surfaces using in situ ^{10}Be and ^{26}Al . *Geology* 24:47. [https://doi.org/10.1130/0091-7613\(1996\)024<0047:ETOID>2.3.CO;2](https://doi.org/10.1130/0091-7613(1996)024<0047:ETOID>2.3.CO;2)
- Balco G (2017) Documentation – v3 exposure age calculator. Online source: <https://sites.google.com/a/bgco.org/v3docs/>. Accessed Sept 2018
- Ballantyne CK, Stone JO (2004) The Beinn Alligin rock avalanche, NW Scotland: cosmogenic ^{10}Be dating, interpretation and significance. *The Holocene* 14:448–453
- Ballantyne CK, Sandeman GF, Stone JO, Wilson P (2014) Rock-slope failure following Late Pleistocene deglaciation on tectonically stable mountainous terrain. *Quat Sci Rev* 86:144–157. <https://doi.org/10.1016/j.quascirev.2013.12.021>
- Borchers B, Marrero S, Balco G, Caffee M, Goehring B, Lifton N, Nishiizumi K, Phillips F, Schaefer J, Stone J (2016) Geological calibration of spallation production rates in the CRONUS-Earth project. *Quat Geochronol* 31:188–198. <https://doi.org/10.1016/j.quageo.2015.01.009>
- Cembrano J, Lavenu A, Reynolds P, Arancibia G, López G, Sanhuenza A (2002) Late Cenozoic transpressional ductile deformation north of the Nazca–South America–Antarctica triple junction. *Tectonophysics* 354:289–314
- Cossart E, Braucher R, Fort M, Bourlès DL, Carcaillet J (2008) Slope instability in relation to glacial debudding in alpine areas (upper durance catchment, southeastern France): evidence from field data and ^{10}Be cosmic ray exposure ages. *Geomorphology* 95:3–26. <https://doi.org/10.1016/j.geomorph.2006.12.022>
- Davies TR, McSaveney MJ (2002) Dynamic simulation of the motion of fragmenting rock avalanches. *Can Geotech J* 39:789–798. <https://doi.org/10.1139/t02-035>
- Davies TR, McSaveney MJ (2009) The role of rock fragmentation in the motion of large landslides. *Eng Geol* 109:67–79. <https://doi.org/10.1016/j.enggeo.2008.11.004>
- Dortch JM, Owen LA, Haneberg WC, Caffee MW, Dietsch C, Kamp U (2009) Nature and timing of large landslides in the Himalaya and Transhimalaya of northern India. *Quat Sci Rev* 28:1037–1054. <https://doi.org/10.1016/j.quascirev.2008.05.002>
- Dufresne A (2012) Granular flow experiments on the interaction with stationary runoff path materials and comparison to rock avalanche events. *Earth Surf Process Landf* 37:1527–1541. <https://doi.org/10.1002/esp.3296>
- Dunning S, Petley D, Strom A (2005) The morphologies and sedimentology of valley confined rock-avalanche deposits and their effect on potential dam hazard. In: Hungr O, Fell R, Couture R, Eberhardt E (eds) *Proceedings of the international conference on landslide risk management*. Taylor & Francis, Balkema, London

- Falaschi D, Tadono T, Masiokas M (2015) Rock glaciers in the Patagonian Andes: an inventory for the Monte San Lorenzo (Cerro Cochrane) massif, 47° s. *Geogr Ann Ser Phys Geogr* 97:769–777. <https://doi.org/10.1111/geoa.12113>
- Glasser NF, Harrison S, Winchester V, Aniya M (2004) Late Pleistocene and Holocene palaeoclimate and glacier fluctuations in Patagonia. *Glob Planet Chang* 43:79–101. <https://doi.org/10.1016/j.gloplacha.2004.03.002>
- Hadley JB (1978) Madison Canyon rockslide, Montana, U.S.A. In: Voight B (ed) *Rockslides and avalanches*. Elsevier, Amsterdam, pp 167–180
- Hermanns RL, Niedermann S, Garcia AV, Sosa Gomez J, Stecker MR (2001) Neotectonics and catastrophic failure of mountain fronts in the southern intra-Andean Puna Plateau, Argentina. *Geology* 29:619. [https://doi.org/10.1130/0091-7613\(2001\)029<0619:NACFOM>2.0.CO;2](https://doi.org/10.1130/0091-7613(2001)029<0619:NACFOM>2.0.CO;2)
- Hermanns RL, Niedermann S, Ivy-Ochs S, Kubik PW (2004) Rock avalanching into a landslide-dammed lake causing multiple dam failure in Las Conchas valley NW Argentina? Evidence from surface exposure dating and stratigraphic analyses. *Landslides* 1:113–122
- Hermanns RL, Oppikofer T, Dahle H, Eiken T, Ivy-Ochs S, Blikra LH (2013) Understanding long-term slope deformation for stability assessment of rock slopes: the case of the Oppstadhornet rockslide, Norway. In: *Proceedings of the International Conference Vajont 1963–2013*, Padua, Italy, 8–10 October 2013
- Hermanns RL, Schleiher M, Böhme M, Blikra LH, Gosse JC, Ivy-Ochs S, Hilger P (2017) Rock-avalanche activity in W and S Norway peaks after the retreat of the Scandinavian Ice Sheet. In: Mikoš M, Vilímek V, Yin Y, Sassa K (eds) *Advancing culture of living with landslides*. Springer International Publishing, Cham, pp 331–338
- Hewitt K, Gosse J, Clague JJ (2011) Rock avalanches and the pace of late Quaternary development of river valleys in the Karakoram Himalaya. *Geol Soc Am Bull* 123:1836–1850
- Hidy AJ, Gosse JC, Froese DG, Bond JD, Rood DH (2013) A latest Pliocene age for the earliest and most extensive Cordilleran Ice Sheet in northwestern Canada. *Quat Sci Rev* 61:77–84. <https://doi.org/10.1016/j.quascirev.2012.11.009>
- Hilger P, Hermanns RL, Gosse JC, Jacobs B, Etzelmüller B, Krautblatter M (2018) Multiple rock-slope failures from Mannen in Romsdal Valley, western Norway, revealed from Quaternary geological mapping and 10Be exposure dating. *The Holocene*. <https://doi.org/10.1177/0959683618798165>
- Ivy-Ochs S, Poschinger AV, Synal H-A, Maisch M (2009) Surface exposure dating of the Flims landslide, Graubünden, Switzerland. *Geomorphology* 103:104–112. <https://doi.org/10.1016/j.geomorph.2007.10.024>
- Lal D (1991) Cosmic ray labeling of erosion surfaces: in situ nuclide production rates and erosion models. *Earth Planet Sci Lett* 104:424–439
- Lifton N, Sato T, Dunai TJ (2014) Scaling in situ cosmogenic nuclide production rates using analytical approximations to atmospheric cosmic-ray fluxes. *Earth Planet Sci Lett* 386:149–160. <https://doi.org/10.1016/j.epsl.2013.10.052>
- Marrero SM, Phillips FM, Borchers B, Lifton N, Aumer R, Balco G (2016) Cosmogenic nuclide systematics and the CRONUScalc program. *Quat Geochronol* 31:160–187. <https://doi.org/10.1016/j.quageo.2015.09.005>
- McCulloch RD, Bentley MJ, Purves RS et al (2000) Climatic inferences from glacial and palaeoecological evidence at the last glacial termination, southern South America. *J Quat Sci* 15:15
- McSaveney MJ (1978) Sherman Glacier rock avalanche, Alaska, U.S.A. In: Voight B (ed) *Rockslides and avalanches*. Elsevier, Amsterdam, pp 197–258
- Mitchell WA, McSaveney MJ, Zondervan A, Kim K, Dunning SA, Taylor PJ (2007) The Keylong Serai rock avalanche, NW Indian Himalaya: geomorphology and palaeoseismic implications. *Landslides* 4:245–254. <https://doi.org/10.1007/s10346-007-0085-0>
- Nagelisen J, Moore JR, Vockenhuber C, Ivy-Ochs S (2015) Post-glacial rock avalanches in the Obersee Valley, Glarner Alps, Switzerland. *Geomorphology* 238:94–111. <https://doi.org/10.1016/j.geomorph.2015.02.031>
- Naranjo JA, Arenas M, Clavero J, Muñoz O (2009) Mass movement-induced tsunamis: main effects during the Patagonian Fjordland seismic crisis in Aisén (45°25'S), Chile. *Andean Geol* 9
- Oppikofer T, Hermanns RL, Redfield TF, Sepúlveda SA, Duhart P, Bascuñán I (2012) Morphologic description of the Punta Cola rock avalanche and associated minor rockslides caused by the 21 April 2007 Aysén earthquake (Patagonia, southern Chile). *Rev Asoc Geol Argent* 69:339–353
- Ostermann M, Ivy-Ochs S, Sanders D, Prager C (2016) Multi-method (^{14}C , ^{36}Cl , ^{234}U / ^{230}Th) age bracketing of the Tschirgant rock avalanche (Eastern Alps): implications for absolute dating of catastrophic mass-wasting. *Earth Surf Process Landf* 42:1110–1118. <https://doi.org/10.1002/esp.4077>
- Pánek T (2015) Recent progress in landslide dating: a global overview. *Prog Phys Geogr* 39:168–198. <https://doi.org/10.1177/0309133314550671>
- Redfield TF, Hermanns RL, Oppikofer T, Duhart P, Mella M, Derch P, Bascuñán I, Arenas M, Fernández J, Sepúlveda S, et al. (2011) Analysis of the 2007 earthquake-induced Punta Cola rockslide and tsunami, Aysén Fjord, Patagonia, Chile (45.3° S, 73.0° W). *15 Sanchez G, Rolland Y, Corsini M, Braucher R, Bourlès D, Arnold M, Aumaitre G (2010) Relationships between tectonics, slope instability and climate change: cosmic ray exposure dating of active faults, landslides and glacial surfaces in the SW Alps. Geomorphology* 117:1–13. <https://doi.org/10.1016/j.geomorph.2009.10.019>
- Savi S, Tofelde S, Wittmann H, Castino F, Schildgen T (2017) Determination limits for cosmogenic ^{10}Be and their importance for geomorphic applications. *Earth Surf Dyn Discuss*:1–26. <https://doi.org/10.5194/esurf-2017-30>
- Schwartz S, Zerathe S, Jongmans D, Baillet L, Carcaillet J, Audin L, Dumont T, Bourlès D, Braucher D, Lebruc V (2017) Cosmic ray exposure dating on the large landslide of Séchillienne (Western Alps): a synthesis to constrain slope evolution. *Geomorphology* 278:329–344. <https://doi.org/10.1016/j.geomorph.2016.11.014>
- Sepúlveda SA, Serey A (2009) Tsunamiogenic, earthquake-triggered rock slope failures during the April 21, 2007 Aisén earthquake, southern Chile (45.5°S). *Andean Geology* 36, number 1
- Sepúlveda SA, Serey A, Lara M, Pavez A, Rebolledo S (2010) Landslides induced by the April 2007 Aysén Fjord earthquake, Chilean Patagonia. *Landslides* 7:483–492. <https://doi.org/10.1007/s10346-010-0203-2>
- Sewell RJ, Barrows TT, Campbell SDG, Fifield LK (2006) Exposure dating (^{10}Be , ^{26}Al) of natural terrain landslides in Hong Kong, China. In: *In situ-produced cosmogenic nuclides and quantification of geological processes*. Geological Society of America, pp 131–146
- Shakun JD, Corbett LB, Bierman PR, Underwood K, Rizzo DM, Zimmermann SR, Caffee MW, Naish T, Golledge NR, Hay CC (2018) Minimal East Antarctic Ice Sheet retreat onto land during the past eight million years. *Nature* 558:284–287. <https://doi.org/10.1038/s41586-018-0155-6>
- Shreve RL (1968) The Blackhawk landslide, Geological Society of America Special Paper. N 108
- Strom A (2006) Morphology and internal structure of rockslides and rock avalanches: grounds and constraints for their modelling. In: *Landslides from Massive Rock Slope Failure*. Springer, pp 305–326
- Yugi Molina FX, Oppikofer T, Hermanns RL, Redfield TF, Bascuñán I, Loew S, Sepúlveda SA (2012) Mechanism and volume estimation of the 2007 Punta Cola rockslide-debris avalanche using terrestrial laser scanning and aerial photogrammetry. *Landslides Eng Slopes Prot Soc Improv Underst* 1:553–559
- Zerathe S, Lebourg T, Braucher R, Bourlès D (2014) Mid-Holocene cluster of large-scale landslides revealed in the southwestern Alps by ^{36}Cl dating. Insight on an Alpine-scale landslide activity. *Quat Sci Rev* 90:106–127. <https://doi.org/10.1016/j.quascirev.2014.02.015>

Electronic supplementary material The online version of this article (<https://doi.org/10.1007/s10346-018-01132-0>) contains supplementary material, which is available to authorized users.

P. Hilger (✉) · R. L. Hermanns

Geohazards and Earth Observation,
Geological Survey of Norway,
N-7491, Trondheim, Norway
Email: paula.hilger@ngu.no

P. Hilger

Department of Geosciences,
University of Oslo,
N-0316, Oslo, Norway

J. C. Gosse

Department of Earth Sciences,
Dalhousie University,
Halifax, B3H 4R2, Canada

R. L. Hermanns

Department of Geoscience and Petroleum,
Norwegian University of Science and Technology,
N-7491, Trondheim, Norway

Paper II

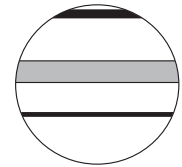
Hilger, P., Hermanns, R.L., Gosse, J.C., Jacobs, B. Etzelmüller, B., Krautblatter, M.:

Multiple rock-slope failures from Mannen in Romsdal Valley, western Norway, revealed from Quaternary geological mapping and ^{10}Be exposure dating


The Holocene 28(12), 1841-1854, doi:10.1177/0959683618798165

Note on contributions

The candidate wrote the paper and carried out all field work and analyses, including Quaternary mapping, geophysical surveys, ^{10}Be sample processing and analyses and calculation of exposure ages. The project idea comes from the second author who contributed significantly during field work and the writing process. Sample preparation and analyses were advised by the third author. All authors contributed to field work and finalising the manuscript.



Multiple rock-slope failures from Mannen in Romsdal Valley, western Norway, revealed from Quaternary geological mapping and ^{10}Be exposure dating

The Holocene
2018, Vol. 28(12) 1841–1854
© The Author(s) 2018
Article reuse guidelines:
sagepub.com/journals-permissions
DOI: 10.1177/0959683618798165
journals.sagepub.com/home/hol


Paula Hilger,^{1,2} Reginald L Hermanns,^{1,3}  John C Gosse,⁴
Benjamin Jacobs,⁵ Bernd Etzelmüller² and Michael Krautblatter⁵

Abstract

Oversteepened valley walls in western Norway have high recurrences of Holocene rock-slope failure activity causing significant risk to communities and infrastructure. Deposits from six to nine catastrophic rock-slope failure (CRSF) events are preserved at the base of the Mannen rock-slope instability in the Romsdal Valley, western Norway. The timing of these CRSF events was determined by terrestrial cosmogenic nuclide dating and relative chronology due to mapping Quaternary deposits. The stratigraphical chronology indicates that three of the CRSF events occurred between 12 and 10 ka, during regional deglaciation. Congruent with previous investigations, these events are attributed to the debuttrressing effect experienced by steep slopes following deglaciation, during a period of paraglacial relaxation. The remaining three to six CRSF events cluster at 4.9 ± 0.6 ka (based on 10 cosmogenic ^{10}Be samples from boulders). CRSF events during this later period are ascribed to climatic changes at the end of the Holocene thermal optimum, including increased precipitation rates, high air temperatures and the associated degradation of permafrost in rock-slope faces. Geomorphological mapping and sedimentological analyses further permit the contextualisation of these deposits within the overall sequence of post-glacial fjord-valley infilling. In the light of contemporary climate change, the relationship between CRSF frequency, precipitation, air temperature and permafrost degradation may be of interest to others working or operating in comparable settings.

Keywords

climate change, cluster, cosmogenic ^{10}Be dating, debuttrressing, fjord-valley infill, rockslides

Received 17 April 2018; revised manuscript accepted 26 June 2018

Introduction

Formerly glaciated valleys often exhibit slope instabilities that lead to catastrophic rock-slope failures (CRSF; Hermanns and Longva, 2012). Although CRSF are often attributed to seismic activity (e.g. Agliardi et al., 2009; Hewitt et al., 2008; Korup, 2004; Moreiras et al., 2015; Penna et al., 2011), many are triggered by climatogenic destabilisations owing to post-glacial debuttrressing, permafrost degradation or precipitation increases (Evans and Clague, 1994; Soldati et al., 2004; Trauth et al., 2000). Deglaciation and valley adjustment in the Lateglacial and Holocene provoke localised stress concentrations in steep fjord rock walls exceeding the crack initiation threshold; coincidentally advancing and retreating permafrost significantly alters rock mass strength properties (Krautblatter and Leith, 2015; Leith et al., 2014). Both in situ stress evolution and rapidly changing material strength due to permafrost advance play a key role in controlling rock slope failure evolution. Changing permafrost conditions alter the strength of (1) intact rock, (2) ice infill and (3) rock ice interfaces by 20–80% and freezing causes high cryostatic stresses and irreversible rock fatigue (Jia et al., 2015, 2017; Krautblatter et al., 2013). Previous studies from Scotland and Norway indicate that CRSF commonly occur within the first 2 ka of deglaciation (Ballantyne and Stone, 2013; Cossart et al., 2008; Holm et al., 2004). Events within this time window are commonly attributed to ‘debuttrressing’ – the unloading and stress release experienced

in paraglacial environments following deglaciation, although it is difficult to preclude seismicity caused by post-glacial isostatic adjustment. CRSF occurring outside of this interval are often attributed to changing climate, in particular higher precipitation rates, air temperatures and, in some cases, permafrost degradation (Allen et al., 2009; Fischer et al., 2006; Krautblatter et al., 2013; Nagelisen et al., 2015). The temporal and spatial distribution of CRSF in Norway reflects the strong influence of debuttrressing on slope stability. However, continued rock-slope activity throughout the Holocene has also been identified (Blikra et al., 2006; Hermanns et al., 2017). Few studies have investigated the relation

¹Geohazard and Earth Observation, Geological Survey of Norway, Norway

²Department of Geosciences, University of Oslo, Norway

³Department of Geoscience and Petroleum, Norwegian University of Science and Technology, Norway

⁴Department of Earth Sciences, Dalhousie University, Canada

⁵Department of Civil, Geo and Environmental Engineering, Technical University of Munich, Germany

Corresponding author:

Paula Hilger, Geohazard and Earth Observation, Geological Survey of Norway, N-7491 Trondheim, Norway.
Email: paula.hilger@ngu.no

between climatic variability and CRSF frequency in Norway (Blikra and Christiansen, 2014; Böhme et al., 2015).

A precise geochronology is necessary to establish cause and assess hazard of CRSF which may have recurrences exceeding millennia. Until the late 90s, most CRSF event chronologies relied on independently dated stratigraphically related sediments for limiting or contemporaneous age control (e.g. Clavero et al., 2002; Topping, 1993). For post-glacial events, radiocarbon dating was frequently used (Hermanns et al., 2000; Orwin et al., 2004; Ostermann et al., 2016). Recently, terrestrial cosmogenic nuclide (TCN) exposure dating is more frequently used to directly date CRSF deposits (Gosse and Phillips, 2001; Ivy-Ochs and Kober, 2008; Sturzenegger et al., 2015; Ostermann et al., 2016). Recent studies have utilised TCN methods to determine the timing of CRSF events and better relate them to otherwise hypothetical triggering mechanisms (e.g. Ballantyne et al., 1998; Dortch et al., 2009; Hermanns et al., 2004, 2015). However, in most mountain environments, the limited number of investigations precludes a comprehensive assessment of the conditioning variables that lead to failure. Exceptions exist for the European Alps, Scotland and Norway where many studies have been conducted (e.g. Ballantyne et al., 2014; Hermanns et al., 2017; Ivy-Ochs et al., 2017).

The rock-slope instability 'Mannen' in Romsdal Valley, Norway, is located in a key region for tourism and is situated above the farming community of Marstein. The risk of rock-slope failure at Mannen has been considered high owing to geological structural pre-conditioning and observed deformation and sliding rates of cliff blocks. In this region, the recurrence interval for a 0.15 Mm³ failure is estimated to be <100 years while the recurrence of a 2–4 Mm³ volume is 100–1000 years (Blikra et al., 2016). Extensive CRSF deposits with volumes between 0.05 and 1.95 Mm³ from previous events have accumulated in the valley bottom beneath Mannen. It is therefore important to decipher the frequency of previous failures in order to assess if historic CRSF events were randomly distributed or clustered in time and if they can be linked to a particular failure mechanism. Using techniques of Quaternary geological mapping, sedimentary stratigraphy, electrical resistivity tomography (ERT), ground-penetrating radar (GPR) and cosmogenic ¹⁰Be exposure dating, we (1) determine the timing of post-glacial CRSF events at Mannen, (2) contextualise the colluvium within the framework of a fjord-valley fill succession and (3) identify the antecedent climate and glacially generating conditions resulting in periods of heightened CRSF activity.

Setting

Mannen is situated along a north-facing slope of the glacially formed, U-shaped Romsdal Valley (62.46°N, 7.77°E; Møre og Romsdal, Norway). This lower reach of the valley is a fjord-valley, or sediment-filled palaeofjord (Corner, 2006) with an underfit stream. Within 10 km of the site, the valley walls reach between 800 and 1400 m above the valley floor. The rock-slope section at Mannen is 1295 m in height with an average slope gradient of 47°. At present, there are four active rock-slope instabilities along the southern and south-western slope of the lower Romsdal Valley (Saintot et al., 2012). Each site is situated above massive rock-avalanche and debris-flow deposits on the valley floor (Figure 1).

Mannen is located in the Western Gneiss Region, which consists of Precambrian crystalline basement rocks of the Scandinavian Caledonides (Roberts, 2003). The Romsdal Valley cuts east-west through dioritic-granitic gneiss with local transitions to quartz-rich gneiss with sillimanite and kyanite and coarse granitic gneiss (Tveten et al., 1998). The Caledonide structural fabrics and mineralogical banding impart critical weaknesses inherent along the glacially oversteepened valley sides.

Here, post-Weichselian deglaciation began by thinning during the Bølling/Allerød interstadial (ca. 15–13 ka), as the outer coast of western Norway became ice-free (Longva et al., 2009). Ice marginal retreat up the Romsdal Valley has been completed between 12.8 and 11.7 ka, following the Younger Dryas cold period (Hermanns et al., 2017; Hughes et al., 2016; Stroeven et al., 2016). During deglaciation, the landscape was inundated by the sea, reaching a marine limit of 120 m above modern sea level in the Romsdal Valley (that is, 60 m above the Rauma River at Mannen; Høgaas et al., 2012). Subsequently, the relative sea level lowered approximately exponentially with glacioisostatic uplift (Svendsen and Mangerud, 1987).

The Quaternary valley infill is the product of processes connected to the Pleistocene glaciation, post-glacial sea-level fall and paraglacial colluvial activity (Figure 1). The geomorphology of the Mannen area in the lower Romsdal Valley is dominated by talus, debris-flow cones and CRSF deposits (Figure 1; Blikra et al., 2006; Saintot et al., 2012). More than 30 historical mass wasting events are documented along the valley (NVE, 2018), dominated by small rock-fall events with a volume <100 m³. Relative to the sea-level history, these deposits stratigraphically post-date ice marginal retreat with varying failure timing throughout the Holocene (Blikra et al., 2006).

The mean annual air temperature ranges from 4°C in the valley bottom to –1.5°C on the plateau above Mannen (1295 m a.s.l.). Annual precipitation during the reference period 1961–1990 lies between 1000 and 1500 mm in the Romsdal Valley. During the winter season, the snow precipitation accumulates an average of 37 cm of snow cover with monthly means of 12–25 cm in November and May and 50–56 cm in December and January. During the last 20 years the values have increased slightly, now usually being close to the upper limits of these ranges. Temperatures have increased as well, particularly since the year 2000 with 1°C in relation to the last reference period 1961–1990 (NVE, met. no and Kartverket, 2018).

Methods

Quaternary geological mapping

High-resolution (1 and 5 m) bare-earth LiDAR-derived digital elevation models (DEM) are the main sources for the recognition of landforms (e.g. Schleier et al., 2016). The digital relief analysis was complemented by field mapping in the summers 2016 and 2017 in the area around Mannen but included a ca. 40 km region extending from the contemporary fjord-head delta to the Skiri rock avalanche (Figure 1). Landform elevations were extracted from the DEM and plotted together with the local relative sea-level curve in order to establish the relationships between the marine transgression and regression and the onshore stratigraphy (cf. Eilertsen et al., 2015). Small excavations and field observations of the sediment characteristics facilitate the classification of different surface levels along the entire Romsdal Valley. The sedimentology characterisations and interpretations are based on field observations, geographic information system (GIS) analyses and previous studies about typical valley-fill stratigraphy in Norwegian fjord valley settings (cf. Corner, 2006; Eilertsen et al., 2006).

The volume of the CRSF deposits was estimated by reconstructing the pre-failure surface from the most recent high-resolution (1 m) LiDAR data. Based on interpolated and modified 5-m contour lines, we created new pre-failure DEM, which were then used to extract the elevation differences and subsequently calculate the volume on a pixel basis.

Two 2D ERT profiles, 900 and 700 m in length and parallel to the valley axis, were obtained on the northern and southern sides of the Rauma River (Figure 1b). ERT utilised an ABEM Terrameter LS and field testing employed the roll-along method using the Schlumberger protocol (e.g. Aizebeokhai, 2010) with four

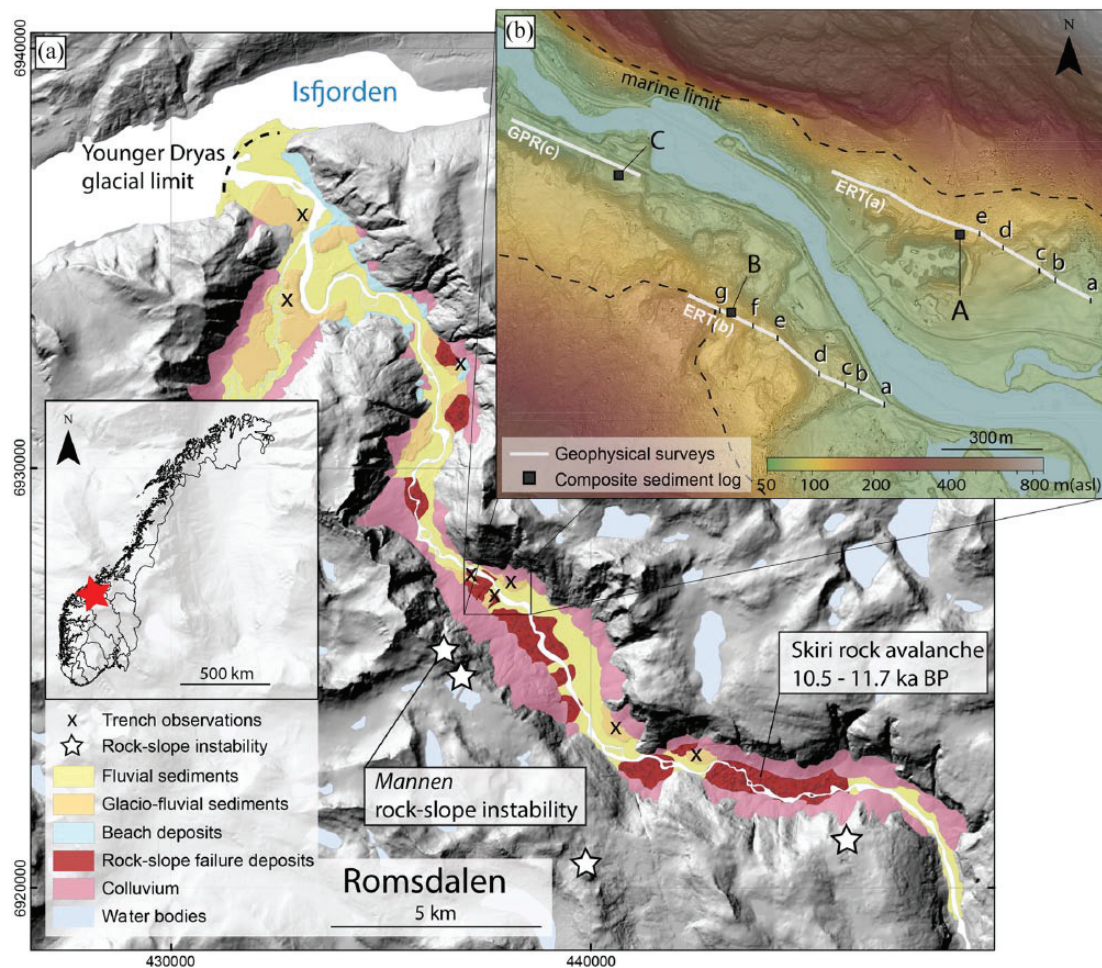


Figure 1. Overview over the study area: (a) Quaternary geology of the lower and mid Romsdal Valley and (b) detail of the main study site and the locations of geophysical surveys and composite sediment logs. Note the stretched colour code.

100-m-long cables and 5 m electrode spacing. To interpret the subsurface geology, the inverse electrical conductivity was derived with RES2DINV (© M.H. Loke, 1995–2015). After the manual extermination of bad data points, the inversion was derived using the robust L_1 -norm.

A single GPR profile was conducted, running along the foot of the valley parallel 20-m step in the relief in the north-west of the study site (Figure 1b). We used a snake antenna with a frequency of 100 MHz, which was towed behind the surveyor. The measurement frequency was 0.5 m. The post-processing was conducted with RadExplorer (©MALÅ Geoscience).

Geochronology

A total of 13 samples were collected and processed for surface exposure dating with cosmogenic ^{10}Be in quartz. We sampled boulders representing at least four of the CRSF deposits below the Mannen rock-slope instability. The boulders are well distributed and their sampled surfaces lie more than 1 m above the surroundings and have an either flat or convex geometry. All samples were taken with hammer and chisel and are 1–6 cm thick (Table 1). Where the foliation was favourable the collected samples have a rather even thickness of 2–3 cm and 20–30 cm of diameter. Generally, the selected sample locations on the CRSF deposits are either on flat or convex boulder surfaces with at least 40 cm distance to the boulder edge to minimise the effect of neutron loss and local shielding. In two cases the samples are only 20 cm from the boulder edge (MANN-31 and MANN-38) and three samples are collected from

boulder surfaces steeper than 30° (MANN-23, MANN-32 and MANN-35). Most sampled boulders were in continuous boulder fields with deep interstitial gaps, lacking the infill of a finer matrix (Figure 2b and c). Many boulders were covered by up to 5-cm-thick moss with a (dry) density of 0.05 g/cm^3 . An open birch forest with 5–20 cm trunk diameter and 2–12 m height covers the CRSF deposits today, with solitary pine trees in places.

Selected samples were cleaned by brushing, crushed, ground and sieved, optimising the 250–355 μm fraction. We subsequently concentrated and purified the quartz at the Cosmic Ray Isotope Sciences at Dalhousie University (CRISDal) lab, Halifax, Canada, using magnetic separation, froth flotation, heavy liquid separation and chemical leaching. The abundance of selected cations including Be was measured with ICP-OES at CRISDal to ensure purity ($<100 \text{ ppm Al}$ and Ti). Following carrier addition (240 mg of Be) to 30 g of pure quartz for each sample, the samples were digested in a mixture of concentrated trace-metal grade perchloric, hydrofluoric, and aqua regia. Be-Carrier-B31 was produced at CRISDal on 28 September 2012 from a deeply sourced Ural Mountains phenacite with low levels of ^{10}Be (averaging 150 atoms ^{10}Be per mg ^9Be over multiple years, for example, $^{10}\text{Be}/^9\text{Be}$ of the carrier averaging 10^{-17} and lower, usually with zero or one counts over 400 s with 20 μA current at Lawrence Livermore National Lab. The Be concentration of the carrier was determined by ICP-OES at CRISDal and by ICP-OES at PRIME Lab to be $282 \pm 5 \mu\text{g/mL}$ with a density of 1.013 g/mL , and this 2% uncertainty is included in the total analytical error of each measurement). Following routine column chemistry with sulphination,

Table 1. Sample characteristics. The boulder height refers to the surrounding ground or boulders.

Sample name	Rock type	Sample thickness (cm (estimated average))	Orientation (dip direction/dip)	Boulder dimensions (a- and b-axis) (m)	Boulder (sample) height (m)	Shortest distance to edge (cm)	Moss cover (cm)
MANN-07	Medium/coarse grained granite	1.0	264/20	2 × 4	3.0	100	3.0
MANN-10	Medium/coarse grained gneiss	2.0–4.0 (2.5)	302/10	5 × 5	3.0	50	5.0
MANN-23	Medium/coarse porphyritic granite	5.0	074/30	1 × 2	1.0	Convex boulder	–
MANN-26	Fine grained micaceous gneiss	3.0	000/20	15 × 7	7.0	70	3.0
MANN-28	Fine grained felsic gneiss	3.0–6.0	234/10	4 × 3	2.5	50	4.0
MANN-31	Medium grained, strongly foliated gneiss	0.5–5.0 (3.5)	358/36	1.5 × 1.5	3.0	20	1.0
MANN-32	Fine grained gneiss	1.0–5.0 (4.0)	254/18; 149/49	12 × 3.5	2.0	Convex boulder	0.5
MANN-35	Medium/coarse grained granitic gneiss	2.5	181/32	7 × 6	2.5	300	–
MANN-36	Medium grained strongly foliated gneiss	2.5	315/12	4 × 3	2.5	150	4.0
MANN-37	Weakly foliated granitic gneiss	1.0–2.0 (1.5)	071/26	8 × 6	8.0	300	4.0
MANN-38	Fine grained gneiss with mid-strength foliation	1.0–6.0 (5.0)	084/20	5 × 2	1.5	20	–
MANN-39	Medium grained gneiss with mid-strength foliation	1.0–2.0 (2.0)	132/26	5 × 2	1.5	40	2.0
MANN-40	Fine grained and weakly foliated gneiss	1.0–5.0 (4.0)	305/15	2.5 × 2	1.0	50	5.0

pH-controlled precipitations with ammonia gas and calcination to BeO over a Bunsen burner flame, the BeO was pulverised in its low-boron quartz vial and mixed well with niobium powder (1:1.5 BeO:Nb by volume). The prepared targets were measured by accelerator mass spectrometry (AMS) at Lawrence Livermore National Laboratory, Livermore (USA) against standard 07KNSTD-31110 ($^{10}\text{Be}/^{9}\text{Be}$ 2.85×10^{-12}) and achieved 2–3% AMS precision on most samples. The process blank correction (5.59×10^3 atoms, $^{10}\text{Be}/^{9}\text{Be}$ 3.3×10^{-16} , which is very close to the average blank since 2016) resulted in the subtraction of <1% of the measured concentrations.

To estimate the topographic shielding, we measured with an inclinometer the azimuth and gradient to several skyline inflection points. As low-level clouds and vegetation affected some measurements, the shielding correction was verified with a high-resolution (5-m) DEM. For this, the elevation for each sample was corrected using the LiDAR data and the angle to the horizon derived for each azimuth. These values are on average 1.3° higher than the corresponding inclinometer measurements but have a much higher resolution and should thus overall be more accurate. Snow shielding was derived after Gosse and Phillips (2001) using historic and modern climate data to estimate the average seasonal snow cover (snow density $\sim 0.3 \text{ g/cm}^3$). This method only represents the snow cover for the last decades and does not include local effects such as vegetation and wind drift. An erosion rate of 1 mm/ka was used for the calculation (Zimmerman et al., 1994). For the calculation of the exposure ages, we used version 3 of the online exposure age calculator formerly known as the CRONUS-Earth online exposure age calculator written by G. Balco, 2017, and the LSDn scaling scheme. The reported 1 σ uncertainty for an exposure age includes the internal and external errors (details in supplementary files, available online).

Results

Quaternary geology and geomorphology

Geomorphological mapping using high-resolution (1 m) LiDAR data. The DEM revealed well-defined 20-m high steps in the relief on both sides of the valley below the Mannen rock-slope instability (transition from green to yellow colouring in Figure 1b; an additional plain hillshade-map can be found in the supplementary files, available online, for comparison). The steep slopes with angles around 35° run almost parallel to the Rauma River

and are connected to rather flat (<5°) elevated surfaces. Upstream, these elevated surfaces end abruptly, where the steep slopes turn towards the rock walls. These stepped landforms are overlain by at least five but possibly up to seven lobate CRSF deposits. While one of these mapped CRSF events, featuring a secondary failure scar, has overrun and modified the steep 20 m high slope, the latter draws through most of the other CRSF deposits. A lobate and hammock-like form on a low elevation basin-like section north-east of the high elevated landforms suggests up to two additional CRSF deposits. A third larger event, exceeding the Rauma River, has been mapped by an intensive GPR survey (Tønnesen, 2009). But since the deposits of this event are no longer visible at the surface, it was not possible to include them into the age determinations of this study.

Longitudinal valley profile and terrace mapping. The valley-fill deposits along the Romsdal Valley were mapped in relation to the longitudinal profile of the Rauma River (Figure 3). The terraced landforms below the Mannen rock-slope instability are the highest valley fill deposits along the Romsdal Valley, exceeding all other valley-fill sediments by more than 10 m. The next highest terraces have been investigated with small (~1 m deep) excavations along the entire valley (Figure 1a). They revealed coarse sand interbedded with fine sand with 1–50 cm large rounded to well-rounded clasts in the upper Romsdal Valley (Figure 3a and b) and patterns of altering sand layers of varying grain sizes without pebbles and cobbles close to the fjord head. The bedded structure and clast roundness imply fluvial deposition processes but because of their high elevations, these terraces are interpreted to be of glacio-fluvial origin, which is in accordance with the most recent regional quaternary geological map (NGU, 2018). High elevated sand deposits with nearly horizontal sandy layers are found on either side of the valley in bay-like settings (Figure 3c) and have previously been interpreted as beach deposits (NGU, 2018). The correlating elevation of these beach deposits and the sandy terrace segments covering large parts of the lower Romsdal Valley (Figure 1a) suggests a possible deposition of distal fine grained glacio-fluvial sediments in a deltaic environment and thus indicating the sea level at the time of deposition.

Sedimentary stratigraphy and interpretation below the Mannen rock-slope instability. The upper ca. 40 m of the fjord-valley fill below the Mannen instability were investigated in three locations

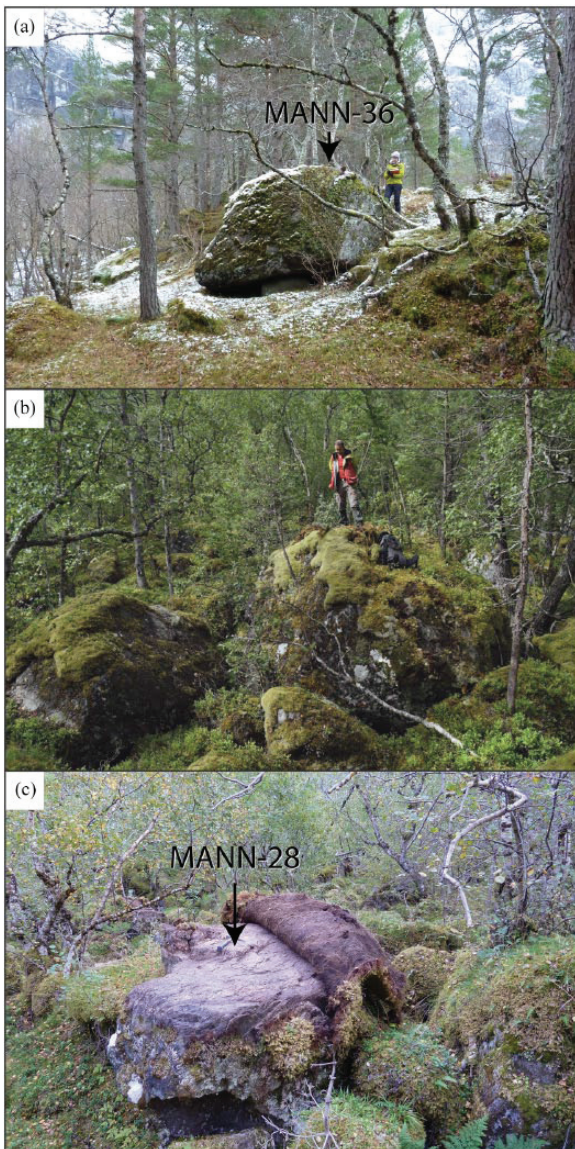


Figure 2. Images of (a) the sample location MANN-36 in a surrounding characterised by soil in contrast to (b) the chaotic boulder field of the south eastern CRSF deposits and (c) the sample location MANN-28 with a pulled back moss cover.

(A–C; Figure 1b). Four sedimentary facies associations (FA I–IV) are identified and likely relate to the progradation of a fjord-head delta system and its associated braided river, rock-slope failure and related processes, including debris flows on colluvial fans. A brief tabular summary of the following sections is provided in the supplementary files, available online.

FA I stratigraphically occupies the lowermost position at the locations A and B (Figure 4). Observed exposures were ca. 22 m in height. FA I consists of stratified sands and gravels, which dip ca. 5° in downstream direction (Figure 4a). Gravel clasts are typically subrounded to rounded. FA I is interpreted to be stratified drift. Similar units of stratified drift consisting of sands and gravels are frequently described in fjord-valleys in western Norway (cf. Corner, 2006). Considering the high relative elevation of these sediments together with their morphological appearance connected to a steep slope facing upstream and downstream dipping sediment layers, FA I could be interpreted to represent an ice-contact glaciomarine fan or delta (cf. Corner, 2006; Eilertsen et al., 2006; Lønne, 1995).

FA II is observed overlying FA I at location A (Figure 1). The deposits are ca. 5 m thick and consist of flat-laying interbedded silty sands and gravels. Gravel clasts are angular to sub-angular. Variations in clast shape reflect changes in the transport distance and sediment source. Angular clasts likely entered the fluvial domain as debris flows from the proximal upstream reaches and hence were transported a short distance prior to deposition. Based on the sedimentary architecture and composition, FA II is interpreted to be fluvial with debris-flow deposits, deposited on the distal parts of colluvial fans (cf. Blikra and Nemeč, 1998).

FA III is encountered at locations B and C (Figure 1) and varies from ca. 8 to >10 m in thickness. Deposits consist of boulders (up to 10 m in diameter) as chaotic block fields or suspended in a gravelly, sandy matrix covered with soil (Figure 4b). FA III is interpreted as CRSF deposits.

FA IV is observed in the upper 7 m at location C. The deposits consist of interlaminated sands and silts (Figure 4c). Isolated, sub-angular to angular, cobble-size fragments are incorporated within FA IV. FA IV is tentatively interpreted as overbank fluvial deposits (cf. Corner, 2006; Eilertsen et al., 2006) with outsized cobbles being debris originating from a steep, proximal slope (Blikra and Nemeč, 1998). If so, FA IV is an indicator for a higher water level than today's river level at time of deposition.

Direct current (DC) resistivity. The tomography of the ERT profiles (Figure 1) generally support our sedimentological and geomorphological observations. Based on the 2D distribution of the electrical resistivity of the profiles ERT (a) and (b), we defined five main electrical resistivity units (ERU): ERU 0, I, II, III and IV, with ERU I, II and III corresponding to FA I, II and III, respectively.

ERU 0 occupies the lower 40 m of both DC resistivity profiles (Figure 5a and b). The unit is characterised by resistivity values from <400 Ωm to 5 kΩm and a transition to high resistivity values of >14 kΩm at 50–60 m a.s.l. The elevation of this transition coincides with the lower limit of the mapped dry and coarse-grained stratified drift (FA I). However, we have no field information about sediment characteristics below this elevation. The similar resistivity patterns of the two profiles suggest that the bottom geologic characteristics are similar over the entire width of the Romsdal Valley. While the fjord-valley models would expect fine grained glaciomarine sediments at the valley bottom, the typical resistivity values for clays do not exceed 100 Ωm. We therefore suggest this lower unit to be either bedrock (Palacky, 1988) or inversion artefacts due to the high values above.

ERU I is characterised by resistivity values of 14 to >36 kΩm and occupies the largest parts of both sections ERT (a) and (b). This unit lies above ERU 0 between ca. 50 and 90 m a.s.l. The highest values in ERT (a) are most likely an artefact due to the proximity of the edge to the open gravel pit. ERU I is interpreted to represent FA I with glacio-fluvial sand and gravels (Palacky, 1988).

ERU II occupies the upper 5–7 m in section ERT (a). Resistivity values range from 350 Ωm in the uppermost 2 m to values above 14 kΩm. But the values are generally lower than in unit I. ERU II represents the sediments interbedded silty sand layers in debris-flow gravels of FA II. The variation of the resistivity values are interpreted to originate from different sedimentation processes related to the talus cone above.

ERU III was only observed in section ERT (b). This unit is characterised by high values (>14 kΩm) at the top 2–5 m with lower values (5–14 kΩm) below this surface layer. At the letter f and g (Figure 5b), CRSF deposits have been mapped in the field. The decrease of resistivity with depth can be explained by the typical grain-size distribution of massive CRSF deposits with large boulders on the surface and an increase in finer matrix material and moisture with depth (Ostermann et al., 2012).

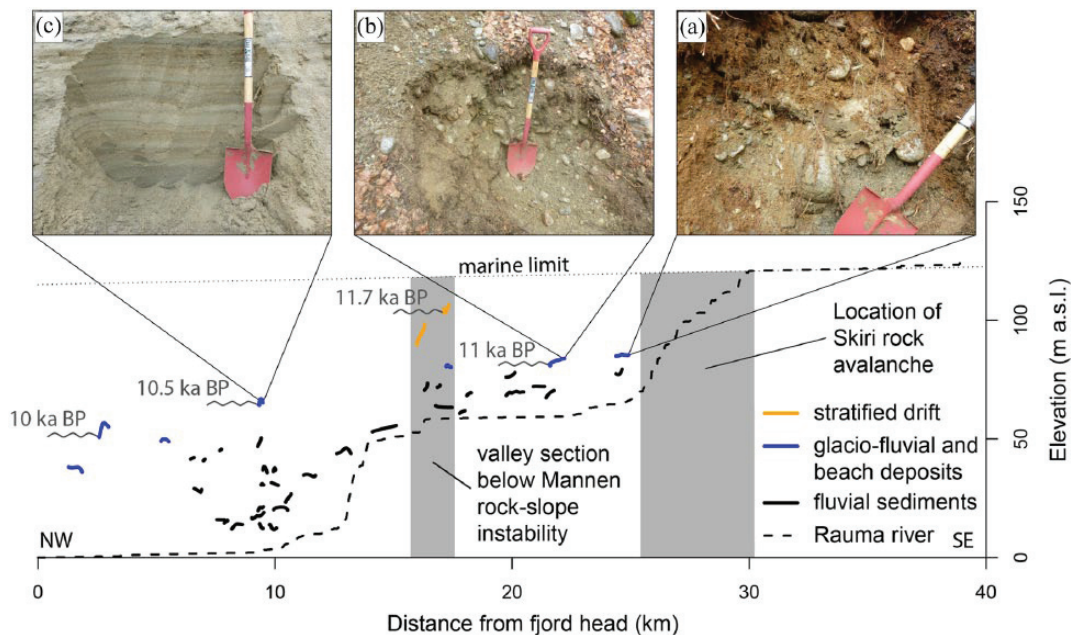


Figure 3. Surface profiles of terrace segments along the Romsdal Valley characterised according to their relative position and (a–c) field observations. Sea-level elevations and their approximate timing are indicated as wavy grey lines next to the glacio-fluvial terrace segments, which could be connected to a delta progradation. The vertical axis is exaggerated by 10 in relation to the horizontal axis.

While the resistivity values are generally lower within the section c–d in the same profile, this unit is also correlated to FA III. Here, up to 20 cm deep surface water was observed in the field indicating a high water content in the subsurface, leading to a decrease in the resistivity.

ERU IV occupies the last 100–200 m of the 900-m-long ERT profile (a) (a–c; Figure 5a), where the electrical resistivity values lie between 50 and 350 Ωm . This section of the profile is part of the basin upriver of the high-elevated valley-fill sediments below Mannen. We suggest this unit to be silty sediments deposited either in a calm water environment or as overbank fluvial deposits similar to FA IV (Groover et al., 2016).

GPR. The surface along most of the GPR profile (Figures 1b and 5c) is characterised by agriculturally used lawn. A chaotic boulder field confining the Rauma River along this section generated a minor knickpoint in the longitudinal profile (Figure 3), which is often the consequence of CRSF into rivers (Korup et al., 2010; Ouimet et al., 2007). The characteristic reflection configurations and analogies to the ERT units allowed defining four main radar units (RU): RU I–IV, where RU III and IV correspond to FA III and IV, respectively.

RU 0 is defined by an area below 45 m a.s.l. where the signal strength decreases abruptly and no clear reflectors are distinguishable. The upper limit of this unit lies only a few metres lower than the upper limit of ERU 0 (50–60 m a.s.l.) wherefore we interpret this unit tentatively as bedrock.

RU I is defined by a partly clear reflecting boundary that can be followed throughout large parts of the profile (thick line, Figure 5c). This reflector becomes rather indistinct at the boundary to RU III and the reflectors within this unit are rather chaotic and unclear. Because of the lack of homogeneous reflectors, we interpret this unit as valley-fill sediments that have been deformed by the impact of the CRSF (cf. Blikra et al., 2006).

The RU II unit is characterised by steeply downstream dipping (35–45°) generally parallel reflectors. Analogue reflectors are commonly observed in deltaic environments (Eilertsen et al., 2011). Considering the fjord-valley setting we interpret RU II to represent delta foreset deposits, indicating a previous sea- or lake-level at ca. 55 m a.s.l.

RU III represents the central section of the GPR survey, where we observe distinguishable parable-shaped reflectors in different elevations. RU III is interpreted as CRSF deposits (FAIII; cf. Schleier et al., 2016), which can be observed at the surface only a few metres north-east of the profile.

The RU IV unit is characterised by smooth parallel and continuous horizontal reflectors with varying thickness. While these characteristics are common for stratified sediments, it is difficult to distinguish between different possible deposition processes. Similar reflectors have been observed for delta bottom/topsets (Eilertsen et al., 2011), lake deposits (Storms et al., 2012) and flood plains (Hansen et al., 2009). Because of its location and our field observations, we interpret this unit as fluvial overbank flow sediments correlating with FA IV.

Quaternary geology map. The Quaternary geology map displays the dominance of CRSF deposits and their position relative to the stratified drift. The volumes of the individual CRSF events vary between 0.05 (Lobe 5) and 1.95 Mm^3 (Lobe 4, Figure 6). The small rock-slope failure Lobe 5 is characterised by a clast-supported chaotic block field with large angular boulders (3–6 m) and little to no matrix exposed at the surface. Considering its short run-out length, Lobe 5 probably represents a large rock-fall event without major disintegration. It exceeds the active extensive talus slope by >150 m. According to a previous GPR survey (Tønnesen, 2009), the CRSF deposits 6a and 6b are much larger than the superficial deposits indicate. The study suggests that the deposits continue below the Rauma River and that the volume is thus much larger than our estimated 0.43 mm^3 .

Geochronology

We have determined the apparent exposure ages of 13 boulder samples using the ^{10}Be -isotope (Figure 6; Table 2). The locations of the two samples with the oldest apparent ^{10}Be ages are adjacent to each other and give a mean exposure age of 9.39 ± 0.64 ka (error-weighted mean with 1σ uncertainty). The majority of the deposit lies below the marine limit, and while only the highest boulders were sampled, shielding by seawater may have reduced

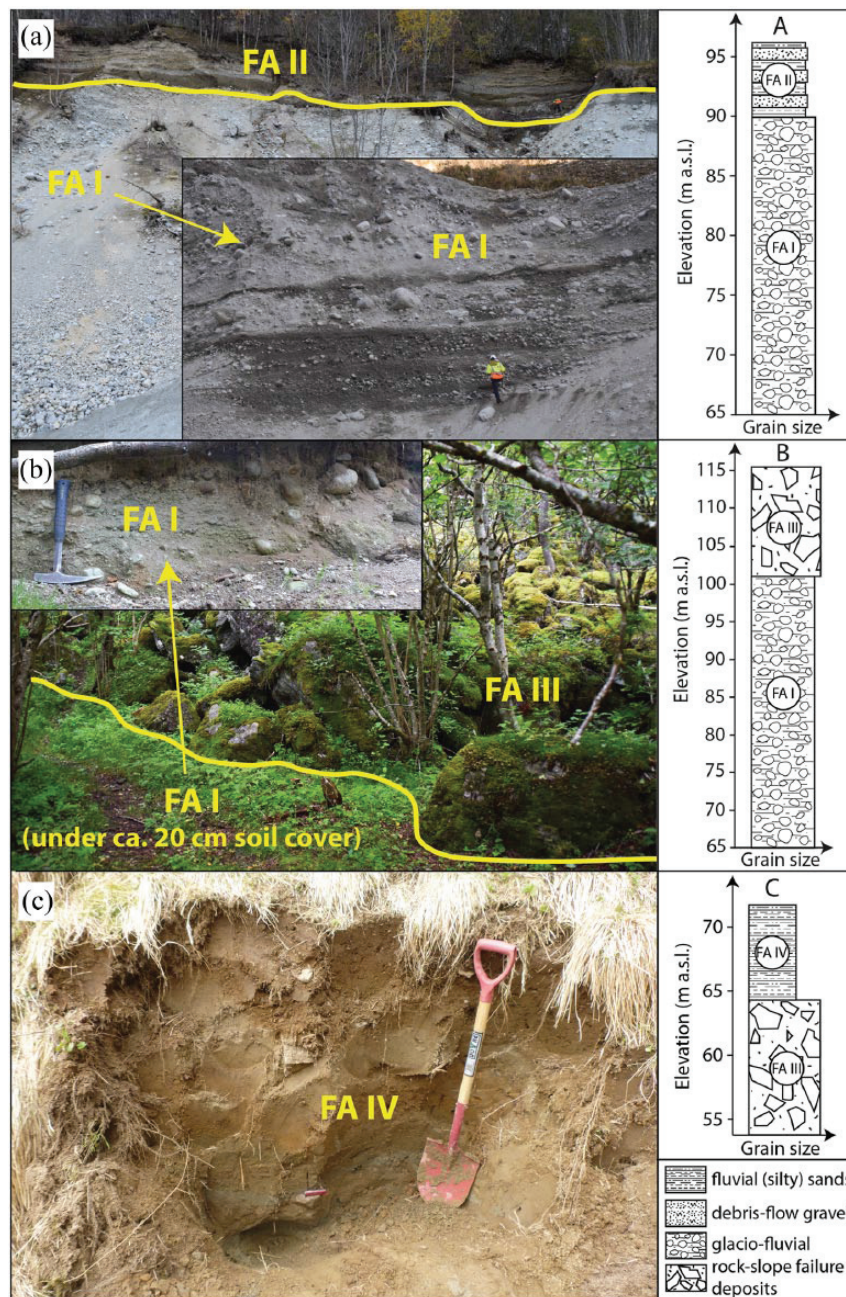


Figure 4. Impressions from the locations of the composite sediment profiles and the sediment characteristics: (a) gravel pit with ca. 35 m stratified drift (FA I) and ca. 7 m interbedded fluvial sands in angular debris-flow gravel (FA II), person is 1.70 m tall; (b) ca. 15 m thick chaotic boulder deposits (FA III) on top of FA I, which is only visible in small outcrops; (c) silty sands with outsized cobbles on top of ca. 10 m thick rock-slope failure boulders.

the ^{10}Be production rate. Thus, assuming no inheritance, these dates are interpreted to be minimum limiting ages. The other 11 exposure ages range from 4.75 ± 0.33 ka to 5.93 ± 0.39 ka. Considering sample MANN-26 as a statistical outlier (beyond the coefficient of variation of the mean of the others) owing possibly to inherited ^{10}Be isotopes from pre-failure production, the range is 4.75 ± 0.33 ka to 5.12 ± 0.36 ka and the ages are indistinguishable within their 1σ uncertainties. Excluding MANN-26, the mean ages for deposits 4a, 5 and 6 (Figure 6) are 4.91 ± 0.30 ka, 4.96 ± 0.33 ka and 4.95 ± 0.31 ka, respectively. The single sample from Lobe 4c gives an age of 4.98 ± 0.34 ka, which lies within the standard deviation of Lobe 4a and, based on their close proximity and stratigraphic relationship, we recommend considering them as one event with a mean age of 4.93 ± 0.30 ka in the

following discussions. The clearly distinguishable deposits of several CRSF events with indistinguishable ages within one standard deviation indicate temporal acluster of multiple failures from the same slope 4.9 ± 0.6 ka ago.

Poor estimations of partial cosmic ray shielding by snow and vegetation provide an unconstrained source of error in our ages. Our shielding estimations for snow, with an average of 37 cm snow depth for a 7-month snow season and an average density of 0.3 g/cm^3 , yielded a value of 0.999 which has a small effect on the absolute exposure ages. The effect of the sparse birch tree forest that covers the sampled CRSF deposits can roughly be estimated. Plug et al. (2007) show that the shielding effect in forests is dependent on stem thickness and tree height, sample location, succession rate and age. Considering the generally small stem

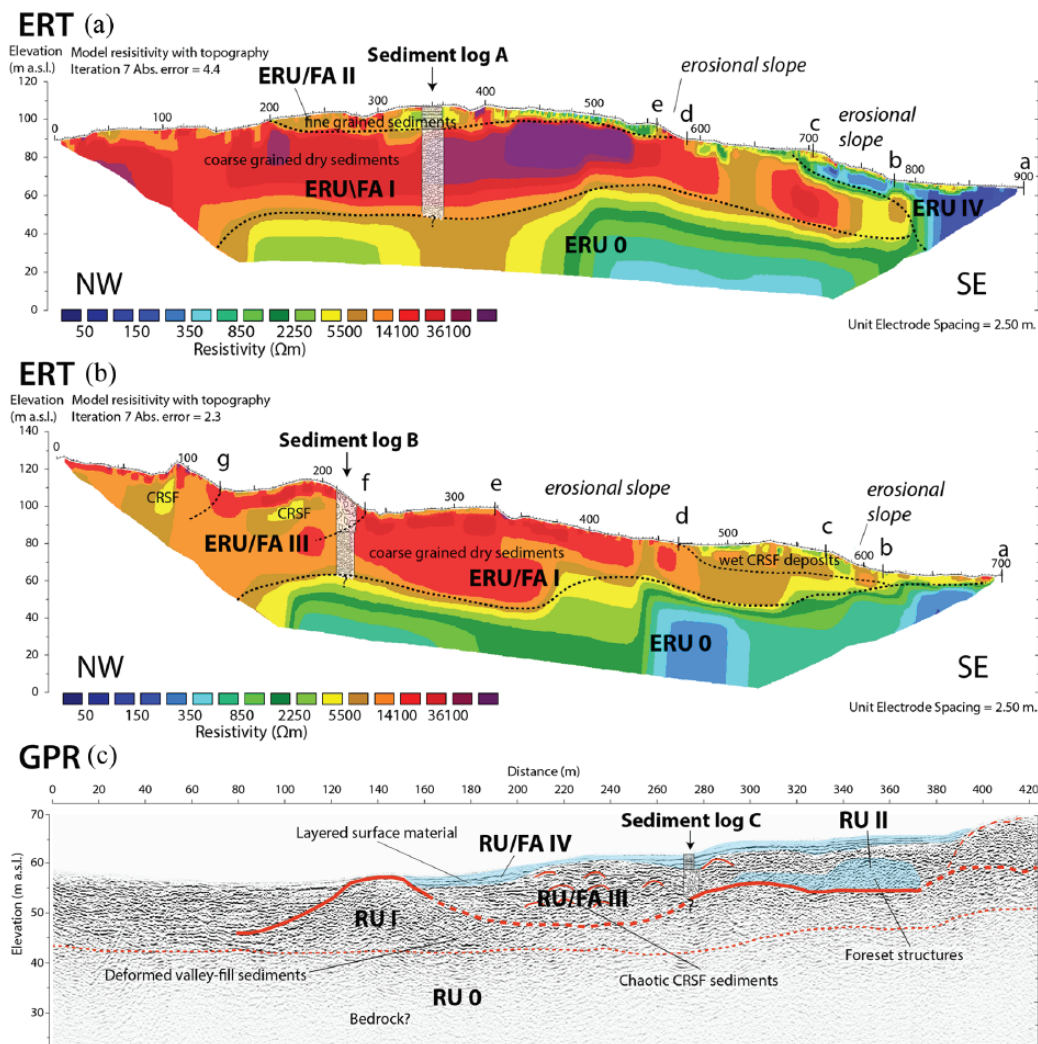


Figure 5. Results of the geophysical surveys: Top: 2D DC resistivity pseudosections of the profiles ERT (a) and ERT (b) (NW-SE) as indicated in Figure 1b. The lowercased letters along the profiles represent prominent relief changes (Figure 1b) that are connected to a change in sediment characteristics in places. Steep and ca. 20 m high steps in the relief are marked by the sections b-c and d-e, respectively. (c) GPR survey over CRSF deposits. Note that the scales differ for visualisation. The y-axes are exaggerated by 1.5 in all profiles. The composite stratigraphy logs from Figure 3 are included in the approximate locations.

diameters (5–20 cm) and forest density, we expect the shielding effect to be smaller than the numerically estimated shielding of <2.25% for Acadian forest in Nova Scotia (Plug et al., 2007).

Potential inheritance of ^{10}Be in each boulder depends on its depth below the cliff face prior to failure and the rate of cliff retreat (frequency of mass wasting). The study area has relatively small CRSF volumes ($0.05\text{--}1.95\text{ mm}^3$). For a conservative realistic scenario of 7 ka pre-failure exposure (4.9 ka subtracted from an exposure history of ~ 12 ka after deglaciation), the effect of inheritance for 10 and 5 m depth below the cliff face are ca. 0.8% and 1.5%, respectively (Hilger et al., unpublished data). However, the average effect becomes >6% for depths smaller than 2 m. But because of the existence of an outlier (MANN-26) that possibly came from a depth <2 m, and otherwise uniform ages, we expect that most of the boulders originate from greater depth. Because shielding by vegetation and inheritance impart opposite effects on exposure ages (decreasing or increasing apparent exposure time), and because they are of similar effect (a few percentage), and considering the tight distribution of the boulder exposure ages, it is possible that the two factors effectively cancel each other. Therefore, we have not adjusted the ages for either factor and interpret the measured exposure ages as the timing of the CRSF events.

Discussion

Timing of CRSF cluster from Mannen

Our study indicates multiple early post-glacial rockslide events and a CRSF cluster during the mid-Holocene. Because of the high marine limit, the sampling of stratigraphically low deposits was restricted to boulders on higher elevations in the study site. Consequently, we are lacking absolute exposure ages for the CRSF deposits 1 and 3 and are dependent on geomorphologic and stratigraphic observations relative to the dated deposits. The geomorphological setting of the deposits clearly indicates that the CRSF events were post-glacial. If the rock-slope failures were deposited supra-glacially, they would have been transported down valley to form moraine ridges with characteristically uniform boulder lithology, as observed by Schleier et al. (2015). Such discontinuous rock-avalanche deposits are very distinctive from intact CRSF lobes deposited in an ice-free valley. In the Romsdal Valley no analogue moraine ridges were observed, and all our CRSF deposits under the Mannen instability form continuous lobate landforms with clear runouts into or across the valley.

Stratigraphic observations (Figure 4) help constraining the timing of CRSF Lobe 1. While boulders from the Lobe 1 event overlie sandy to gravelly stratified drift (FA I), fine-grained stratified

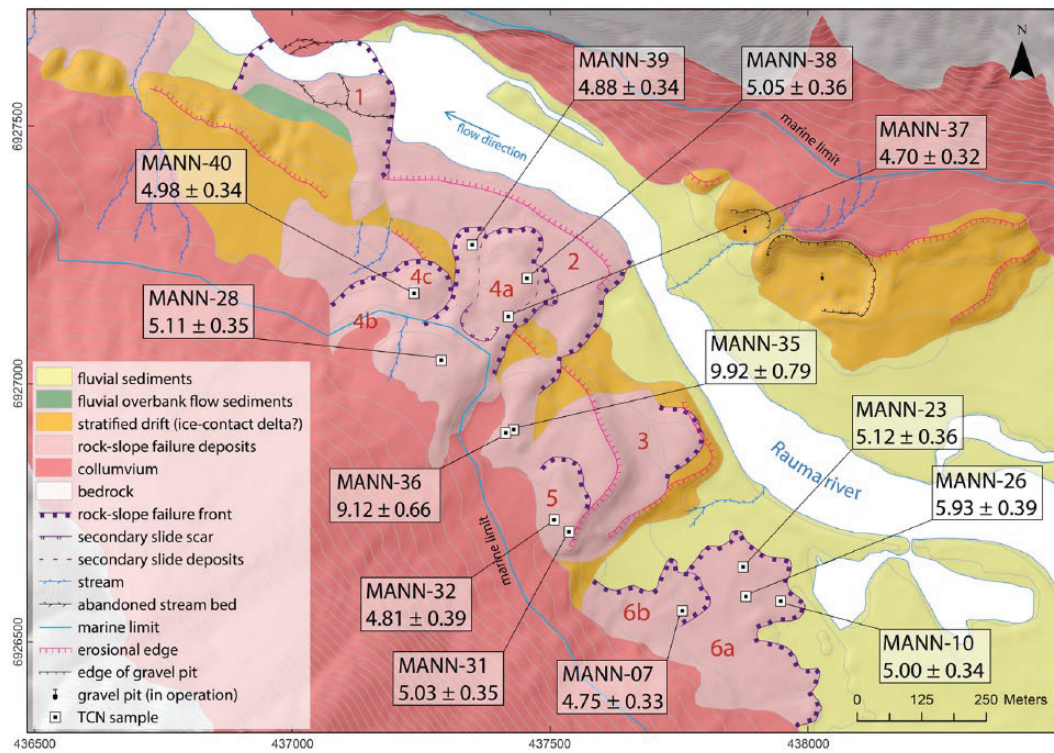


Figure 6. Quaternary geology map of the study site in the lower Romsdal Valley below the Mannen rock-slope instability. The individual apparent exposure ages are stated with 1σ uncertainties. The CRSF deposits are numbered for further discussions.

Table 2. Analytical data and calculated exposure ages with the LSDn scaling scheme.

Sample name	Latitude (dd)	Longitude (dd)	Altitude (m a.s.l.)	^{10}Be concentration (10^4 at/g)	1σ analytical unc. (10^4 at/g)	Shielding correction	Age (ka)	Age unc. internal (ka)	Age unc. external (ka)	Lobe	Error weighted mean with int. (ext.) unc.
MANN-07	62.46503	7.793195	70	21.30	0.75	0.9128	4.75	0.12	0.33	6b	4.95 ± 0.10 (0.31)
MANN-10	62.46522	7.796929	63	22.00	0.69	0.9173	5.00	0.16	0.34		
MANN-23	62.46579	7.795452	68	22.10	0.84	0.9152	5.12	0.20	0.36	6a	
MANN-26*	62.46529	7.795589	68	26.00	0.77	0.9165	5.93*	0.18	0.39		
MANN-31	62.46634	7.788837	111	22.80	0.80	0.9100	5.03	0.17	0.35	5	4.96 ± 0.15 (0.33)
MANN-32	62.46655	7.788266	110	21.70	1.21	0.9084	4.81	0.18	0.39		
MANN-35	62.46807	7.786672	118	45.40	2.33	0.9059	9.92	0.27	0.79	2	9.39 ± 0.30 (0.64)
MANN-36	62.46801	7.786364	117	41.80	1.69	0.9054	9.12	0.52	0.66		
MANN-28	62.46924	7.783871	138	23.40	0.79	0.9033	5.11	0.37	0.35	4a	4.93 ± 0.09 (0.30)
MANN-37	62.47001	7.786400	95	21.10	0.69	0.8946	4.70	0.16	0.32		
MANN-38	62.47067	7.787071	88	21.60	0.82	0.8901	5.05	0.17	0.36		
MANN-39	62.47122	7.784973	78	21.20	0.73	0.8856	4.88	0.16	0.36		
MANN-40	62.47038	7.782797	117	22.30	0.75	0.8956	4.98	0.20	0.34	4c	

Shielding values include the topographic shielding as well as shielding by snow. Sample marked with * is defined as a statistical outlier.

sediments (FA IV) also cover the bouldery CRSF material at this location (GPR; Figure 5). The deltaic foreset structures of RU II are observed at the same elevation as the chaotic CRSF structures, which lie downriver of RU II and seem to ‘truncate’ the delta. Both units are covered by the bank overflow sediments (FA/RU IV). The relative stratigraphy of these units narrows the failure timing for CRSF Lobe 1 to between 12 ka, when the valley became ice free, and 10.5 ka, when the coastline dropped below the recent riverbed of 50 m a.s.l. (Figure 7). Observations of abandoned erosional channels through the CRSF deposits several metres above today’s river level support this interpretation.

The adjacent CRSF deposit (Lobe 2) is the oldest of our dated events with an apparent exposure age of 9.39 ± 0.64 ka (Table 2). The approximated sea-level curve after Svendsen and Mangerud

(1987) indicates that the location was effectively above sea-level 11 ka ago (Figure 7a). The age therefore may represent the time of failure and not the timing of sea-level drop. According to the morphology in the DEM, it is possible that this deposit underlies CRSF Lobe 1, which would mean that the real age lies in the upper range of the uncertainties and has thus been deposited into a shallow fjord or high river level, shortly after deglaciation.

To identify CRSF Lobe 3, we had to rely on the high-resolution DEM and relief analysis, as the deposit is hardly distinguishable from the surrounding landforms. In most places, it could only be mapped by the characteristic chaotic boulder fields covering the surface. This indicates that the deposits have been modified by the same erosional processes, as the underlying sediments. We therefore suggest that this deposit is older or the same age as

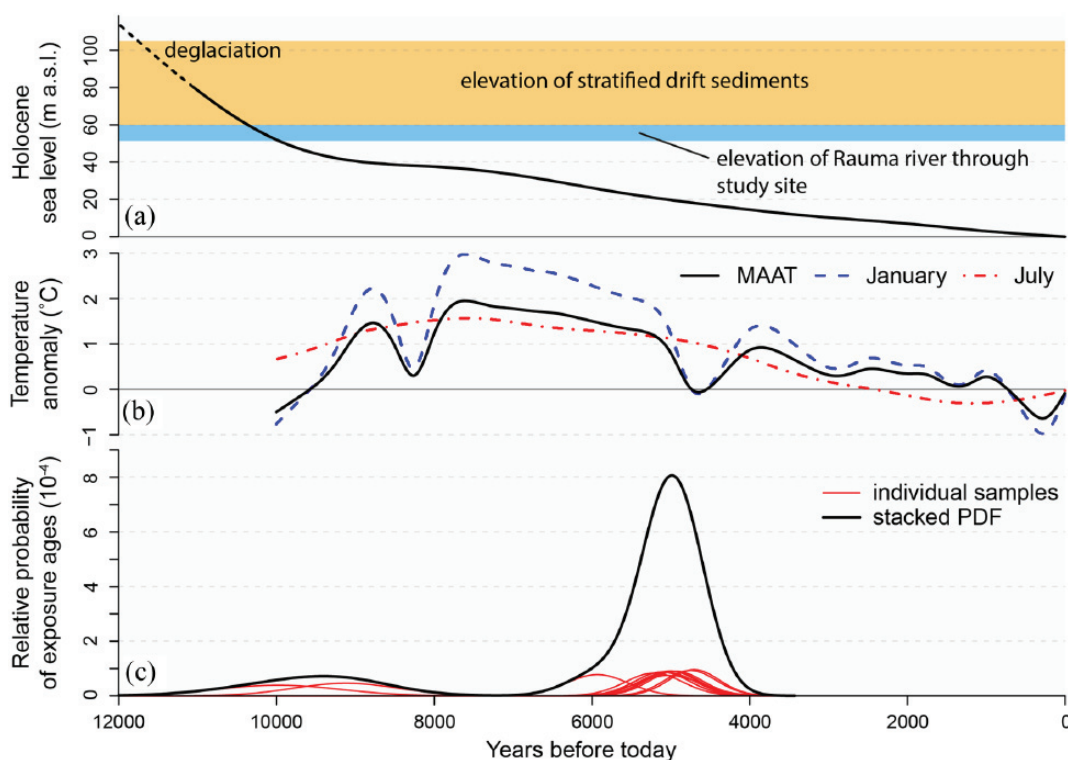


Figure 7. Local sea-level curve approximated after Svendsen and Mangerud (1987) (a) and approximated Holocene temperature anomalies for southern Norway (Lilleøren et al., 2012) (b) above apparent exposure ages as individual probability density functions (PDF) and stacked PDF (c).

CRSF Lobe 1 and 2. Thus, according to the regional deglaciation, the composite stratigraphy and morphology, the reconstructed curve of sea-level drop and the TCN ages, we can place three CRSF events (Lobes 1-3) from Mannen into a 2000 year time period between 12 and 10 ka ago.

Ten of our 13 ^{10}Be ages fall into the time range of 4.5–5.5 ka (Figure 7c) considering their external errors. The overlapping ages of the different deposits indicate that there have been several failures from the same slope within a couple of 100 years at most, witnessing a ‘geological crisis’ during this time period. Based on the morphology, it is not clear if the deposits 4a-c are only one or up to three individual events. The same applies for the CRSF deposits 6a and 6b. The ‘geological crisis’ thus included three to six failures from the same slope. The phenomenon of spatial rock-slope failure clusters and multiple failures from the same slope has been observed worldwide (Jarman et al., 2014; Orwin et al., 2004). In Norway this has happened at the Loen site, which has failed repeatedly within a few decades in the early 20th century. Together with a large scale rock-slope failure in Taffjord, CRSF became the natural hazards in Norway with the highest death toll (Grimstad and Nesdal, 1991; Hermanns et al., 2006a; Reusch, 1907).

Possible conditioning for multiple CRSFs at Mannen

Some of the regional and local clusters of CRSF in the Karakoram, the Andes, the Alps and the Scottish Highlands are discussed to be conditioned by tectonic or isostatic uplift and related stresses and seismic activity (Ballantyne et al., 2014; Hermanns and Strecker, 1999; Hewitt et al., 2011; Köpfler et al., 2017). However, in regions with recent low seismicity, this connection is often ambiguous and temporal rock-avalanche clusters are also linked to climatic changes and increased precipitation (Sanchez et al., 2010; Zerathe et al., 2014). Studies about rock-avalanche clusters in the Alps suggest that lithology and the structural predisposition is

the most important long-term control on rock-avalanching (Hermanns et al., 2006a; Ostermann and Sanders, 2017), while seismicity is often the trigger with climate conditions as a second-order control.

The deposits at Mannen cluster not only in space but also in time, in contrast to many regional clusters where CRSFs seem to have happened throughout the Holocene with rather low recurrence intervals implying a relaxation of the rock slope after failure (Schleier et al., 2015, 2016). This compares with the increasing number of studies globally which show that one slope of the same mountain can fail repeatedly within only a few years and decades (Crosta et al., 2017; Hermanns et al., 2001, 2004; McSaveney, 2002; Plafker and Ericksen, 1978). Hermanns et al. (2006b) argue that sudden stress release due to a failure causes a reorganisation of the stress field and can thus have a destabilising effect on the rock slope, which is in agreement with the structural simulations by Crosta et al. (2017).

In the Romsdal Valley, the regional clustering of CRSF within a geological unit supports the strong pre-conditioning based on the geological and structural setting. Considering that neo-tectonic activity has so far not been demonstrated in western Norway, the relatively short recurrent interval indicates that driving factors other than tectonic activity may play a significant role in this region.

The age of the first three CRSF at the Mannen rock-slope instability closely post-dates the local deglaciation (12.8–11.7 ka) and coincides with the main peak of rock-avalanche activity in Norway (Böhme et al., 2015; Hermanns et al., 2017). Thus, sudden failure was most likely conditioned by the paraglacially-induced stress increases in the over-steepened slopes during and immediately following deglaciation.

The later timing of the mid-Holocene cluster 5 ka ago invites for a speculation of how changing climate conditions in the Holocene may have contributed to these events. There are two main climatic factors which can contribute to Coulomb failure by

decreasing effective shear strength owing to reduced coefficient of friction, increased pore-water pressure, increased slopes and redistribution of centre of mass: (1) regional precipitation changes (amount and type) and (2) temperature changes leading to changes in possible permafrost conditions. There is evidence from several studies in western Norway that a climatic deterioration initiated about 6 ka ago, after a long warm period of the Holocene thermal optimum (HTO). Glacier growth (Nesje et al., 2001) and changing vegetation (Barnett et al., 2001) indicate a generally cooler and wetter climate in this period, and studies documenting Holocene debris flows, snow avalanches, and flooding events suggest a strong seasonality with severe winters and warm summers at this time (Blikra and Nemeč, 1998; Blikra and Selvik, 1998; Vasskog et al., 2011). Precipitation between 6 and 5 ka ago was 170% greater than during the reference period 1961–1990 (Bøe et al., 2006). Lilleøren et al. (2012) approximated the temperature anomalies based on published climate proxies for southern Norway for the last 10 ka compared to the same reference period (Figure 7b), which was about 1°C colder than mean annual air temperatures (MAAT) today. The MAAT during and after the HTO was warmer than during the reference period, with very mild winters and warm summers, driven by higher solar radiation due to the Earth's orbital position. Cooling from 6 ka ago was most likely driven by low winter temperatures, while the summer temperatures decreased less extremely, reflecting a strong seasonality. The documented glacier growth in southern Norway (Nesje et al., 2001) indicates additional high precipitation rates in winter after 6 ka ago. The timing of our 'geological crisis' with at least three CRSF within a short period of time coincides with this period of strong winter temperature decrease, high precipitation rates and strong seasonality, following the HTO with high air temperatures.

Not much is known about the rock mechanics and the history of stream discharge and fluvial dynamics at Mannen. The mountain section seems to be generally very dry where no surface discharge is observed and precipitation and snow-melt water drains by baseflow through fractures underground. Continuous monitoring at the most active part of the Mannen instability '*Veslemannen*' reveals that rock mass deformation is very sensitive to precipitation and is stable during the winter season (Oppikofer et al., 2013). This could imply that increasing precipitation in the mid-Holocene together with warm summer temperatures led to widespread and repeated rock-slope destabilisation at Mannen. A continued climate warming combined with a more pronounced seasonality leading to increased snow melt could thus cause sudden destabilisation of the Mannen rock-slope in the future causing one or multiple CRSF events.

The other first-order control is the regional degradation of permafrost during the HTO and after the 6 ka cooling period. Thermal measurements today in crevasses and the back scarp of the Mannen instability along with regional permafrost mapping indicates that Mannen is situated at the present mountain permafrost limit in the area (Gisnås et al., 2013; Steiger et al., 2016; Westermann et al., 2013). When the Mannen area became ice-free after the YD, the climate was 7–9°C cooler than today based on Greenland ice-core analysis (e.g. North Greenland Ice Core Project Members, 2004). First approximations through a modelling approach suggests the build-up of several tens to hundreds of metres of permafrost in mostly snow-free rock walls during the period of deglaciation until MAAT reached similar levels to today (ca. 10 ka ago; Myhra et al., 2017). Rock joint weakening due to permafrost aggradation and degradation during this 2 ka period after deglaciation may have played a role in addition to debuitressing for the first three CRSFs at Mannen (Krautblatter et al., 2013). The permafrost certainly degraded during the HTO, but the degradation rate is depending on cracks and the ice content in the steep slopes because of thermal inertia. Thawing permafrost is widely recognised as an important factor for CRSFs (Blikra and Christiansen, 2014;

Fischer et al., 2006, 2012) due to melting of ice-bonds in cracks and generally weakening of tensile and compressive strength in rock masses (Krautblatter et al., 2013; Murton et al., 2006) and has to be taken into account when discussing possible former rock slide conditioners in high-mountain environments. However, a more substantial conclusion on this can only be drawn through sensitivity studies using coupled thermo-mechanical models (Grämiger et al., 2017).

Conclusion

Below the Mannen instability in the lower Romsdal Valley, western Norway, a cluster of at least six post-glacial CRSF deposits complements a complex valley-fill stratigraphy. The present landforms are the result of the concurrence of sedimentation processes connected to deglaciation, isostatic rebound and sea-level drop, and mass wasting from the slopes. Prominent steep steps in the relief, parallel to the valley, are evidence for erosional processes either by strong tidal currents or fluvial incision. These processes have modified both stratified drift and three of the rock-slope failure deposits, supporting the stratigraphically derived time constraints of failure timing.

A set of 13 exposure ages together with sedimentologic and morphologic analyses allowed for the age determination of the six to nine distinct CRSF events. They divide into two periods of CRSF activity, one shortly after deglaciation and one 5.5–4.5 ka ago, where multiple CRSF from the same slope occurred within a short period of time. The fact that one slope fails repeatedly with recurrence intervals of a few years or decades has been observed before and must be considered for future failure scenarios. Debuitressing is a probable conditioner for the early multiple failures between 12 and 10 ka, that coincide with a major peak in rock-avalanche activity in Norway. The timing of a mid-Holocene cluster with three to six individual CRSF events has been connected to climate variation during the Holocene, especially in relation to a climatic deterioration at the end of the Holocene Climate Optimum. Higher precipitation connected to a strong seasonality, temperature changes and rock mass strength alterations related to permafrost degradation are possible climatic conditions responsible for the mid-Holocene crisis at Mannen.

Acknowledgements

The TCN sample preparation was mostly completed by the first author at CRISDAL at Dalhousie University under supervision of G. Yang. Field assistance was provided by F. Magnin, B. Altena and S. Westermann (all University of Oslo) and B.R. Snook (NTNU). Discussions about the mapping investigations with R. Eilertsen, L. Rubensdotter and L. Hansen (all NGU) improved the study significantly. We thank G. Gilbert for reviewing and improving the manuscript significantly before submission and thank S. Zerathe and two anonymous reviewers for their suggestions that allowed improving the former version of the manuscript.

Funding

The study is part of the project 'CryoWALL – Permafrost slopes in Norway' (243784/CLE) funded by the Research Council of Norway (RCN). Additional funding was provided by the Norwegian Geological Survey, Trondheim, and the Department of Geosciences, University of Oslo. JCG acknowledges support for the TCN laboratory from Canada Foundation for Innovation (21305 and 36158), NSERC and NSRIT grants.

ORCID iD

Reginald L Hermanns  <https://orcid.org/0000-0001-5577-5004>

References

- Agliardi F, Zanchi A and Crosta GB (2009) Tectonic vs. gravitational morphostructures in the Central Eastern Alps (Italy): Constraints on the recent evolution of the mountain range. *Tectonophysics* 474: 250–270.
- Aizebeokhai AP (2010) 2D and 3D geoelectrical resistivity imaging: Theory and field design. *Scientific Research and Essays* 5: 3592–3605.
- Allen SK, Gruber S and Owens IF (2009) Exploring steep bedrock permafrost and its relationship with recent slope failures in the Southern Alps of New Zealand. *Permafrost and Periglacial Processes* 20: 345–356.
- Ballantyne CK and Stone JO (2013) Timing and periodicity of paraglacial rock-slope failures in the Scottish Highlands. *Geomorphology* 186: 150–161.
- Ballantyne CK, Sandeman GF, Stone JO et al. (2014) Rock-slope failure following Late Pleistocene deglaciation on tectonically stable mountainous terrain. *Quaternary Science Reviews* 86: 144–157.
- Ballantyne CK, Stone JO and Fifield LK (1998) Cosmogenic ^{36}Cl dating of postglacial landsliding at the Storr, Isle of Skye, Scotland. *The Holocene* 8: 347–351.
- Barnett C, Dumayne-Peaty L and Matthews JA (2001) Holocene climatic change and tree-line response in Leirdalen, central Jotunheimen, south central Norway. *Review of Palaeobotany and Palynology* 117: 119–137.
- Blikra LH and Christiansen HH (2014) A field-based model of permafrost-controlled rockslide deformation in northern Norway. *Geomorphology* 208: 34–49.
- Blikra LH and Nemeč W (1998) Postglacial colluvium in western Norway: Depositional processes, facies and palaeoclimatic record. *Sedimentology* 45: 909–959.
- Blikra LH and Selvik SF (1998) Climatic signals recorded in snow avalanche-dominated colluvium in western Norway: Depositional facies successions and pollen records. *The Holocene* 8: 631–658.
- Blikra LH, Longva O, Braathen A et al. (2006) Rock slope failures in Norwegian fjord areas: Examples, spatial distribution and temporal pattern. In: Evans SG, Mugnozsa GS, Strom A et al. (eds) *Landslides from Massive Rock Slope Failure* (NATO Science Series, vol. 49). Dordrecht: Springer, pp. 475–496.
- Blikra LH, Majala G, Anda E et al. (2016) *Fare-og risikoklassifisering av ustabile fjellparti – Faresoner, arealhåndtering og tiltak*. Report no. 77–2016, September. Oslo: NVE (in Norwegian).
- Bøe A-G, Dahl SO and Lie Nesje ØA (2006) Holocene river floods in the upper Glomma catchment, southern Norway: A high-resolution multiproxy record from lacustrine sediments. *The Holocene* 16: 445–455.
- Böhme M, Oppikofer T, Longva O et al. (2015) Analyses of past and present rock slope instabilities in a fjord valley: Implications for hazard estimations. *Geomorphology* 248: 464–474.
- Clavero J, Sparks R, Huppert H et al. (2002) Geological constraints on the emplacement mechanism of the Parinacota debris avalanche, northern Chile. *Bulletin of Volcanology* 64: 40–54.
- Corner GD (2006) A transgressive-regressive model of Fjord-Valley fill: Stratigraphy, facies and depositional controls. In: Dalrymple RW, Leckie DA and Tillman RW (eds) *Incised Valleys in Time and Space*. Broken Arrow, OK: SEPM (Special Publication no. 85), pp. 161–178.
- Cossart E, Braucher R, Fort M et al. (2008) Slope instability in relation to glacial debuitressing in alpine areas (Upper Durance catchment, southeastern France): Evidence from field data and ^{10}Be cosmic ray exposure ages. *Geomorphology* 95: 3–26.
- Crosta GB, Hermanns RL, Dehls J et al. (2017) Rock avalanches clusters along the northern Chile coastal scarp. *Geomorphology* 289: 27–43.
- Dortch JM, Owen LA, Haneberg WC et al. (2009) Nature and timing of large landslides in the Himalaya and Transhimalaya of northern India. *Quaternary Science Reviews* 28: 1037–1054.
- Eilertsen RS, Corner GD, Aasheim O et al. (2006) Valley-fill stratigraphy and evolution of the Målselv Fjord Valley, Northern Norway. In: Dalrymple RW, Leckie DA and Tillman RW (eds) *Incised Valleys in Time and Space*. Broken Arrow, OK: SEPM (Special Publication no. 85), pp. 179–195.
- Eilertsen RS, Corner GD, Aasheim O et al. (2011) Facies characteristics and architecture related to palaeodepth of Holocene fjord-delta sediments: Facies characteristics and architecture. *Sedimentology* 58: 1784–1809.
- Eilertsen RS, Corner GD and Hansen L (2015) Using LiDAR data to characterize and distinguish among different types of raised terraces in a fjord-valley setting. *GFF* 137: 353–361.
- Evans SG and Clague JJ (1994) Recent climatic change and catastrophic geomorphic processes in mountain environments. *Geomorphology* 10: 107–128.
- Fischer L, Käab A, Huggel C et al. (2006) Geology, glacier retreat and permafrost degradation as controlling factors of slope instabilities in a high-mountain rock wall: The Monte Rosa east face. *Natural Hazards and Earth System Sciences* 6: 761–772.
- Fischer L, Purves RS, Huggel C et al. (2012) On the influence of topographic, geological and cryospheric factors on rock avalanches and rockfalls in high-mountain areas. *Natural Hazards and Earth System Sciences* 12: 241–254.
- Gisnås K, Eitzelmüller B, Farbrot H et al. (2013) CryoGRID 1.0: Permafrost distribution in Norway estimated by a spatial numerical model. *Permafrost and Periglacial Processes* 24: 2–19.
- Gosse JC and Phillips F (2001) Terrestrial in situ cosmogenic nuclides: Theory and application. *Quaternary Science Reviews* 20: 1475–1560.
- Grämiger LM, Moore JR, Gischig VS et al. (2017) Beyond debuitressing: Mechanics of paraglacial rock slope damage during repeat glacial cycles. *Journal of Geophysical Research: Earth Surface* 122: 1004–1036.
- Grimstad E and Nerdal S (1991) Loen rockslides: A historical review. In: Barton M and Stephansson W (eds) *Rock Joints*. Rotterdam: Balkema, pp. 1–6.
- Groover KD, Burgess MK, Howle JF et al. (2016) *Electrical Resistivity Investigation of Fluvial Geomorphology to Evaluate Potential Seepage Conduits to Agricultural Lands Along the San Joaquin River, Merced County, California, 2012–13*. Report No. 2016–5172. Reston, VA: U.S. Geological Survey.
- Hansen L, Beylich A, Burki V et al. (2009) Stratigraphic architecture and infill history of a deglaciated bedrock valley based on georadar, seismic profiling and drilling. *Sedimentology* 56: 1751–1773.
- Hermanns RL and Longva O (2012) Rapid rock-slope failures. In: Clague JJ and Stead D (eds) *Landslides*. Cambridge: Cambridge University Press, pp. 59–70.
- Hermanns RL and Strecker M (1999) Structural and lithological controls on large quaternary rock avalanches (Sturzstroms) in arid northwestern Argentina. *Geological Society of America Bulletin* 111: 934–948.
- Hermanns RL, Blikra LH, Naumann M et al. (2006a) Examples of multiple rock-slope collapses from Köfels (Ötztal valley, Austria) and western Norway. *Engineering Geology* 83: 94–108.
- Hermanns RL, Fauqué L and Wilson CGJ (2015) ^{36}Cl terrestrial cosmogenic nuclide dating suggests Late Pleistocene to Early Holocene mass movements on the south face of Aconcagua

- mountain and in the Las Cuevas–Horcones valleys, Central Andes, Argentina. *Geological Society* 399: 345–368.
- Hermanns RL, Niedermann S, Garcia AV et al. (2001) Neotectonics and catastrophic failure of mountain fronts in the southern intra-Andean Puna Plateau, Argentina. *Geology* 29: 619.
- Hermanns RL, Niedermann S, Garcia AV et al. (2006b) Rock avalanching in the NW Argentine Andes as a result of complex interactions of lithologic, structural and topographic boundary conditions, climate change and active tectonics. In: Evans SG, Mugnozza GS, Strom A et al. (eds) *Landslides from Massive Rock Slope Failure*. Dordrecht: Springer, pp. 497–520.
- Hermanns RL, Niedermann S, Ivy-Ochs S et al. (2004) Rock avalanching into a landslide-dammed lake causing multiple dam failure in Las Conchas valley (NW Argentina)? Evidence from surface exposure dating and stratigraphic analyses. *Landslides* 1: 113–122.
- Hermanns RL, Schleier M, Böhme M et al. (2017) Rock-avalanche activity in W and S Norway peaks after the retreat of the Scandinavian Ice Sheet. In: Mikoš M, Vilimek V, Yin Y et al. (eds) *Advancing Culture of Living with Landslides*. Cham: Springer, pp. 331–338.
- Hermanns RL, Trauth MH, Niedermann S et al. (2000) Tephrochronologic constraints on temporal distribution of large landslides in northwest Argentina. *Geology* 108: 35–52.
- Hewitt K, Clague JJ and Orwin JF (2008) Legacies of catastrophic rock slope failures in mountain landscapes. *Earth-Science Reviews* 87: 1–38.
- Hewitt K, Gosse JC and Clague JJ (2011) Rock avalanches and the pace of late quaternary development of river valleys in the Karakoram Himalaya. *Geological Society of America Bulletin* 123: 1836–1850.
- Høgaas F, Hansen L, Rinstad BI et al. (2012) *Database for registrering av marin grense (MG) i Norge*. Report No. 2012.063, December. Trondheim: Geological Survey of Norway (in Norwegian).
- Holm K, Bovis M and Jakob M (2004) The landslide response of alpine basins to post-Little Ice Age glacial thinning and retreat in southwestern British Columbia. *Geomorphology* 57: 201–216.
- Hughes ALC, Gyllencreutz R, Lohne ØS et al. (2016) The last Eurasian ice sheets – A chronological database and time-slice reconstruction, DATED-1. *Boreas* 45: 1–45.
- Ivy-Ochs S and Kober F (2008) Surface exposure dating with cosmogenic nuclides. *Quaternary Science Journal* 57: 179–209.
- Ivy-Ochs S, Martin S, Campedel P et al. (2017) Geomorphology and age of the Marocche di Dro rock avalanches (Trentino, Italy). *Quaternary Science Reviews* 169: 188–205.
- Jarman D, Calvet M, Corominas J et al. (2014) Large-scale rock slope failures in the eastern Pyrenees: Identifying a sparse but significant population in paraglacial and parafluvial contexts. *Geografiska Annaler: Series A, Physical Geography* 96: 357–391.
- Jia H, Leith K and Krautblatter M (2017) Path-dependent frost-wedging experiments in fractured, low-permeability granite. *Permafrost and Periglacial Process* 28: 698–709.
- Jia H, Xiang W and Krautblatter M (2015) Quantifying rock fatigue and decreasing compressive and tensile strength after repeated freeze-thaw cycles. *Permafrost and Periglacial Process* 26: 368–377.
- Köpfli P, Grämiger L, Moore JR et al. (2017) The Oeschinensee rock avalanche, Bernese Alps, Switzerland: A co-seismic failure 2300 years ago? *Swiss Journal of Geosciences* 111: 205–219.
- Korup O (2004) Geomorphometric characteristics of New Zealand landslide dams. *Engineering Geology* 73: 13–35.
- Korup O, Densmore AL and Schlunegger F (2010) The role of landslides in mountain range evolution. *Geomorphology* 120: 77–90.
- Krautblatter M and Leith K (2015) Glacier- and permafrost-related slope instabilities. In: Huggel C, Carey M, Clague JJ et al. (eds) *The High-Mountain Cryosphere: Environmental Changes and Human Risks*. Cambridge: Cambridge University Press, pp. 147–165.
- Krautblatter M, Funk D and Günzel FK (2013) Why permafrost rocks become unstable: A rock-ice-mechanical model in time and space. *Earth Surface Processes and Landforms* 38: 876–887.
- Leith K, Moore JR, Amann F et al. (2014) In situ stress control on microcrack generation and macroscopic extensional fracture in exhuming bedrock. *Journal of Geophysical Research: Solid Earth* 119: 594–615.
- Lilleøren KS, Etzelmüller B, Schuler TV et al. (2012) The relative age of mountain permafrost – Estimation of Holocene permafrost limits in Norway. *Global and Planetary Change* 92–93: 209–223.
- Longva O, Blikra LH and Dehls JF (2009) *Rock Avalanches: Distribution and Frequencies in the Inner Part of Storfjorden, Møre og Romsdal County*. Report No. 2009.002, 15 March. Trondheim: Geological Survey of Norway (in Norwegian).
- Lønne I (1995) Sedimentary facies and depositional architecture of ice-contact glaciomarine systems. *Sedimentary Geology* 98: 13–43.
- McSaveney MJ (2002) Recent rockfalls and rock avalanches in Mount Cook National Park, New Zealand. In: Evans SG and Degraff JV (eds) *Catastrophic Landslides: effects, occurrence, and mechanisms*. Boulder, CO: Geological Society of America, pp. 35–70.
- Moreiras SM, Hermanns RL and Fauqué L (2015) Cosmogenic dating of rock avalanches constraining quaternary stratigraphy and regional neotectonics in the Argentine Central Andes (32° S). *Quaternary Science Reviews* 112: 45–58.
- Murton JB, Peterson R and Ozouf J-C (2006) Bedrock fracture by ice segregation in cold regions. *Science* 314: 1127–1129.
- Myhra KS, Westermann S and Etzelmüller B (2017) Modelled distribution and temporal evolution of permafrost in steep rock walls along a latitudinal transect in Norway by CryoGrid 2D. *Permafrost and Periglacial Processes* 28: 172–182.
- Nagelisen J, Moore JR, Vockenhuber C et al. (2015) Post-glacial rock avalanches in the Obersee Valley, Glarner Alps, Switzerland. *Geomorphology* 238: 94–111.
- Nesje A, Matthews JA, Dahl SO et al. (2001) Holocene glacier fluctuations of Flatebreen and winter-precipitation changes in the Jostedalbreen region, western Norway, based on glaciolacustrine sediment records. *The Holocene* 11: 267–280.
- NGU (2018) Kwartærgeologiske Kart (Løsmassekart). Available at: <http://geo.ngu.no/kart/losmasse/> (accessed 17 April 2018) [in Norwegian].
- North Greenland Ice Core Project Members (2004) High-resolution record of Northern Hemisphere climate extending into the last interglacial period. *Nature* 431: 147–151.
- NVE (2018) NVE Atlas. Available at: <https://atlas.nve.no/Html5Viewer/index.html?viewer=nveatlas#> (accessed 13 February 18) [in Norwegian].
- NVE, met.no and Kartverket (2018) seNorge. Available at: <http://www.senorge.no/> (accessed 17 April 2018).
- Oppikofer T, Saintot A, Otterå S et al. (2013) *Investigations on Unstable Rock Slopes in Møre og Romsdal – Status And Plans After Field Surveys in 2012*. Report No. 2013.014, 13 November. Trondheim: Geological Survey of Norway (in Norwegian).
- Orwin JF, Clague JJ and Gerath RF (2004) The Cheam rock avalanche, Fraser Valley, British Columbia, Canada. *Landslides* 1: 289–298.
- Ostermann M and Sanders D (2017) The Benner pass rock avalanche cluster suggests a close relation between long-term

- slope deformation (DSGSDs and translational rock slides) and catastrophic failure. *Geomorphology* 289: 44–59.
- Ostermann M, Ivy-Ochs S, Diethard S et al. (2016) Multi-method (^{14}C , ^{36}Cl , $^{234}\text{U}/^{230}\text{Th}$) age bracketing of the Tschirgant rock avalanche (Eastern Alps): Implications for absolute dating of catastrophic mass wasting. *Earth Surface Processes and Landforms* 42: 1110–1118.
- Ostermann M, Sanders D, Ivy-Ochs S et al. (2012) Early Holocene (8.6ka) rock avalanche deposits, Obernberg valley (Eastern Alps): Landform interpretation and kinematics of rapid mass movement. *Geomorphology* 17: 183–293.
- Ouimet WB, Whipple KX, Royden LH et al. (2007) The influence of large landslides on river incision in a transient landscape: Eastern margin of the Tibetan Plateau (Sichuan, China). *Geological Society of America Bulletin* 119: 1462–1476.
- Palacky GJ (1988) Resistivity characteristics of geologic targets. In: Nabighian M (ed.) *Electromagnetic Methods in Applied Geophysics, Theory: Investigations in Geophysics*. Tulsa, OK: SEG Books, pp. 52–129.
- Penna IM, Hermanns RL, Niedermann S et al. (2011) Multiple slope failures associated with neotectonic activity in the Southern Central Andes (37° – $37^{\circ}30'\text{S}$), Patagonia, Argentina. *Geological Society of America Bulletin* 123: 1880–1895.
- Plafker G and Ericksen GE (1978) Nevados Huascarán Avalanches, Peru. In: Voight B (ed.) *Developments in Geotechnical Engineering, Rockslides and Avalanches*, vol. 1. New York: Elsevier, pp. 277–314.
- Plug LJ, Gosse JC, McIntosh JJ et al. (2007) Attenuation of cosmic ray flux in temperate forest. *Journal of Geophysical Research: Earth Surface* 112: F02022.
- Reusch H (1907) Skredet i Loen 15. Januar 1905. Norges Geologiske Undersøkelse, Aarbok 1907. Kristiania: Aschehoug & Co., 20 pp (in Norwegian with English summary).
- Roberts D (2003) The Scandinavian Caledonides: Event chronology, palaeogeographic settings and likely modern analogues. *Tectonophysics* 365: 283–299.
- Saintot A, Dahle H, Derron M-H et al. (2012) Large gravitational rock slope deformation in Romsdalen valley (Western Norway). *Revista de la Asociación Geológica Argentina* 69: 354–371.
- Sanchez G, Rolland Y, Corsini M et al. (2010) Relationships between tectonics, slope instability and climate change: Cosmic ray exposure dating of active faults, landslides and glacial surfaces in the SW Alps. *Geomorphology* 117: 1–13.
- Schleier M, Hermanns RL, Gosse JC et al. (2016) Subaqueous rock-avalanche deposits exposed by post-glacial isostatic rebound, Innfjordalen, Western Norway. *Geomorphology* 289: 117–133.
- Schleier M, Hermanns RL, Rohn J et al. (2015) Diagnostic characteristics and paleodynamics of supraglacial rock avalanches, Innerdalen, Western Norway. *Geomorphology* 245: 23–39.
- Soldati M, Corsini A and Pasuto A (2004) Landslides and climate change in the Italian Dolomites since the Late glacial. *CATENA* 55: 141–161.
- Steiger C, Eitzelmüller B, Westermann S et al. (2016) Modelling the permafrost distribution in steep rock walls. *Norwegian Journal of Geology* 96: 329–341.
- Storms JEA, de Winter IL, Overeem I et al. (2012) The Holocene sedimentary history of the Kangerlussuaq Fjord-valley fill, West Greenland. *Quaternary Science Reviews* 35: 29–50.
- Stroeven AP, Hätttestrand C, Kleman J et al. (2016) Deglaciation of Fennoscandia. *Quaternary Science Reviews* 147: 91–121.
- Sturzenegger M, Stead D, Gosse J et al. (2015) Reconstruction of the history of the Palliser Rockslide based on ^{36}Cl terrestrial cosmogenic nuclide dating and debris volume estimations. *Landslides* 12: 1097–1106.
- Svendsen JI and Mangerud J (1987) Late Weichselian and Holocene sea-level history for a cross-section of western Norway. *Journal of Quaternary Science* 2: 113–132.
- Tønnesen JF (2009) *Georadarmålinger ved Rønningen og Horgheim i Romsdalen for undersøkelse av løsmassetyper i dalbunnen under det ustabile fjellpartiet Mannen*. Report No. 2009.062, 11 November. Trondheim: Geological Survey of Norway (in Norwegian).
- Topping DJ (1993) Paleogeographic reconstruction of the Death Valley extended region: Evidence from Miocene large rock-avalanche deposits in the Amargosa Chaos Basin, California. *Geological Society of America Bulletin* 105: 1190–1213.
- Trauth MH, Alonso RA, Haselton KR et al. (2000) Climate change and mass movements in the NW Argentine Andes. *Earth and Planetary Science Letters* 179: 243–256.
- Tveten E, Lutro O and Thorsnes T (1998) *Geologisk kart over Norge, berggrunnskart Ålesund, 1:250,000*. Trondheim: Geological Survey of Norway.
- Vasskog K, Nesje A, Støren EN et al. (2011) A Holocene record of snow-avalanche and flood activity reconstructed from a lacustrine sedimentary sequence in Oldevatnet, western Norway. *The Holocene* 21: 597–614.
- Westermann S, Schuler TV, Gislén K et al. (2013) Transient thermal modeling of permafrost conditions in Southern Norway. *The Cryosphere* 7: 719–739.
- Zerathe S, Lebourg T, Braucher R et al. (2014) Mid-Holocene cluster of large-scale landslides revealed in the Southwestern Alps by ^{36}Cl dating. Insight on an Alpine-scale landslide activity. *Quaternary Science Reviews* 90: 106–127.
- Zimmerman SR, Evenson EB, Gosse JC et al. (1994) Extensive Boulder erosion resulting from a range fire on the type-pinedale Moraines, Fremont Lake, Wyoming. *Quaternary Research* 42: 255–265.

Paper III

Hilger, P., Hermanns, R.L., Etzelmüller, B., Myhra, K.S., Gosse, J.C.:

Is climate a first order control on rock-slope deformation in Norway? - Reconstructing the sliding and permafrost history of selected rockslides

Manuscript prepared for submission

Note on contributions

The candidate wrote the paper and carried out all field work and analyses, including sample processing, calculation of exposure ages and acquiring and analysing climate data. The project idea and sampling strategy comes from the second author who contributed significantly by selecting field sites and providing data. Additional climate data was collected and prepared for permafrost modelling by the third author, who contributed considerably during the writing process of the manuscript. The fourth author developed and applied the long-term permafrost model, while the fifth author advised the candidate during sample processing and age calculations. All authors contributed to finalising the manuscript.

Part III

Appendices

A Tables

Table A.1: Sample characteristics for all samples processed (and re-analysed) during this doctoral study

Site	Sample name	Lat.	Long.	Elev.	Rock type	Land-form	Thickness	Boulder dimensions	Dip direction/dip	Total shielding	Year	
		dd	dd	m asl.			cm	m				
Mannen	MANN-00	62.4559	7.7714	1290.0	quartzite	1	2.5		flat	0.9975	2015	
	MANN-07	62.4650	7.7932	70.3	granite	3	1.0	2 x 4 x 3	264/20	0.9134	2015	
	MANN-10	62.4652	7.7969	62.9	gneiss	3	2.5	5 x 5 x 2.5	302/10	0.9179	2015	
	MANN-23	62.4658	7.7955	67.8	granite	3	5.0	2 x 1 x 0.5	074/30	0.8987	2015	
	MANN-26	62.4653	7.7956	68.1	gneiss	3	3.5	15 x 7 x 7	000/20	0.9166	2015	
	MANN-28	62.4692	7.7839	138.6	gneiss	3	4.5	4 x 3 x 2.5	234/10	0.9039	2015	
	MANN-31	62.4663	7.7888	111.3	gneiss	3	3.5	4 x 1.5 x 4	358/36	0.8960	2015	
	MANN-32	62.4665	7.7883	110.2	gneiss	3	4.0	12 x 3,5 x 2	254/18	0.8715	2015	
	MANN-35	62.4681	7.7867	117.4	gneiss	3	2.5	7 x 6 x 2.5	181/32	0.8933	2015	
	MANN-36	62.4680	7.7864	116.3	gneiss	3	2.5	4 x 3 x 2.5	315/12	0.9059	2015	
	MANN-37	62.4700	7.7864	95.4	gneiss	3	1.5	8 x 6 x 8	071/26	0.8947	2015	
	MANN-38	62.4707	7.7871	87.9	gneiss	3	5.0	5 x 1.5 x 1.5	084/20	0.8899	2015	
	MANN-39	62.4712	7.7850	78.3	gneiss	3	2.0	5 x 2 x 1.5	132/26	0.8761	2015	
	MANN-40	62.4704	7.7828	116.9	gneiss	3	4.0	2.5 x 2 x 1	305/15	0.8959	2015	
	Punta Cola	PCOL-01	-45.3782	-73.0019	240.0	granite	3	2.5	2 x 2 x 2	226/26	0.9312	2016
		PCOL-02	-45.3801	-73.0013	247.0	granite	3	3.0	4 x 2 x 5	211/14	0.9435	2016
PCOL-03		-45.3797	-73.0030	224.0	granite	3	1.5	2.5 x 2 x 1.5	280/29	0.9432	2016	
PCOL-04		-45.3820	-73.0077	111.0	granite	3	0.7	1 x 1.5 x 0.5	176/13	0.9054	2016	
PCOL-07		-45.3867	-73.0089	65.0	granite	3	2.0	2.5 x 5 x 1.5	089/20	0.9635	2016	
PCOL-08		-45.3829	-73.0065	144.0	granite	3	1.5	1.5 x 1.5 x 2	188/10	0.9254	2016	

A Tables

Revdalsfjellet 1	RDF-01	69.4705	20.3574	663.3	quartzite	1	2.0	1 x 1 x 0.2	230/10	0.9977	2015
	REV-01	69.4703	20.3558	643.9	gneiss	2	6.0		326/80	0.6841	2009
	REV-02	69.4703	20.3558	642.6	gneiss	2	5.5		322/62	0.6664	2009
	REV-04	69.4703	20.3558	636.6	gneiss	2	2.5		315/82	0.6523	2009
	REV-06	69.4703	20.3558	633.0	gneiss	2	2.0		320/51	0.6225	2009
	RDF-03	69.4729	20.3583	680.5	gneiss	1	3.0	bedrock	flat	0.9980	2015
Revdalsfjellet 2	REV-11	69.4728	20.3578	675.1	gneiss	2	5.0		298/53	0.7499	2009
	REV-13	69.4728	20.3578	669.7	gneiss	2	2.5		300/59	0.6618	2009
	REV-16	69.4728	20.3578	661.1	gneiss	2	3.5		310/59	0.6621	2009
	REV-17	69.4728	20.3578	658.5	gneiss	2	3.5		310/59	0.7150	2009
	Opp-1*	62.6982	6.8333	696.0	gneiss	2	3.0			0.7700	2003
Opp...t	Opp-4*	62.6982	6.8333	689.0	gneiss	2	3.0			0.7685	2003
	Opp-5*	62.6982	6.8333	687.0	gneiss	2	3.0			0.7677	2003
	SKJ-01†	61.4422	7.4168	779.1	phyllite	2	4.0		115/72	0.7042	2008
Skjer...haugane 1-3	SKJ-03†	61.4422	7.4168	773.8	phyllite	2	2.0		114/55	0.6918	2008
	SKJ-04†	61.4438	7.4194	738.3	phyllite	2	4.0		122/65	0.6992	2008
	SKJ-08†	61.4438	7.4194	725.0	phyllite	2	5.0		111/60	0.7243	2008
	SKJ-09†	61.4423	7.4181	757.4	phyllite	2	5.0		130/39	0.8830	2008
	SKJ-12†	61.4423	7.4181	746.3	phyllite	2	3.0		117/58	0.7016	2008
	ROM-01	68.4431	17.6133	75.0	mica schist	3	1.5	8 x 8 x 10	156/10	0.9705	2016
Rombakstøtta	ROM-03	68.4413	17.6129	116.0	mica schist	3	1.5	5 x 6 x 3	210/08	0.9623	2016
	ROM-04	68.4415	17.6147	119.0	mica schist	3	2.0	4 x 3 x 4	298/25	0.9619	2016
	ROM-05	68.4405	17.6152	174.0	mica schist	3	1.5	7 x 7 x 4	020/27	0.9715	2016
	ROM-06	68.4403	17.6147	160.0	mica schist	3	3.0	2 x 5 x 1.5	080/23	0.9659	2016

ROM-08	68.4400	17.6143	170.0	mica schist	3	1.5	4 x 3 x 3	flat	0.9642	2016
ROM-09	68.4436	17.6014	75.0	mica schist	3	2.0	2 x 3 x 3	271/10	0.9579	2016
ROM-12	68.4430	17.6024	102.0	mica schist	3	3.0	1.5 x 2.5 x 1	290/27	0.9502	2016
ROM-13	68.4427	17.6008	119.0	mica schist	3	3.0	5 x 3 x 5	235/36	0.9225	2016
FLAAM-01	60.8324	7.1304	274.3	phyllite	3	2.0	4 x 4 x 3	282/05	0.9690	2016
FLAAM-02	60.8323	7.1282	213.5	phyllite	3	2.5	8 x 2 x 1	332/12	0.9576	2016
FLAAM-03	60.8309	7.1258	162.3	phyllite	3	1.0	6 x 8 x 6	320/25	0.9607	2016
FLAAM-05	60.8403	7.1402	533.2	phyllite	3	2.5	1.5 x 2 x 1.5	205/08	0.9383	2016
FLAAM-06	60.8402	7.1416	569.5	phyllite	3	3.0	3.5 x 2 x 2	205/22	0.9628	2016
FLAAM-07	60.8418	7.1433	591.1	phyllite	3	2.0	6 x 3 x 3	358/13	0.9538	2016
FLAAM-09	60.8406	7.1272	165.7	phyllite	3	2.0	1.5 x 2 x 1.5	152/07	0.9582	2016
FLAAM-10	60.8401	7.1275	167.2	phyllite	3	1.5	4 x 1.5 x 4	183/19	0.9541	2016
FLAAM-11	60.8403	7.1268	177.7	phyllite	3	4.0	3 x 1.5 x 3	095/15	0.9602	2016
FLAAM-12	60.8369	7.1300	247.2	phyllite	3	5.0	10 x 5 x 2	135/16	0.9649	2016
FLAAM-13	60.8375	7.1294	229.9	phyllite	3	2.0	10 x 8 x 10	280/32	0.9593	2016
FLAAM-14	60.8371	7.1288	205.4	phyllite	3	3.0	4 x 2.5 x 1.5	328/24	0.9586	2016

Fammanosi

*Hermanns et al. (2013c)

†Hermanns et al. (2012b)

A Tables

Table A.2: ^{10}Be concentrations and apparent exposure ages of all sampled CRSF boulders calculated with the LSDn scaling scheme (Lifton, 2016).

Site	Sample name	^{10}Be concentration	^{10}Be conc. uncertainty	Apparent exposure age	Int./ext. uncertainty
		10^3 atoms g^{-1}	10^3 atoms g^{-1}	ka	ka
Mannen	MANN-07	21.27	0.75	4.75	0.17/0.33
	MANN-10	22.04	0.69	5.00	0.16/0.34
	MANN-23	22.10	0.83	5.12	0.20/0.36
	MANN-26	26.03	0.77	5.93	0.18/0.39
	MANN-28	23.38	0.79	5.11	0.17/0.35
	MANN-31	22.81	0.80	5.03	0.18/0.35
	MANN-32	21.73	1.21	4.81	0.27/0.39
	MANN-35	45.42	2.34	9.92	0.52/0.79
	MANN-36	41.77	1.69	9.12	0.37/0.66
	MANN-37	21.07	0.69	4.70	0.16/0.32
	MANN-38	21.64	0.82	5.05	0.19/0.36
	MANN-39	21.19	0.73	4.88	0.17/0.34
	MANN-40	22.29	0.75	4.98	0.17/0.34
Punta Cola	PCOL-01	1.12	0.15	0.33	0.04/0.05
	PCOL-02	1.66	0.22	0.46	0.06/0.07
	PCOL-03	0.72	0.25	0.22	0.08/0.08
	PCOL-04	1.13	0.18	0.37	0.06/0.06
	PCOL-07	1.17	0.16	0.38	0.05/0.06
	PCOL-08	6.97	1.68	1.76	0.42/0.44
Rombakstøtta	ROM-01	47.37	1.37	9.77	0.29/0.65
	ROM-03	49.32	165	9.86	0.33/0.68
	ROM-04	35.37	1.14	7.09	0.23/0.48
	ROM-05	52.74	1.47	9.87	0.28/0.65
	ROM-06	51.00	1.88	9.86	0.37/0.69
	ROM-08	63.74	1.79	12.13	0.35/0.80
	ROM-09	43.65	1.26	9.16	0.27/0.61
	ROM-12	0.437	0.34	0.86	0.07/0.08
	ROM-13	15.53	0.58	3.20	0.12/0.23
Ramnanosi	FLAAM-01	30.04	0.97	5.38	0.17/0.36
	FLAAM-02	39.54	1.26	7.63	0.25/0.52
	FLAAM-03	41.45	1.19	8.21	0.24/0.54
	FLAAM-05	96.36	2.63	14.04	0.39/0.93
	FLAAM-06	89.07	2.45	12.35	0.35/0.82
	FLAAM-07	55.81	1.74	7.52	0.24/0.51
	FLAAM-09	65.93	1.82	13.29	0.37/0.88
	FLAAM-10	51.17	1.42	10.23	0.29/0.67
	FLAAM-11	41.40	1.21	8.45	0.25/0.56
	FLAAM-12	19.17	0.97	3.60	0.18/0.28
	FLAAM-13	20.83	1.25	3.91	0.24/0.33
	FLAAM-14	28.62	1.08	5.59	0.21/0.39

B Publications

B.1 Peer-reviewed journal publications

Hilger P, Hermanns RL, Gosse JC, Jacobs B, Etzelmüller B, Krautblatter M, 2018. Multiple rock-slope failures from Mannen in Romsdal Valley, western Norway, revealed from Quaternary geological mapping and ^{10}Be exposure dating. *The Holocene* 28(12), 1841-1854, doi:10.1177/0959683618798165

Hilger P, Gosse JC, Hermanns RL, 2019. How significant is inheritance when dating rockslide boulders with terrestrial cosmogenic nuclide dating? — a case study of an historic event. *Landslides*, doi:10.1007/s10346-018-01132-0

Bøhme M, Hermanns RL, Gosse JC, **Hilger P**, Eiken T, Lauknes TR and Dehls J, 2019. Displacement acceleration on the Gamanjunni wedge compound slide, northern Norway: comparison of monitoring data with paleo-slip rates. *Geology*, doi:10.1130/G45684.1

Magnin F, Etzelmüller B, Westermann S, Isaksen K, **Hilger P** and Hermanns RL, 2019. Permafrost distribution in steep slopes in Norway: measurements, statistical distribution modelling and geomorphological implications. *Earth Surf. Dynam. Discuss.*, in review, doi:10.5194/esurf-2018-90

Hilger P, Hermanns RL, Etzelmüller B, Myhra KS, Gosse JC. Is climate a first order control on rock-slope deformation in Norway? - Reconstructing the sliding and permafrost history of selected rockslides. *manuscript prepared for submission*

B.2 Conference paper

Hermanns RL, Schleier M, Böhme M, Blikra LH, Gosse J, Ivy-Ochs S and **Hilger P**, 2017. Rock-avalanche activity in W and S Norway peaks after the retreat of the Scandinavian Ice Sheet. In: Mikoš M, Vilímek V, Yin Y et al. (eds) *Advancing Culture of Living with Landslides*. Cham: Springer, pp. 331–338.

B.3 Conference proceedings

Hilger P, Hermanns RL, Gosse JC and Etzelmüller B, 2016. *Evaluation of rock slope failures and rockslides in steep permafrost slopes using ^{10}Be - and ^{36}Cl -dating*. In: Proceedings of the 3rd Nordic Workshop on cosmogenic nuclide techniques; 2016 June 8-10, Stockholm University, Sweden, pp. 8f.

Hilger P, Hermanns RL, Etzelmüller B, Westermann S, Krautblatter M, Gosse JC, Magnin F and Jacobs B, 2016. *Evaluation of rock slope failures in steep permafrost slopes in Norway - first insights in the geological history of the Mannen unstable rock slope in Møre og Romsdal*. In: Proceedings of the XI. International Conference On Permafrost; 2016 June 20-24, Potsdam, Germany.

Hilger P, Hermanns RL, Etzelmüller B and Magnin F, 2016. *Climate factors as triggering mechanism for rock slope failures and rockslides in Norway*. In: Proceedings of the Nordic Climate PhD Conference; 2016 September 26-28, Upsete, Norway.

Hilger P, Hermanns RL, Gosse JC, Jacobs B and Krautblatter M, 2016. *Rekonstruktion der postglazialen Hanginstabilitäten am Mannen (Norwegen) mithilfe von ^{10}Be - und ^{36}Cl Datierung*. In: Proceedings of the AK Geomorphologie; 2016 October 6-7, Friedrich-Schiller-Universität Jena, Germany.

Hilger P, Hermanns RL, Sæterdal Myhra K, Gosse JC, Ivy-Ochs S and Etzelmüller B, 2017. *Rock slope failure activity and geological crises in western Norway*. In: Proceedings of the EGU General Assembly 2017; May 24-28, Vienna, Austria. (presented by R. Hermanns)

Hilger P, Sæterdal Myhra K, Hermanns RL, Magnin F, Etzelmüller B and Gosse JC, 2017. *Post-glacial timing of rock-slope destabilisation*. In: Proceedings of the 2nd Asian Conference on Permafrost ACOP; 2017 July 3-6, Sapporo, Japan.

Hilger P, Penna I, Hermanns RL, Oppikofer T and Gosse JC, 2017. *Insights into landslide systematics nine years after the Punta Cola rock-avalanche failure, Aysén Fjord, Chile*. In: Proceedings of the 4th Central European Geomorphology Conference; 2017 October 09-13, University of Bayreuth, Germany.

Hilger P, Hermanns RL, Myhra KS, Gosse JC and Etzelmüller B, 2017. *Temporal distribution of rock-slope failure activity in western and northern Norway*. In: Proceedings of Geofaredagen 2017; October 19-20, Norges geofysiske institutt (NGI) Oslo, Norway.

Hilger P, Hermanns RL, Magnin F, Myhra KS, Etzelmüller B and Gosse JC, 2018. *Destabilisation and deformation patterns of rock-slope instabilities in northern and western Norway*. In: Proceedings of the 33rd Nordic Geological Winter Meeting; January 10-12, Geological Society of Denmark, Copenhagen, Denmark.

Hilger P, Hermanns RL, Gosse JC, Myhra KS, Magnin F and Etzelmüller B, 2018. *Initial failure timing of gradually moving rockslides in northern and western Norway*. In: Geophysical Research Abstracts, Vol. 20, EGU General Assembly 2018, April 8-13, Vienna, Austria.

Hilger P, Hermanns RL and Gosse JC, 2018. *Implications of inherited isotope concentrations when dating landslides with terrestrial cosmogenic nuclide dating*. In: Proceedings of the 4th Nordic Workshop on Cosmogenic Nuclides, June 4-6, University of Bergen, Gairanger, Norway.

Hilger P, Hermanns RL, Etzelmüller B, Myhra KS, Magnin F and Gosse JC, 2018. *Do deformation patterns and initial failure timing of rock-slope instabilities in Norway relate to permafrost dynamics?* In: Proceedings of the 5th European Conference on Permafrost, June 23-July 1, Chamonix, France.

B.4 Blog

Hilger P, 2018. *Mannern rockslide: The postman always rings twice; two post-glacial stability crises with multiple catastrophic rock-slope failures – is there more to come?* Guest post in: AGU landslide blog, November 7, Online access: blogs.agu.org/landslideblog/2018/11/07/mannern-holocene-1/.